CHAPTER 6 RESULTS AND DISCUSSION

6.1 Forces and Moment and Motions

Results are presented and discussed first for the data from the $FR_{z\theta}$ condition. Time-mean and -histories of the forces and moment data from static and dynamic PMM tests are presented in Section 6.1.1. In Section 6.1.2, hydrodynamic derivatives from forces and moment data are determined with the '*Multiple-Run*' and the '*Single-Run*' methods as introduced in Section 2.3.5, and results are compared between the methods by defining and evaluating the data-reconstruction error, E_R. Forces and moment, and the resulting hydrodynamic derivatives from the three different facilities data using ship-models with different size are compared in Section 6.1.3, where the trends of the hydrodynamic derivatives with the model-size are discussed. Heave, pitch, and roll motions of the model during the static and dynamic PMM tests for the $FR_{z\theta}$ and $FR_{z\theta\phi}$ conditions are presented in Section 6.1.4. Lastly, the effects of different mount-conditions including FX_0, $FX_{\sigma\tau}$, and $FR_{z\theta\phi}$ are discussed in Section 6.1.5. Note that all data presented herein are corrected for asymmetry as per discussed in Section 5.1.5.

6.1.1 Time-mean and -histories of Data

Time-mean values of static drift X, Y, and N are shown in Fig. 6-1 (a), (b), and (c), respectively, for Fr = 0.138, 0.280, and 0.410 cases. Data are fitted to quadratic, $X = A + B\beta^2$, and cubic, $Y, N = A\beta + B\beta^3$, functions, respectively, which can be re-written as $X = A \cdot (1 + \lambda)$ and $Y, N = A\beta \cdot (1 + \lambda)$, respectively, where λ is defined as

$$\lambda \equiv \frac{B}{A}\beta^2 \tag{6.1}$$

which is the ratio of the non-linear terms to the linear terms, representing the degree of non-linearity of data[9]. For $\beta << 10°$, $\lambda \approx 0$ (at $\beta = 5°$, $\lambda = 0.06$, 0.04, and 0.02 for X, Y, and N, respectively, at $Fr = 0.280$) and X in (a) is close to a constant value, i.e. $X = A$, and Y and N in (b) and (c) are nearly linear, i.e. $Y, N = A\beta$, with slope A seemingly independent of Fr. This is consistent with Longo et al. (2002) where the authors measured the resistance C_T, side force C_S, and drift moment C_M (corresponding to X, Y, and N, respectively) of the Series 60 $C_B = 0.6$ model in oblique towing for a range of $\beta = 0° - 10°$ and $Fr = 0.1 - 0.35$. The authors curve-fitted data as $C_T = a\beta + b$ and $C_{S,M} = a\beta^2 + b\beta + c$, respectively, and reported that for the former a is independent of Fr and for the latter b is nearly independent of Fr. For $\beta > 10°$, however, data become non-linear as $\lambda > 0$ (at $\beta = 10°$, $\lambda = 0.26$, 0.18, and 0.07 for X, Y, and N, respectively, at $Fr = 0.280$) and B exhibits rather strong dependency on Fr for all variables (See Fig. 6-9, where X_*, Y_v, and N_v correspond to A; X_{vv}, Y_{vvv}, and N_{vvv} correspond to B; and Δu corresponds to Fr).

Time-histories of the forced PMM motions, and those of the responses in forces and moment are shown in Fig. 6-2 for pure sway (left column), pure yaw (center column), and yaw and drift tests (right column), respectively. Forced motions are defined in equations (2.14a) – (2.14c) and (2.15) for pure sway, (2.16a) – (2.16c) for pure yaw, and (2.17a) – (2.17b) for yaw and drift tests, respectively (typical examples of the motions are illustrated in Fig. 2-4 (b), (c), and (d), respectively). Shown in Fig. 6-2 (a) are drift angle β for pure sway test (for β_{max} = 2°, 4°, and 10° cases), heading ψ for pure yaw (for r_{max} = 0.05, 0.15, 0.30, 0.45, 0.60, and 0.75 cases) and yaw and drift tests (for β = 9°, 10°, and

---

[9] λ can be rewritten by using the mathematic models (2.19a), (2.19b), and (2.19c) for X, Y, and N as:

$$\lambda = \frac{X_{vv}}{X_*}v^2;\ \frac{Y_{vvv}}{Y_v}v^2;\ \frac{N_{vvv}}{N_v}v^2$$

respectively.

11° cases with r_{max} fixed at 0.30), respectively. Specific test conditions are summarized in Table 3-3.

The responses in X, Y, and N shown in Fig. 6-2 are typically the 2nd-order dominant oscillations for X with super posed on the period-mean values, whereas the 1st-order dominant oscillations for Y and N with phase shifted with respect to the forced motions, except for the yaw and drift. For yaw and drift, the 1st-order oscillations are dominant with superposed on the period mean value for all variable. The forces and moment time-histories are expressed in Fourier series (FS) forms such as

$$\chi(t) = \chi_0 + \sum_n \chi_n \cos\left(n\omega t + \varphi_{\chi n}\right) \tag{6.2}$$

for $\chi = X$, Y, and N, where χ_0 is the period-mean of χ, and χ_n and $\varphi_{\chi n}$ are the nth-order amplitude and phase terms, respectively. In Table 6-1, the harmonic amplitudes χ_n for n = 1, … , 6 are presented in percentages of the data oscillation amplitudes and in averages of all β_{max} , r_{max} , and β cases, respectively. For pure sway, the 2nd-order amplitude X_2 is the largest, 72.8%, while the 4th- and 6th-order amplitudes X_4 and X_6 are also fairly large, 12.7% and 33.1%, respectively, for X; the 1st-order amplitudes Y_1 and N_1 are predominant 99.3% and 98%, respectively, whereas the higher-order amplitudes Y_3, Y_5 and N_3, N_5 are all small, less than about 3%, for Y and N. For pure yaw, the overall trends are similar as for pure sway whereas the 3rd-order amplitudes Y_3 and N_3 are relatively larger, 11.6% and 5.8%, respectively. For yaw and drift, the 1st-order amplitude X_1 is dominant, 69.4%, but the higher-order amplitudes $X_{2,3,4,5,6}$ are also large, about 10% - 30%, for X, and the 1st-order amplitudes Y_1 and N_1 are the largest, 93.5% and 98.0%, respectively, the 2nd-order amplitudes Y_2 and N_2 are the 2nd largest, 22.2% and 11.1%, respectively, and the higher-order amplitudes $Y_{3,4,5,6}$ and $N_{3,4,5,6}$ are all small, less than about 5%, for Y and N.

The 1st-order phase angles φ_{Y1} and φ_{N1} are seemingly constant from Fig. 6-2 where $\varphi_{Y1}/2\pi$ and $\varphi_{N1}/2\pi$ values about 0.09 (32°) and 0.02 (9°) for pure sway, about

0.28 (102°) and 0.29 (105°) for pure yaw, and about 0.29 and 0.28 for yaw and drift, respectively. However, those phase values are functions of the motion parameters such as y_{max}, ψ_{max}, ω, and/or β (or v_{max}, r_{max}, ω, and/or v) as will be discussed later.

Table 6-1 Harmonics of Dynamic Tests Time-histories (% Amplitude, Fr = 0.280).

Test	Var (χ)	χ_1	χ_2	χ_3	χ_4	χ_5	χ_6
Pure sway	X	-	72.8	-	12.7	-	33.1
	Y	99.3	-	3.1	-	2.1	-
	N	98.0	-	2.5	-	0.4	-
Pure yaw	X	-	66.8	-	23.9	-	31.8
	Y	89.2	-	11.6	-	2.9	-
	N	95.7	-	5.8	-	1.1	-
Yaw and drift	X	69.4	30.4	14.6	9.5	10.8	21.7
	Y	93.5	22.2	5.8	2.1	1.6	1.9
	N	98.0	11.1	3.0	0.7	0.9	0.8

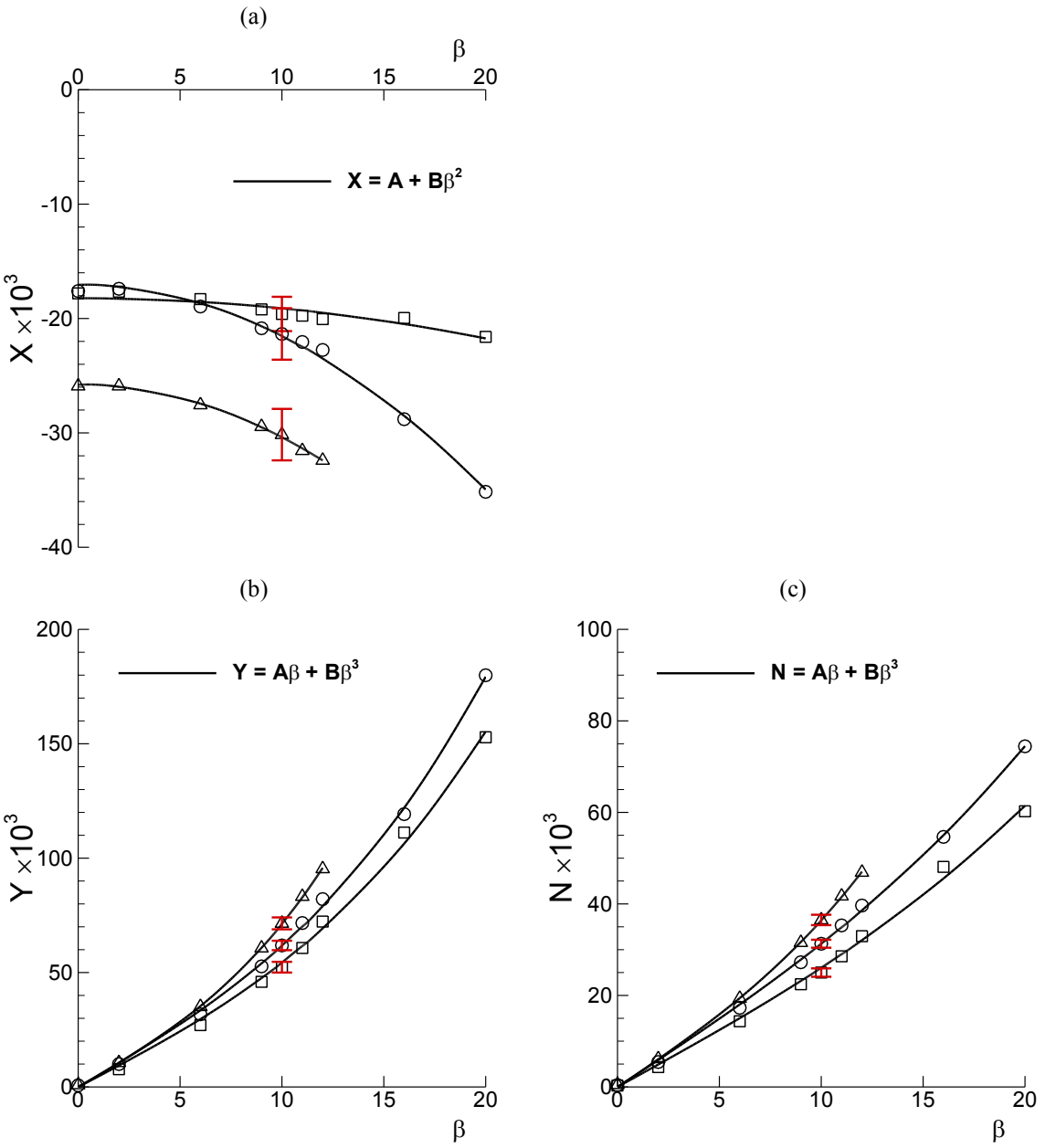

Figure 6-1 Static drift test data (Corrected for symmetry): (a) X, (b) Y, and (c) N. Symbols: □ Fr = 0.138, o Fr = 0.280, Δ Fr = 0.410.

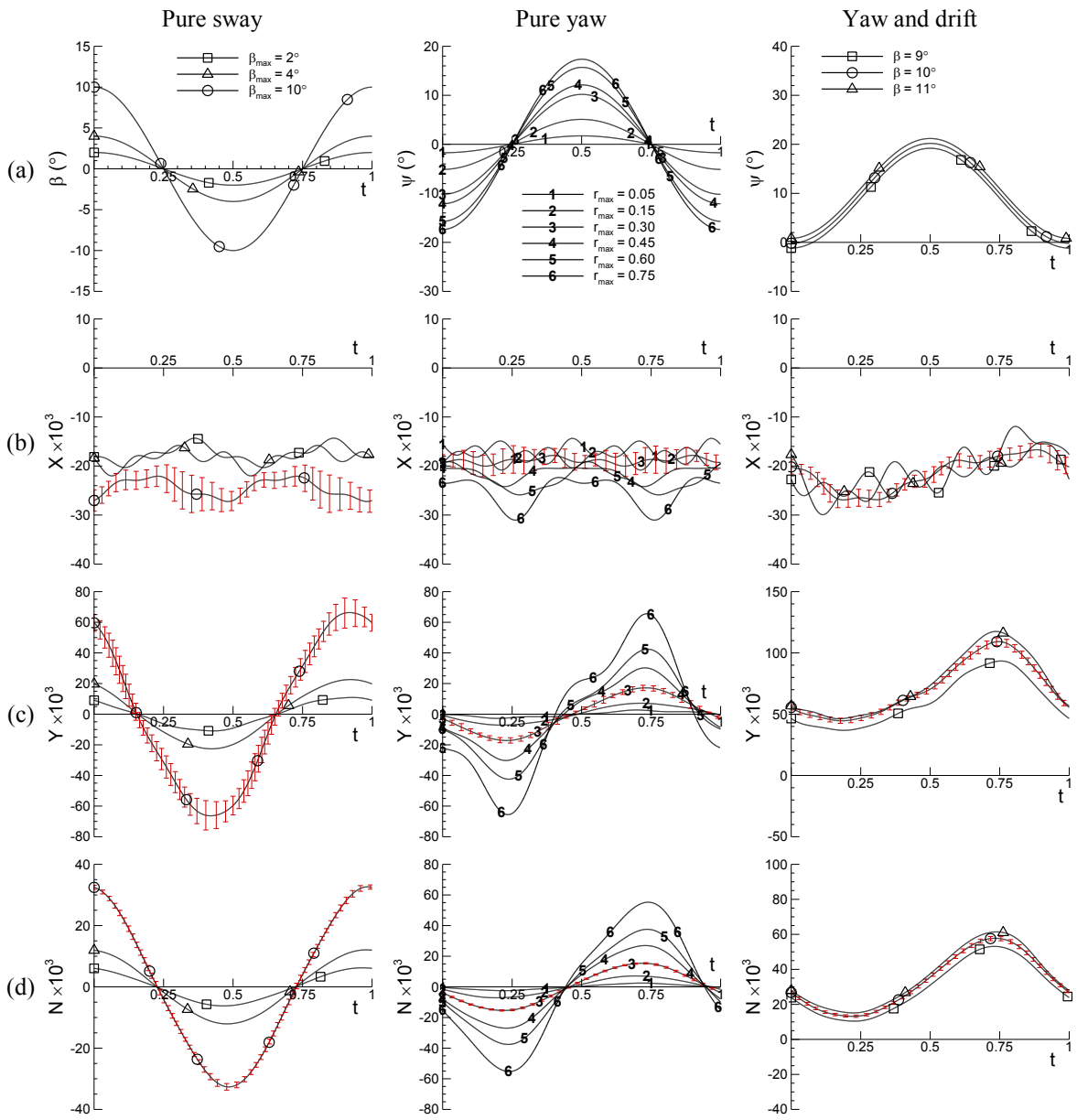

Figure 6-2 Time-histories for pure sway (left), pure yaw (center), and yaw and drift (right) tests at Fr = 0.280 (Corrected for symmetry): Forced-motions (a) β and ψ; and responses in (b) X, (c) Y, and (d) N.

6.1.2 Hydrodynamic Derivatives

6.1.2.1 Static drift test

Hydrodynamic derivatives X_*, X_{vv}, Y_v, Y_{vvv}, N_v, and N_{vvv} in the mathematic models (2.19) in Section 2.3.3 are presented in Table 6-2. Those derivatives were determined by fitting the time-mean values of static drift X, Y, and N data shown in Fig. 6-1 to the polynomial equations (2.27) by using the relation $v = -\sin\beta$ derived in (2.13). The polynomial coefficients A's and B's in (2.27) were evaluated by using a Least-Squared-error (LS) method and then used in (2.28) to determined the derivatives.

6.1.2.2 Dynamic tests

Hydrodynamic derivatives in the mathematic models (2.20), (2.22), and (2.24) in Section 2.3.3 are determined from the pure sway, pure yaw, and yaw and drift tests data, respectively, through the harmonics forms of the mathematic models, (2.21), (2.23), and (2.25), respectively. The harmonics X_0, X_{Sn}, X_{Cn}, Y_0, Y_{Sn}, Y_{Cn}, N_0, N_{Sn}, and N_{Cn} for n = 1, 2, or 3, in the mathematic models were evaluated as per (2.30) in Section 2.3.5 for the dynamic PMM tests X, Y, and N time-histories (e.g. Fig. 6-2), plotted in Figs. 6-3, 6-4, and 6-5 for pure sway, pure yaw, and yaw and drift tests data, respectively. In the figures, the harmonics data are plotted against v_{max} , $\dot{v}_{max}$, r_{max} , $\dot{r}_{max}$, or v as necessary per the mathematic models summarized in Table 2-3. Determinations of hydrodynamic derivatives are as per introduced in Section 2.3.5, either by using the '*Multiple-Run*' method (including MR_L and MR_H) or by using the '*Single-Run*' method (including SR_L and SR_H), as summarized in Tables 2-4 and 2-5, respectively.

'Multiple-Run' method:

Hydrodynamic derivatives using the MR_L and MR_H methods are presented in Tables 21 and 22, respectively. Herein, the results for MR_L are discussed first in the or-

der of sway, yaw, and cross-coupled derivatives, and then the derivatives from MR_H are compared with the MR_L.

Sway derivatives X_{vv} (including X_*), and Y_v, Y_{vvv} and N_v, N_{vvv}, and $Y_{\dot{v}}$ and $N_{\dot{v}}$ are determined from the pure sway data FS harmonics, shown in Fig. 6-3 (a) X_0, (c) Y_{C1} and N_{C1}, and (d) Y_{S1} and N_{S1}, respectively, for β_{max} = 2°, 4°, and 10° (correspond to v_{max} = 0.035, 0.070, and 0.174, respectively) cases. From Fig. 6-3 (a) and (c), harmonics data exhibit quadratic for X_0 and cubic for Y_{C1} and N_{C1} trends with v_{max} (i.e. with β_{max}), respectively, similarly as static drift data discussed previously in Section 6.1.1. However, the magnitudes of data are in general larger, smaller, and similar with (than) the static drift X, Y, and N data (shown as dashed lines), respectively. When λ is defined[10] similarly as for static drift data in (6-1), with β replaced with β_{max}, then λ = 0.43, 0.25, and 0.07 for X_0, Y_{C1}, and N_{C1} at β_{max} = 10°, respectively, indicating that the non-linearity of those harmonics data are more stronger than the static drift X, Y, and N data (λ = 0.26, 0.18, and 0.07, respectively, at β = 10° and at Fr = 0.280). This will be discussed again later at the MR_H method part. Y_{S1} and N_{S1} data shown in Fig. 6-3 (d) exhibit linear trend with $\dot{v}_{max}$ as expected from their mathematic models presented Table 2-3. In that Y_{S1} and N_{S1} stem from the acceleration terms ('added-mass') in the mathematic models (2.20b) and (2.20c) and Y_{C1} and N_{C1} from the velocity terms ('damping'), the ratios between the harmonics may of interest. For Y as an example, Y_{S1}/Y_{C1} represents the ratio

---

[10] λ can be rewritten by using the mathematic models for X_0, Y_{C1}, and N_{C1} shown in Table 2-3 as:

$$\lambda = \frac{1}{2}\frac{X_{vv}}{X_*}v_{max}^2 \; ; \; \frac{3}{4}\frac{Y_{vvv}}{Y_v}v_{max}^2 \; ; \; \frac{3}{4}\frac{N_{vvv}}{N_v}v_{max}^2$$

respectively.

between the 'added-mass' and 'damping' forces, which corresponds to the tangent value of the 1st-order phase of the Y time-history as[11]

$$\tan\varphi_{Y1} = \frac{Y_{\dot{v}}\omega}{Y_v(1+\lambda)} \tag{6.3}$$

Similarly, $\tan\varphi_{N1}$ can be written by replacing $Y_{\dot{v}}$ and Y_v in (6-3) with $N_{\dot{v}}$ and N_v, respectively. For λ = 0, then, the ratio (or the 1st-order phase) is a constant value, for present case, 0.730 and 0.135 (or, φ_{Y1} = 36.1° and φ_{N1} = 7.7°) for Y and N, respectively, for a given ω = 1.672, indicating that the 'damping' force is larger than the 'added-mass' force for Y and the former is predominant for N, respectively.

X_*, X_{vv}, Y_v, Y_{vvv}, N_v, and N_{vvv} are compared in Table 6-3 with those from the static drift data at Fr = 0.280 presented in Table 6-2. In general, the linear derivatives X_*, Y_v, and N_v are close to static drift values with ratios 1.02, 0.88, and 1.01, respectively, whereas the non-linear derivatives X_{vv}, Y_{vvv}, and N_{vvv} are larger with ratios 3.12, 1.53, and 1.30, respectively, possibly due to the stronger non-linearity in the pure sway FS harmonics data discussed previously.

Yaw derivatives X_{rr} (including X_*), and Y_r and Y_{rrr}, and $Y_{\dot{r}}$, and N_r and N_{rrr}, and $N_{\dot{r}}$ are determined from the pure yaw data FS harmonics, shown in Fig. 6-4 (a) X_0, (c) Y_{S1}, (d) Y_{C1}, (f) N_{S1}, and (g) N_{C1}, respectively, for r_{max} = 0.05 – 0.75 cases at Fr = 0.138, 0.280, and 0.410. In general, X_0, Y_{S1}, and N_{S1} in Fig. 6-4 (a), (c), and (f) exhibit curve shapes similar as the static drift X, Y, and N curves shown in Fig. 6-1. However, pure

---

[11] A combination of sine and cosine functions, $A\sin\omega t + B\cos\omega t$, can be rewritten as $\sqrt{A^2+B^2}\cdot\cos(\omega t+\varphi)$ where,

$$-\tan\varphi = A/B$$

In this case, $A = Y_{S1}$ and $B = Y_{C1}$, where $Y_{S1} = Y_{\dot{v}}\dot{v}_{max}$ and $Y_{C1} = -\left(Y_v v_{max} + \frac{3}{4}Y_{vvv}v_{max}^3\right)$, which can be rewritten as $Y_{S1} = Y_{\dot{v}}\omega\cdot v_{max}$ and $Y_{C1} = -Y_v\lambda\cdot v_{max}$, respectively.

yaw harmonics data are less non-linear with r_{max} with λ = 0.08, 0.06, and 0.07, respectively, at r_{max} = 0.30 (ψ_{max} = 10.2°) at Fr = 0.280, defined[12] similarly as (6-1) with β replaced with r_{max}, than static drift X, Y, and N data (λ = 0.26, 0.18, and 0.07, respectively, at β = 10° and at Fr = 0.280). Y_{C1} and N_{C1} shown in Fig. 6-4 (d) and (g) exhibit linear trend with $\dot{r}_{max}$ as expected from their mathematic models shown in Table 2-3, whereas more scatters in data curve-fits are observed (particularly for Y_{C1} at Fr = 0.280) than the pure sway Y_{S1} and N_{S1} data shown in Fig. 6-3 (d). The ratio Y_{S1}/Y_{C1} or N_{S1}/N_{C1} can be similarly defined as (3) for pure sway as (See footnote 11)

$$-\tan\varphi_{Y1} = \frac{Y_r(1+\lambda)}{Y_{\dot{r}}\omega} \tag{6.4}$$

and $\tan\varphi_{N1}$ as well, which are the ratios of the 'damping' force to the 'added-mass' force as discussed previously. For λ = 0 (and for a fixed ω = 1.672), the ratios are 3.223 and 4.144 (or, φ_{Y1} = 107.2° and φ_{N1} = 103.6°) for Y and N, respectively, at Fr = 0.280, indicating that the 'damping' forces are about three and four times, respectively, larger than the 'added-mass' forces.

Cross-coupled derivatives X_{vr}, Y_{rvv} and N_{rvv}, and Y_{vrr} and N_{vrr} are from the yaw and drift data FS harmonics, shown in Fig. 6-5 (b) X_{S1}, (d) Y_0 and N_0, and (e) Y_{S1} and N_{S1}, respectively, for β = 9°, 10°, and 11° (correspond to v = -0.156, -0.174, and -0.191, respectively) cases. X_{S1} in Fig. 6-5 (b) is solely due to the cross-couple effect between the sinusoidal yaw motion and the drift angle β, which is not measured from pure yaw tests. Data exhibit roughly linear trend with v, however, with rather large scatters in the

---

[12] λ can be rewritten by using the mathematic models for X_0, Y_{S1}, and N_{S1} shown in Table 2-3 as:

$$\lambda = \frac{1}{2}\frac{X_{rr}}{X_*}r_{max}^2 \;;\; \frac{3}{4}\frac{Y_{rrr}}{Y_r}r_{max}^2 \;;\; \frac{3}{4}\frac{N_{rrr}}{N_r}r_{max}^2$$

respectively.

curve-fit. Y_0 and N_0 shown in Fig. 6-5 (d) are from both of the drift angle β and the cross-couple effect, and those harmonics values are about 11% and 5% larger at β = 10° than the static drift Y and N at the same drift angle (shown as dashed and dash-dot lines, respectively). Y_{S1} and N_{S1} in Fig. 6-5 (e) are from both of the sinusoidal yaw motion and the cross-couple effect. Cross-couple effect is rather stronger for Y_{S1} and N_{S1} than for Y_0 and N_0 cases, and their values at β = 10° are about 89% and 44% larger than the pure yaw Y_{S1} and N_{S1} data (shown as dashed and dash-dot lines, respectively) at the same r_{max} = 0.3 condition.

Non-linear derivatives X_{vv}, X_{rr}, Y_{vvv}, Y_{rrr}, Y_{vrr}, N_{vvv}, N_{rrr}, and N_{vrr} determined using the MR_H method are presented in Table 6-4. For MR_H, X_{vv} is determined from the 2nd-order cosine harmonic X_{C2} of pure sway data, shown in Fig. 6-3 (b), where the data exhibit quadratic trend with v_{max} as expected from its mathematic model shown in Table 2-3. The MR_H, however, gives rather smaller X_{vv} value than the MR_L, with a ratio 0.27, nevertheless, the value is closer to static drift X_{vv} value with a ratio 0.85 than the MR_L value (the ratio was 3.12 in Table 6-3). The MR_H gives smaller X_{rr} values than the MR_L similarly for X_{vv}, showing ratio values between 0.2 – 0.5 presented in Table 6-4. This may indicate that the X force in dynamic PMM is more non-linear than the 2nd-order, i.e., functions of v^2 or r^2 as assumed in the mathematic models (2.20a) and (2.22a), respectively, and suggests to include higher order terms such as v^4, v^6 and r^4, r^6 to the mathematic models, which result in additional terms $\frac{3}{8}X_{vvvv}v_{max}^4$, $\frac{5}{16}X_{vvvvvv}v_{max}^6$ and $\frac{3}{8}X_{rrrr}r_{max}^4$, $\frac{5}{16}X_{rrrrrr}r_{max}^6$ to the 0th-order harmonic X_0, respectively. Those higher order terms as well result in the 4th- and the 6th-order harmonics $X_{C4}\cos 4\omega t$ and $X_{C6}\cos 6\omega t$ to the X mathematic models (2.21a) and (2.23a), which may explain the relatively larger X_4 and X_6 in the pure sway and pure yaw X time-histories discussed previously in Section 6.1.1. On the other hand, the Y derivatives such as Y_{vvv}, Y_{rrr}, and Y_{vrr} and the N derivatives such as N_{vvv}, N_{rrr}, and N_{vrr} values from MR_H are usually larger than those from MR_L with the ratios about 1.0 – 3.0 except for a few cases as shown in Table 6-4.

'Single-Run' Method:

Sway derivatives using the 'Single-Run' (SR) method are shown in Fig. 6-6 for (a) linear derivatives Y_v, N_v, $Y_{\dot{v}}$, and $N_{\dot{v}}$ including X_* and (b) non-linear derivatives X_{vv}, Y_{vvv}, and N_{vvv}, for β_{max} = 2°, 4°, and 10° cases. In the figures, the derivatives are shown as scaled values to the MR_L for comparisons. Typically, the linear derivatives shown in Fig. 6-6 (a) are close to MR_L with ratios between 0.9 – 1.1 except for a few cases. In contrast, the non-linear derivatives in Fig. 6-6 (b) are in general larger than MR_L values with ratios 1.0 – 3.0 except for a few cases, showing a tendency to approach to the MR_L values as β_{max} increases.

Yaw derivatives using the SR method are shown in Fig. 6-7 for (a) Y_r, N_r, $Y_{\dot{r}}$, and $N_{\dot{r}}$ including X_* and (b) X_{rr}, Y_{rrr}, and N_{rrr}, respectively, for r_{max} = 0.05 – 0.75 at Fr = 0.138, 0.280, and 0.410 conditions, with scaled to the MR_L values. The overall trends are similar as the sway derivatives; values are close to MR_L for the linear derivatives and larger than MR_L for the non-linear derivatives. The linear derivatives shown in Fig. 6-7 (a) at small r_{max} are in general smaller or larger than the MR_L with ratios 0.1 – 1.7 and approach to the MR_L values as r_{max} increases, except for Y_r at Fr = 0.138 and 0.280, continuously decreasing with r_{max}. The non-linear derivatives shown in Fig. 6-7 (b) exhibit huge ratio values ranging between -210 and 60 (used in the figure are the absolute values for the log scale), decreasing with r_{max} but still larger ratio values 0.5 – 3.5 at r_{max} = 0.75.

Cross-coupled derivatives X_{vr}, Y_{vrr}, N_{vrr}, Y_{rvv}, and N_{rvv} are shown in Fig. 6-8 (a) with scaled to the MR_L values, where the Y_{vrr} and N_{vrr} are from the SR_L method and those from the SR_H are shown in Fig. 6-8 (b), respectively, for β = 9°, 10°, and 11° cases. X_{vr}, Y_{rvv}, and N_{rvv} shown in Fig. 6-8 (a) are fairly close to the MR_L values with ratios 0.8 – 1.2. The ratios for Y_{vrr} and N_{vrr} using the SR_L method shown in Fig. 6-8 (a) are relatively large, 0.5 – 1.4, whereas the ratios for those derivatives using the SR_H method

shown in Fig. 6-8 (b) are very close to 1.0 for Y_{vrr} and relatively large, 1.4 – 1.7, for N_{vrr}, respectively.

In summary, the '*Single-Run*' method gives the linear sway and yaw, and the cross-coupled derivatives similar values as the '*Multiple-Run*' method as the dynamic PMM motion becomes larger (i.e, larger β_{max} and r_{max} values), whereas it gives typically larger or smaller non-linear sway and yaw derivatives values particularly at smaller PMM motion conditions.

Reconstruction Errors:

The validities of the hydrodynamic derivatives determined using the '*Multiple-Run*' and '*Single-Run*' methods are evaluated by examining the errors in reconstruction of forces and moment time-histories data. Reconstructions are by using the mathematic models (2.21), (2.23), and (2.25) where first the harmonic amplitude terms such as X_0, X_{C2}, …, N_{S3} are calculated using the derivatives values and then the time-histories of X, Y, and N are reconstructed (also see Table 2-3). Subsequently, the reconstruction error E_R is defined as

$$E_R(\%) = \frac{\sum_i^M |D_i - R_i|}{\sum_i^M |D_i|} \times 100 \tag{6.5}$$

where, D_i is the measured data from the PMM tests, R_i is the reconstructed data by using the mathematic models, subscript i represents the time t_i, and M is the total number of data points.

The E_R's in reconstructing the time-histories of pure sway, pure yaw, and yaw and drift data shown in Fig. 6-2 are calculated using the sway, yaw, and cross-coupled derivatives, respectively, using the '*Multiple-Run*' (MR_L and MR_H) and the '*Single-Run*' (SR) methods, and the average errors $\overline{E_R}$ for all β_{max}, r_{max}, and β cases, respectively, are presented in Tables 6-5, 6-6, and 6-7, respectively. For sway and yaw derivatives in

Tables 6-5 and 6-6, the $\overline{E_R}$'s are the smallest for the derivatives using the MR_L method, and the $\overline{E_R}$'s for the derivatives using the MR_H method are relatively larger in general. The $\overline{E_R}$'s for derivatives using the SL method are typically large, particularly for the derivatives from the smallest motion cases such as the sway derivatives from the pure sway data for β_{max} = 2° case ($SR_{2°}$) and the yaw derivatives from the pure yaw data for r_{max} = 0.30 case ($SR_{0.30}$), and tend to decrease as the PMM motions become large, showing similar values as the MR_H in general. In Table 6-5, the $\overline{E_R}$'s for the sway derivatives from the static drift test are compared with those from the pure sway test, of which values are relatively larger than those for MR_L method but close to those for MR_H method case. For cross-coupled derivatives in Table 6-7, the $\overline{E_R}$'s are similarly small for all method cases as the yaw and drift motions are sufficiently large (β = 9°, 10°, and 11° and r_{max} = 0.30) from which the derivatives are determined. Consequently, the '*Multiple-Run*' (MR_L) method is more rigorous than the '*Single-Run*' method determining the hydrodynamic derivatives and the latter method is suggested only when the PMM motions are large enough.

6.1.2.3 Speed variation test

Surge derivatives were evaluated as per Section 2.3.5 using the sway and yaw derivatives determined previously for three *Fr*'s, 0.138, 0.280, and 0.410, cases. For this, the sway derivatives from the static drift tests (Table 6-2) and the yaw derivatives using the MR_L method (Table 6-3) were used, which are shown in Fig. 6-9 as functions surge velocity, u. In the figure, surge velocity is non-dimensionalized such that $\Delta u = (u - U)/U$, where u is the surge velocity at each *Fr* and U is that at *Fr* where the surge derivatives are determined (herein, *Fr* = 0.280). In the figure, all derivatives were normalized with the values at *Fr* = 0.280. From Fig. 6-9 (a), for sway derivatives, X_* and X_{vv} show strong dependency on Δu, i.e. *Fr*, with their normalized values changing between 1.1 to 1.5 and 0.2 to 1.0, respectively. Whereas Y_v and N_v are almost independent on Δu showing the normalized values ranging between 0.9 and 1.0 and 0.8 and 1.0, respectively.

The yaw derivatives in Fig. 6-9 (b) show similar trends. The normalized X_{rr} values increase rather monotonically from 0.3 to 1.4 within the speed range, and the normalized Y_r and N_r values vary moderately between 0.6 ~ 1.1 and 0.8 ~ 1.0. In summary, typically the linear derivative such Y_v, N_v, Y_r, and N_r are nearly in dependent with the speed (Fr) changes, whereas the non-linear derivatives X_{vv}, Y_{vvv}, N_{vvv}, X_{rr}, Y_{rrr}, and N_{rrr} exhibit rather strong dependency on the speed (Fr) changes.

Subsequently, those derivatives were curve fitted to the 2nd-order polynomial functions of Δu as per equation (2.35), from which surge derivatives such as X_u, X_{uu} and X_{vvu}, Y_{vu}, Y_{vuu}, N_{vu}, N_{vuu} are evaluated using (2.36) and (2.37), respectively, and presented in Table 26. Note that the derivatives X_{uuu} and X_{vru} are not evaluated herein due to the limited number of Fr cases in the present PMM test matrix (shown in Table 3-3) for static drift and yaw and drift tests, respectively.

Table 6-2 Hydrodynamic Derivatives (Static Drift).

Derivative	Fr = 0.138	Fr = 0.280	Fr = 0.410
X_*	-0.0182	-0.0170	-0.0258
X_{vv}	-0.0301	-0.1528	-0.1544
Y_v	-0.2637	-0.2961	-0.2963
Y_{vvv}	-1.6256	-1.9456	-3.7914
N_v	-0.1396	-0.1667	-0.1717
N_{vvv}	-0.3426	-0.4355	-1.2591

Table 6-3 Hydrodynamic Derivatives (MR_L Method).

Derivative	Fr = 0.280	Derivative	Fr = 0.138	Fr = 0.280	Fr = 0.410	Derivative	Fr = 0.280
X_*	-0.0173 (1.02)	X_*	-0.0181 (0.99)	-0.0177 (1.04)	-0.0260 (1.01)		
X_{vv}	-0.4765 (3.12)	X_{rr}	-0.0078	-0.0282	-0.0385	X_{vr}	0.0819
Y_v	-0.2601 (0.88)	Y_r	-0.0276	-0.0485	-0.0548	Y_{vrr}	-0.8682
Y_{vvv}	-2.9686 (1.53)	Y_{rrr}	-0.0370	-0.0452	-0.0710	Y_{rvv}	-1.5172
N_v	-0.1681 (1.01)	N_r	-0.0382	-0.0485	-0.0548	N_{vrr}	-0.1989
N_{vvv}	-0.5677 (1.30)	N_{rrr}	-0.0211	-0.0505	-0.0821	N_{rvv}	-0.7220
$Y_{\dot{v}}$	-0.1135	$Y_{\dot{r}}$	-0.0146	-0.0090	-0.0127		
$N_{\dot{v}}$	-0.0136	$N_{\dot{r}}$	-0.0065	-0.0070	-0.0077		

( ): ratio to static drift

Table 6-4 Hydrodynamic Derivatives (MR_H Method).

Derivative	Fr = 0.280	Derivative	Fr = 0.138	Fr = 0.280	Fr = 0.410	Derivative	Fr = 0.280
X_{vv}	-0.1296 (0.27)	X_{rr}	-0.0016 (0.21)	-0.0132 (0.47)	-0.0163 (0.42)		
Y_{vvv}	-2.2962 (0.77)	Y_{rrr}	-0.0927 (2.51)	-0.1305 (2.89)	-0.1210 (1.70)	Y_{vrr}	-0.9066 (1.04)
N_{vvv}	-0.8533 (1.50)	N_{rrr}	-0.0312 (1.48)	-0.0473 (0.94)	-0.0387 (0.47)	N_{vrr}	-0.3161 (1.59)

( ): ratio to MR_L

Table 6-5 Reconstruction Errors (Sway derivatives).

Errors	Var.	MR_L	[1)]MR_H	$SR_{2°}$	$SR_{4°}$	$SR_{10°}$	[2)]Static drift
$\overline{E_R}$ (%)	X	9.4	12.0	22.8	9.4	19.5	12.2
	Y	5.5	6.2	5.1	10.1	7.3	10.5
	N	2.9	4.0	30.2	6.1	3.9	3.6

[1)] $Y_{\dot{v}}$, $N_{\dot{v}}$, Y_v, and N_v from the MR_L were used for reconstructions
[2)] $Y_{\dot{v}}$ and $N_{\dot{v}}$ from the MRL were used for reconstructions

Table 6-6 Reconstruction Errors (Yaw derivatives).

Errors	Var.	MR_L	[1)]MR_H	$SR_{0.05}$	$SR_{0.15}$	$SR_{0.30}$	$SR_{0.45}$	$SR_{0.60}$	$SR_{0.75}$
$\overline{E_R}$ (%)	X	7.6	9.5	549.4	52.2	12.1	8.5	9.2	13.8
	Y	17.2	29.5	106.2	56.3	25.2	27.2	31.2	45.7
	N	5.2	5.2	616.2	22.4	5.3	6.6	5.5	6.7

[1)] $Y_{\dot{r}}$, Y_r, $N_{\dot{r}}$, N_r values from the MR_L method were used for reconstructions.

Table 6-7 Reconstruction[1)] Errors (Cross-coupled derivatives).

Errors	Var.	MR_L	[2)]MR_H	$SR_{L9°}$	$SR_{L10°}$	$SR_{L11°}$	[3)]$SR_{H9°}$	[3)]$SR_{H10°}$	[3)]$SR_{H11°}$
$\overline{E_R}$ (%)	X	11.0	-	11.1	11.0	11.0	-	-	-
	Y	3.5	3.5	3.6	5.2	5.5	3.6	3.5	3.7
	N	2.7	3.0	2.4	2.4	4.6	2.9	2.5	3.6

[1)] For reconstructions, X_*, X_{vv}, Y_v, Y_{vvv}, N_v, and N_{vvv} from static drift, and $Y_{\dot{r}}$, Y_r, Y_{rrr}, $N_{\dot{v}}$, N_r, and N_{rrr} using the MR_L method were used.
[3)] X_{vr}, Y_{rvv}, N_{rvv} using MR_L were used for reconstructions
[4)] X_{vr}, Y_{rvv}, N_{rvv} using SR_L were used for reconstructions.

Table 6-8 Surge-derivatives (Fr = 0.280).

Derivative	Value	Derivative	Value
X_u	-0.0088		
X_{uu}	-0.0220		
X_{vvu}	-0.1172	X_{rru}	-0.0308
Y_{vu}	-0.0307	Y_{ru}	-0.0268
Y_{vuu}	0.0653	Y_{ruu}	0.0284
N_{vu}	-0.0311	N_{ru}	-0.0183
N_{vuu}	0.0439	N_{ruu}	-0.0066

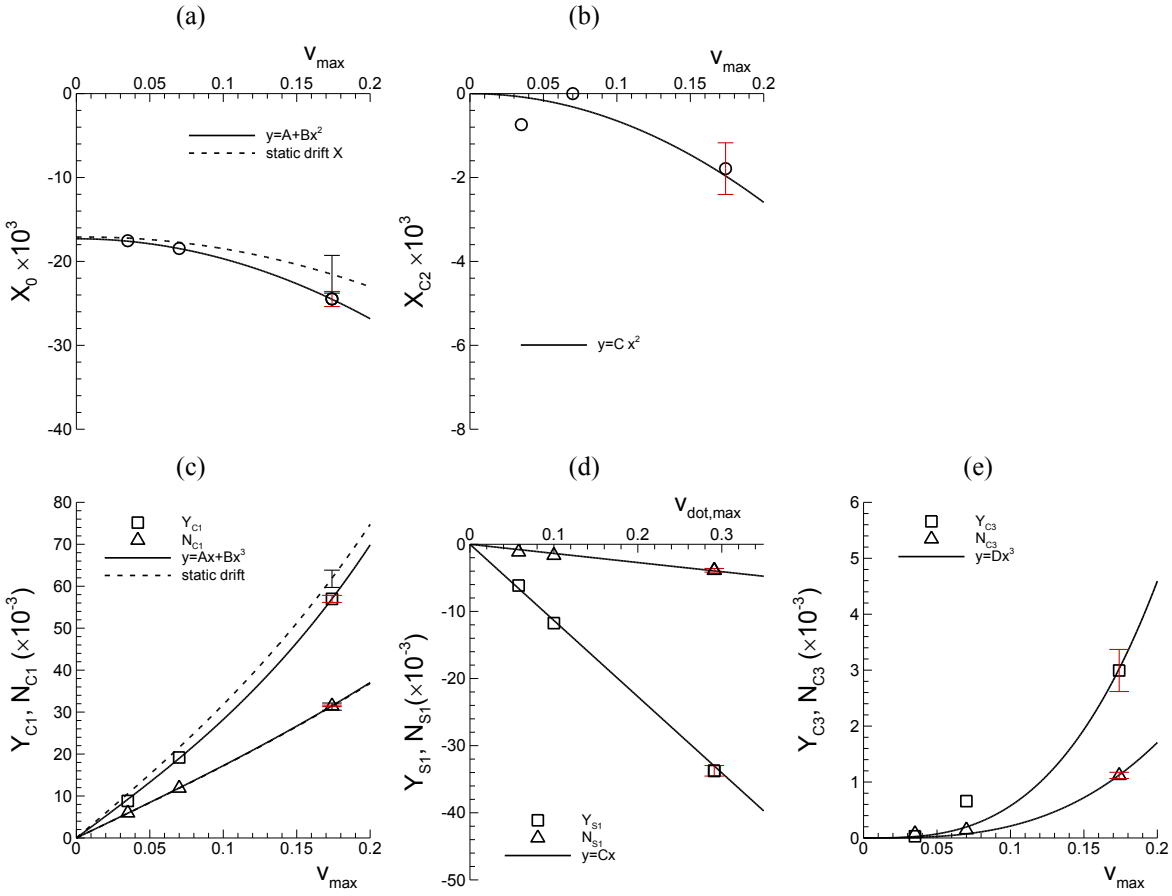

Figure 6-3 Pure sway X, Y, and N data FS harmonics: (a) X_0, (b) X_{C2}, (c) $Y_{C1}$and N_{C1}, (d) Y_{S1} and N_{S1}, and (e) Y_{C3} and N_{C3}.

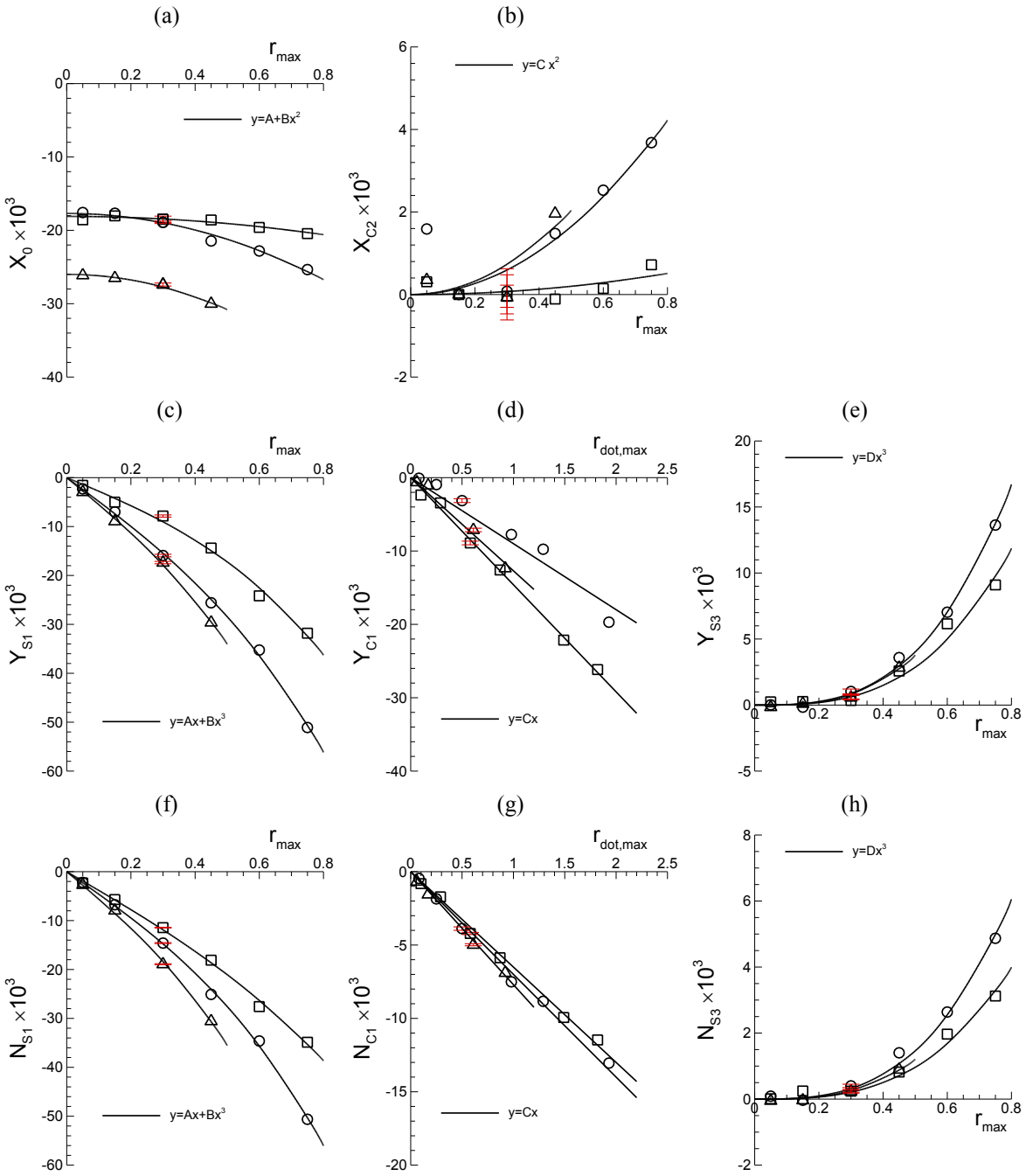

Figure 6-4 Pure yaw X, Y, and N data FS harmonics: (a) X_0, (b) X_{C2}, (c) Y_{S1}, (d) Y_{C1}, (e) Y_{S3}, (f) N_{S1}, (g) N_{C1}, and (h) N_{S3}. Simbols: □, Fr = 0.138; o, Fr = 0.280; Δ, Fr = 0.410.

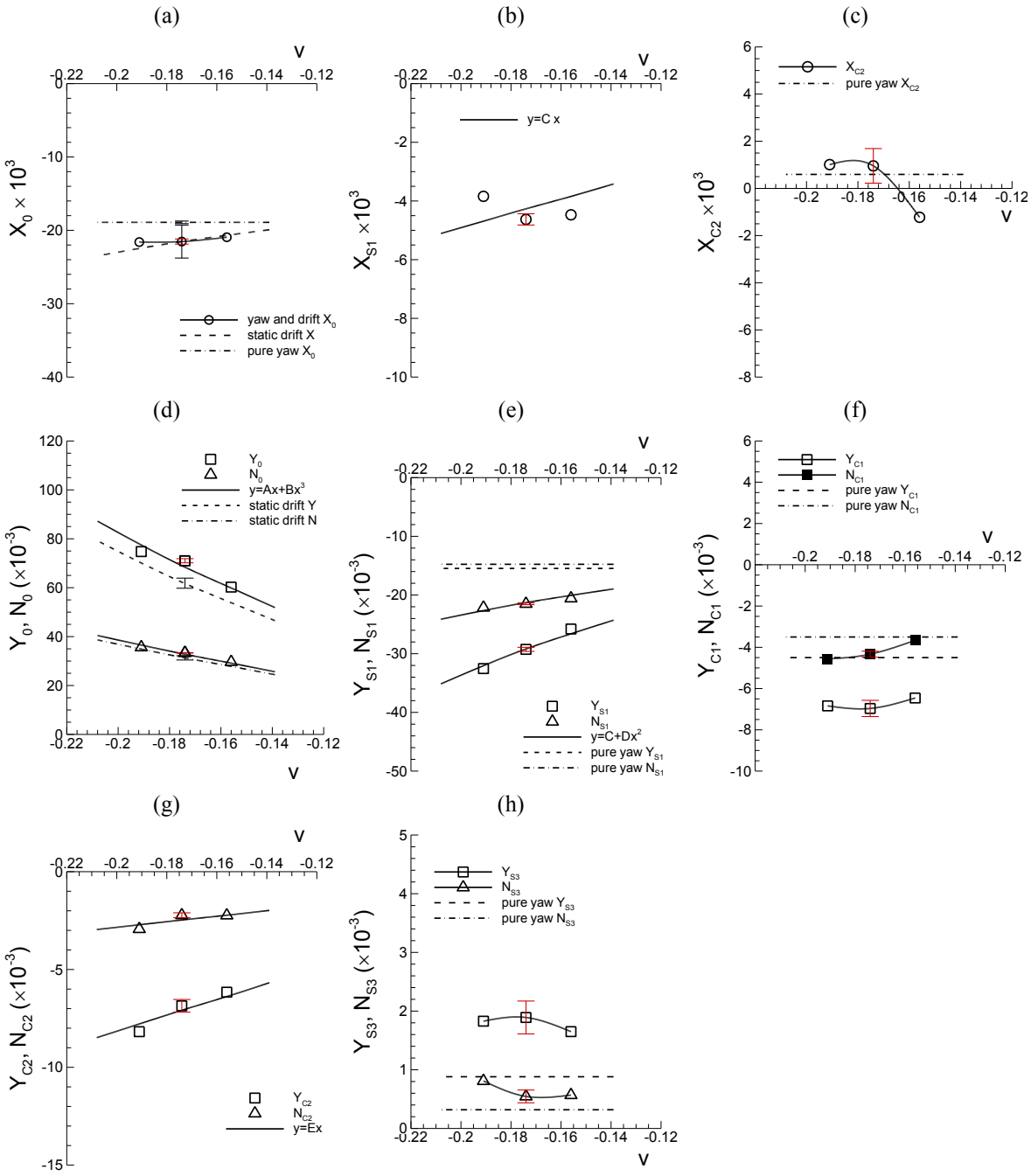

Figure 6-5 Yaw and drift X, Y, and N data FS harmonics: (a) X_0, (b) X_{S1}, (c) X_{C2}, (d) Y_0 and N_0, (e) Y_{S1} and N_{S1}, (f) Y_{C1} and N_{C1}, (g) Y_{C2} and N_{C2}, and (h) Y_{S3} and N_{S3}.

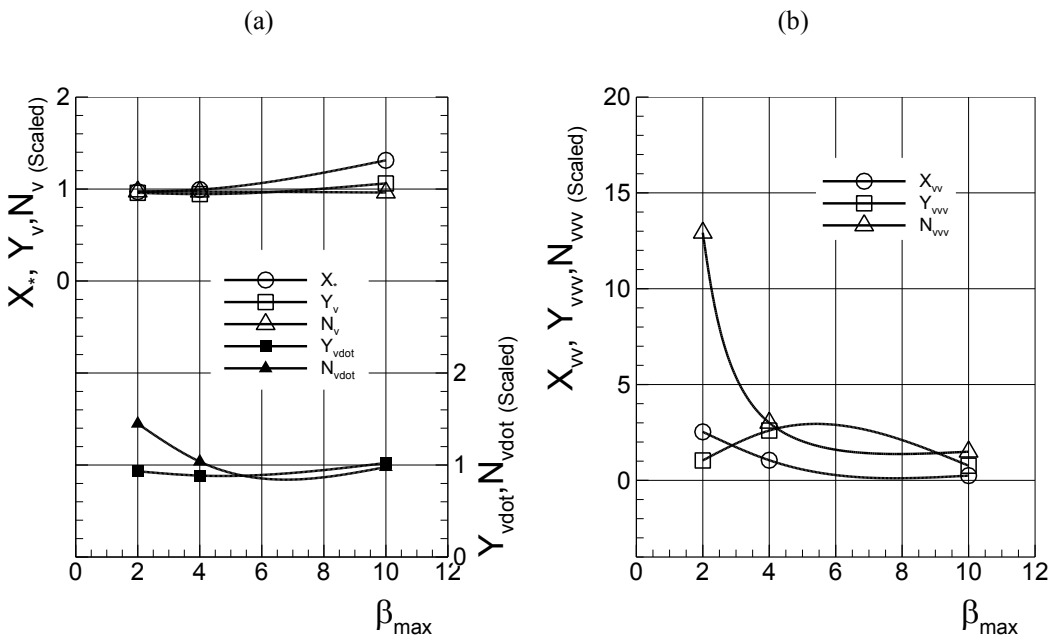

Figure 6-6 Single-run method (sway derivatives): (a) linear and (b) non-linear derivatives. Hydrodynamic derivatives shown are scaled with MR_L.

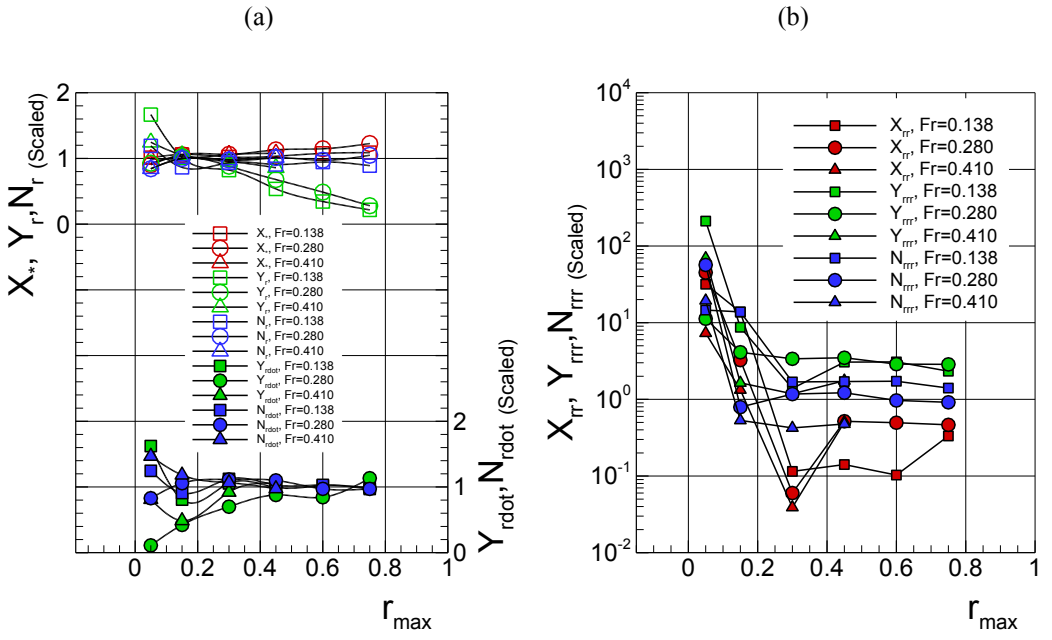

Figure 6-7 Single-run method (yaw derivatives): (a) linear and (b) non-linear derivatives. Hydrodynamic derivatives shown are scaled with MR_L.

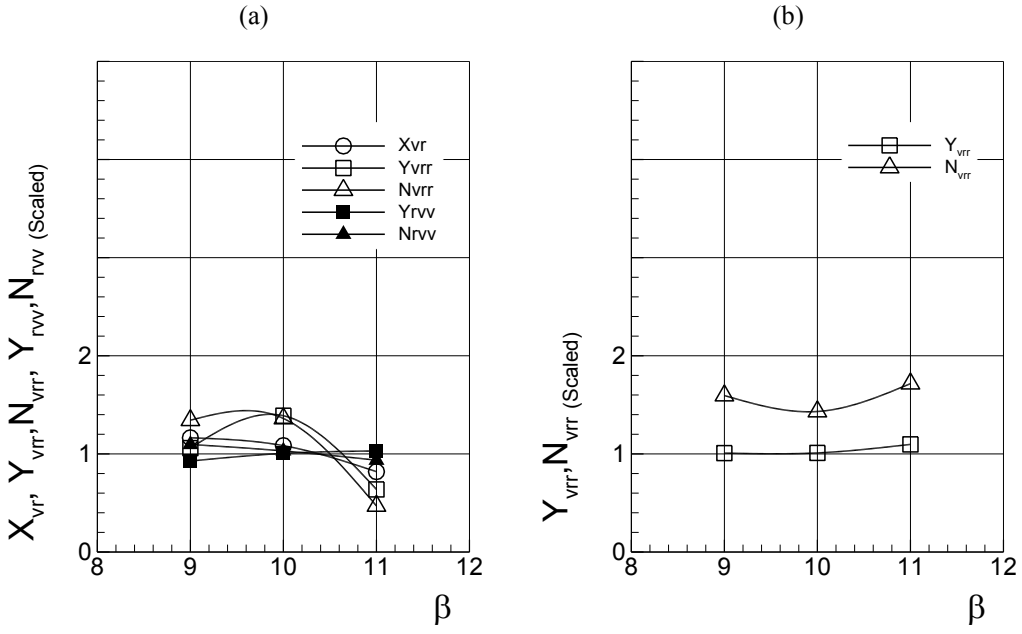

Figure 6-8 Single-Run method (cross-coupled derivatives): (a) SR_L (b) SR_H. Hydrodynamic derivatives shown are scaled with MR_L.

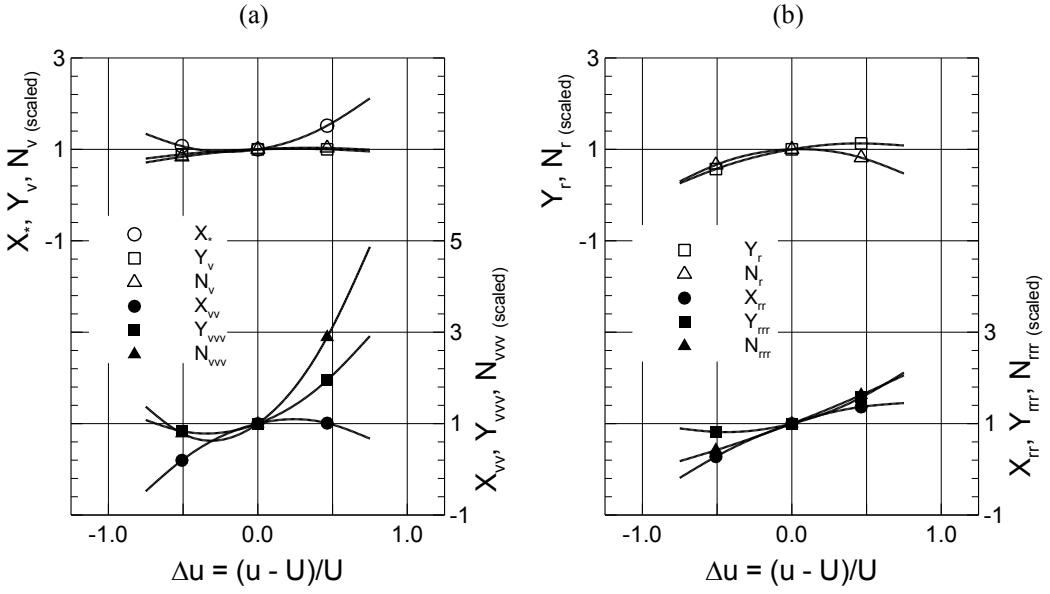

Figure 6-9 Speed variation test: Hydrodynamic derivatives with surge velocity change Δu: (a) Sway and (b) yaw derivatives. Hydrodynamic derivatives shown are scaled with the values at $\Delta u = 0$ (Fr = 0.280).

6.1.3 Comparisons between Facilities

Forces and moment and subsequent hydrodynamic derivatives from three facilities (IIHR, FORCE, and INSEAN) are compared. All the facilities shared the same geometry (DTMB 5415) and the same PMM test matrix (Table 3-3, for the $FR_{z\theta}$ condition only). The model length L used for each facility is 3.048 m, 4.002 m, and 5.720 m, respectively, and the specific model particulars are summarized in Table 3-1. The comparisons include evaluations of the standard deviation[13] from the facility mean values (the mean values of the three facilities data) of the time-mean values of X, Y, and N data for static drift test and those of the harmonic amplitude and phase of the time-histories data as per (2) for dynamic tests. Herein, the standard deviation values are presented in percent of the facility mean values. Subsequently, hydrodynamic derivatives are compared between the facilities data and possible effects of model size are discussed.

Static drift X, Y, and N are shown in Fig. 6-10 (a), (b), and (c), respectively, for Fr = 0.138 (left), 0.280 (middle), and 0.410 (right) cases, respectively. The facility mean and standard deviation values of X, Y, and N data at β = 10° for the three Fr cases are presented in Table 6-9. From Fig. 6-10 (a), X data exhibit relatively large deviations from facility to facility with standard deviations about 9% - 11% at β = 10°. Y and N data in Fig. 6-10 (b) and (c) in general show good agreements between facilities, where the standard deviations at β = 10° are about 1% - 4% except for a few cases. In the figure, data are curve fitted (solid lines for FORCE and INSEAN, and dashed lines for IIHR) to quadratic, $X = A + B\beta^2$, and cubic, $Y, N = A\beta + B\beta^3$, functions similarly as discussed in Section 6.1.1. For X in Fig. 6-10 (a), the intercept A is different from facility to facility, more or less, whereas the 2nd-order coefficient B is seemingly similar between

[13] Although the number of facilities, three, is minimal for a normal distribution, nevertheless the standard deviation shows a value close to the average deviation of data from the facility mean values.

facilities except for the Fr = 0.138 case. For Y and N in Fig. 6-10 (b) and (c), the 1st-order (linear) coefficient A is similar between facilities, whereas the 3rd-order (non-linear) coefficient B is different from facility to facility in general. The quantitative comparisons of those coefficients will be discussed later with related to the comparisons of the sway derivatives.

Dynamic test time-histories of X, Y, and N are shown in Fig. 6-11 (a), (b), and (c), respectively, for pure sway (left, β_{max} = 10° case), pure yaw (middle, r_{max} = 0.30 case), and yaw and drift (right, β = 10° case) tests for Fr = 0.280 case, respectively. While the data exhibit in general good agreements between facilities, the mean and standard deviation values of the dominant harmonic amplitude and phase are presented in Table 6-10. In Fig. 6-11 (a), X time-histories show relatively large deviations between facilities data. Nonetheless, the standard deviations of the 0th-order amplitude X_0 are fairly small, 14.9%, 6.2%, and 7.5% for pure sway, pure yaw, and yaw and drift tests, respectively, whereas those of the 2nd-order amplitude X_2 and phase φ_{X2} (for yaw and drift X_1 and φ_1) are in general large, 42.9%, 8.3%, and 69.2%, respectively, for the former, and 5.8%, 307.3%, and 76.8%, respectively, for the latter. For Y and N, the time-histories shown in Fig. 6-11 (b) and (c) exhibit good agreements between facilities, where the standard deviations of the 1st-order amplitude Y_1 and phase φ_{Y1} are small, about 4% - 6% and about 2% - 10%, respectively, for all test types. For yaw and drift Y and N, the standard deviations of the 0th-order amplitude Y_0 and N_0 are also small about 2%.

Hydrodynamic derivatives from the facilities data are compared in Tables 6-11 through 6-14 for the sway, yaw, cross-coupled, and surge derivatives, respectively. Presented in the tables are the facility mean and standard deviation values and the ratio values of each facility data to the facility mean values. The sway velocity derivatives X_{vv}, Y_v, Y_{vvv}, N_v, and N_{vvv}, including X_*, are determined from the static drift data and the sway acceleration derivatives $Y_{\dot{v}}$ and $Y_{\dot{v}}$ are from the pure sway data using the MR_L method. The yaw derivatives X_{rr}, Y_r, Y_{rrr}, $Y_{\dot{r}}$, N_r, N_{rrr}, and $N_{\dot{r}}$ and the cross-coupled de-

rivatives X_{vr}, Y_{vrr}, Y_{rvv}, N_{vrr}, and N_{rvv} are as well using the MR_L method. The surge derivatives X_u, X_{uu}, X_{vvu}, Y_{vu}, Y_{vuu}, N_{vu}, N_{vuu}, X_{rru}, Y_{ru}, Y_{ruu}, N_{ru}, and N_{ruu} are derived from the aforementioned sway and yaw derivatives as per (2.36) and (2.37) in Section 2.3.5.

Sway and yaw derivatives are compared in Tables 6-11 and 6-12 where the facility mean and standard deviation values are presented. For sway derivatives, X_* and X_{vv} correspond to the intercept A and the 2nd-order coefficient B of the static drift X data curve fits, and Y_v, N_v and Y_{vv}, N_{vvv} correspond to the 1st- and 3rd-order coefficients A and B of the static drift Y and N data curve fits, respectively, discussed previously. Recalling Fig. 6-10 (a), the standard deviation of the intercept values of X data (X_*) is relatively large, about 10% - 14%, whereas the standard deviation of the 2nd-order coefficient (X_{vv}) is relatively small, about 7% - 10% except for the Fr = 0.138 case. For Y and N in Fig. 6-10 (b) and (c), the standard deviations of the 1st-order coefficients (Y_v and N_v) are small, about 2% - 7%, whereas the 3rd-order coefficients (Y_{vvv} and N_{vvv}) are large, about 10% - 30%. On the other hand, from Table 6-11, the standard deviations of the sway acceleration derivatives $Y_{\dot{v}}$ and $N_{\dot{v}}$ are small, 4.4% and 8.8%, respectively. Similar overall trends in comparisons are observed from the yaw derivatives in Table 6-12; relatively small deviations of linear derivatives and large deviations of non-linear derivative, whereas the standard deviation values are rather larger than the sway derivatives cases. The standard deviations of the linear derivatives Y_r and N_r are about 5% - 27%, while those of the non-linear derivatives X_{rr}, Y_{rrr}, and N_{rrr} are fairly large, 37% - 91%, 15% - 72%, and 20% - 55%, respectively. The standard deviations of $Y_{\dot{r}}$ and $N_{\dot{r}}$ are 21% - 34% and 15% - 25%, respectively, which are larger than the sway acceleration derivatives cases.

Ratios of the derivative values to the facility means presented in Tables 6-11 and 6-12 are plotted against the model length in Figs. 6-12 and 6-13 for sway and yaw derivatives, denoted with a '*' symbol, respectively, revealing the possible effect of model size. In the figures, the model lengths of each facility, IIHR, FORCE, and INSEAN, are scaled with the smallest model size corresponding to $L^* = L/L_{3.048\ m} = 1.0$, 1.31, and 1.88, respectively. Subsequently, the ratio values are linear-curve fitted to $y = AL^* + B$, where the coefficient $A = \Delta y/\Delta L^*$ indicates the amount of change of derivative value, Δy, (in fraction of the facility mean value) as the model size is doubled, i.e $\Delta L^* = 1$. From Fig. 6-12 (a), the ratios of the linear derivatives, Y_v^* and N_v^*, are close to 1.0 whereas the ratios of the non-linear derivatives, X_{vv}^*, Y_{vvv}^*, and N_{vvv}^*, are distributed over a rather wide range in general between 0.6 and 1.04. The curve-fit coefficient A's for the linear and non-linear derivatives are near to zero, 0.01 and -0.03, respectively, indicating that the derivatives are nearly independent of model size. The ratios $Y_{\dot{v}}^*$ and $N_{\dot{v}}^*$ shown in Fig. 6-12 (b) are also near to 1.0, similarly as Y_v^* and N_v^*, whereas the values tend to decrease with model size, however, the number of data (6 points) is very limited for a general remark. From Fig. 6-13 (a), the ratios of the linear derivatives, Y_r^* and N_r^*, are close to 1.0 distributed between 0.8 and 1.2, whereas the ratios of the non-linear derivatives, X_{rr}^*, Y_{rrr}^*, and N_{rrr}^* are distributed over a quite wide range between 0.2 and 1.8. The curve-fit coefficient A's are 0.14 and -0.16 for the linear and non-linear derivatives, respectively, indicating that those derivatives values can increase 14% and decrease 16%, respectively, as the model length is doubled. The ratios of yaw acceleration derivatives, $Y_{\dot{r}}^*$ and $N_{\dot{r}}^*$, exhibit rather strong dependency on the model size as shown in Fig. 6-13 (b). The curve-fit coefficient A is large, $A = 0.52$, meaning that $Y_{\dot{r}}$ and $N_{\dot{r}}$ values can increase as much as 52% as the model size is doubled. In summary, generally, sway derivatives are nearly independent of model size whereas yaw derivatives (particularly yaw acceleration derivatives) exhibit considerable dependency on the model size. However, general conclusions

are precluded for the non-linear derivatives due to large scatters in the ratio values distributions.

Cross-coupled derivatives and Surge derivatives are compared in Tables 6-13 and 6-14, respectively. The standard deviations from and the ratios to the facility mean values of those derivatives values are typically larger than those for the sway and yaw derivatives, and clear trends with the model size are not observed for those derivatives.

Table 6-9 Comparisons between Facilities: Static drift test (β = 10°).

Var.	Fr = 0.138		Fr = 0.280		Fr = 0.410	
	Mean	StDev(%)	Mean	StDev(%)	Mean	StDev(%)
X	-0.0176	9.2	-0.0197	10.7	-0.0281	9.2
Y	0.0559	3.4	0.0616	1.0	0.0746	6.3
N	0.0250	7.5	0.0300	3.9	0.0372	4.1

Table 6-10 Comparisons between Facilities: Dynamic tests (Fr = 0.280).

Var.	Harmonics	Pure sway		Pure yaw		Yaw and drift	
		Mean	StDev(%)	Mean	StDev(%)	Mean	StDev(%)
X	X_0	-0.0210	14.9	-0.0182	6.2	-0.0225	7.5
	X_2	0.0017	42.9	0.0007	8.3	[1)]0.0026	69.2
	φ_{X2}	-0.75 π	5.8	-0.18 π	307.3	[2)]0.25 π	76.8
Y	Y_0	-	-	-	-	0.0698	2.0
	Y_1	0.0665	3.8	0.0175	6.4	0.0318	6.1
	φ_{Y1}	0.17 π	7.0	0.58 π	2.1	0.59 π	3.2
N	N_0	-	-	-	-	0.0333	1.6
	N_1	0.0315	3.7	0.0153	5.8	0.0221	5.8
	φ_{N1}	0.04 π	10.1	0.59 π	2.2	0.57 π	1.8

[1)] X_1 and [2)] φ_{X1} for yaw and drift test.

Table 6-11 Comparisons between Facilities (Sway derivatives).

Derivative	Fr	Mean	StDev (%)	Facility data (ratio to Mean)		
				IIHR	FORCE	INSEAN
X_*	0.138	-0.0164	13.7	1.11	1.04	0.85
	0.280	-0.0155	12.4	1.10	1.05	0.86
	0.410	-0.0239	9.8	1.08	1.03	0.89
Y_v	0.138	-0.2673	5.4	0.99	0.95	1.06
	0.280	-0.3000	1.8	0.99	0.99	1.02
	0.410	-0.2941	2.9	1.01	1.02	0.97
N_v	0.138	-0.1351	5.9	1.03	1.04	0.93
	0.280	-0.1628	2.2	1.02	1.00	0.98
	0.410	-0.1749	7.0	0.98	0.94	1.08
X_{vv}	0.138	-0.0427	51.6	0.70	0.70	1.60
	0.280	-0.1421	6.5	1.08	0.96	0.96
	0.410	-0.1392	9.5	1.11	0.94	0.96
Y_{vvv}	0.138	-1.7940	13.9	0.91	1.16	0.93
	0.280	-1.7875	7.8	1.09	0.97	0.94
	0.410	-4.5105	25.7	0.84	0.86	1.30
N_{vvv}	0.138	-0.2866	31.2	1.20	1.16	0.64
	0.280	-0.3284	31.0	1.33	0.96	0.71
	0.410	-1.3113	11.0	0.96	1.12	0.92
Y_p	0.280	-0.1111	4.4	1.02	1.03	0.95
N_p	0.280	-0.0131	8.8	1.04	1.07	0.90

Table 6-12 Comparisons between Facilities (Yaw derivatives).

Derivative	Fr	Mean	StDev (%)	Facility (ratio to Mean)		
				IIHR	FORCE	INSEAN
Y_r	0.138	-0.0313	15.3	0.88	1.17	0.95
	0.280	-0.0457	27.2	1.06	0.70	1.24
	0.410	-0.0572	5.6	0.96	0.98	1.06
N_r	0.138	-0.0372	5.8	1.03	0.93	1.04
	0.280	-0.0487	5.4	0.94	1.05	1.01
	0.410	-0.0543	14.5	0.84	1.03	1.13
X_{rr}	0.138	-0.0090	36.9	0.87	0.71	1.42
	0.280	-0.0191	41.5	1.48	0.71	0.81
	0.410	-0.0190	91.4	2.03	0.68	0.29
Y_{rrr}	0.138	-0.0454	31.5	0.82	0.82	1.36
	0.280	-0.0570	71.8	0.79	1.80	0.41
	0.410	-0.0608	14.6	1.17	0.93	0.90
N_{rrr}	0.138	-0.0255	31.8	0.83	0.81	1.37
	0.280	-0.0342	55.3	1.48	0.39	1.13
	0.410	-0.0773	20.1	1.06	0.78	1.16
$Y_{\dot{r}}$	0.138	-0.0162	21.0	0.90	0.86	1.24
	0.280	-0.0136	33.3	0.66	1.01	1.33
	0.410	-0.0184	33.5	0.69	0.95	1.36
$N_{\dot{r}}$	0.138	-0.0073	17.8	0.89	0.91	1.21
	0.280	-0.0096	24.6	0.73	1.07	1.21
	0.410	-0.0092	14.6	0.83	1.06	1.10

Table 6-13 Comparisons between Facilities (Cross-coupled derivatives).

Derivative	Mean	StDev (%)	Facility (ratio to Mean)		
			IIHR	FORCE	INSEAN
X_{vr}	0.0300	152.1	2.73	0.39	-0.12
Y_{vrr}	-1.3683	42.7	1.48	0.65	0.87
N_{vrr}	-0.4011	64.3	1.72	0.48	0.81
Y_{rvv}	-1.7067	12.1	1.10	1.03	0.87
N_{rvv}	-0.5512	20.8	0.79	1.00	1.21

Table 6-14 Comparisons between Facilities (Surge derivatives).

Derivative	Mean	StDev (%)	Facility (ratio to Mean)		
			IIHR	FORCE	INSEAN
X_u	-0.0087	2.3	1.01	1.01	0.97
X_{uu}	-0.0205	7.9	1.07	1.00	0.92
X_{vvu}	-0.0903	31.6	1.30	1.03	0.67
X_{rru}	-0.0094	212.5	3.28	0.65	-0.93
Y_{vu}	-0.0242	98.7	1.27	1.83	-0.09
N_{vu}	-0.0397	54.3	0.78	0.60	1.62
Y_{vuu}	0.0794	18.2	0.82	0.99	1.19
N_{vuu}	0.0294	71.3	1.49	1.33	0.18
Y_{ru}	-0.0265	14.3	1.01	0.85	1.14
N_{ru}	-0.0208	12.5	0.88	1.00	1.13
Y_{ruu}	0.0033	1728.6	8.61	-19.03	13.45
N_{ruu}	0.0034	486.6	-1.94	6.56	-1.65

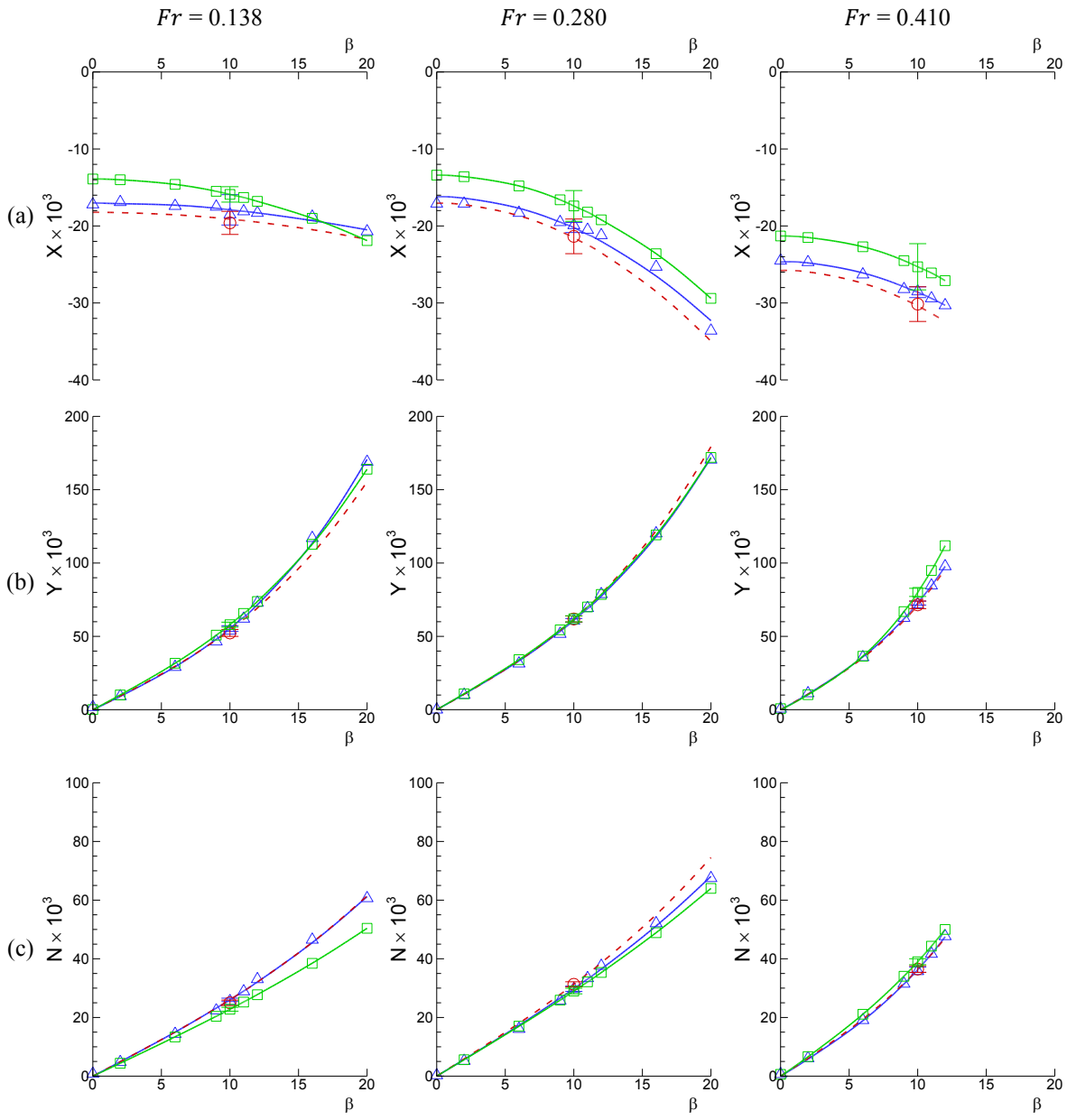

Figure 6-10 Comparisons between facilities – Static drift data (Corrected for symmetry): (a) X, (b) Y, and (c) N at Fr =0.138 (left), 0.280 (center), 0.410 (right), respecitively. Symbols: O, IIHR; Δ, FORCE; □, INSEAN.

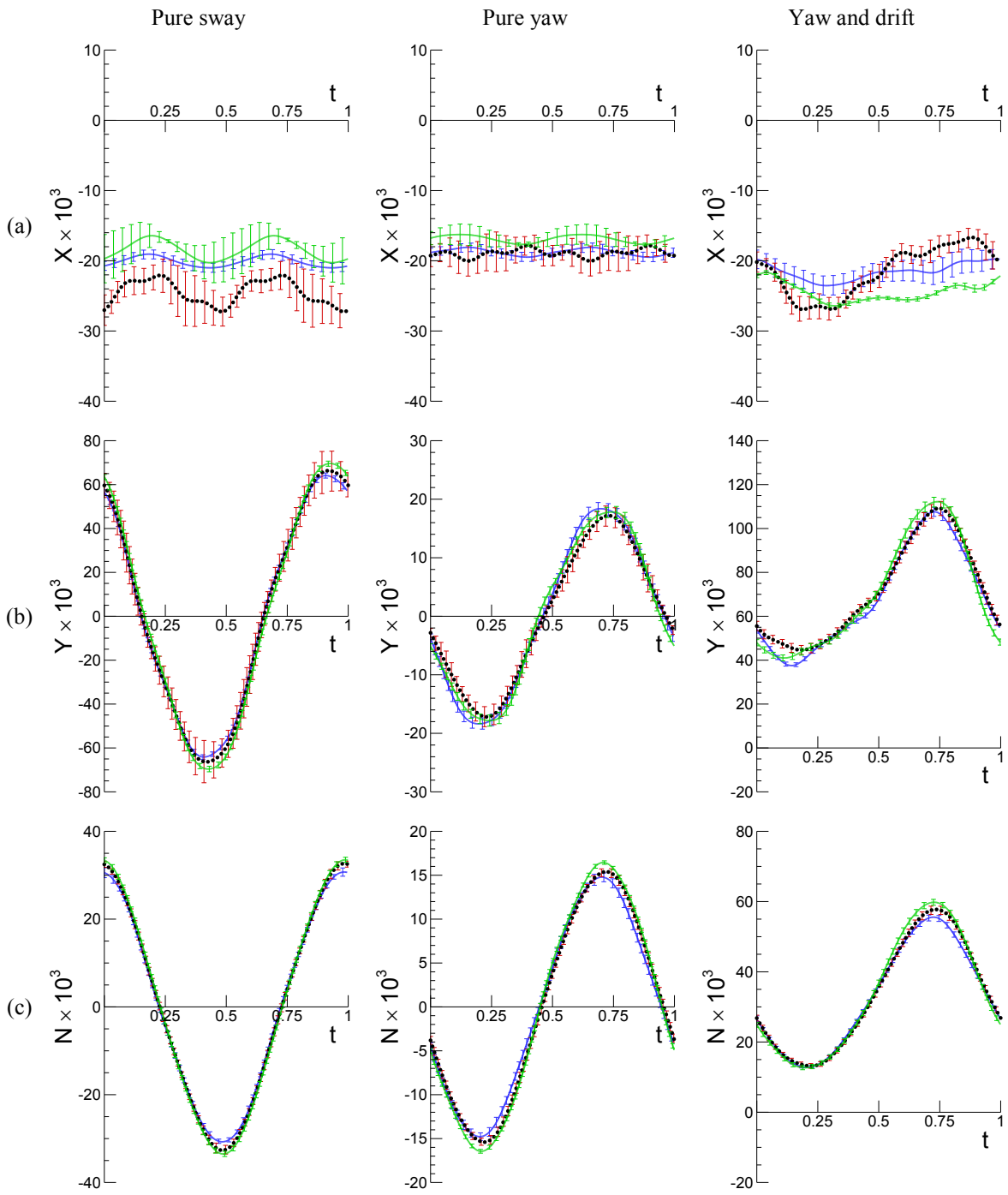

Figure 6-11 Comparisons between facilities – Dynamic tests data (Corrected for symmetry): (a) X, (b) Y, and (c) N for pure sway (left, β_{max} = 10°), pure yaw (center, r_{max} = 0.30), and yaw and drift (right, β = 10°) tests at Fr = 0.280, respectively. Symbols (colors): •, IIHR; —, FORCE; and —, INSEAN.

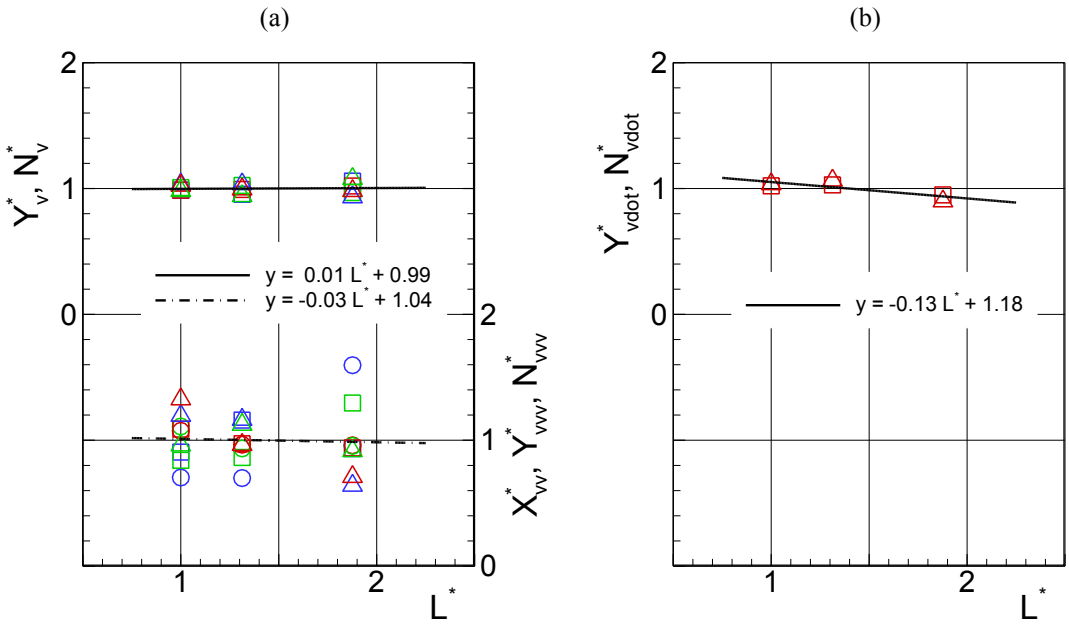

Figure 6-12 Comparisons between facilities: (a) sway-velocity and (b) -acceleration derivatives. Derivatives and model lengths are scaled values. Symbols: O, X_{vv}; □, Y_v^*, Y_{vvv}^*, or $Y_{\dot{v}}^*$; and Δ, N_v^*, N_{vvv}^*, or $N_{\dot{v}}^*$, respectively. Color codes: Fr = 0.138 (blue), 0.280 (red), and 0.410 (green), respectively.

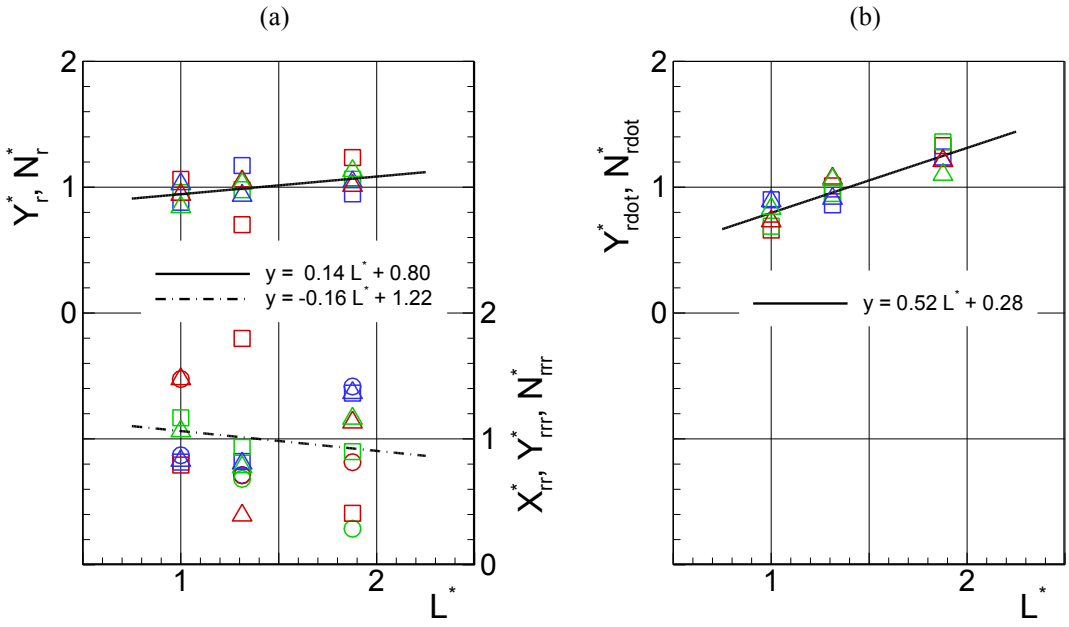

Figure 6-13 Comparisons between facilities: (a) yaw-rate and (b) -acceleration derivatives. Derivatives and model lengths are scaled values. Symbols: O, X_{rr}^*; □, Y_r^*, Y_{rrr}^*, or $Y_{\dot{r}}^*$; and Δ, N_r^*, N_{rrr}^*, or $N_{\dot{r}}^*$, respectively. Color codes: Fr = 0.138 (blue), 0.280 (red), and 0.410 (green), respectively.

6.1.4 Heave, Pitch, and Roll Motions

Time-mean values of static drift z, θ, and ϕ data are shown in Fig. 6-14 (a), (b), and (c), respectively. From (a) and (b), z and θ increase with β from the values at 0° to positive for the former (downward sinkage) and to negative for the latter (bow-down trim), respectively. From (c), ϕ is zero at β = 0° and increases to positive (heel to star-board) with β. Data are curve fitted to quadratic or cubic functions of β such that $z, \theta = A + B\beta^2$ and $\phi = A\beta + B\beta^3$, respectively, where the coefficients A's and B's are presented in Table 6-15. In general, both of the polynomial coefficients A and B are functions of *Fr*. From Fig. 6-14 (a) and (b), while the A (corresponding to the values at β = 0°) is increasing monotonically with *Fr* for z and oscillating for θ, respectively, more complete trends will be discussed later at the next Section with related to surge force X. The 2nd-order coefficient B for z and θ are shown in Fig. 6-14 (d) and (e), respectively, plotted against *Fr* numbers. In the figures, *Fr* is scaled with the lowest number, *Fr* = 0.138, and B is scaled with its value at the *Fr*, which are designated as Fr^* and B^*, re-spectively. Note that B for θ shown in Fig. 6-14 (e) is scaled with the value at Fr = 0.280 to avoid using a near-to-zero B value at Fr = 0.138 for the $FR_{z\theta}$ condition case. From the figures, B^* for z is quadratic whereas that for θ is nearly linear with Fr^*, respectively, indicating that

$$\Delta z \sim Fr^2 \cdot \beta^2 \quad \text{and} \quad \Delta\theta \sim Fr \cdot \beta^2 \tag{6.6}$$

where $\Delta z = z - A$ and $\Delta\theta = \theta - A$, respectively. Similarly, A^* and B^* for ϕ are shown in Fig. 6-14 (f) where the A^* increases nearly linearly for $Fr^* < 2$ and then more steeply with Fr^*, whereas the B^* is almost independent of Fr^*, thus, approximately for small *Fr* and β,

$$\phi \sim Fr \cdot \beta \tag{6.7}$$

For z and θ, also presented in Table 6-15 are the ratio ζ_ϕ values, defined in (6-13), for the polynomial coefficients for $FR_{z\theta}$ condition to those for $FR_{z\theta\phi}$ condition revealing the effect of roll motion to heave and pitch motions. As $\phi = 0$ at $\beta = 0°$, the ζ_ϕ for A's reveal no more than the errors in measurement of z and θ at the drift angle. For z, the ζ_ϕ values for B are close to unity, indicating that the effect of roll motions on heave is small or that the heave motion is independent with the roll motion. For θ, in contrast, ζ_ϕ values for B are considerably larger than unity, about 4 ~ 12, revealing that the pitch and roll motions are rather strongly coupled each other.

Time-histories of z, θ, and ϕ are shown in Fig. 6-15 (b), (c), and (d), respectively, for pure sway (left column), pure yaw (center column), and yaw and drift (right column) tests at $Fr = 0.280$, respectively. Shown in Fig. 6-15 (a) are the forced PMM motions; drift angle β for pure sway and heading angle ψ for pure yaw and yaw and drift tests, which are identical with those shown in Fig. 6-2 (a) for forces and moment. The FS harmonic amplitudes of the time-histories are evaluated as per (2) and summarized in Table 6-16 for $\beta_{max} = 10°$ case of pure sway test, $r_{max} = 0.30$ case of pure yaw test, and $\beta = 10°$ case of yaw and drift test, respectively. In the table, A is the oscillation amplitude of z, θ, and ϕ time-histories, respectively, and $z_{10°}$, $\theta_{10°}$, and $\phi_{10°}$ represent the static drift z, θ, and ϕ values at $\beta = 10°$, respectively.

For the heave z shown in Fig. 6-16 (b), the 2nd-order amplitude z_2 is most dominant for pure sway and pure yaw, about 100% of A. The oscillation amplitude A is small compared to the static drift, about 20% and 10% of $z_{10°}$ for pure sway and pure yaw, respectively. The 0th-order amplitude z_0, i.e. the period-mean value, is comparable with static drift, about 70% and 60% of $z_{10°}$ for pure sway and pure yaw, respectively. For yaw and drift, both A and z_0 are larger than those for pure sway and pure yaw, about 30% and 110% of $z_{10°}$, respectively. The 1st-order amplitude z_1 is dominant for yaw and drift, about 95% of A, and the 2nd-order amplitude z_2 is the second dominant, about 20% of A. For all test types harmonic amplitudes higher than 3rd-order $z_{3,4,5,6}$ are small, usually less

than 5% of A. Comparing the results between $FR_{z\theta\phi}$ and $FR_{z\theta}$ conditions, the ratio ζ_ϕ values for the dominant harmonic amplitudes including A's are close to unity, between about 0.8 – 1.4, indicating that the effects of the roll motions shown in Fig. 6-16 (d) on the heave motions are small.

For the pitch θ shown in Fig. 6-15 (c), the 2nd-order amplitude θ_2 is most dominant for pure sway and pure yaw, similarly as for heave, about 100% of A. Despite the fact for static drift test that θ for $FR_{z\theta\phi}$ condition is considerably larger than that for $FR_{z\theta}$ as shown in Fig. 6-14 (b) (where $\zeta_\phi = 2.67$ for θ at $\beta = 10°$), for pure sway test, however, similar values of the 0th-order amplitude θ_0 ($\zeta_\phi = 0.81$) and oscillation amplitude A ($\zeta_\phi = 0.86$) are observed from both of the conditions. The magnitudes of those θ_0 and A are about 80% and 40% of $\theta_{10°}$ for $FR_{z\theta}$ condition, respectively, and about 20% and 10% for $FR_{z\theta\phi}$ condition, respectively. In contrast, for pure yaw test, A for $FR_{z\theta\phi}$ is considerably large than that for $FR_{z\theta}$ ($\zeta_\phi = 2.14$) whereas θ_0 is similar for both conditions ($\zeta_\phi = 0.78$), indicating that the effect of roll motion on pitch is mainly for the oscillation amplitude A for pure yaw test. The magnitudes of those θ_0 and A are about 60% and 30% of $\theta_{10°}$ for $FR_{z\theta}$ condition, respectively, and about 15% and 20% for $FR_{z\theta\phi}$ condition, respectively. For yaw and drift test, both θ_0 and A for $FR_{z\theta\phi}$ is larger than those for $FR_{z\theta}$ ($\zeta_\phi = 2.62$ and 2.38, respectively), which are 142% and 152% of $\theta_{10°}$ for the former condition, respectively, and 123% and 120% for the latter condition, respectively. The harmonic amplitudes of higher than 3rd-order $\theta_{3,4,5,6}$ are small for all the test types, usually less than 5% of A, except for θ_4 for pure sway and pure yaw tests, about 10%.

For the roll ϕ shown in Fig. 6-15 (d), the 1st-order amplitude ϕ_1 is the most dominant, about 100% of A, for all test types. The oscillation amplitude A for pure sway test is larger than static drift ϕ, 124% of $\phi_{10°}$, whereas smaller for pure yaw and yaw and drift tests, about 70%, respectively. For yaw and drift test the 0th-order amplitude ϕ_0 is slightly larger than static drift ϕ, 106% of $\phi_{10°}$. Higher-order harmonic amplitudes $\phi_{2,3,4,5,6}$ are all small, usually less than 5% of A, for all test types, except for a few cases.

The 0th- and 2nd-order harmonic amplitudes of the heave motions z_0 and z_2 for all pure yaw test cases at Fr = 0.138, 0.280, and 0.410 are shown in Fig. 6-16 (a) and (b), respectively, with plotted against r_{max} values. In general, the overall appearances of z_0 data resemble the static drift z data shown in Fig. 6-14 (a), accordingly data are curve-fitted as $z_0 = A + Cr_{max}^2$ where the same A values for static drift z curve-fit corresponding to each Fr case is used for the curve-fits. z_2 shown in Fig. 6-16 (b) also exhibits quadratic trends with r_{max} and data are curve-fitted as $z_2 = D + Er_{max}^2$. Subsequently, the curve-fit coefficients C and E are scaled with those values for Fr = 0.138 case, designated as C^* and E^*, respectively, and shown in Fig. 6-16 (c) and (d), respectively, plotted against the Fr^* similarly as B^* shown in Fig. 6-14 (d) for static drift z data. From Fig. 6-16 (c), C^* increases with Fr^* roughly following a cubic line, which is much faster than the quadratic increase of B^*. Whereas from Fig. 6-16 (d), the E^* follows a $Fr^{*2.5}$ line, slower than C^* yet relatively faster than B^*. Accordingly, for those harmonic amplitudes,

$$\Delta z_0 \sim Fr^3 \cdot r_{max}^2 \qquad \text{and} \qquad \Delta z_2 \sim Fr^{2.5} \cdot r_{max}^2 \tag{6.8}$$

respectively, where $\Delta z_0 = z_0 - A$ and $\Delta z_2 = z_2 - D$, respectively. The coefficient D will be discussed later at next paragraph for pitch motion. Consequently, for dynamic pure yaw test, the magnitudes of z_0 and z_2 are smaller than static drift z, respectively about 80% and 10% from discussions above, however increases with Fr faster than static drift z.

Similarly, the 0th- and 2nd-order harmonic amplitudes of the pitch motions θ_0 and θ_2 for all pure yaw test cases are shown in Fig. 6-17 (a) and (b), respectively. Data are curve-fitted as $\theta_0 = A + Cr_{max}^2$ and $\theta_2 = D + Er_{max}^2$, respectively, and the scaled coefficients C^* and E^* are shown in Fig. 6-17 (c) and (d), respectively, for the former coefficient similarly as B^* for static drift θ shown in Fig. 6-14 (e) and for the latter coefficient similarly as E^* for z_2 discussed previously. From Fig. 6-17 (a), the overall appearances

of θ_0 are similar to those of the static drift θ data shown in Fig. 6-14 (b), whereas the θ_0 at $Fr = 0.410$ increases with r_{max} in contrast to the static drift θ at the same Fr, decreasing with β. Accordingly, the C^* shown in Fig. 6-17 (c) exhibits more complicated curve pattern than the simple linear pattern of static drift B^{**} shown in Fig. 6-14 (e), rather the E^* shown in Fig. 6-17 (e) exhibits linear trend with Fr^*. Thus, for those harmonic amplitudes,

$$\Delta\theta_0 \sim C(Fr)\cdot r_{max}^2 \qquad \text{and} \qquad \Delta\theta_2 \sim Fr\cdot r_{max}^2 \tag{6.9}$$

respectively, where $\Delta\theta_0 = \theta_0 - A$ and $\Delta\theta_2 = \theta_2 - D$, respectively, and more data may be necessary to determine a functional form for $C(Fr)$. For $FR_{z\theta\phi}$ condition, however, the θ_2 values are much larger than those for $FR_{z\theta}$ condition, as shown in Fig. 6-17 (b), due to the cross coupling between pitch and roll motions. When ϕ_1^* and θ_2^* are defined similarly as for the scaled coefficients for the data curve-fits, both exhibit quadratic trends with Fr^* as shown in Fig. 6-17 (e), thus it can be written as $\Delta\theta_2 \sim Fr^2\cdot r_{max}^2$ for $FR_{z\theta\phi}$ condition.

The 2nd-order harmonic amplitudes z_2 and θ_2 of heave and pitch motions are supposed to become zero as the forced PMM motions are getting smaller, e.g. $r_{max} \rightarrow 0$ for pure yaw test. Thus, the non-zero z_2 and θ_2 values at $r_{max} = 0.05$ shown in Fig. 6-16 (b) and Fig. 6-17 (b), respectively, (accordingly non-zero D's for the curve-fits) are out of expectation.

Table 6-15 Polynomial Fit Coefficients for Static Drift Motions Data.

Coeff.	Fr	$z \times 10^2$			θ (°)			ϕ (°)
		$FR_{z\theta}$	$FR_{z\theta\phi}$	ζ_ϕ	$FR_{z\theta}$	$FR_{z\theta\phi}$	ζ_ϕ	$FR_{z\theta\phi}$
A	0.138	0.006	-0.017	-2.83	-0.039	-0.004	0.10	0.056
	0.280	0.176	0.217	1.23	-0.097	-0.026	0.27	0.119
	0.410	0.434	0.516	1.19	0.396	0.453	1.14	0.239
$B \times 10^3$	0.138	0.284	0.291	1.02	-0.153	-1.759	11.50	0.096
	0.280	0.983	0.810	0.82	-1.326	-6.875	5.18	0.139
	0.410	2.692	2.428	0.90	-2.769	-10.609	3.83	0.115

Table 6-16 Harmonic Amplitudes[1)] of Motions for Dynamic Tests (Fr = 0.280).

Var.	Harmonic amplitude	Pure Sway (β_{max} = 10°)			Pure Yaw (r_{max} = 0.30)			Yaw and Drift (β = 10°)		
		$FR_{z\theta}$	$FR_{z\theta\phi}$	ζ_ϕ	$FR_{z\theta}$	$FR_{z\theta\phi}$	ζ_ϕ	$FR_{z\theta}$	$FR_{z\theta\phi}$	ζ_ϕ
z	z_0	0.67	0.81	1.16	0.54	0.76	1.37	1.12	1.12	0.96
	A	0.24	0.19	0.76	0.09	0.08	0.80	0.32	0.27	0.83
	z_1	-	-	-	-	-	-	0.95	0.94	0.82
	z_2	1.01	0.99	0.75	0.98	1.00	0.82	0.21	0.21	0.82
	z_3	-	-	-	-	-	-	0.01	0.02	1.40
	z_4	0.05	0.04	0.74	0.12	0.12	0.79	0.00	0.03	6.00
	z_5	-	-	-	-	-	-	0.00	0.02	7.00
	z_6	0.03	0.03	0.65	0.06	0.07	1.00	0.02	0.01	0.50
θ	θ_0	0.77	0.21	0.81	0.60	0.15	0.78	1.42	1.23	2.62
	A	-0.42	-0.12	0.86	-0.30	-0.22	2.14	-1.52	-1.20	2.38
	θ_1	-	-	-	-	-	-	0.97	0.99	2.44
	θ_2	0.99	1.03	0.89	0.99	1.01	2.19	0.12	0.14	2.90
	θ_3	-	-	-	-	-	-	0.02	0.01	1.62
	θ_4	0.09	0.10	1.02	0.13	0.05	0.78	0.00	0.01	4.30
	θ_5	-	-	-	-	-	-	0.00	0.01	6.06
	θ_6	0.01	0.02	2.48	0.04	0.02	1.14	0.00	0.01	6.87
ϕ	ϕ_0	-	-	-	-	-	-	-	1.06	-
	A	-	1.24	-	-	0.71	-	-	0.67	-
	ϕ_1	-	1.00	-	-	1.01	-	-	1.03	-
	ϕ_2	-	-	-	-	-	-	-	0.02	-
	ϕ_3	-	0.09	-	-	0.01	-	-	0.04	-
	ϕ_4	-	-	-	-	-	-	-	0.01	-
	ϕ_5	-	0.06	-	-	0.01	-	-	0.01	-
	ϕ_6	-	-	-	-	-	-	-	0.01	-

[1)] Those values presented herein are χ_0 ($\chi = z, \theta, \phi$) and A in % of $\chi_{10°}$ and χ_n (n = 1, 2, …, 6) in % of A, respectively, where $\chi_{10°}$ represents the static drift χ value at β = 10°.

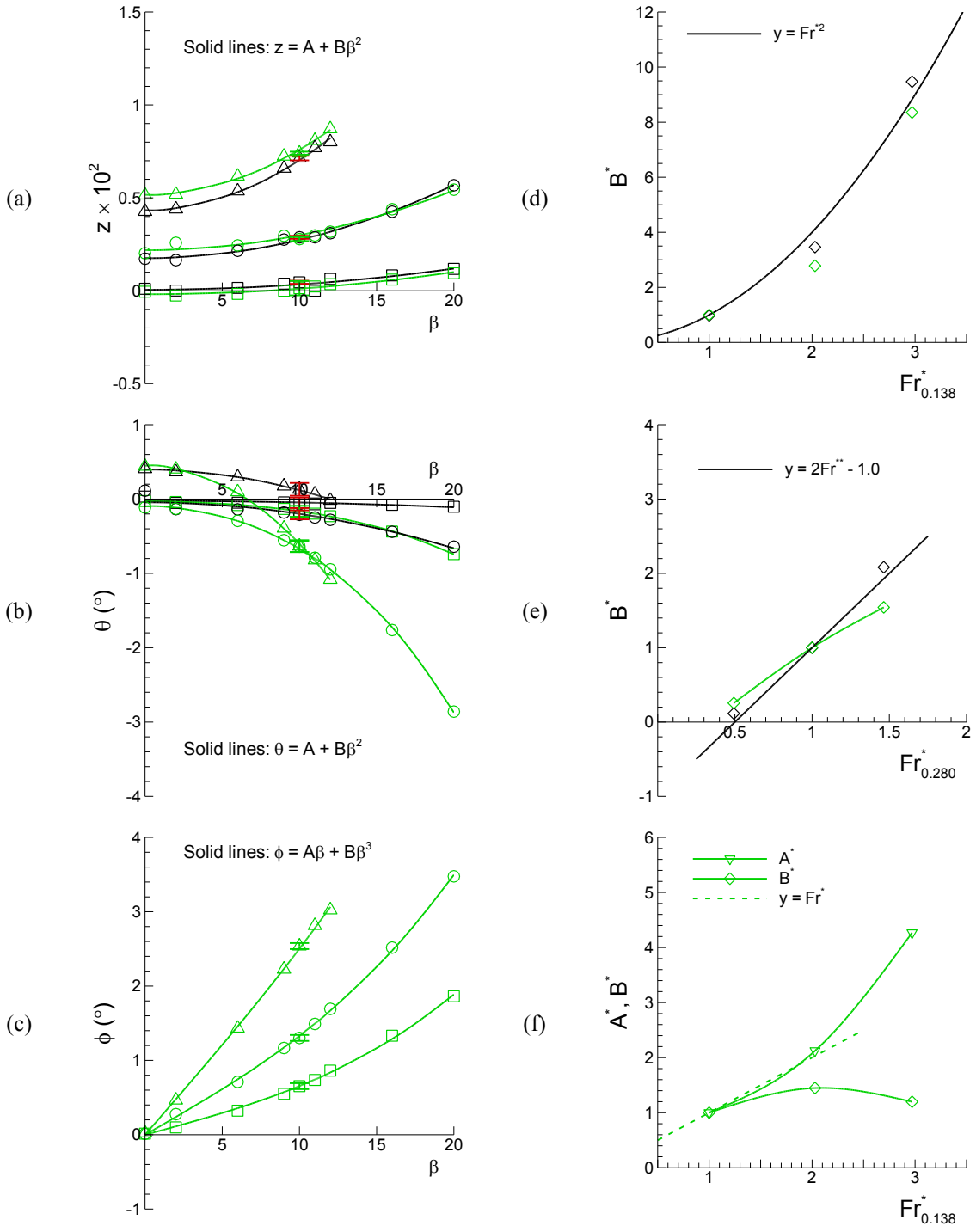

Figure 6-14 Motions data for static drift tests (Corrected for symmetry): (a) z, (b) θ, and (c) ϕ, and the polynomial-fit coefficients (scaled): (d) B^* for z, (e) B^* for θ, and (f) A^* and B^* for ϕ, respectively. Symbols for (a), (b), and (c): □, Fr = 0.138; o, Fr = 0.280; Δ, Fr = 0.410; ∇, A^*; ◊, B^*. Color codes: —, $FR_{z\theta}$ and —, $FR_{z\theta\phi}$.

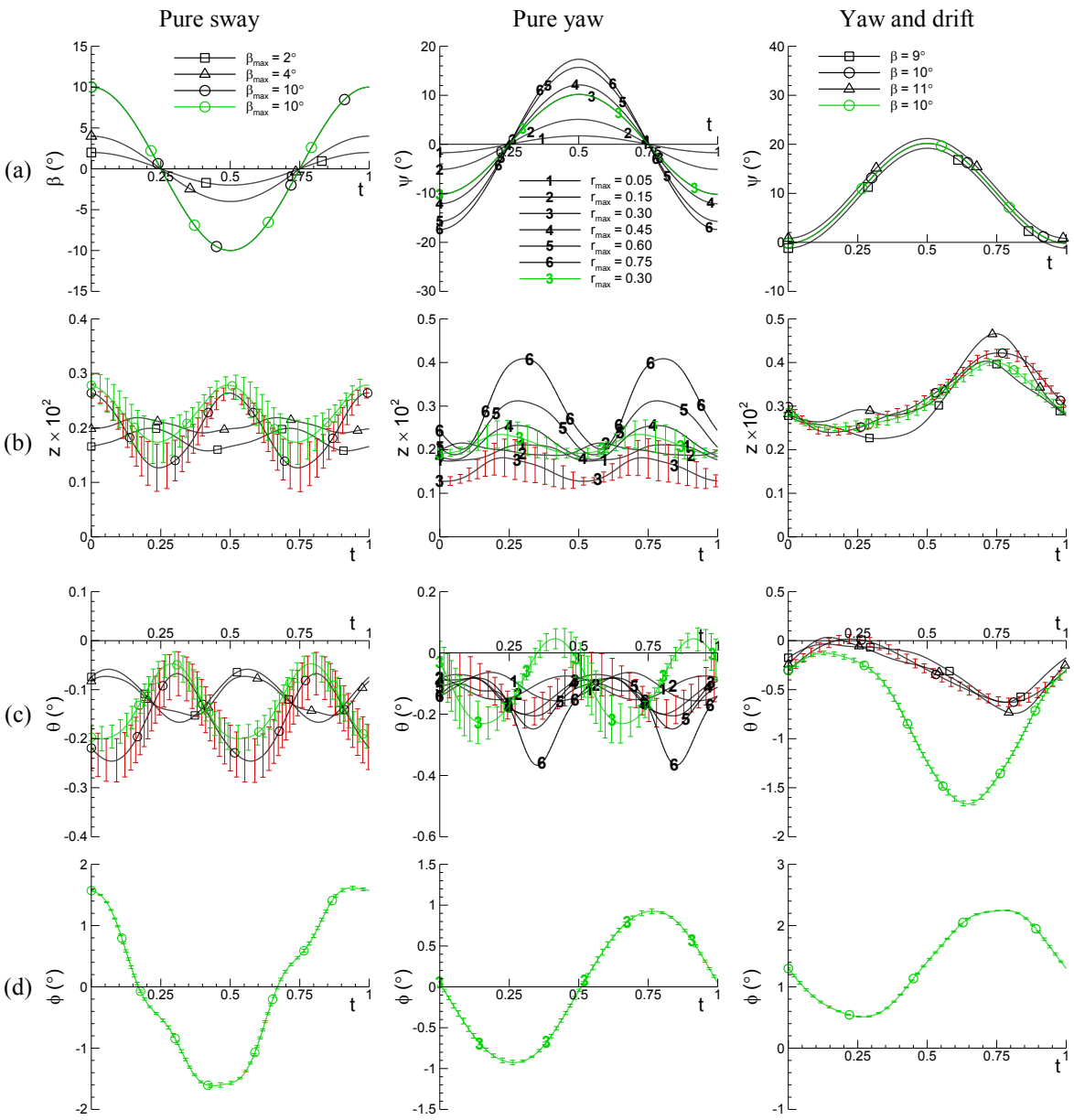

Figure 6-15 Time-histories of motions data (Corrected for symmetry) for pure sway test (left column), pure yaw test (center column), and yaw and drift test (right column) at $Fr = 0.280$, resepctively: (a) input motions β or ψ, and responses in (b) z, (b) θ, and (c) ϕ. Color codes: —, $FR_{z\theta}$ and —, $FR_{z\theta\phi}$.

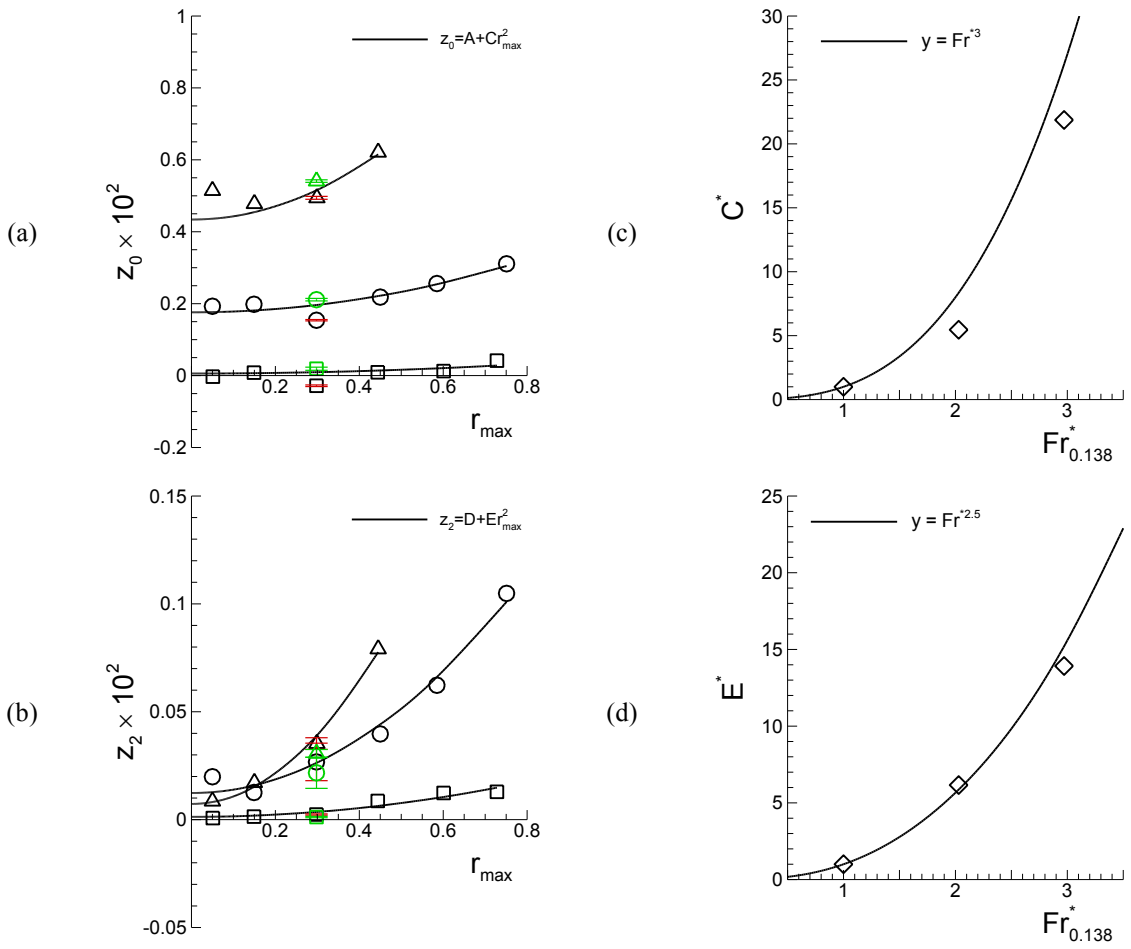

Figure 6-16 Pure yaw heave 0th- and 2nd-order harmonic amplitudes: (a) z_0 and (b) z_2, and scaled curve-fit coefficients: (c) C^* and (d) E^*. Simbols for (a) and (b): □ $Fr = 0.138$, o $Fr = 0.280$, Δ $Fr = 0.410$. Color code: —, $FR_{z\theta}$ and —, $FR_{z\theta\phi}$.

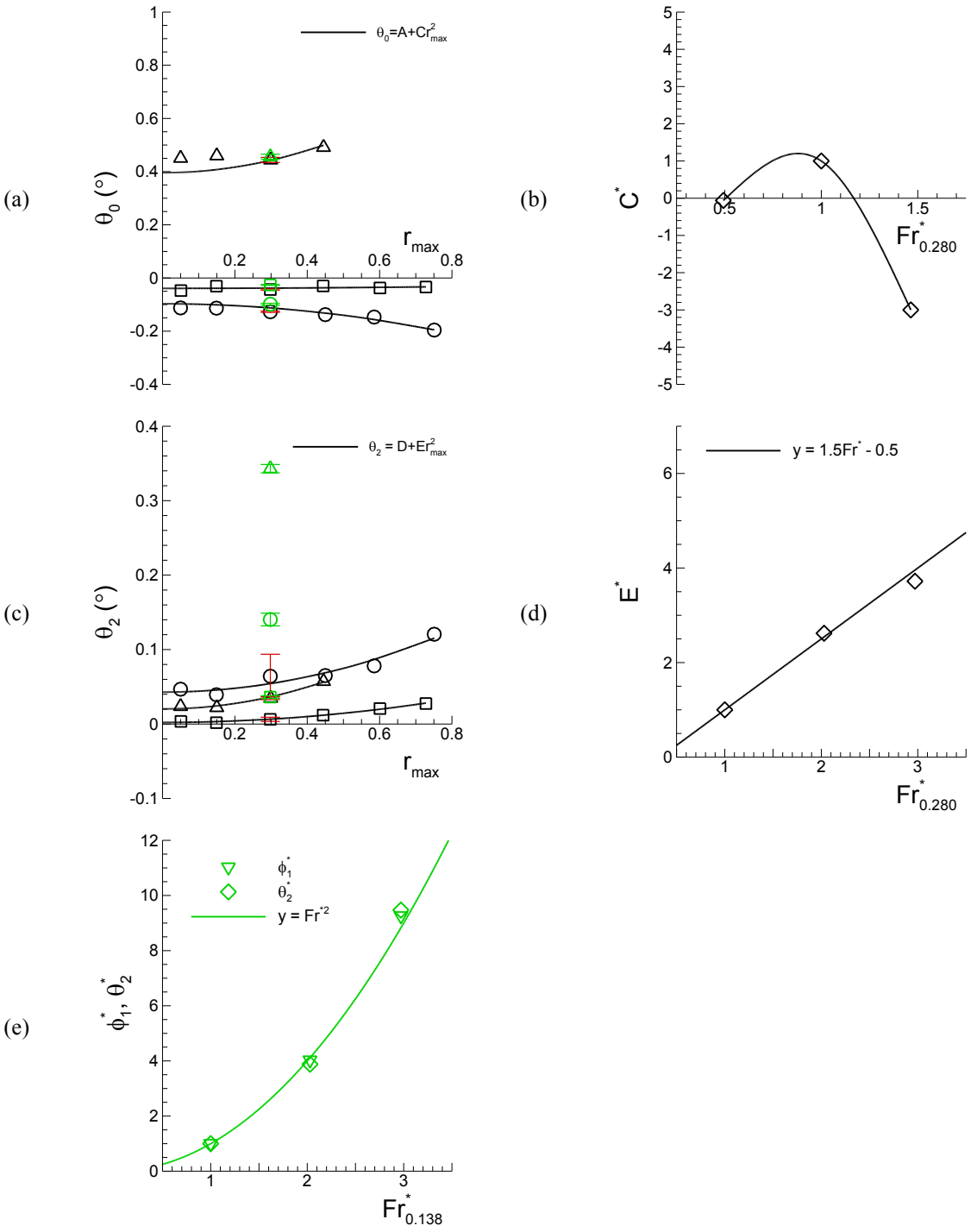

Figure 6-17 Pure yaw pitch 0th- and 2nd-order harmonic amplitudes: (a) θ_0 and (b) θ_2, and scaled curve-fit coefficients: (c) C^* and (d) E^*, and (e) scaled 1st-order roll and 2nd-order pitch harmonic amplitudes, ϕ_1^* and θ_2^*. Simbols for (a) and (b): □ Fr = 0.138, o Fr = 0.280, Δ Fr = 0.410. Color codes: —, $FR_{z\theta}$ and —, $FR_{z\theta\phi}$.

6.1.5 The Effects of Motions and Mount Conditions

Forces and moment and subsequent hydrodynamic derivatives are compared between four mount-conditions, FX_0, $FX_{\sigma\tau}$, $FR_{z\theta}$, and $FR_{z\theta\phi}$ (Sections 3.3 and 3.4), and the effect of heave, pitch, and roll motions on those variables are discussed. For the comparisons the ratios of data $\xi_{\sigma\tau}$, $\xi_{z\theta}$, and $\xi_{z\theta\phi}$ are defined as

$$\xi_{\sigma\tau,z\theta,z\theta\phi} \equiv \frac{x_{\sigma\tau,z\theta,z\theta\phi}}{x_0} \tag{6.10}$$

where $x_{\sigma\tau}$, $x_{z\theta}$, $x_{z\theta\phi}$, and x_0 can be any quantity from the $FX_{\sigma\tau}$, $FR_{z\theta}$, $FR_{z\theta\phi}$, and FX_0 conditions, respectively. As all motions are restrained for FX_0 condition (except for the forced PMM motions), the ratios $\xi_{\sigma\tau}$, $\xi_{z\theta}$, and $\xi_{z\theta\phi}$ signify the effect of sinkage and trim, heave and pitch motions, and heave, pitch, and roll motions, respectively, on the variable x of interest. Note that ζ_ϕ defined in (6-13) is equivalent to $\xi_{z\theta\phi}/\xi_{z\theta}$ such that $\zeta_\phi = \xi_{z\theta\phi}/\xi_{z\theta}$, which emphasizes the effect of roll motion. The ratios values for some select cases are presented for static drift X, Y, and N in Table 35 and for the dominant harmonic amplitude and phase of dynamic tests in Table 36, respectively.

Static drift X, Y, and N data for all mount conditions are shown in Fig. 6-18. In general, data are close between the $FX_{\sigma\tau}$ and FX_0 conditions and as well between the $FR_{z\theta}$ and $FRz_{\theta\phi}$ conditions, whereas considerably different between the $FR_{z\theta}$ and FX_0 conditions. Between $FX_{\sigma\tau}$ and FX_0, at $Fr = 0.280$ (middle column) in Fig. 6-18, $\xi_{\sigma\tau} = 1.05$ in average for X, Y, and N at $\beta = 10°$ indicating that the forces and moment increased about 5% due to sinkage and trim ($\sigma = 0.192\times10^{-2}\ L$ and $\tau = -0.136°$; fixed) from those for FX_0 condition ($\sigma = \tau = 0$; fixed). When the model is released free in heave and pitch for $FR_{z\theta}$ condition ($z = 0.288\times10^{-2}\ L$ and $\theta = -0.212°$ at $\beta = 10°$; $z/\sigma = 1.5$ and $\theta/\tau = 1.6$), then the increase in forces and moment from FX_0 becomes considerably larger, where $\xi_{z\theta} = 1.14$ in average at $\beta = 10°$. As β increased to 20°, the increase in forces and moment as well grows with β for $FR_{z\theta}$ condition ($\xi_{z\theta} = 1.28$ in average), whereas remains

almost constant with β for $FX_{\sigma\tau}$ condition ($\xi_{\sigma\tau}$ = 1.05 in average), respectively. The forces and moment increase even larger at Fr = 0.410 for $FR_{z\theta}$ condition, shown at the right column of Fig. 6-18, where $\xi_{z\theta}$ = 1.28 in average at β = 10°. On the other hand, for $FR_{z\theta\phi}$ condition, forces and moment data are not different from those for $FR_{z\theta}$ with $\xi_{z\theta\phi}$ values close to $\xi_{z\theta}$ for all cases, i.e. $\zeta_\phi \approx 1.0$, indicating that the effect of roll motion (ϕ = 0.7°, 1.3°, and 2.5° at β = 10° for Fr = 0.138, 0.280, and 0.410, respectively) on the forces and moment is almost negligible.

For the $FR_{z\theta}$ condition, the increase of forces and moment from FX_0, say Δx for x = X, Y, or N, can be written as

$$\Delta x = x_{z\theta} - x_0 = x_0\left(\xi_{z\theta} - 1\right) \tag{6.11}$$

where $x_{z\theta}$ and x_0 are the x of $FR_{z\theta}$ and FX_0 conditions, respectively. Shown in Fig. 6-19 are (a) the Δx for X, Y, and N of Fr = 0.280 case over $0 < \beta < 20°$ range and (b) those at β = 10° of Fr = 0.138, 0.28, and 0.410 cases, respectively. In the figures, the β values and Fr numbers at the abscissa are scaled with 10° and 0.138, respectively, denoted as β^* and Fr^*, respectively, and the Δx values at the ordinate are scaled with its value at β =10° and at Fr = 0.138, respectively, denoted as Δx^*. Consequently, the results indicate that Δx is proportional to β^{*2} and $Fr^{*1.5}$ such as

$$\Delta x \sim Fr^{1.5} \cdot \beta^2 + f(Fr) \tag{6.12}$$

where $f(Fr)$ is for β = 0° and f = 0 for Y and N. Recalling (6.6) in Section 6.1.4 that $\Delta z \sim Fr^2 \cdot \beta^2$ and $\Delta\theta \sim Fr \cdot \beta^2$ for static drift heave and pitch at $\beta > 0$, the rate of increase in forces and moment Δx is similar as heave and pitch with β whereas relatively slow with Fr, respectively. In that, however, pitch motion is strongly coupled with roll motion as discussed in Section 6.1.4 (with $\zeta_\phi > 4$ for θ) whereas Δx is almost independent of roll

with $\zeta_\phi \approx 1.0$ as discussed above, it is considered that Δx for $\beta > 0$ is mainly attributed to the heave motion.

On the other hand, from (6.12), $\Delta x \sim f(Fr)$ at $\beta = 0°$ for X. As $\beta = 0°$ corresponds to the steady, straight towing condition, the X, z, and θ values at $\beta = 0°$ shown in Fig. 6-1 (a), Fig. 6-14 (a), and Fig. 6-14 (b), respectively, are converted into the total resistance C_T, sinkage σ, and trim τ of the model, respectively[14]. The $C_{T_{15C}}$, σ, and τ data are presented in Fig. 6-20 showing good agreements with Longo et al. (2005)[15] where the authors used the same DTMB 5512 model as the present study and measured $C_{T_{15C}}$, σ, and τ over a range of Fr = 0.05 - 0.45. The Results of Longo et al. reveals more clearly the Fr trends of $C_{T_{15C}}$, σ, and τ, i.e. X, z, and θ at $\beta = 0°$; C_{T15C} first decreases for $Fr < 0.25$, oscillates small at $0.25 < Fr < 0.35$, and sharply increases for $Fr > 0.35$; σ increases rather monotonically; τ increases first to negative (bow-down), then oscillates, and sharply increases to positive (bow-up), respectively. Noticing similar Fr trends between the data, C_{T15C} data were curve-fitted with σ and τ data using a regression equation[16] $y(\sigma, \tau) =$

---

[14] Those are defined as:

$$C_T = -F_x/0.5\rho U_C^2 S;\ \sigma = (\Delta FP + \Delta AP)/2L;\ \tau = (\Delta AP - \Delta FP)/L$$

respectively, where S is the wetted-surface area of the model and ΔFP and ΔAP are the model displacements at the forward- (FP) and aft-perpendiculars (AP), respectively, related to z and θ as:

$$\Delta FP = z - \tfrac{1}{2}L\sin\theta \text{ and } \Delta AP = z + \tfrac{1}{2}L\sin\theta$$

respectively. Typically, C_T is converted into $C_{T_{15C}}$ with all data calibrated to a standard water temperate 15°C, which allows direct comparisons of the C_T values between tests at different Reynolds number (Re) conditions.

[15] Those data presented in Longo et al. (2005) were found to be erroneous as confirmed with the authors by personal communications. The C_{T15C} in Fig. 3 and σ and τ data in Fig. 4 of Longo et al. (2005) were found to be C_T, 4σ, and 2τ, respectively, accordingly those data were corrected for Fig. 21 of the present study.

[16] Also tested were three other regression equations: $y = a + b\sigma$; $y = a + c\tau$; $y = a + b\sigma + c\tau$. The resulting correlation coefficients were r = 0.80, 0.93, and 0.96, respectively.

$a + b\sigma + c\tau + d\sigma\tau$. The result shown in Fig. 6-20 (a) demonstrates a good agreement between C_{T15} and $y(\sigma, \tau)$ with a correlation coefficient r = 0.99, indicating that C_{T15C}, i.e. X for static drift, is strongly correlated with σ and τ, i.e. heave and pitch, such that $X \sim f(\sigma, \tau; Fr)$ at $\beta = 0°$.

Dynamic test results are shown Fig. 6-21 for pure sway at β_{max} = 10° (left column), pure yaw at r_{max} = 0.3 (middle column), and yaw and drift at β = 10° (right column) cases, respectively. Overall trends are similar as for static drift; for dominant harmonic amplitudes such as the 0th-order amplitude X_0 and the 1st-order amplitudes Y_1 and N_1, data are close between the $FX_{\sigma\tau}$ and FX_0 conditions and between the $FR_{z\theta}$ and $FR_{z\theta\phi}$ conditions, but different between the $FR_{z\theta}$ and FX_0 conditions. Between the $FX_{\sigma\tau}$ and FX_0 conditions, for pure sway and pure yaw tests, data are fairly close each other with $\xi_{\sigma\tau}$ = 0.9 ~ 1.0 for X_0 and $\xi_{\sigma\tau}$ = 1.0 ~ 1.1 for Y_1 and N_1. For $FR_{z\theta}$ condition, compared to FX_0 condtion, the dominant harmonic amplitudes are fairly larger for pure sway data with $\xi_{z\theta}$ = 1.1 ~ 1.3, and moderately larger for pure yaw data with $\xi_{z\theta}$ = 1.0 ~ 1.1 and for yaw and drift data with $\xi_{z\theta}$ = 1.1 ~ 1.2, respectively. For yaw and drift data, however, the 1st-order amplitude X_1 of $FR_{z\theta}$ is significantly larger than FX_0 with $\xi_{z\theta}$ = 3.7. Those data for $FR_{z\theta\phi}$ condition are close to $FR_{z\theta}$ in general with similar values of $\xi_{z\theta}$ for the dominant harmonic amplitudes and thus $\zeta_\phi \approx 1.0$ indicating the effect of roll motions on those dominant harmonics data is small or nearly negligible. In contrast, the 1st-order phases φ_{Y1} and φ_{N1} are close between all mount conditions for all test types, with $\xi_{\sigma\tau}$, $\xi_{z\theta}$, $\xi_{z\theta} \approx 1.0$, implying that the ratios between the added-mass and the damping forces, as shown in (3) and (4), remains almost constant despite the changes in the harmonic amplitudes Y_1 and N_1 between mount conditions. Nonetheless, no clear trend of those data such as (12) for static drift data, is observed from the dominant harmonics data with the PMM motion parameters such as β_{max}, r_{max}, or β, or with Fr.

Hydrodynamic derivatives are compared between the mount conditions in Table 6-19 for sway, yaw, and cross-coupled derivatives. For the sway derivatives, sway velocity derivatives Y_v, N_v, X_{vv}, Y_{vvv} and N_{vvv} are by using the static drift data and the sway acceleration derivatives $Y_{\dot{v}}$ and $N_{\dot{v}}$ are using the MR_L method (Section 2.3.5) for the pure sway test data, respectively. The yaw derivatives Y_r, N_r, X_{rr}, Y_{rrr}, N_{rrr}, $Y_{\dot{r}}$, $N_{\dot{r}}$ and the cross-coupled derivatives X_{vr}, Y_{vrr}, Y_{rvv}, N_{vrr}, N_{rvv} are as well using the MR_L method for the pure yaw and yaw and drift tests data, respectively. Note that those derivatives for $FR_{z\theta\phi}$ condition are using the SR_L method (Section 2.3.5) due to the limited number of test case, except for the sway velocity derivatives. As $FR_{z\theta}$ is the most common mount condition for PMM tests, of interest herein are the ratios ζ_0, $\zeta_{\sigma\tau}$, and ζ_ϕ of those derivatives for FX_0, $FX_{\sigma\tau}$, and $FR_{z\theta\phi}$ condition, respectively, to for $FR_{z\theta}$ condition defined as

$$\zeta_{0,\sigma\tau,\phi} \equiv \frac{x_{0,\sigma\tau,z\theta\phi}}{x_{z\theta}} \tag{6.13}$$

where x_0, $x_{\sigma\tau}$, $x_{z\theta\phi}$, and $x_{z\theta}$ can be any quantity from the FX_0, $FX_{\sigma\tau}$, $FR_{z\theta\phi}$, and $FR_{z\theta}$ conditions, respectively. For sway derivatives, linear derivatives Y_v and N_v values of FX_0 condition are slight smaller than $FR_{z\theta}$ about 10% with $\zeta_0 = 0.9$ in average, while those of $FX_{\sigma\tau}$ condition are close to $FR_{z\theta}$ with $\zeta_{\sigma\tau} \approx 1.0$, respectively. The non-linear derivatives X_{vv}, Y_{vvv}, and N_{vvv} of both FX_0 and $FX_{\sigma\tau}$ conditions, however, are considerably smaller than $FR_{z\theta}$ with ζ_0, $\zeta_{\sigma\tau} \approx 0.6$, and the sway acceleration derivatives $Y_{\dot{v}}$ and $N_{\dot{v}}$ are as well smaller, with ζ_0, $\zeta_{\sigma\tau} \approx 0.8$ for the former derivative and ζ_0, $\zeta_{\sigma\tau} \approx 0.6$ for the latter, respectively. On the other hand, for $FR_{z\theta\phi}$ condition, all the sway derivative values are close to $FR_{z\theta}$ with $\zeta_\phi \approx 1.0$ except for a few cases. For yaw derivatives, linear derivatives Y_r and N_r of all mount conditions are close to $FR_{z\theta\phi}$ typically with ζ_0, $\zeta_{\sigma\tau}$, $\zeta_\phi = 0.9 \sim 1.2$, whereas the non-linear derivatives X_{rr}, Y_{rrr}, N_{rrr} are usually smaller than $FR_{z\theta\phi}$ for FX_0 and $FX_{\sigma\tau}$ conditions with ζ_0, $\zeta_{\sigma\tau} = 0.5 \sim 0.7$ in general. Those non-linear derivatives of $FR_{z\theta\phi}$ condition, however, are rather scattering both magnitude and sign of the derivatives

as those are determined using the 'Single-Run' method usually unreliable determining non-linear derivatives as discussed previously in Section 6.1.2. The yaw acceleration derivative $Y_{\dot{r}}$ values also scatter between the mount conditions with ζ_0, $\zeta_{\sigma\tau}$, ζ_ϕ = 0.5 ~ 1.3 but without consistency between cases, while $N_{\dot{r}}$ values for FX_0 and $FX_{\sigma\tau}$ conditions are smaller than $FR_{z\theta}$ with ζ_0, $\zeta_{\sigma\tau} \approx 0.8$ and for $FR_{z\theta\phi}$ condition larger with ζ_ϕ = 1.1 ~ 1.2, respectively. The comparisons results for the cross-coupled derivatives X_{vr}, Y_{vrr}, Y_{rvv}, N_{vrr}, and N_{rvv} are similar with for $N_{\dot{r}}$ but with larger ratio values; $\zeta_0 \approx 0.3$ for FX_0 condition (except for Y_{vrr} and Y_{rvv} for which ζ_0 = 1.0 and 0.8, respectively) and ζ_ϕ = 1.1 ~ 1.3 for $FR_{z\theta\phi}$ condition, respectively.

Consequently, by imposing a fixed amount of singkage and trim or by allowing the model to move freely in heave, pitch, or roll, the forces and moment increased up to about 10% and up to about 30% within the range of test conditions, respectively, from a condition where the model is completely restrained in all motions. For static drift test, the increase in forces and moment was mainly attributed to the heave motion for $\beta > 0°$, whereas at $\beta = 0°$, X force was correlated with both heave (sinkage) and pitch (trim) motions. Typically, the effect of roll motion was small or negligible for both static and dynamic forces and moment, possibly due to the small magnitudes of the roll motions. Despite the differences in forces and moment due to the heave and pitch motions, usually the linear hydrodynamic derivatives were close between the mount conditions, within a range of 90% ~ 110% range, whereas the non-linear derivative values were smaller for the fixed-model conditions typically more or less than 40% ~ 70% compared to the free-model conditions. The effect of roll motions was as well small or negligible for the hydrodynamic derivatives.

Table 6-17 Comparisons between mount-conditions (Static drift).

β	Var.	Fr = 0.138			Fr = 0.280				Fr = 0.410		
		$\xi_{z\theta}$	$\xi_{z\theta\phi}$	ζ_ϕ	$\xi_{\sigma\tau}$	$\xi_{z\theta}$	$\xi_{z\theta\phi}$	ζ_ϕ	$\xi_{z\theta}$	$\xi_{z\theta\phi}$	ζ_ϕ
0°	X	1.05	1.04	0.98	1.03	1.07	1.10	1.03	1.26	1.30	1.03
10°	X	1.08	1.07	0.99	1.03	1.14	1.14	1.00	1.32	1.37	1.03
	Y	1.08	1.06	0.99	1.05	1.11	1.12	1.00	1.25	1.29	1.03
	N	1.10	1.09	0.99	1.07	1.17	1.18	1.00	1.29	1.29	1.00
20°	X	1.16	1.15	0.99	1.03	1.26	1.21	0.96	-	-	-
	Y	1.06	1.07	1.01	1.06	1.24	1.21	0.98	-	-	-
	N	1.09	1.11	1.01	1.07	1.33	1.26	0.95	-	-	-

Table 6-18 Comparisons between mount-conditions (Dynamic tests at Fr = 0.280).

Var.	Har.	Pure Sway (β_{max} = 10°)				Pure Yaw (r_{max} = 0.30)				Yaw and Drift (β = 10°)		
		$\xi_{\sigma\tau}$	$\xi_{z\theta}$	$\xi_{z\theta\phi}$	ζ_ϕ	$\xi_{\sigma\tau}$	$\xi_{z\theta}$	$\xi_{z\theta\phi}$	ζ_ϕ	$\xi_{z\theta}$	$\xi_{z\theta\phi}$	ζ_ϕ
X	X_0	0.98	1.34	1.17	0.87	0.94	1.10	1.09	0.99	1.14	1.12	0.99
	X_1	-	-	-	-	-	-	-	-	3.74	4.05	1.08
Y	Y_0	-	-		-	-	-		-	1.13	1.12	0.99
	Y_1	1.08	1.12	1.13	1.01	1.00	1.00	0.99	0.99	1.13	1.09	0.97
	φ_{Y1}	1.00	1.03	1.03	1.00	1.03	0.98	0.98	1.00	0.98	1.00	1.02
N	N_0	-	-		-	-	-		-	1.22	1.22	1.00
	N_1	1.09	1.21	1.21	1.00	1.10	1.13	1.13	1.00	1.25	1.21	0.97
	φ_{N1}	1.00	1.03	1.02	1.00	1.01	1.00	1.00	1.00	1.00	1.00	1.00

Table 6-19 Comparisons between mount-conditions (Hydrodynamic derivatives).

Derivative	Fr	ζ_0	$\zeta_{\sigma\tau}$	ζ_ϕ
Y_v	0.138	0.92	-	0.97
	0.280	0.96	1.00	1.02
	0.410	0.89	-	1.07
N_v	0.138	0.90	-	0.97
	0.280	0.90	0.97	1.03
	0.410	0.86	-	1.05
X_{vv}	0.138	0.40	-	1.02
	0.280	0.65	0.67	0.89
	0.410	0.54	-	1.03
Y_{vvv}	0.138	0.98	-	1.07
	0.280	0.62	0.67	0.92
	0.410	0.56	-	0.91
N_{vvv}	0.138	0.95	-	1.14
	0.280	0.27	0.27	0.69
	0.410	0.41	-	0.78
$Y_{\dot{v}}$	0.280	0.81	0.87	1.02
$N_{\dot{v}}$		0.55	0.57	0.95
Y_r	0.138	1.05	-	0.65
	0.280	0.98	1.08	0.86
	0.410	1.18	-	1.19
N_r	0.138	0.98	-	0.95
	0.280	1.12	0.99	0.98
	0.410	0.91	-	1.17
X_{rr}	0.138	-0.55	-	-0.14
	0.280	0.71	1.02	-0.31
	0.410	0.57	-	0.02
Y_{rrr}	0.138	1.43	-	2.54
	0.280	0.47	0.47	3.56
	0.410	0.68	-	-0.36
N_{rrr}	0.138	1.00	-	1.53
	0.280	0.44	0.72	1.06
	0.410	0.55	-	0.06
$Y_{\dot{r}}$	0.138	0.73	-	1.12
	0.280	1.29	0.46	0.71
	0.410	0.98	-	0.95
$N_{\dot{r}}$	0.138	0.89	-	1.18
	0.280	-0.59	0.80	1.16
	0.410	0.81	-	1.06
X_{vr}	0.280	0.28	-	1.17
Y_{vrr}		1.03	-	1.26
Y_{rvv}		0.84	-	0.93
N_{vrr}		0.30	-	1.27
N_{rvv}		0.21	-	0.98

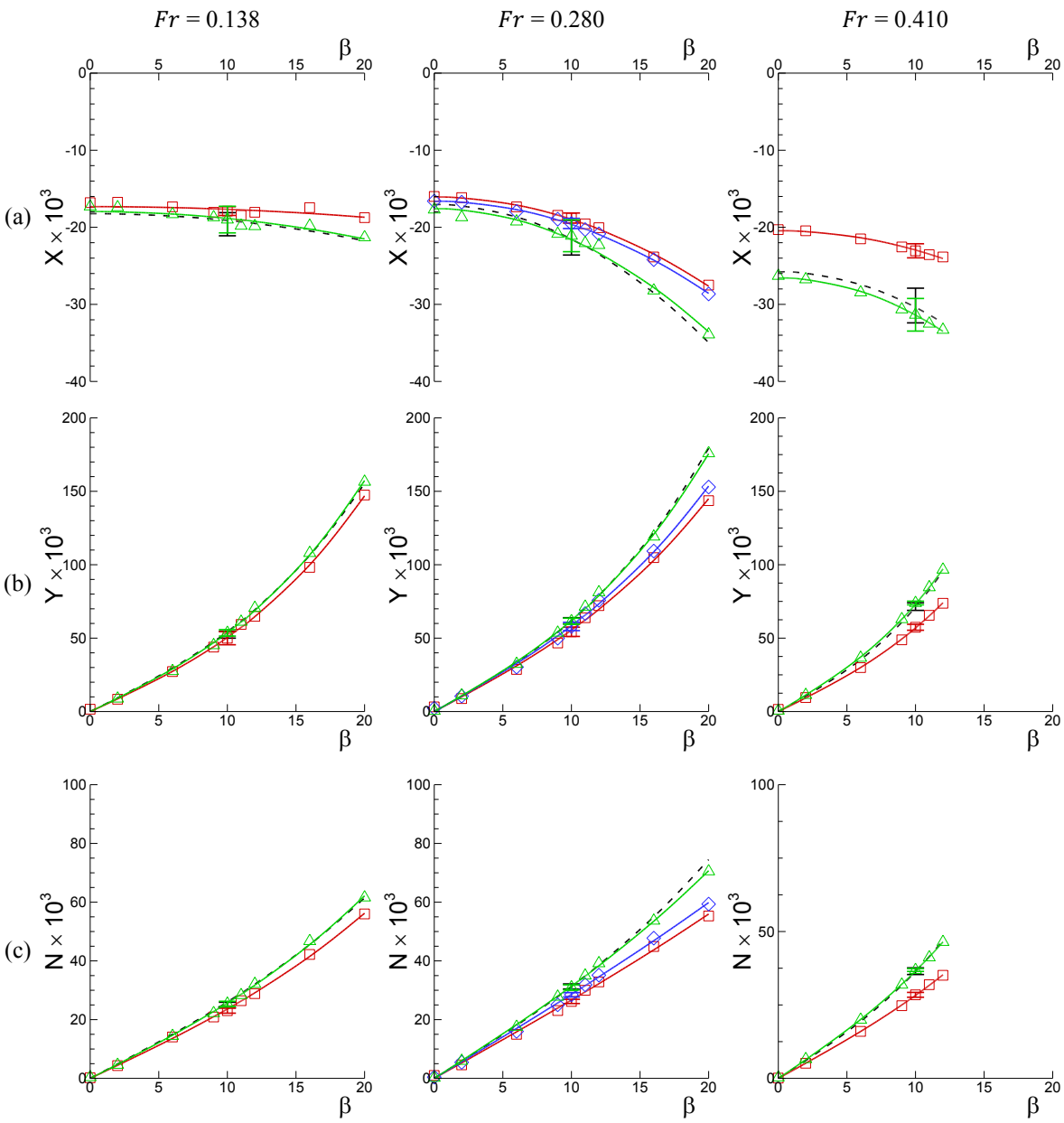

Figure 6-18 Comparisons between mount-conditions – Static drift data (Corrected for symmetry) at Fr=0.138 (left), 0.280 (center), and 0.410 (right): (a) X, (b) Y, and (c) N. Symbols (colors): □, FX_0; ◊, $FX_{z\theta}$; dash-line, $FR_{z\theta}$; and Δ, $FR_{z\theta\phi}$.

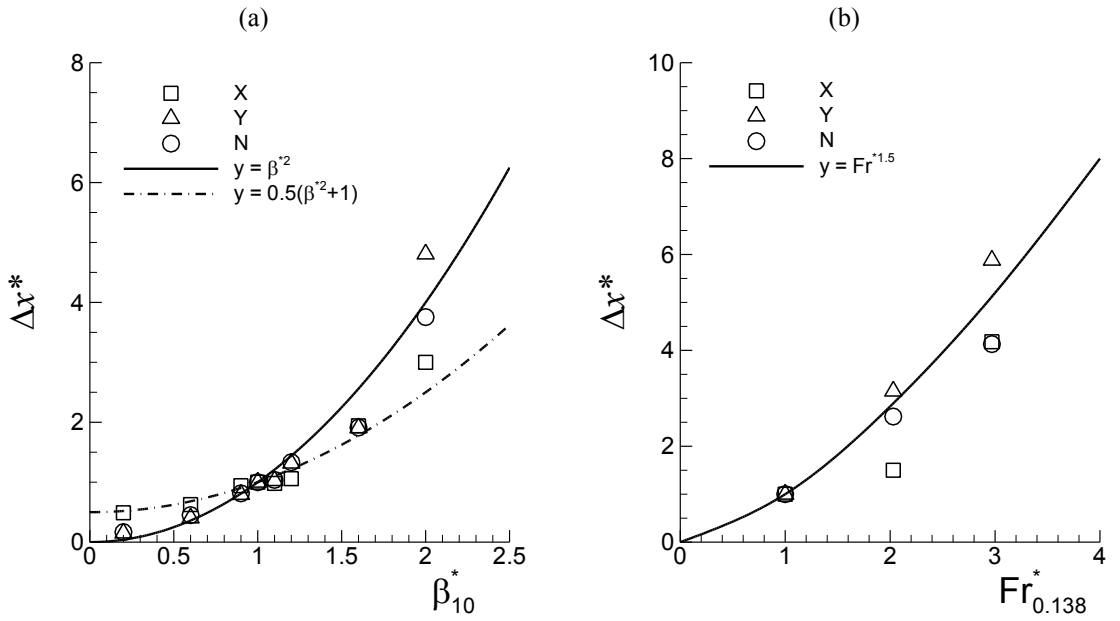

Figure 6-19 Comparisons of static drift X, Y, and N data between the $FR_{z\theta}$ and FX_0 mount conditions: (a) Δx vs. β at $Fr = 0.280$ and (b) Δx vs. Fr at $\beta = 10°$, where the Δx values are scaled with those at $\beta = 10°$ and with those at $Fr = 0.138$, respectively.

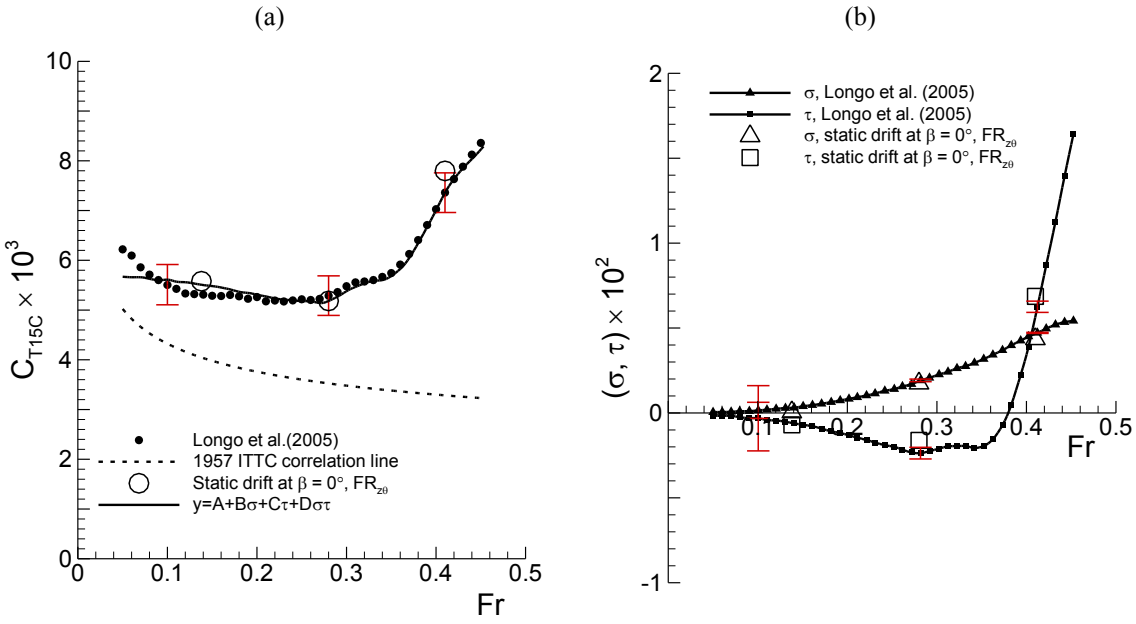

Figure 6-20 Comparisons of the static drift X, z, and θ data at $\beta = 0°$ with the resistance test (Longo et al. 2005): (a) C_{T15C} and (b) σ and τ.

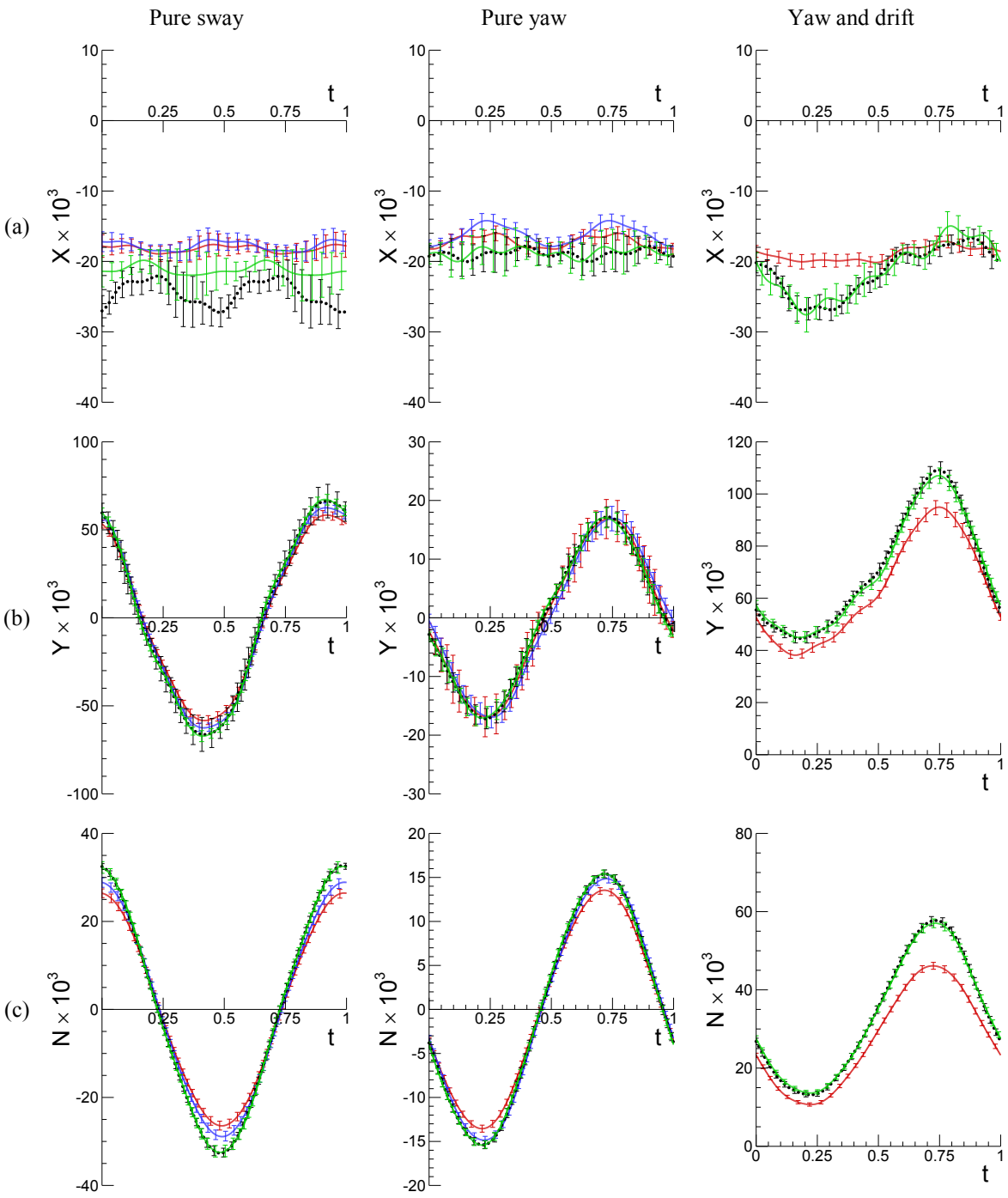

Figure 6-21 Comparisons between mount-conditions – Pure sway (left, β_{max} = 10° case), pure yaw (center, r_{max} = 0.30 case), and yaw and drift (right, β = 10° case) tests at Fr = 0.280 (Corrected for symmetry): (a) X, (b) Y, (c) N, (d) z, (e) θ, and (f) ϕ. Symbols (colors): —, FX_0; —, $FX_{z\theta}$; •, $FR_{z\theta}$; and —, $FR_{z\theta\phi}$.

6.2 Stereo-PIV measured flow fields

6.2.1 Pure sway flow field

The trajectory of model and overviews of flow around the model in pure sway motion are shown in Fig. 6-22. At the top of the figure model trajectory, i.e. the path line of model mid-ship point, is shown with a dashed line. The trajectory or the path line for pure sway motion is a combination of a constant towing carriage speed U_C and a cyclic sway motion $y = -y_0 \cdot \sin\omega t$, where the amplitude $y_0 = 0.104\ L$ and the frequency $\omega = 1.672\ U_C/L$ (period $T = 2\pi/\omega = 3.748\ L/U_C$) and $L = 3.048$ m is the model length and $U_C = 1.531$ m/s. In physical units, the sway frequency $f = 0.134$ Hz and the sway period $T = f^{-1} = 7.463$ sec. In the figure, the outlines of the model water-plane are shown at every 45° phases of the pure sway motion, $\gamma = \omega t = 0°$, 45°, 90°, 135°, 180°, 225°, 270°, 315°, and 360°, with numbered 1 through 9, respectively. For the first half of the cycle, model moves with its maximum negative (toward portside) sway velocity $v = -y_0\omega = -0.174$ at (1) $\gamma = 0°$ and decelerates through (2) $\gamma = 45°$ to (3) $\gamma = 90°$ where $v = 0$, and then changes its sway direction (toward starboard) and accelerates through (4) $\gamma = 135°$ to (5) $\gamma = 180°$. For the second half of the cycle, 5, 6, 7, and 8 are anti-symmetric with the 1, 2, 3, and 4, respectively, and 9 is identical with 1.

Below the model trajectory in Fig. 6-22, shown are the overviews of the SPIV measured flow field around the model at each of those phase positions. As well shown is the model path line (the curved lines with colored in light blue through the model) to emphasize the movement of model. As the model moving along the path line, accordingly the direction of incoming flow changes with the phase angle continuously, e.g. 10°, 7°, 0°, and -7° at $\gamma = 0°$, 45°, 90°, and 135°, respectively, (shown as blue arrows below at the model sonar dome in Fig. 6-1) with respect to the model center line, and in the opposite directions at the second half of the sway cycle. The flow field data presented in the figures are the contours of axial velocity U (≤ 0.95) and the cross flow streamlines, respec-

tively at four longitudinal locations, x = 0.135, 0.235, 0.735, and 0.935. Note that the streamlines are relative to model movements, i.e., seen from onboard. The overall flow pattern is with growing boundary layers in the longitudinal direction (thin at the fore body and thick at the aft body), and is mainly lateral flow in the cross planes where several apparent vortices are seen clearly, in general at the leeward side of the cross flow.

6.2.1.1 Vortical structure of the flow

More complete vortical structure of the flow can be seen from CFD simulations such as Sakamoto (2009) where the flows around DTMB 5512 geometry in steady and dynamic PMM motions are simulated. Simulation results for steady PMM motions are shown in Fig. 6-23, presenting the vortical flow structures for (a) straight-ahead and (b) static drift with drift angle $\beta = 10°$ cases. Sakamoto (2009) visualized the vortical flow structures by using the Q-criterion (Hunt et al., 1988) along with the relative helicity values; positive values for counterclockwise rotation (red colored) when viewed from behind a body and negative values for clockwise rotation (blue colored). For the straight-ahead case, i.e. $\beta = 0°$, the vortical structure is symmetry about hull center plane and with vortices in pairs of counter-rotating vortices. At the fore body sonar dome vortex (SD) and fore body keel vortex (FK) are generated behind the sonar dome and along the keel line, respectively. At the aft body, bilge keel vortex (BK), aft body keel vortex (AK), and transom vortex (T) are seen behind the bilge keels, neat at the aft body keel, and after the transom, respectively, however those vortices persist locally and are small in size in general. Note that the subscripts of the labels in the figure such as P, S, and C represent the portside, starboard, and center keel of the hull, respectively, where the vortices are generated. For $\beta = 10°$, the vortical structure is asymmetric about the hull center plane and vortices becomes considerably larger and global compared to the straight-ahead case.

The vortical flow structures for pure sway are shown in Fig. 6-24 (a) and (b), with vortices visualized from the CFD simulations by Sakamoto (2009) and from the vorticity

field measured by SPIV, respectively. In the figures vortical structures are shown at four sequential sway phase positions, $\gamma = 0°$, 45°, 90°, and 135°, in a column, so that the trajectory of the hull and the dynamic features of the vortical structures are envisioned. For CFD in (a), the vortical structures are in general similar with those for static drift with $\beta =$ 10° case shown in Fig. 6-23 (b), whereas the size, location, and the sign (direction of vortex rotation) of the vortices may change along the sway motion. For SPIV in (b), vortices are visualized with the vorticity ω_x contours with colored in red for $\omega_x \geq 20$ and in blue for $\omega_x \leq -20$ representing the counter-clockwise and clockwise rotations seen from behind the model in accordance with the helicity color coding for CFD. The ω_x contours are compared with the helicity iso-surfaces of CFD and corresponding vortices are identified with labeled in the figure. From CFD, SD_S vortex is first short and away from the hull at $\gamma = 0°$ and stretching in length and approaching toward the hull at $\gamma = 45°$ and thinning and straightened and close to the center plane at $\gamma = 90°$ and then detaches from the sonar dome and begins a counter rotating SD_P vortex at $\gamma = 135°$. Sakamoto (2009) reported that the angle between the SD_S and the hull center plane α_{SDs1} ~15° at non-dimensional time $t/T \sim 0.14$ or at $\gamma \sim 50°$. BK_P vortex at the portside, the second largest one, exhibits similar trend as SD; stretching and straightening, thinning, and then begins a counter rotating vortex. From SPIV, SD is not captured well at the stern side for $\gamma = 0°$ and 45°, maybe its location is out of the SPIV measurement area. At the fore body and for $\gamma = 90°$ and 135°, however, SD vortices can be seen clearly from the SPIV and seemingly in good agreement with CFD in terms of their size, location, and sign. FK vortices are not detected from SPIV or hard to be seen due to the lack of spatial resolution of SPIV measurement in the longitudinal direction, only two locations, $x = 0.135$ and 0.235, at the fore body where the FK vortices are from CFD. Whereas both BK_P and BK_S clearly seen from SPIV and in general exhibit qualitatively good agreements with CFD for their size, location, and direction of rotation, from a visual inspection. For other vortices, AK_C vortex near at the center of x = 0.935 plane in general matches well between CFD and SPIV,

whereas FS vortices are not clear from SPIV due to its limited amount of data and relatively larger uncertainty in measurements near at the free surface. The transom vortex T of CFD is out of SPIV measurement scope.

6.2.1.2 Phase-averaged velocity field

Phase-averaged mean axial velocity U is shown in Fig. 6-25 for the four longitudinal locations, x = 0.135, 0.235, 0.735, and 0.935 (from top to bottom), and for the four pure sway phase positions, γ = 0°, 45°, 90°, and 135° (from left to right), where the SPIV measurements were made. The flows at the later phase positions, γ = 180°, 225°, 270°, and 315°, are the horizontally mirrored images of those, respectively. In the figures, contours (with flooded) are presented for $U \leq 0.95$ and those for $U > 0.95$ are blanked out and not shown, to emphasize the parts where the flow is retarded from the incoming free stream (or the boundary layers) only. As well shown are the cross-sections of the model (the light gray part) cut at the four longitudinal x locations and the front part of the model from the cut positions with projected into the paper (the darker gray part) to highlight the details of the model hull form such as the locations of the sonar dome and the bilge keels. The flow is seen from behind the model, looking upstream, thus, the longitudinal direction of the incoming flow is out of paper from the figures. The transverse direction of the incoming flow is from the portside to starboard (left to right in the figure) with respect to the model for the first two phases, γ = 0° and 45°, and with no transversal flow at 90° and in reverse (right to left in the figure) for 135°. The incoming flow directions at the several sway phase positions are depicted in Fig. 6-1, together with the path lines of the model in the pure sway motion.

From Fig. 6-25, the mean axial velocity contours at x = 0.135 reveal very thin boundary layers near around the hull, and under the keel a retarded flow region that is in the SD vortex and in the wake of the sonar dome. At x = 0.235, the retarded flow region becomes smaller in size and is confined at near beneath the keel, may be the flow is out

of the sonar dome wake and recovers its momentum. At $x = 0.735$, the boundary layer thickens at the girth-wise middle of the bilges at portside and starboard, $(y, z) = (-0.04, -0.03)$ and $(0.04, -0.03)$, respectively, thicker at leeward side, and apparently interacting with the BK vortices. At $x = 0.935$, the boundary layer thickens considerably, and a large size dead-flow zone where $U < 0.5$ appears at $\gamma = 90°$, underneath the aft body keel, near around $(y, z) = (0, -0.1)$.

The shape and size of the boundary layers typically changes along with the model sway motion, possibly interacting with nearby vortices; mainly with the SD vortex at $x = 0.135$ and 0.235, with the BK and SD vortices at $x = 0.735$, and with the BK, AK, and SD vortices at $x = 0.935$. The shape of boundary layers at $\gamma = 0°$, 45°, and 135°, as expected, is asymmetry with respect to the hull center plane (i.e., $y = 0$) due to the transverse flow caused by the model sway motion, whereas it is notable that the boundary layer is as well asymmetry, particularly at the aft body, even at $\gamma = 90°$ where the incoming free stream flow is zero in transverse direction such that the incoming free stream flow is tangential to the model path line, i.e. straight ahead condition. This is due to the dynamic motions of the model such that while the vortices around the model are changing their size, spatial location relative to the model, and the direction of rotation, dynamically, as shown in Fig. 6-24, those changes may not in-phase with the model sway motions. The phase difference between the vortices and the model motion will be discussed later together with the vorticity field.

In Figs. 6-26 and 6-27, the average $U_{\leq 0.9}$ and minimum $U_{\min}$ values of the phase-average axial velocity U within the boundary layers at each phase (top) and the Fourier Series (FS) 0^{th}- and 2^{nd}-order harmonics, H_0 and H_2, of those values respectively (bottom) are presented. The $U_{\leq 0.9}$ and $U_{\min}$ are the average value for $U \leq 0.9$ and the minimum value, respectively, out of the SPIV measured U data within the boundary layer at each phase positions and x locations shown in Fig. 6-25. Note that the $U_{\leq 0.9}$ and $U_{\min}$ for $180° \leq \gamma < 360°$ shown in Figs. 6-26 (top) and 6-27 (top) are the mirrored values from those for

$0° \le \gamma < 180°$ anti-symmetrically. From Fig. 6-26 (top), in spite of the considerable dynamic changes of the boundary layers in shape and size, the $U_{\le 0.9}$ values are almost constant about 0.8 through the sway phase and along the hull longitude. From Fig. 6-26 (bottom), H_0 of $U_{\le 0.9}$, the period mean value, first slightly increases from 0.81 at x = 0.135 to 0.84 at x = 0.235, and then decreases at the aft body to 0.81 and 0.79 at x = 0.735 and 0.939, respectively. From Fig. 6-26 (bottom), H_2, i.e. the oscillation amplitude of $U_{\le 0.9}$ values along with the sway motion, is 0.014 in average, corresponding to about 2% of H_0, which has the largest value of 0.022 at x = 0.735, about 3% of H_0. In contrast, from Fig. 6-27, the changes of $U_{\min}$ with γ and x are larger than $U_{\le 0.9}$. The H_0 of $U_{\min}$ is 0.65 at x = 0.135 and then decreases to 0.43 at x = 0.935 rather monotonically. The average H_2 value along x is 0.056, about 10% of average H_0 = 0.55, and the maximum H_2 is 0.092 at x = 0.735, about 18% of the H_0 value at the location.

Cross flow velocity (V, W) vector field is shown in Fig. 6-28. In the figure, shown are the every 6th vectors from the SPIV measurement grid points in both y and z directions. While the vector field exhibits directions of the flow and the presence of vortices around the model, as an alternative way presenting the cross flow, in Fig. 6-29, the cross flow vector magnitude $S = (V^2 + W^2)^{1/2}$ and the cross flow streamlines are shown together. The spots where flow is accelerating or stagnant are obvious from the S contours and directions of the flow is clear from the streamlines and the location and size of the vortices exposed as well from the streamlines. At the fore body, x = 0.135 and 0.235, the cross flow at γ = 0° and 45° is directed downward and accelerating along the hull at the portside and overturns the keel and the SD vortex (that is not generated by the cross flow, rather it is being pushed and displaced by the cross flow stream to the leeward side) and then merges with the flow at the starboard. The SD vortex at x = 0.135 is small in size, $\phi \sim 0.01\ L$, and grows at x = 0.235, $\phi \sim 0.02\ L$. ϕ is the diameter of concentric streamline spirals. At γ = 90° where the incoming flow is tangent to the model path line, flow is nearly symmetry about the model center plane and mainly down- and outward

with displaced by the volume of fore body. At $\gamma = 135°$, the whole flow reverses as the model changes its direction in sway motion. At the aft body, $x = 0.735$ and 0.935, the flow at $\gamma = 0°$ and 45° is nearly lateral at the portside and turns to upward past the center plane becoming reversal in part where it meets the BK vortex at starboard. At $\gamma = 90°$, flow is mainly up- and inward, however, the flow is not symmetry about the center plane due to the presence of the SD vortex at the starboard. The flow reverses at $\gamma = 135°$, similarly as at the fore body.

6.2.1.3 Turbulent kinetic energy and Reynolds stresses

Turbulent kinetic energy k field is shown in Fig. 6-30. In the figure, the k field is shown only for $k \geq 0.001$ and blanked out for $k < 0.001$. Reynolds number of the flow is $\mathrm{Re} = U_C L/\nu = 4.6\times10^6$ where U_C and L are the towing carriage speed and model length, respectively, and ν is the kinematic viscosity of fresh water. It is noted that for pure sway test only a limited number of data (N) is used for phase-averaging, typically $N \sim 60$ for $x = 0.135$, 0.235, 0.735 and $N \sim 200$ for $x = 0.935$. Thus, phase-averaged turbulent variable values such as Reynolds stresses including the turbulent kinetic energy may not be fully converged statistically, and may include the statistical convergence error E_U up to 50% for data at the former and to 25% at the later x locations, respectively (See Chapter 4 and Fig. 4-7b for $s^2/s_{\mathrm{ref}}^2 = 1.0$). From Fig. 6-30, the shapes of k contours in general coincide with those of the mean axial velocity contours shown in Fig. 6-25, and typically k exhibits larger value inside the boundary layer of the model and at the core region of the vortices.

In Figs. 6-31 and 6-32, presented are the time histories (top) and the FS harmonics (H_0 and H_2 respectively for 0^{th}- and 2^{nd}-order) of the time history (bottom) for k_{mean} and k_{max}, respectively. Herein k_{mean} and k_{max} are defined as the average k value for $k \geq 0.001$ and for $k \geq 0.01$, respectively, which represents approximately the mean and the maximum k values within the flow region of interest, respectively. The $k = 0.001$ contour line

corresponds to the boundary line (flow side) of each contour plot, and the $k = 0.01$ contour line is shown at each contour plots in Fig. 6-30 (white colored contour lines), respectively. From Fig. 6-31 (top), k_{mean} is oscillating between 0.004 ~ 0.008 ($I = 0.052$ ~ 0.073, or about 5 ~ 7% of U_C) at $x = 0.135$ and 0.235, whereas almost flat with $k_{mean} \approx$ 0.004 ($I = 0.052$ or about 5% of U_C) at $x = 0.735$ and 0.935. From Fig. 6-31 (bottom), H_0 = 0.006 and $H_2 = 0.002$ at $x = 0.135$ are respectively the largest, and then both decreases gradually to $H_0 = 0.004$ and $H_2 \sim 0$ at $x = 0.935$. On the other hand, from Fig. 6-32 (top), k_{max} is between 0.011 ~ 0.015 and oscillates with the sway phase γ. The turbulent intensity within the flow region is $I = (2/3 \cdot k)^{1/2} = 0.086 \sim 0.1$, corresponding to about 9 ~ 10% of U_C. From Fig. 6-32 (bottom), the period mean value of k_{max} is the largest at $x = 0.135$ with $H_0 = 0.014$ and the oscillation amplitude is the largest at $x = 0.235$ with $H_2 = 0.002$ that is about 14% of the largest H_0 value. In a mean sense, consequently, the flow may have $k \sim 0.013$ ($I \sim 9\%$ of U_C) locally at the high turbulent region and $k \sim 0.005$ ($I \sim 6\%$ of U_C) in overall average, typically larger at the bow but tend to be local while decreasing along the ship length gradually.

Reynolds normal (*uu*, *vv*, *ww*) and shear (*uv*, *uw*, *vv*) stress fields are shown in Fig. 6-33 through Fig. 6-38. Of the normal stresses, *uu* and *vv* fields shown in Figs. 6-33 and 6-34, respectively, exhibit almost and nearly similar appearances as the *k* field shown in Fig. 6-30, respectively, indicating that those components are dominant, whereas *ww* field shown in Fig. 6-35 is seemingly weaker than the other components. On the other hand, the shear stress *uv*, *uw*, and *vw* fields shown in Figs. 6-36 ~ 6-38, respectively, reveal smaller order of magnitude than the normal stresses, where the *uv* is apparently the dominant component. The Reynolds stresses are averaged over the regions where $k \geq$ 0.001 and $k \geq 0.01$, similarly as for k_{mean} and k_{max}, respectively, and the period mean values of those (corresponding to H_0) are shown in Figs. 6-39 and 6-40, respectively, with the normal stresses shown at top and the shear stresses at the bottom, respectively. For the region where $k \geq 0.001$ (i.e. the overall field average), from Fig. 6-39, the mean nor-

mal stress *uu*, *vv*, *ww* values are 0.005, 0.003, 0.002, respectively, and the mean shear stress *uv*, *uw*, *vw* values are 0.002, 0.001, and 0.001, respectively. For the region where $k \geq 0.01$, from Fig. 6-40, the mean values of normal stresses *uu*, *vv*, *ww* are 0.013, 0.009, 0.004 along the ship length, respectively, and those of the shear stresses *uv*, *uw*, *vw* are 0.006, 0.002, 0.002, respectively. The Reynolds stresses are anisotropic, if normalized with the isotropic stress value, $(2/3)\cdot k$, the normal stresses *uu*, *vv*, *ww* are 1.5, 1.0, 0.5, respectively, and the shear stresses *uv*, *uw*, *vw* are 0.7, 0.2, and 0.2, respectively, which are almost common for both of the $k \geq 0.01$ and $k \geq 0.001$ regions.

6.2.1.4 Axial vorticity field

Axial vorticity ω_x field is shown in Fig. 6-41, where presented are vorticity fields with values $\omega_x \geq 10$ and $\omega_x \leq -10$, otherwise blanked and not shown. The vorticity field is seen from behind the model and the axis is out of the paper from the figures, thus the positive axial vorticity ($\omega_x > 0$, colored in red) is rotating counter-clockwise and the negative axial vorticity ($\omega_x < 0$, colored in blue) is rotating clock-wise in the figure, respectively. Several vortices are observed from the ω_x field, such as the sonar dome (SD) vortex at the fore body, at $x = 0.135$ and 0.235, below and underneath the keel, respectively, and bilge keel (BK) vortices at the aft body, at $x = 0.735$ and 0.935, at the mid-bilge positions and below around the bottom profile, respectively, and the aft body keel (AK) vortex beneath the center keel position. A couple of minor vortices can be observed at the fore body, such as the fore body keel (FK) vortex beneath the keel and the free surface (FS) vortex typically at the windward side free surface, however, those vortices are in general not clear from the figures, and for the latter vortex its locations maybe out of the view of present SPIV measurement and measured partially. The overall structure of the vortical flow is presented in Fig. 6-24, and therein the CFD simulation result (Sakamoto 2009) discloses more complete pictures of the vortical flow.

In Fig. 6-42, the time histories of the maximum/minimum ω_x value of the SD vortex along the model sway motion phase position γ, respectively for x = 0.135 and 0.235 locations. The maximum ωx value is when the SD vortex has positive ω_x values, e.g. at γ = 0° and 45° from Fig. 6-41, and the minimum value is when negative ω_x value, e.g. at γ = 135° from Fig. 6-41. When the maximum/minimum values are FS reconstructed such that $H\cdot\cos(\omega t - \phi)$, the harmonic amplitude H = 293 and 213 and ϕ = 11° and 27° at x = 0.135 and 0.235, respectively, indicating about 3% decrease of its magnitude and a phase difference $\Delta\phi$ = 16° between the two locations, respectively. The trend of SDV vortex at the later x locations, however, is precluded, due to the lack of the measurement data at the after body locations.

Similarly, in Fig. 6-43, the maximum/minimum ωx value time histories of the BK vortex are shown for x = 0.735 and 0.935 locations. Note that the time history of BK vortex, however, is defined in a different way form the SD case. As can be seen from Fig. 6-41 for x = 0.735 location, the BK vortices at the portside and starboard are asymmetry respectively with respect to the model sway motion; one is at the wind side and the other is at the leeward side and after one half cycle respectively at the reverse side. Thus, the time histories at the portside/starboard may not be continuous along the model sway motion, i.e. along γ, but at the wind/leeward side of the flow. In other words, from Fig. 6-43, the data at the first half of the cycle are from the BK vortices at the portside and those at the second half are from the BK vortices at the starboard side, which are at the wind side through the cycle. When data are FS reconstructed similarly as for the SD vortex, H = 424 and 274 and ϕ = 19.4 and 35.9° at x = 0.735 and 0.935, respectively. The H's of the BK vortices at x = 0.735 and 0.935 are 145% and 85% of the SD vortex H value at x = 0.135, indicating that BK vortex may be stronger than SD vortex locally and decay fast. Whereas the phase difference of the BK vortices between the two x locations, $\Delta\phi$ = 16.5°, is similar with that for the SD vortex.

Lastly, the time history of AK vortex maximum/minimum ωx is shown in Fig. 6-44. The AK vortex is located nearly at the aft body keel center position and its behavior is symmetry with respect to the model sway motion, and the time history is defined as the same way as for SD vortex. AK vortex is observed only at $x = 0.935$, where H = 189 (about 65% of SD vortex H at $x = 0.135$) and $\phi = -11.3°$ from the FS reconstruction.

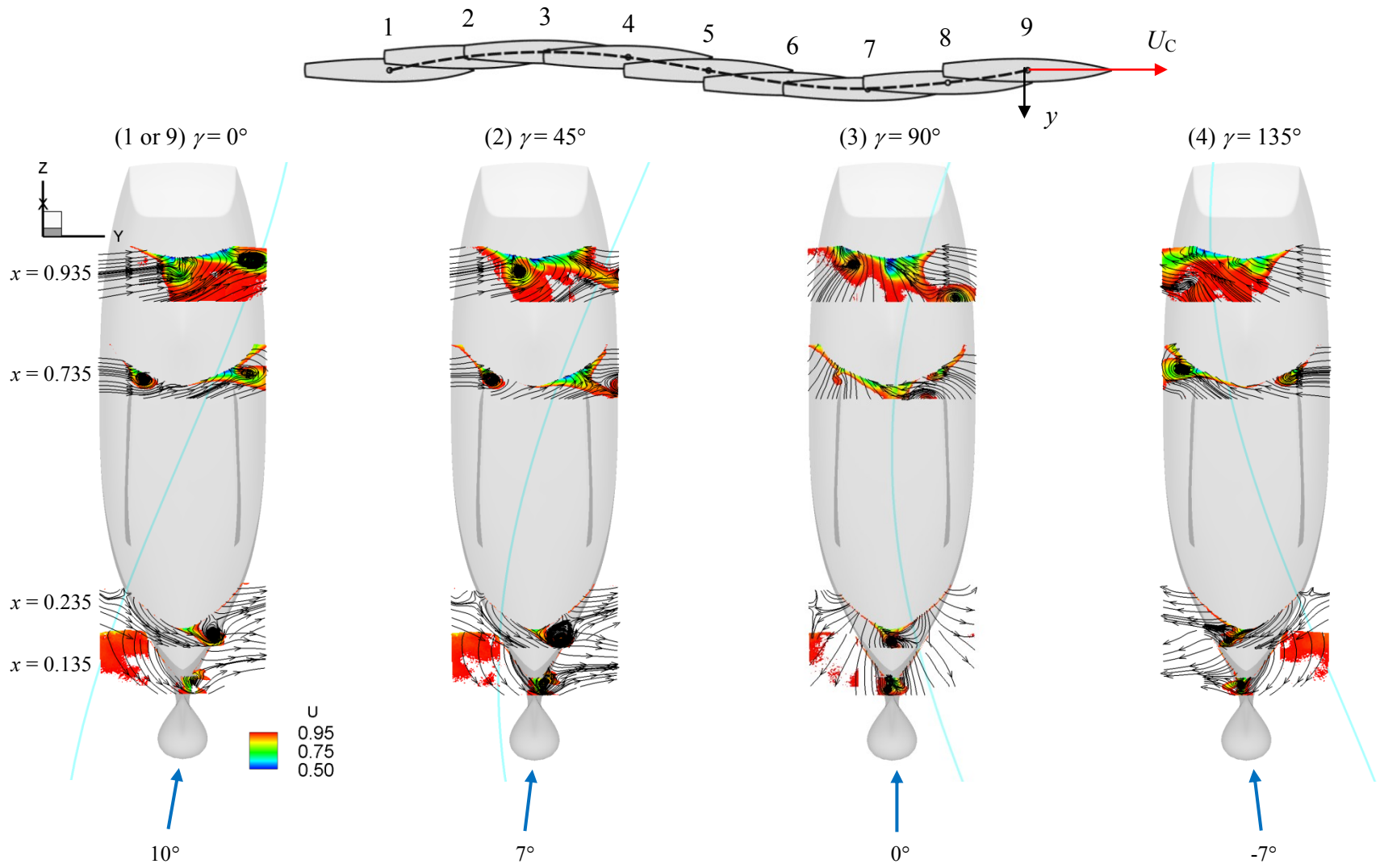

Figure 6-22 Trajectory of model in pure sway motion (top) and overviews of the flow around the model (below).

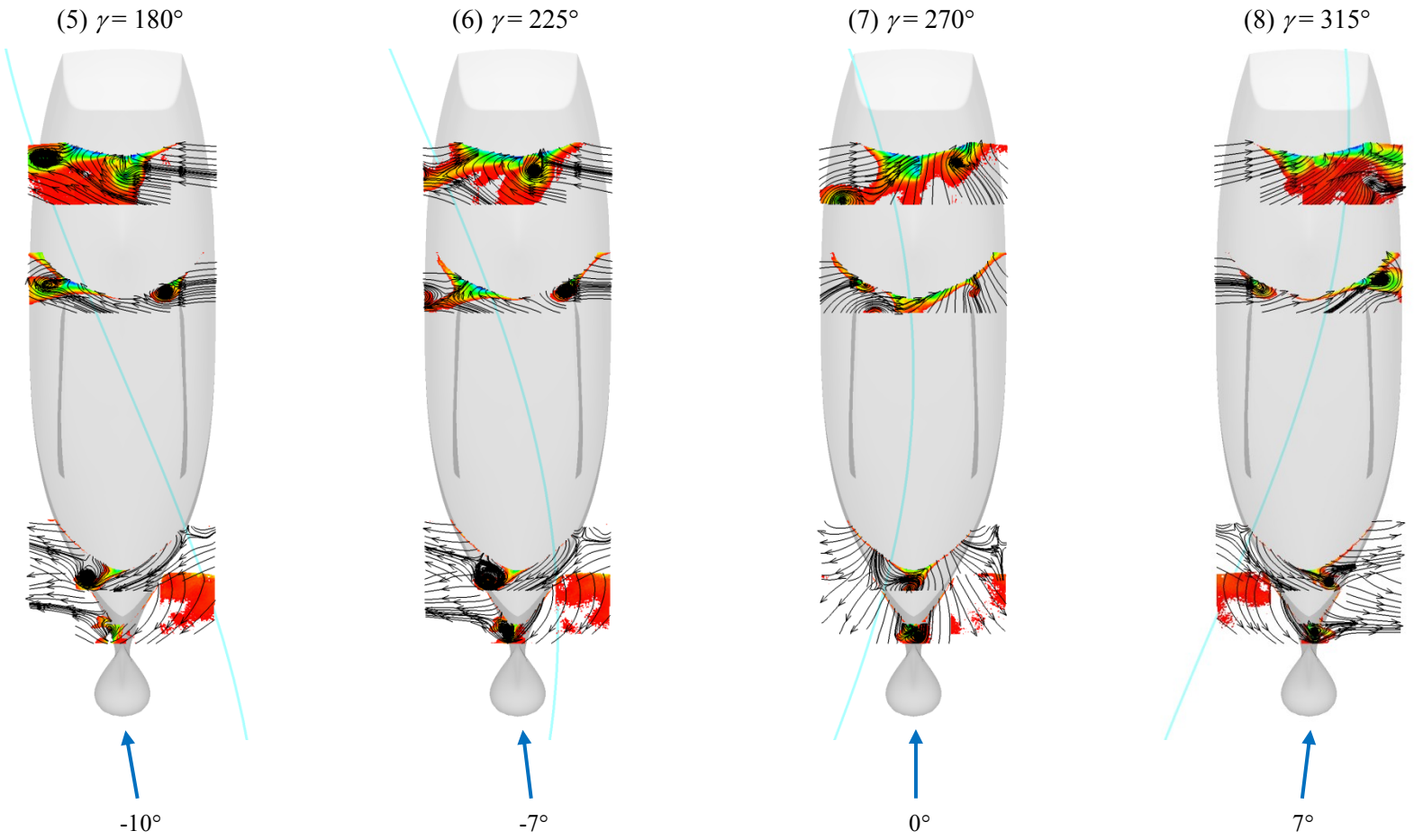

Figure 6-22–Continued

(a) (b)

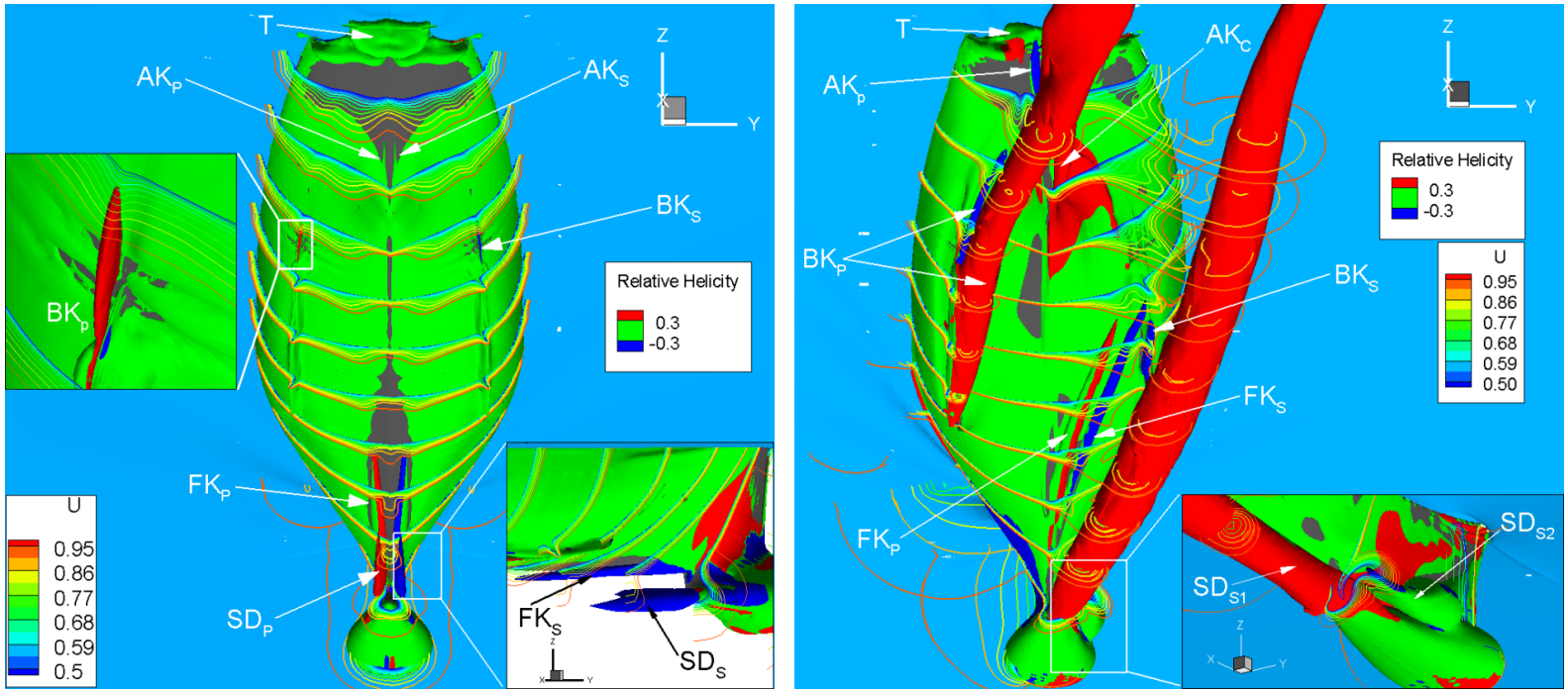

Figure 6-23 Vortical flow structures around the DTMB 5512 geometry in steady maneuvers for: (a) straight-ahead and (b) static drift at $\beta = 10°$ cases. (CFD simulations by Sakamoto 2009).

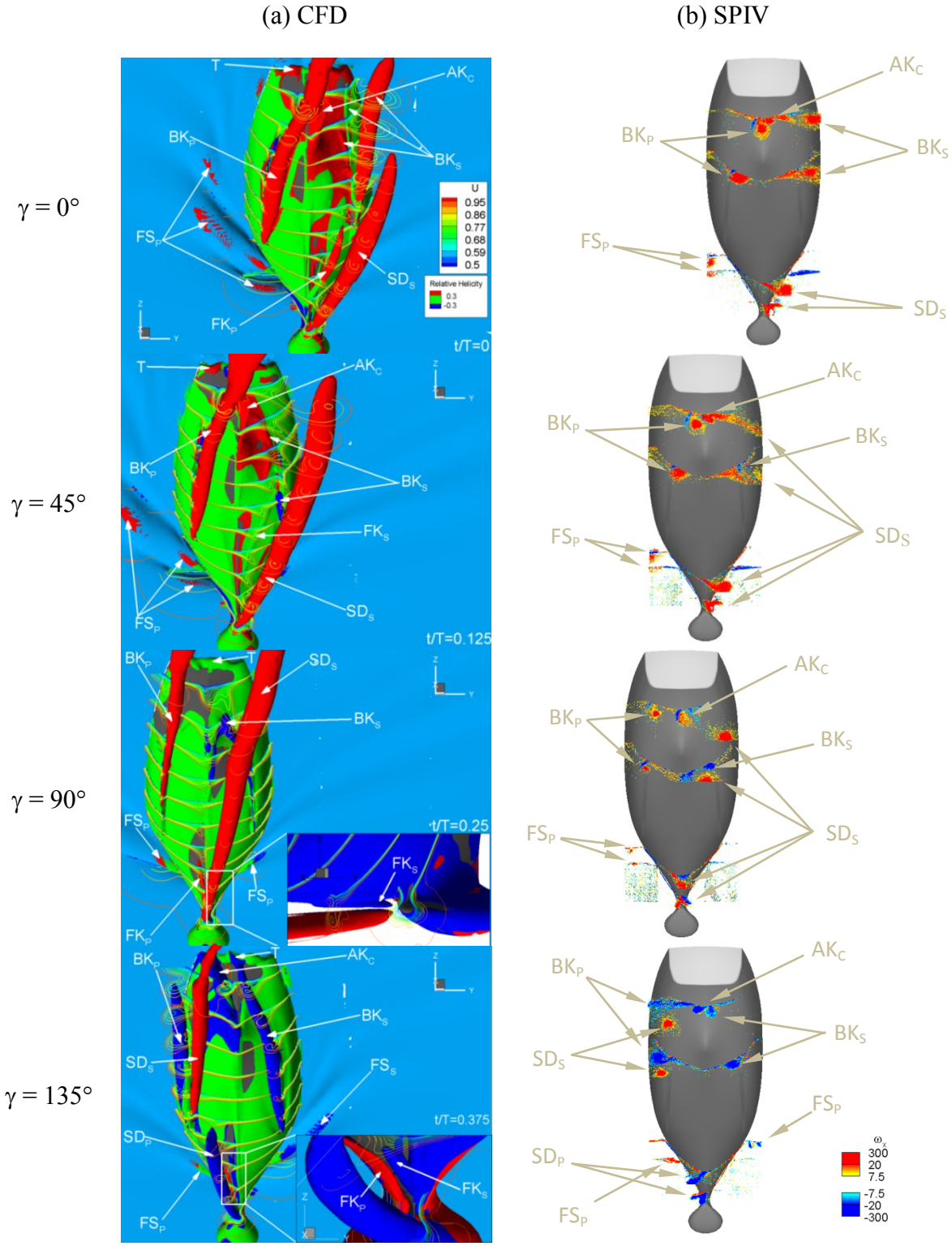

Figure 6-24 Vortical flow structures around the DTMB 5512 geometry in pure sway maneuvering with β_{max} = 10°: (a) Iso-surfaces of relative helicity (CFD simulations by Sakamoto 2009) and (b) contours of axial vorticity (SPIV).

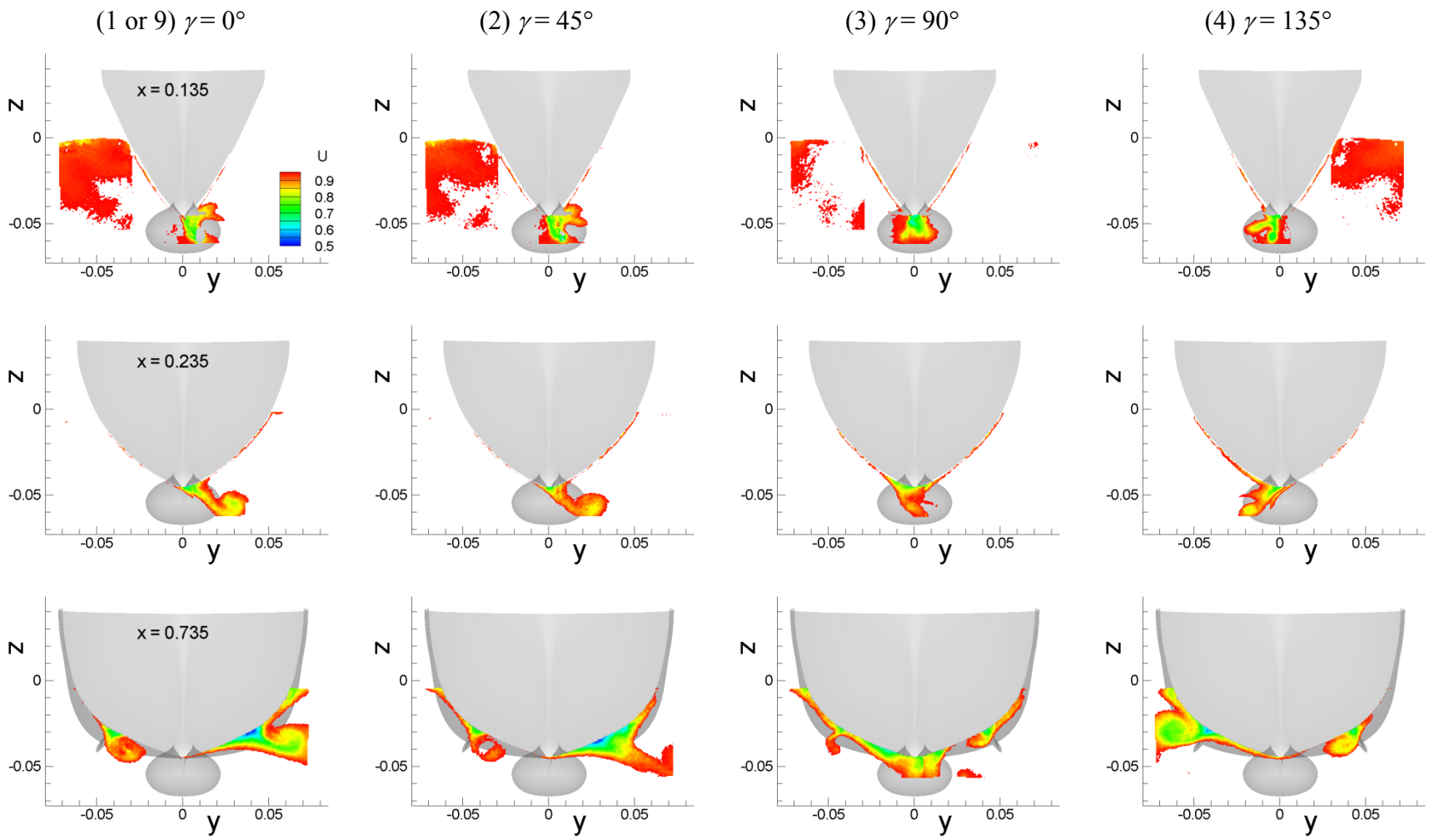

Figure 6-25 Phase-averaged axial velocity *U* field for pure sway test.

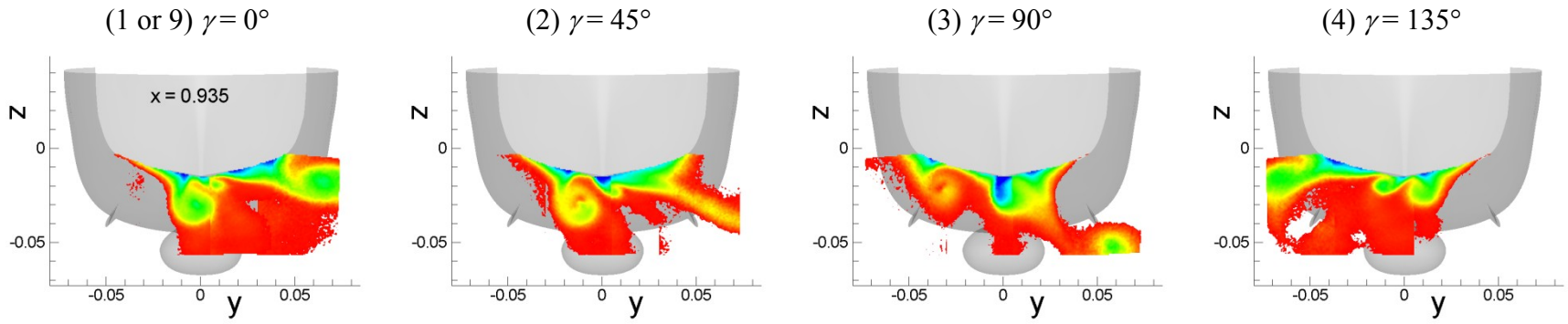

Figure 6-25–Continued

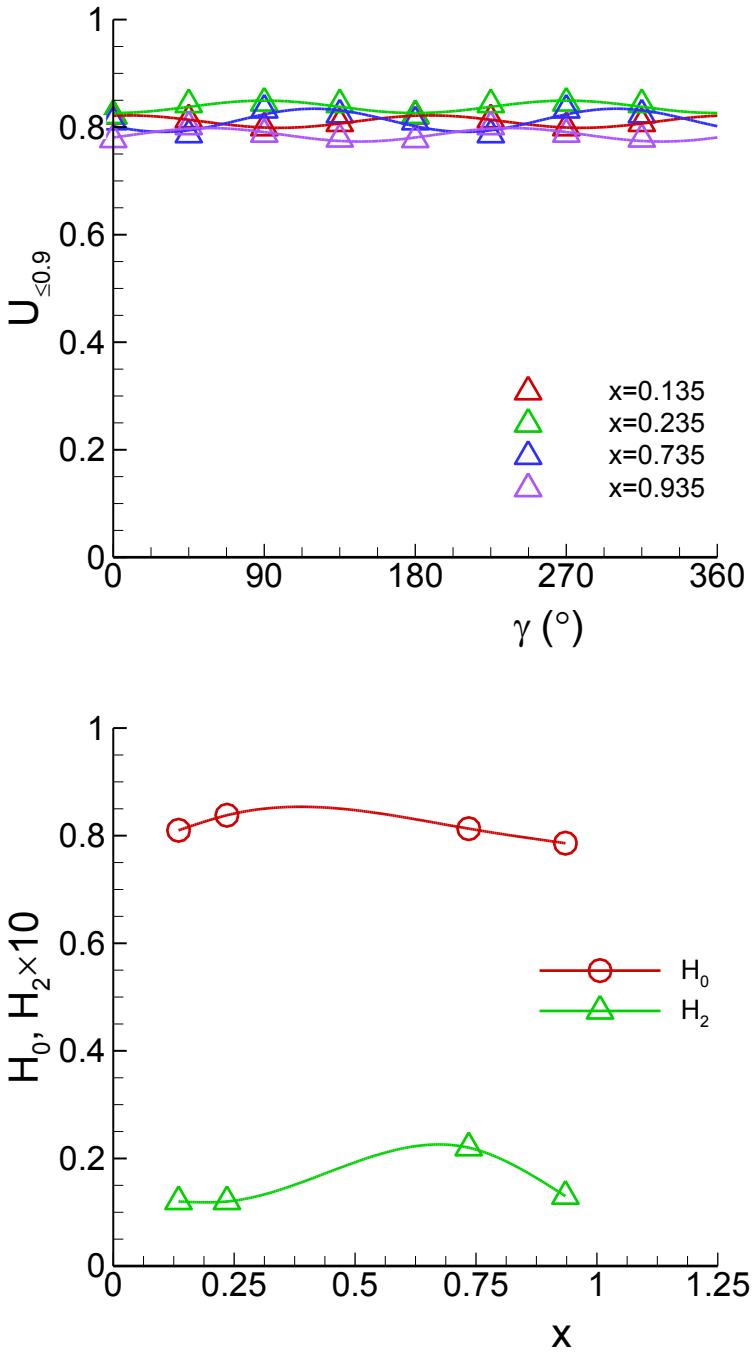

Figure 6-26 Time histories of the average axial velocity $U_{\leq 0.9}$ (top) and FS harmonics (bottom) for pure sway test.

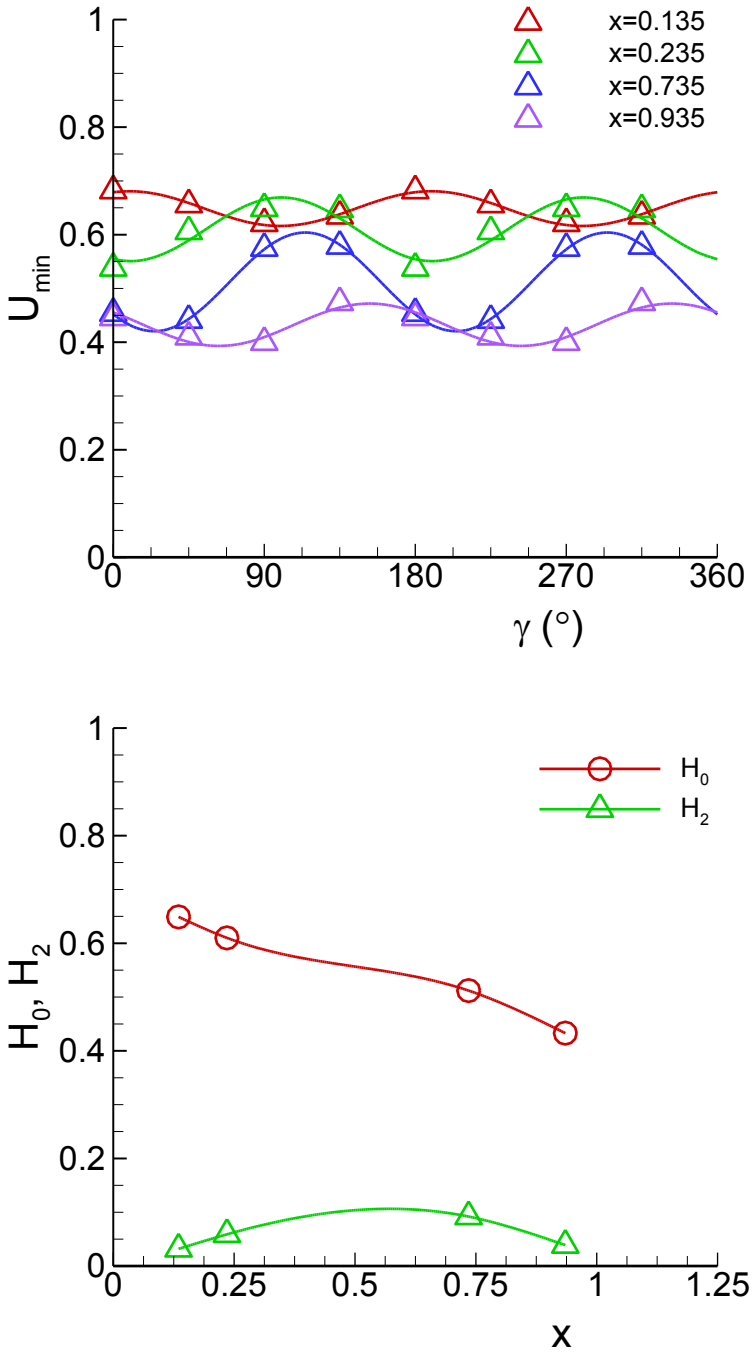

Figure 6-27 Time histories of the minimum axial velocity U_{min} (top) and FS harmonics (bottom) for pure sway test.

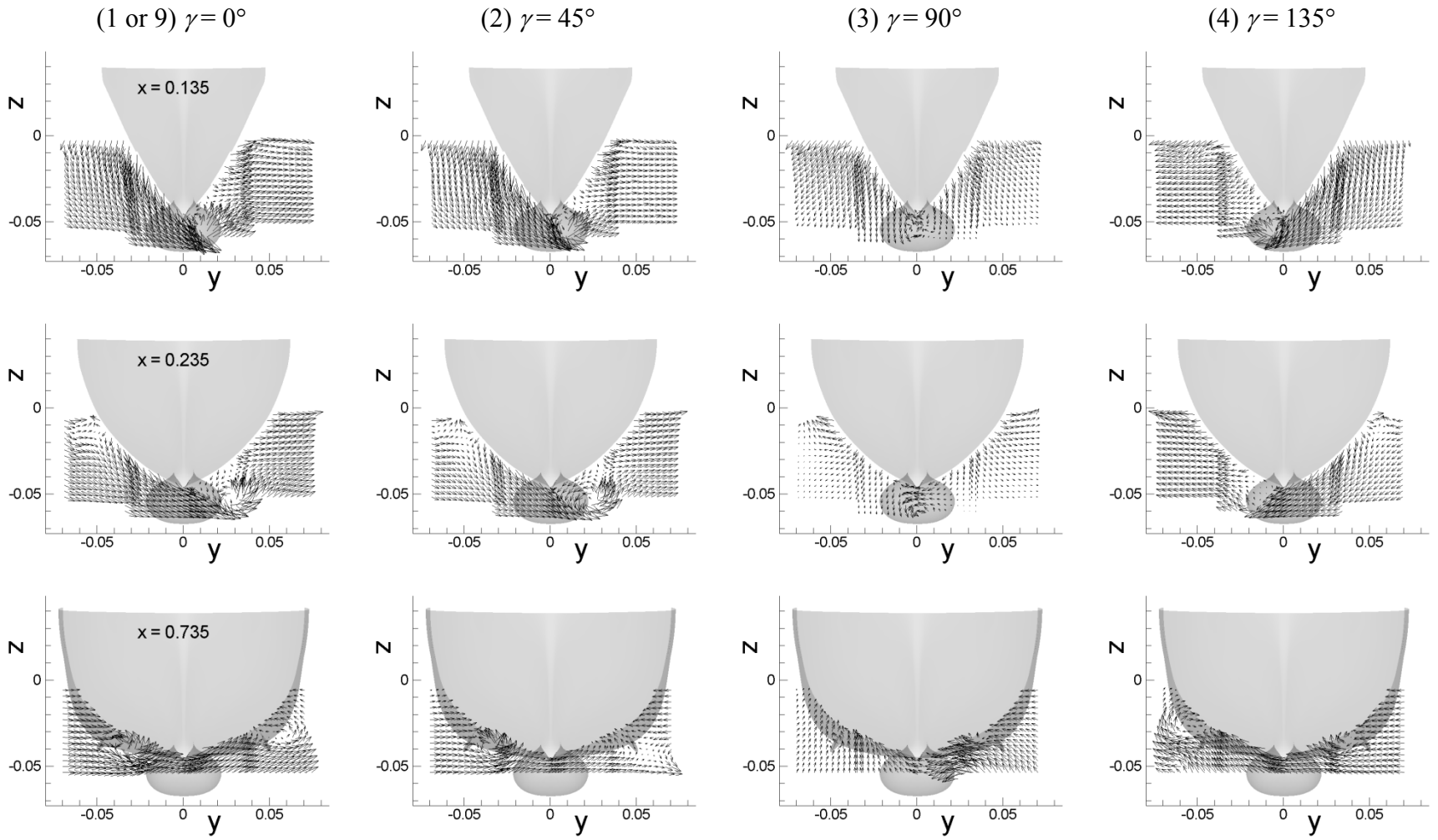

Figure 6-28 Phase-averaged cross-flow (V,W) vector field for pure sway test.

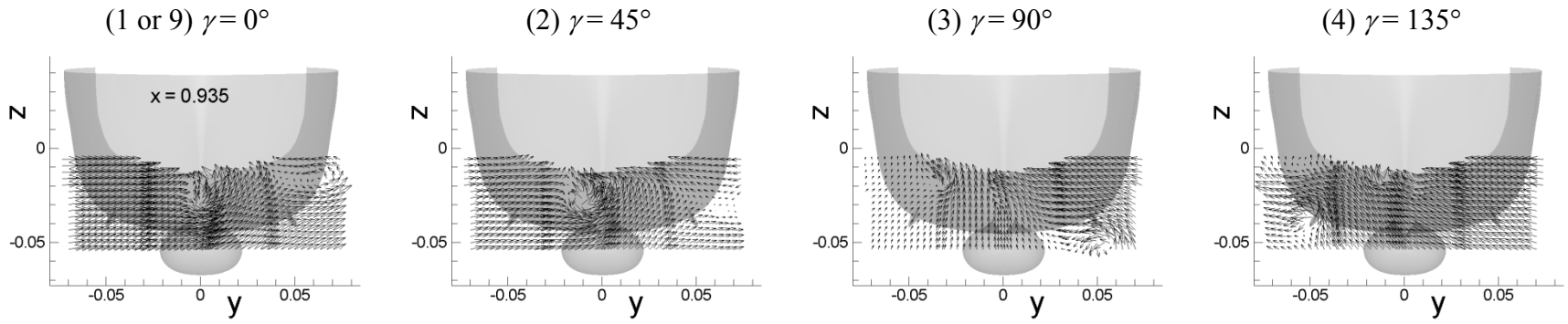

Figure 6-28–Continued

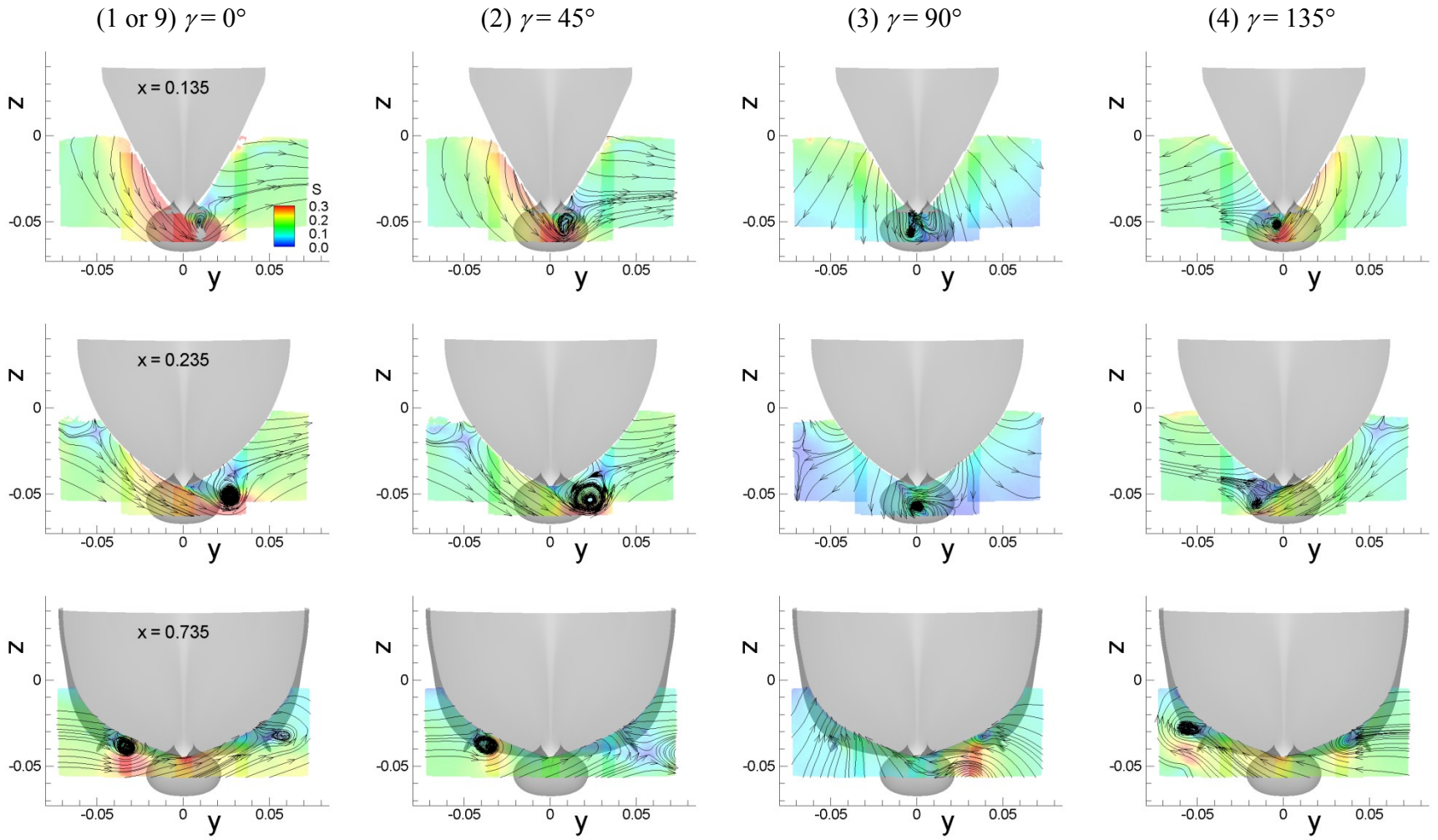

Figure 6-29 Cross flow velocity vector magnitude $S = (V^2 + W^2)^{1/2}$ and streamlines for pure sway test.

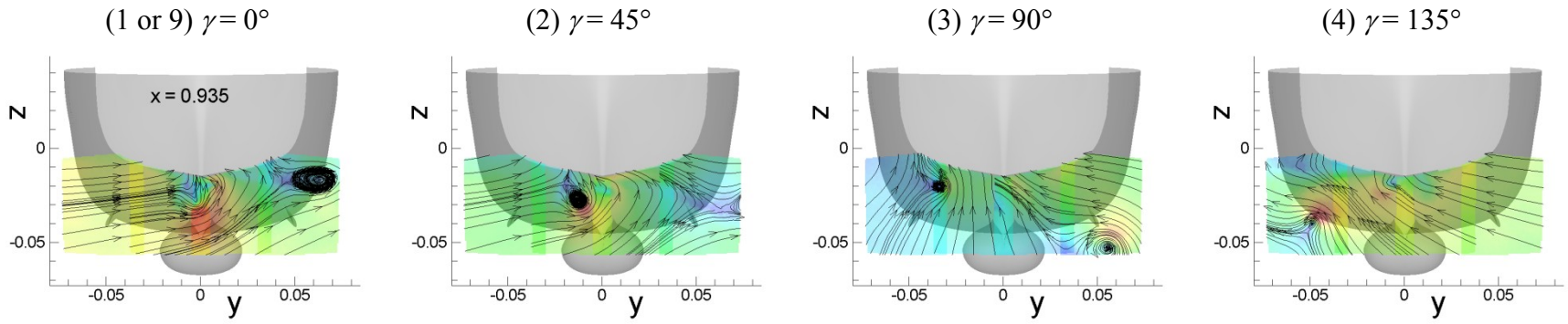

Figure 6-29–Continued

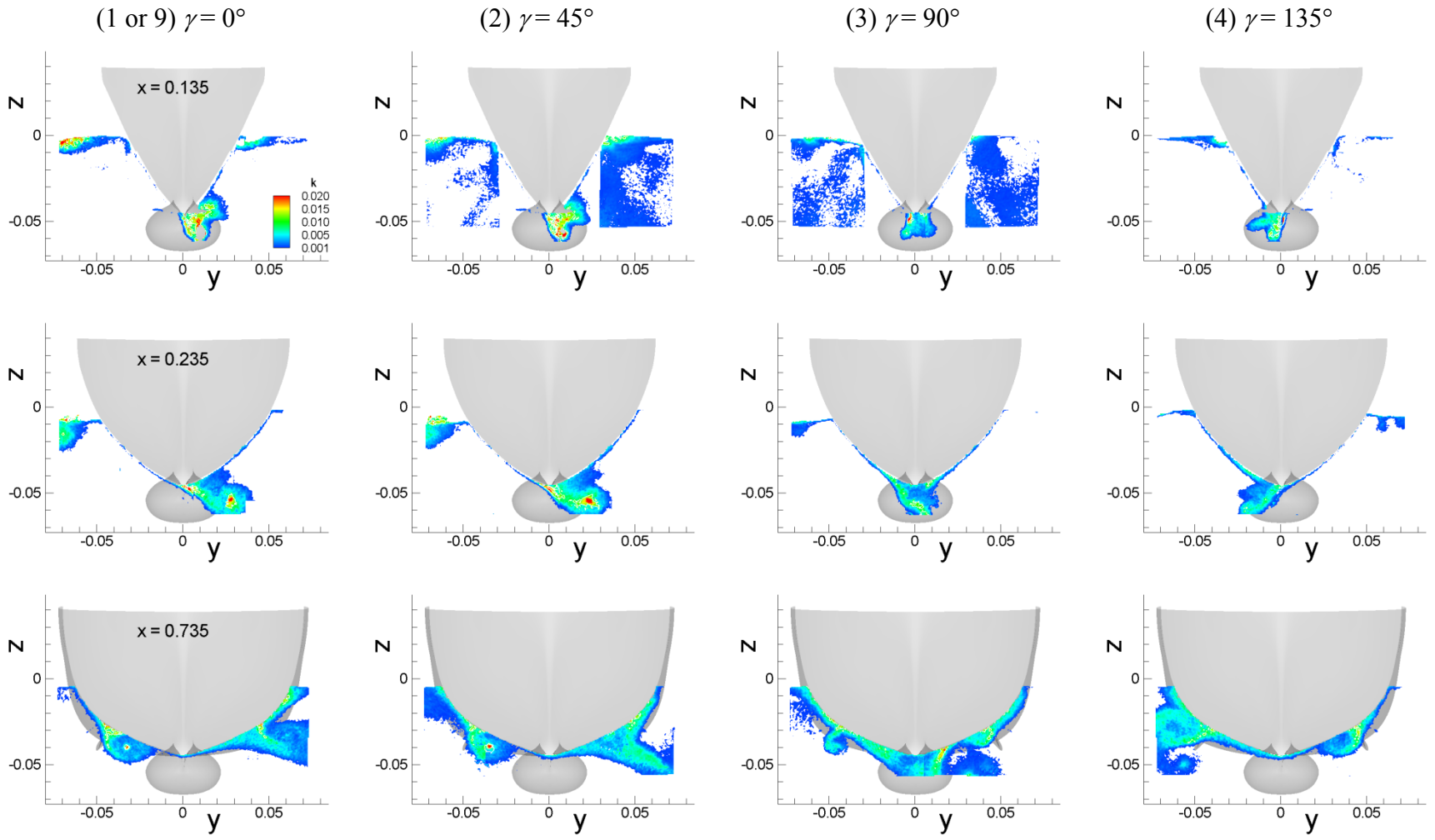

Figure 6-30 Phase-averaged turbulent kinetic energy *k* field for pure sway test.

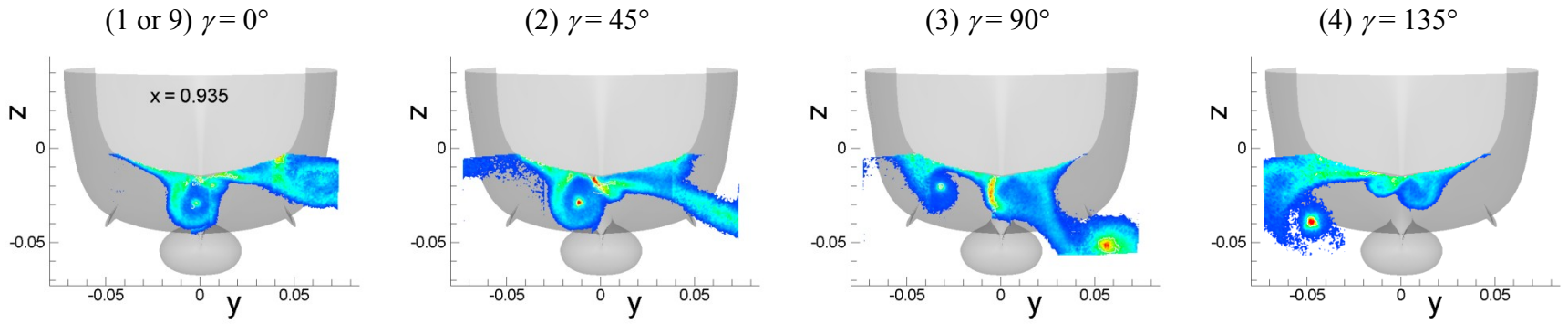

Figure 6-30–Continued

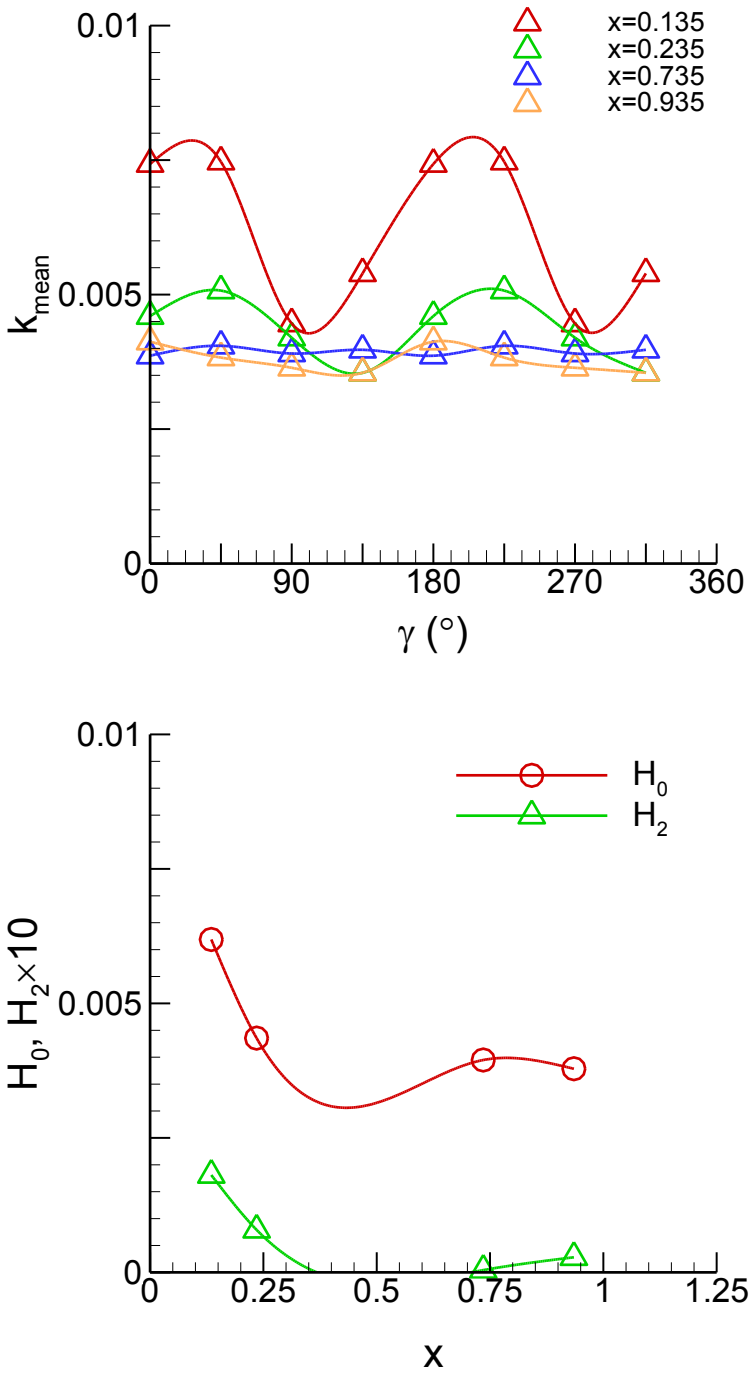

Figure 6-31 Time histories of k_{mean} (top) and FS harmonics (bottom) for pure sway test.

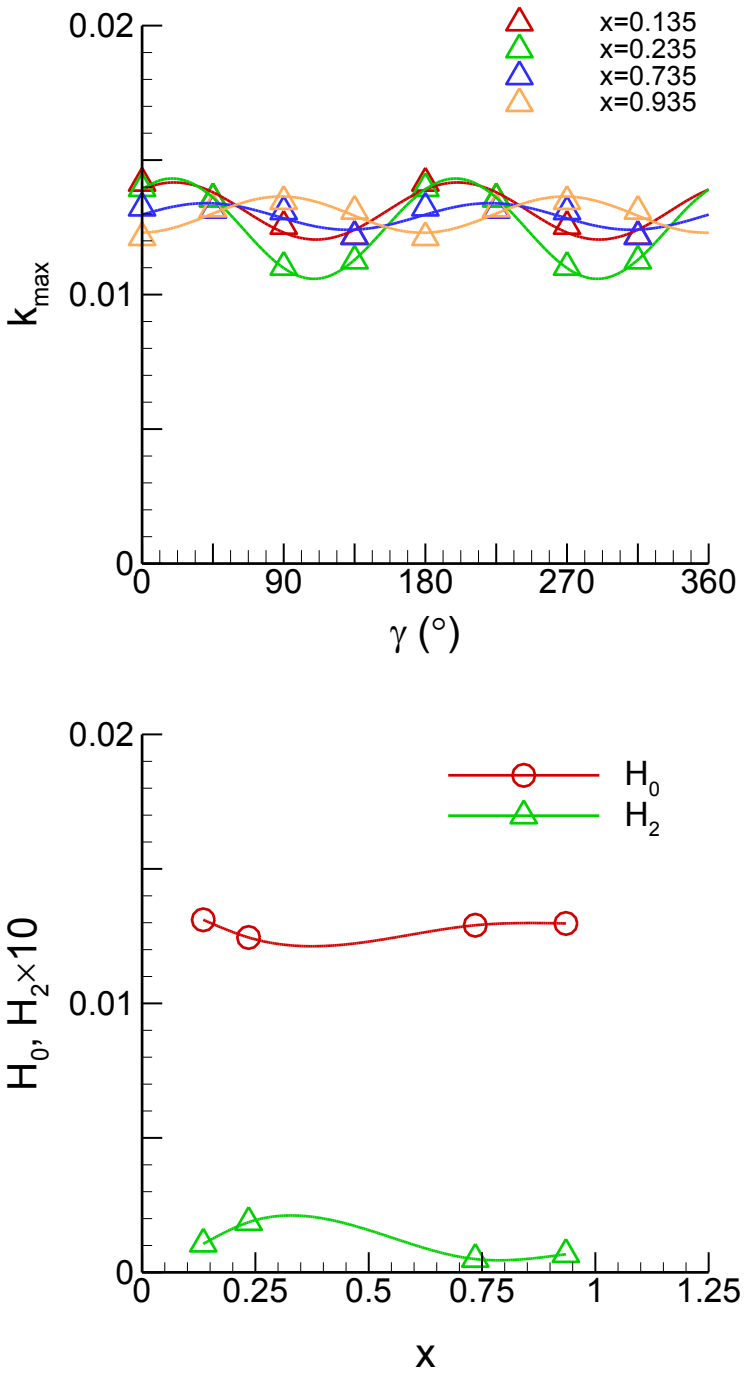

Figure 6-32 Time histories of k_{max} (top) and FS harmonics (bottom) for pure sway test.

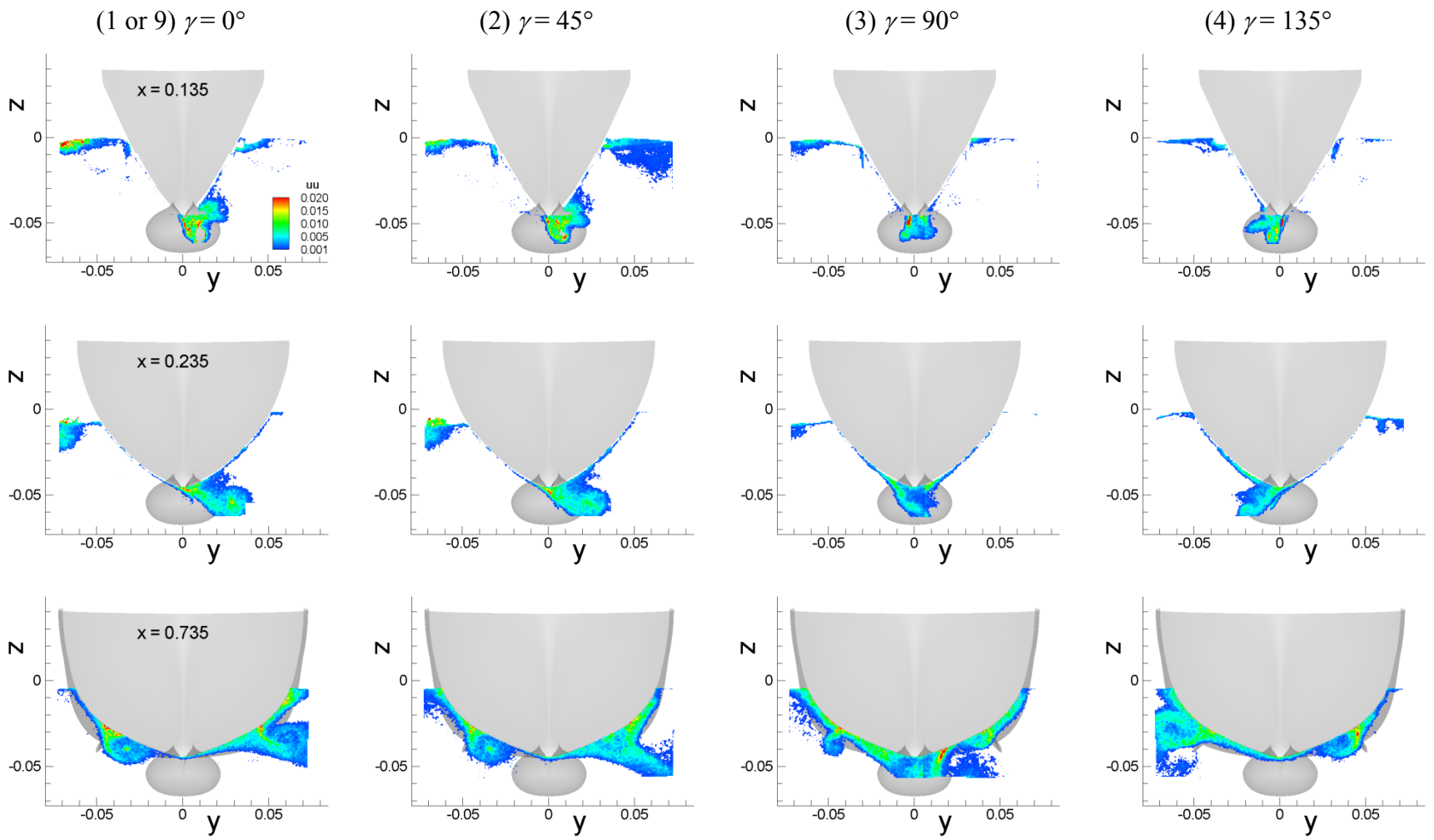

Figure 6-33 Phase-averaged Reynolds stress *uu* field for pure sway test.

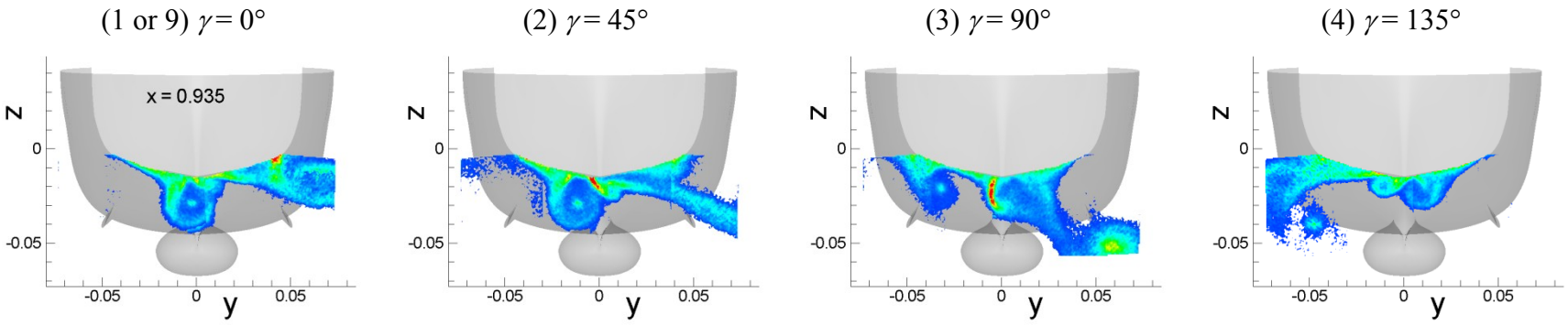

Figure 6-33–Continued

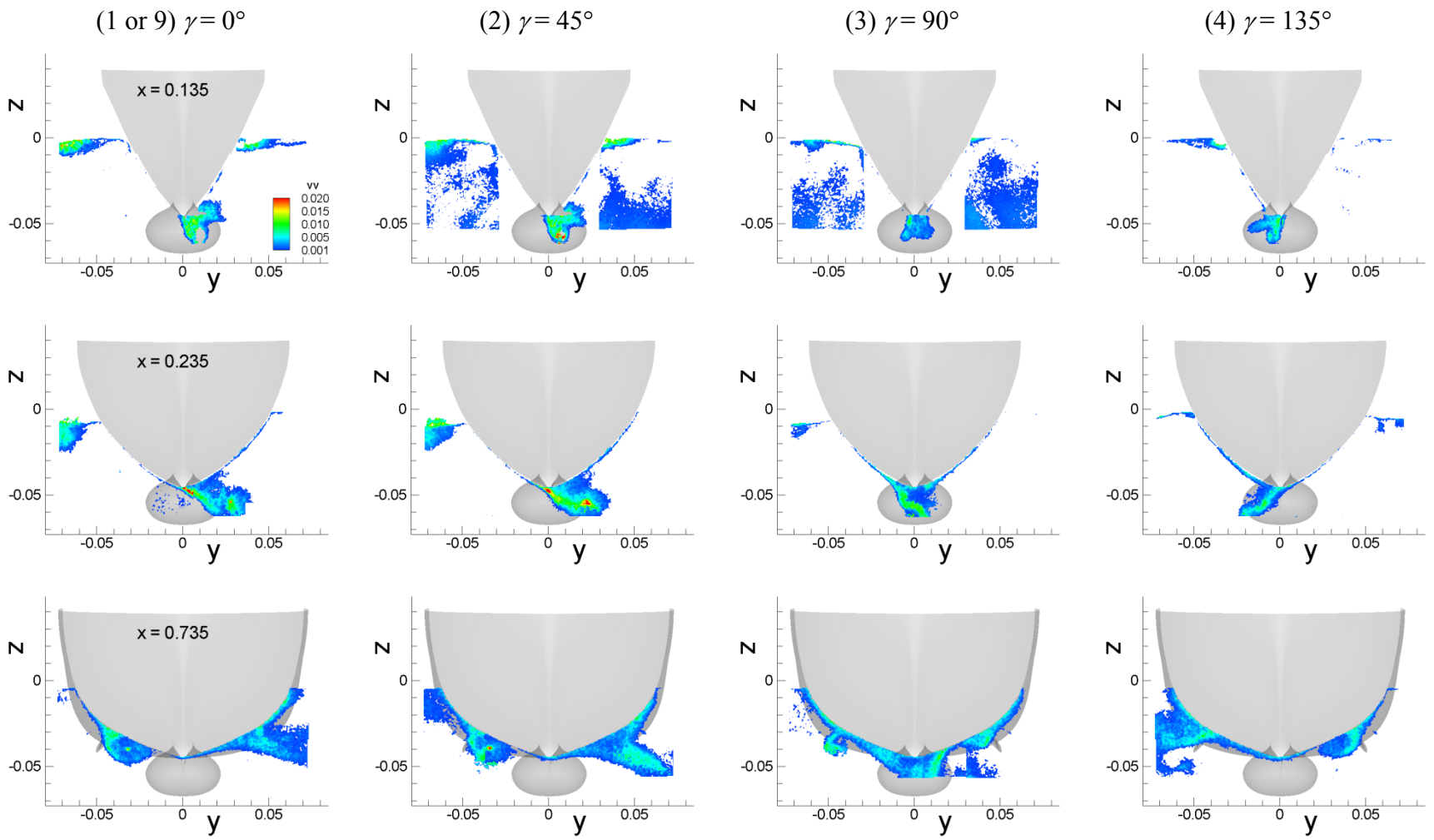

Figure 6-34 Phase-averaged Reynolds stress *vv* field for pure sway test.

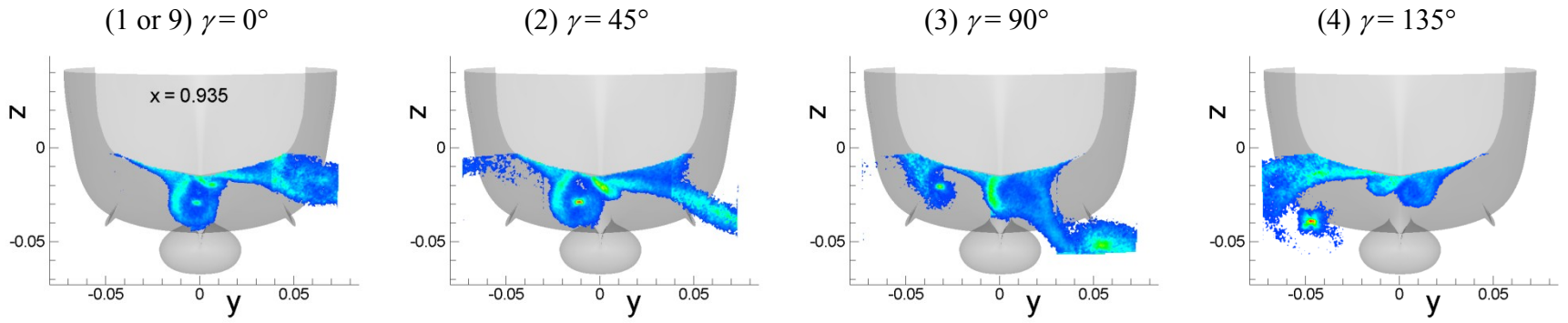

Figure 6-34–Continued

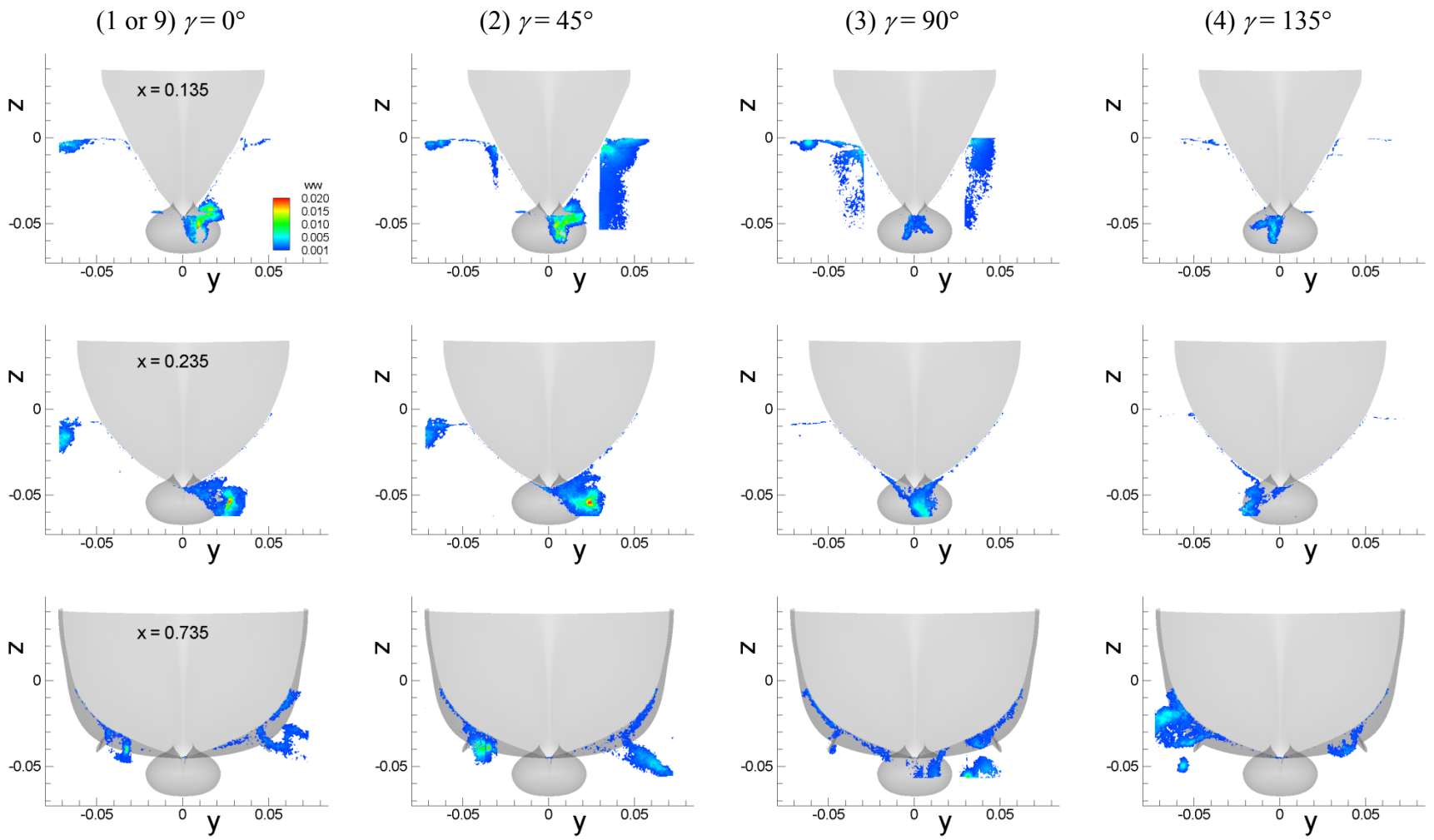

Figure 6-35 Phase-averaged Reynolds stress *ww* field for pure sway test.

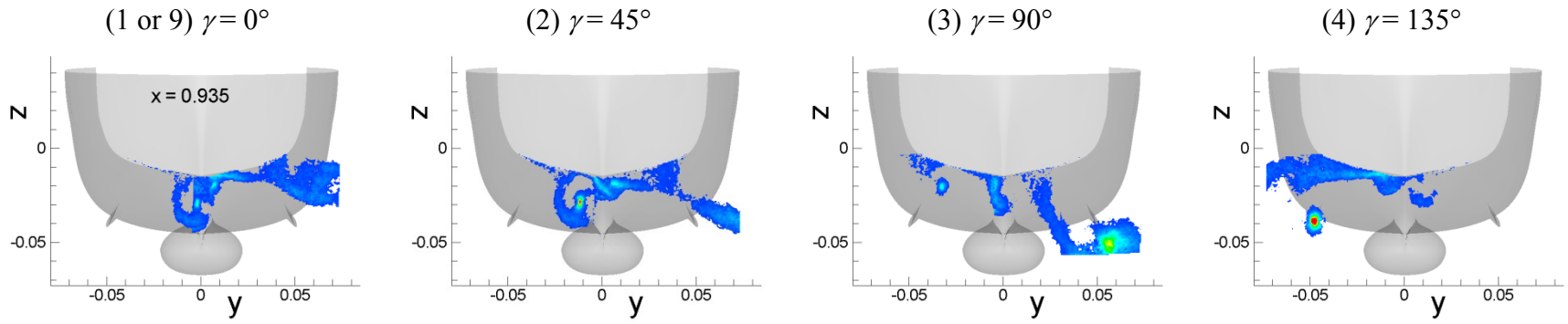

Figure 6-35–Continued

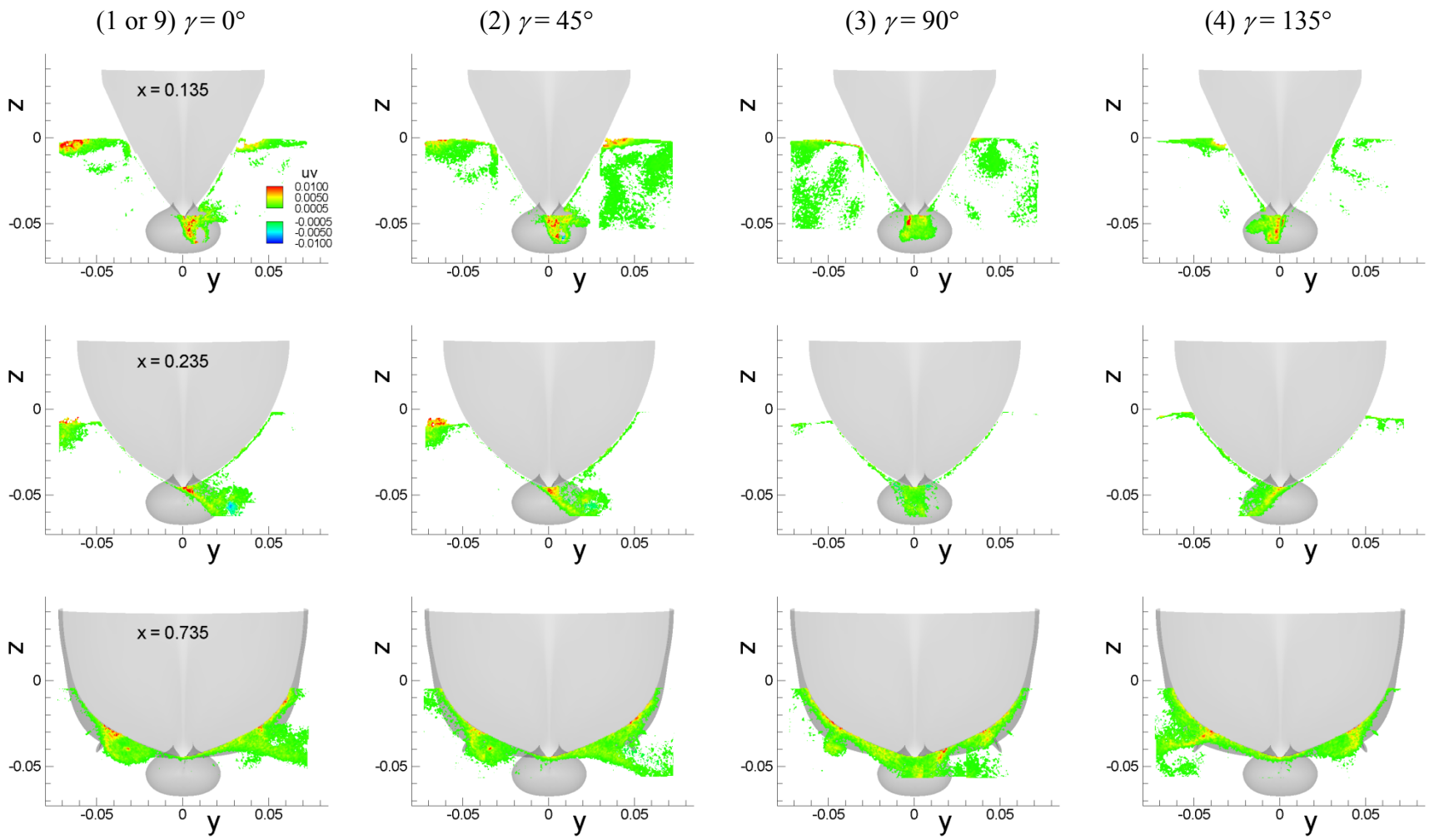

Figure 6-36 Phase-averaged Reynolds stress *uv* field for pure sway test.

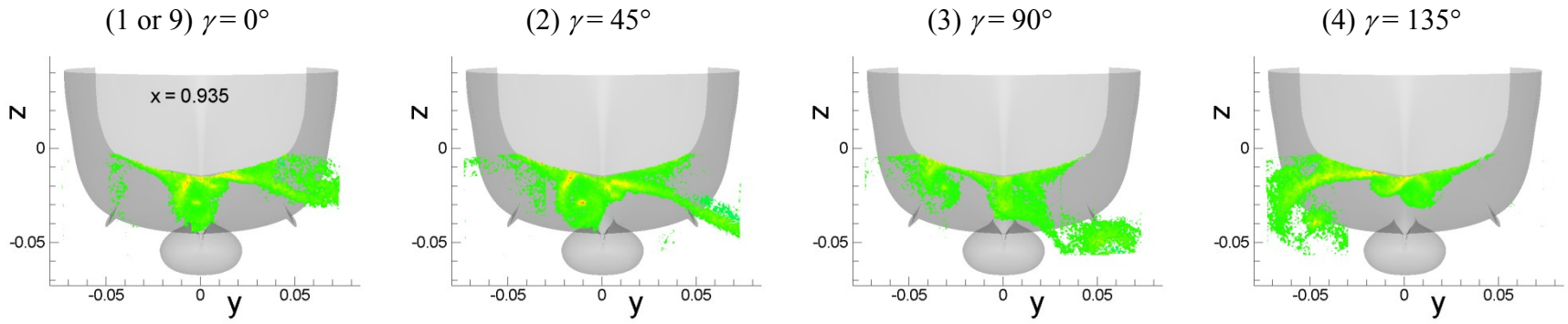

Figure 6-36–Continued

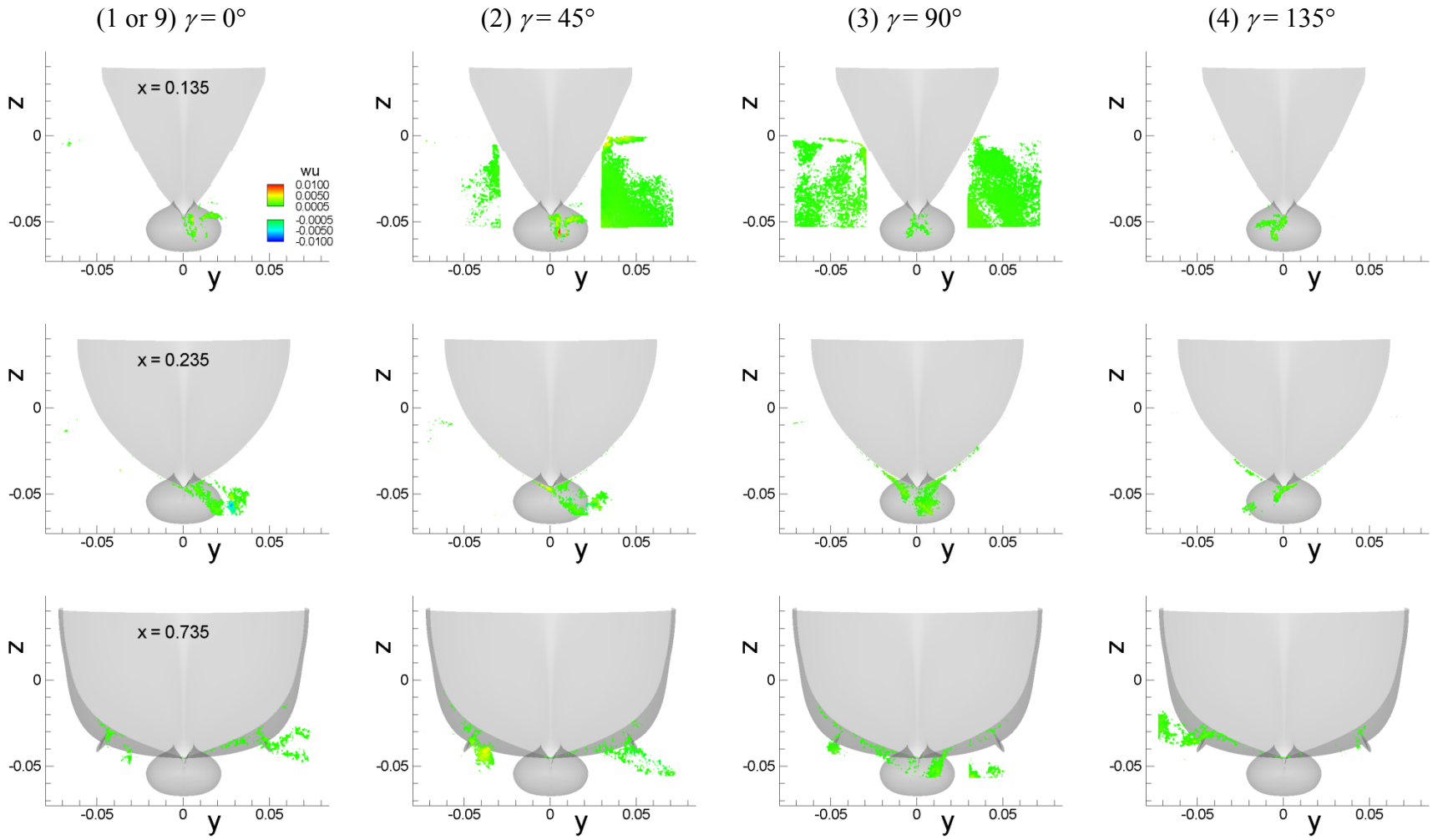

Figure 6-37 Phase-averaged Reynolds stress *uw* field for pure sway test.

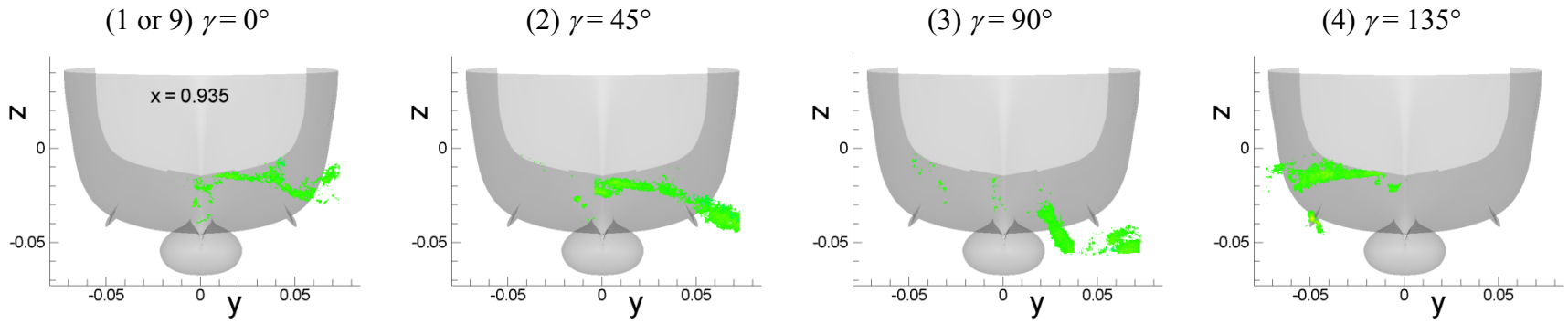

Figure 6-37–Continued

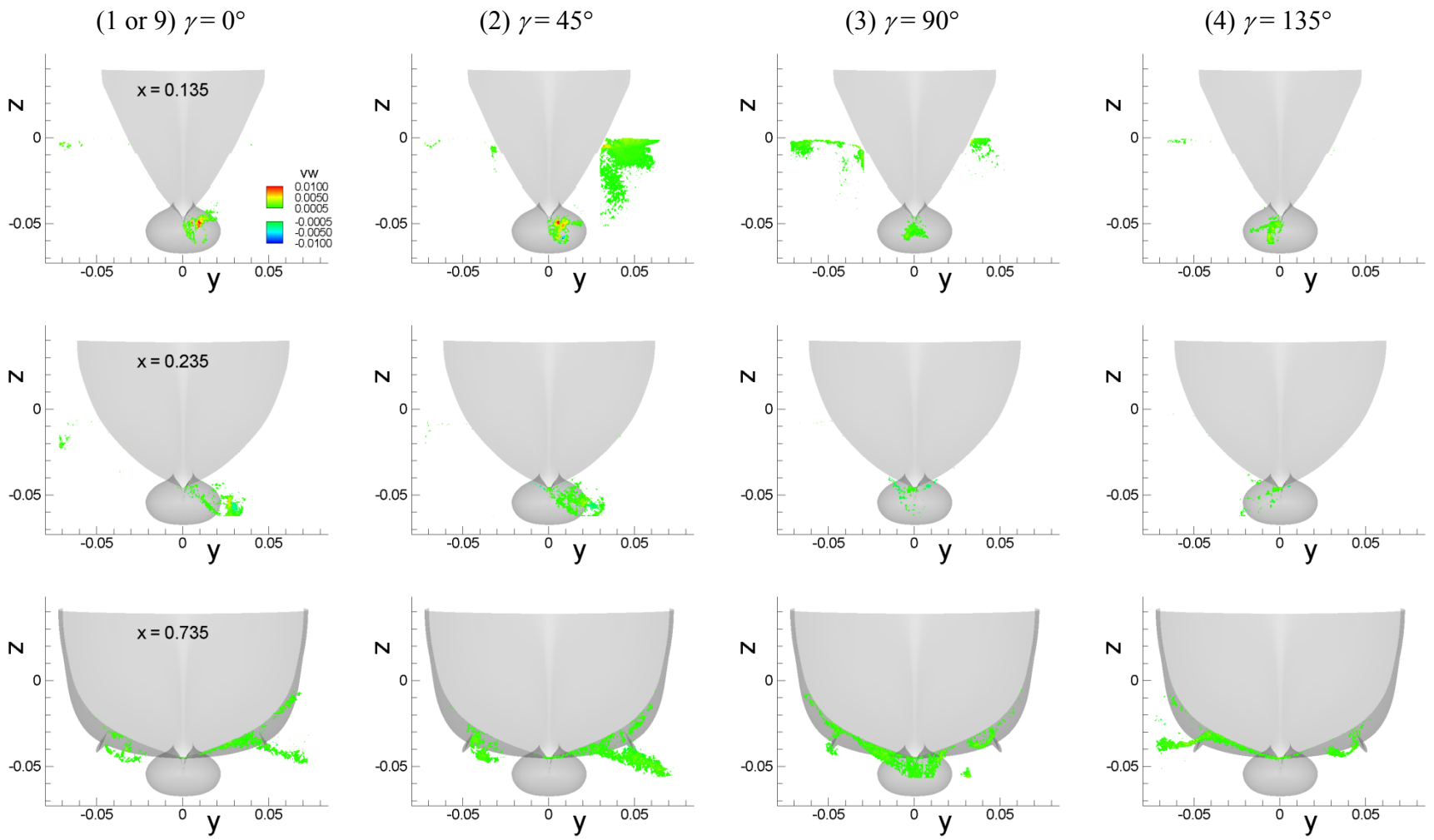

Figure 6-38 Phase-averaged Reynolds stress *vw* field for pure sway test.

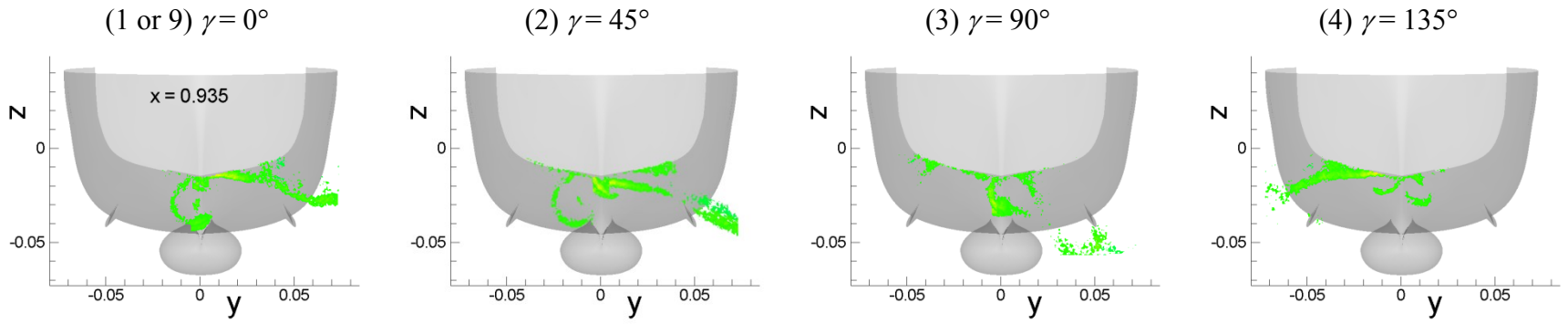

Figure 6-38–Continued

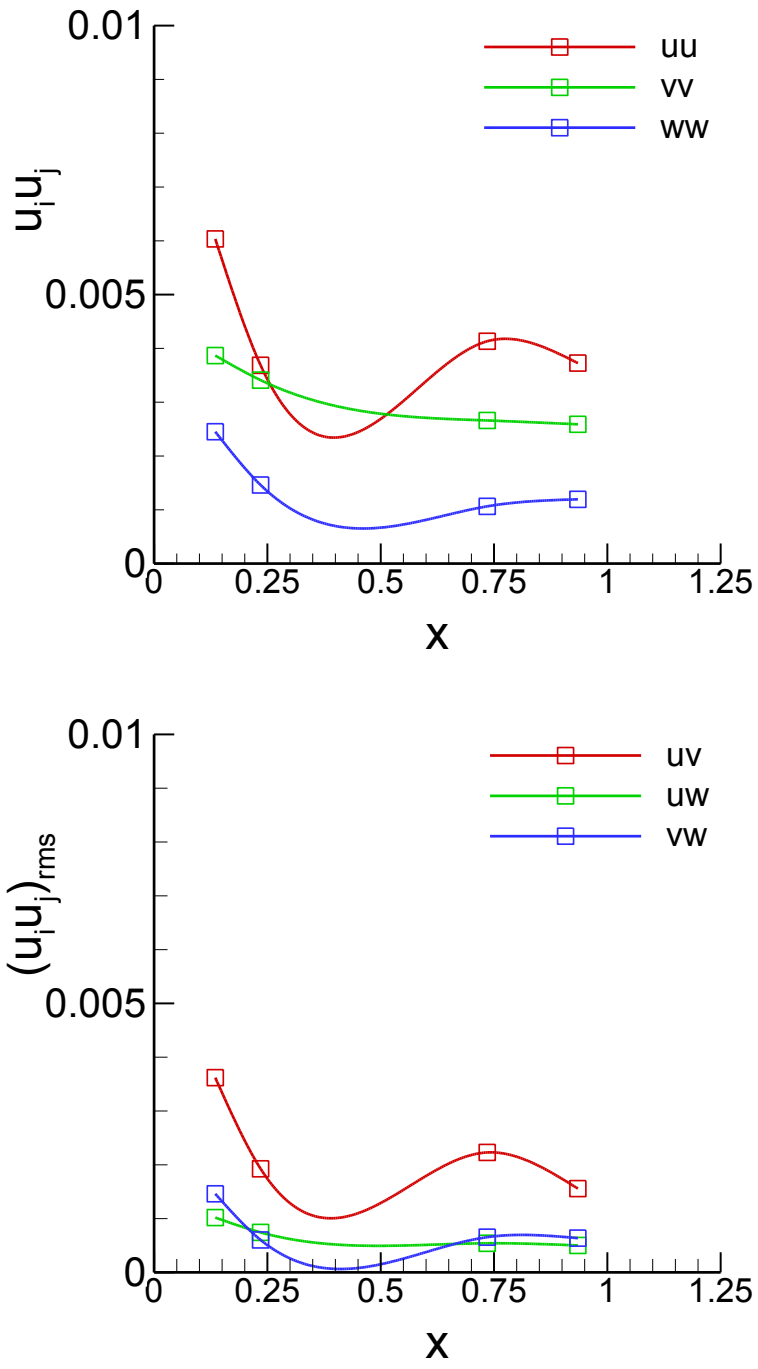

Figure 6-39 Average normal (top) and shear (bottom) Reynolds stresses for k_{mean} (Pure sway test).

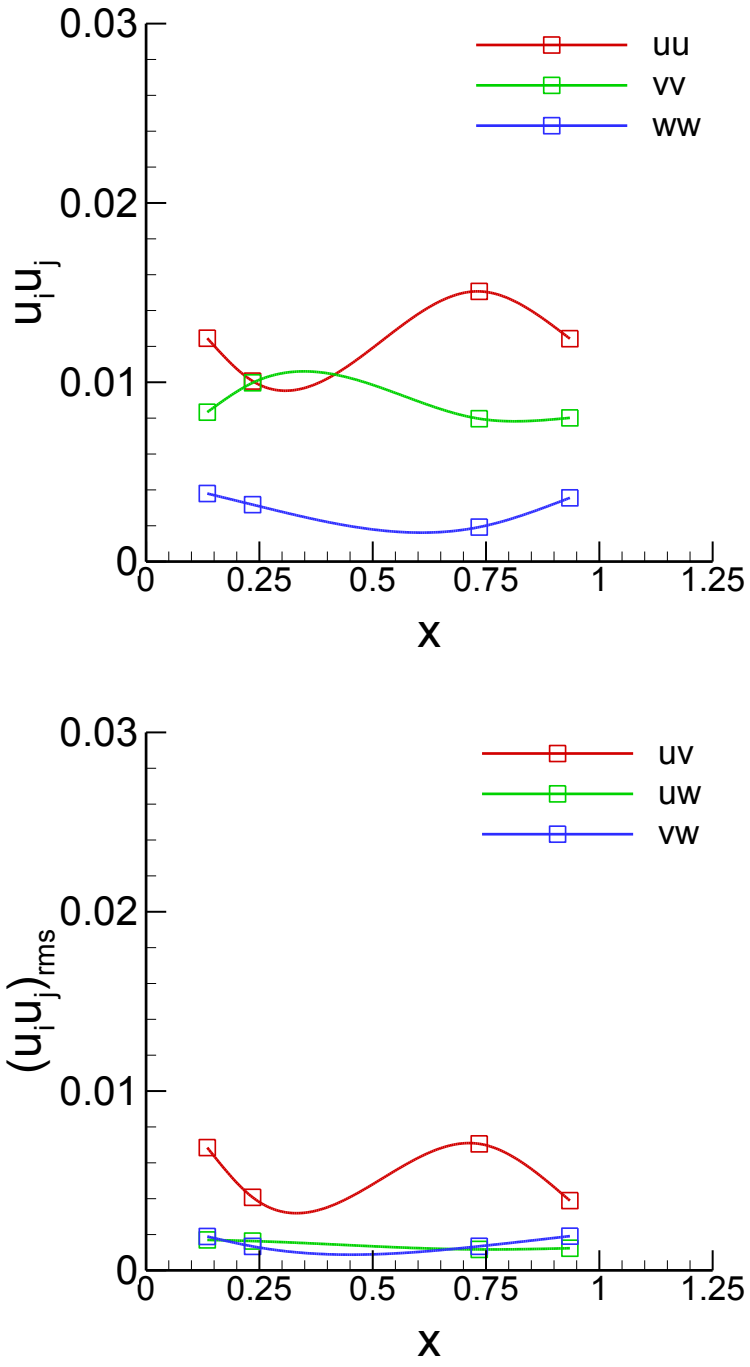

Figure 6-40 Average normal (top) and shear (bottom) Reynolds stresses for k_{max} (Pure sway test).

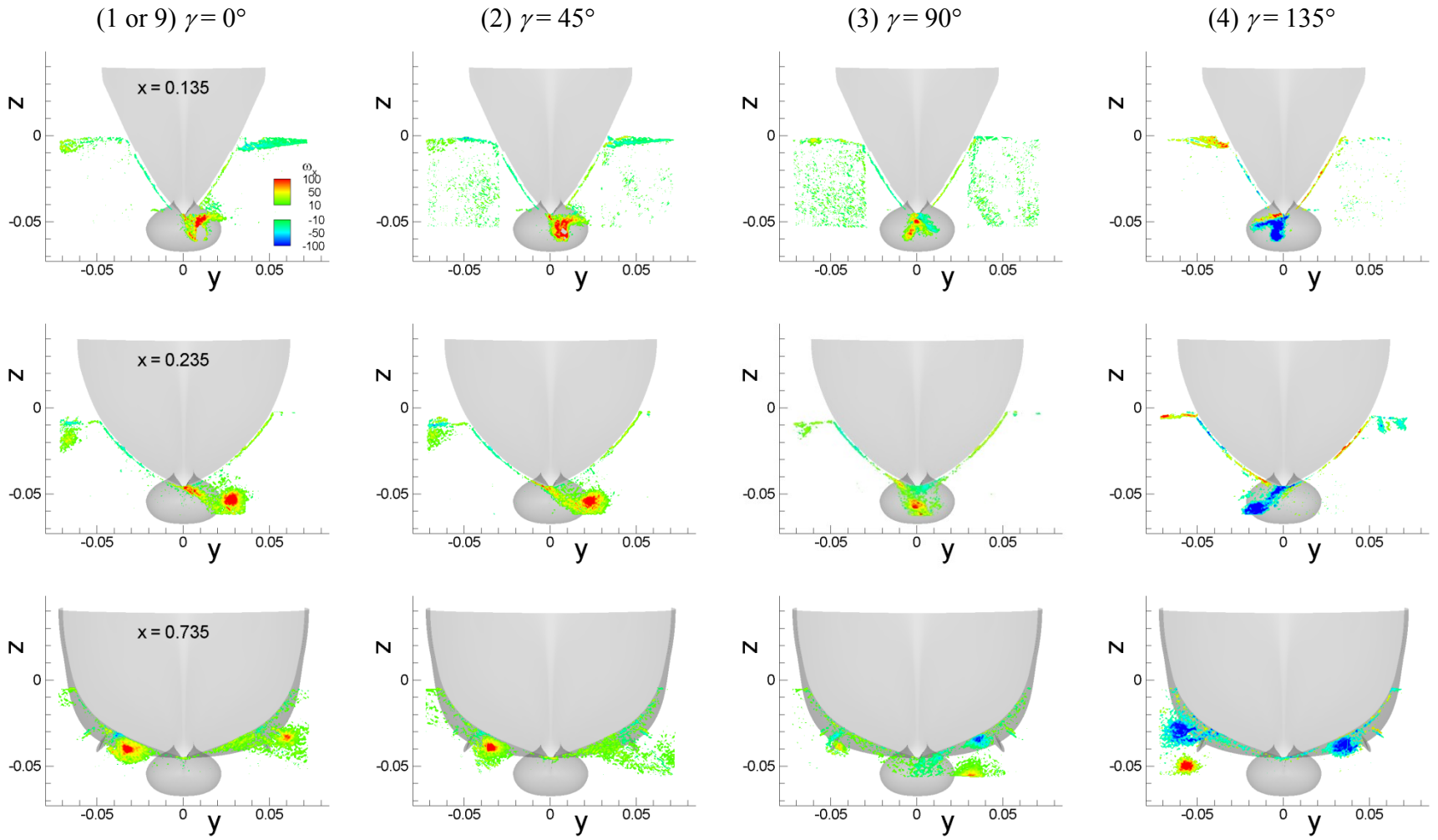

Figure 6-41 Axial vorticity ω_x field for pure sway test.

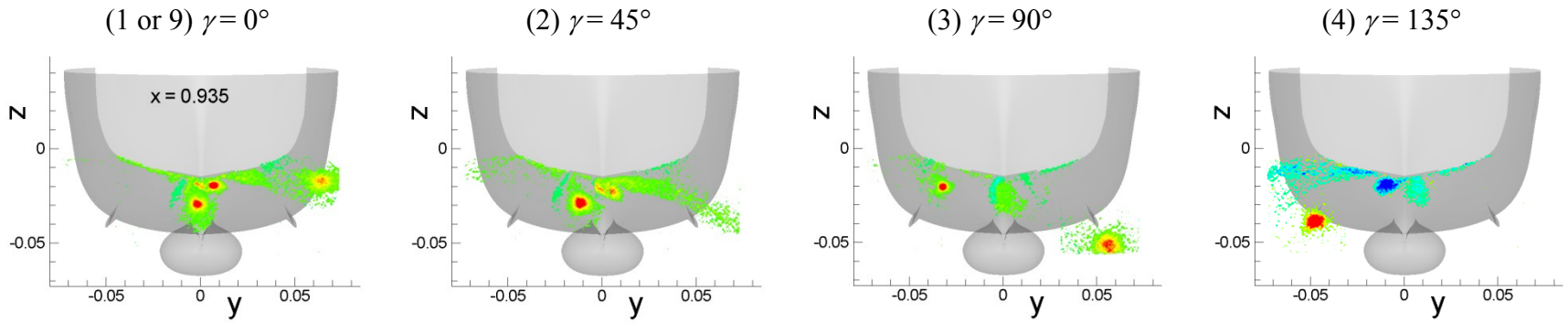

Figure 6-41–Continued

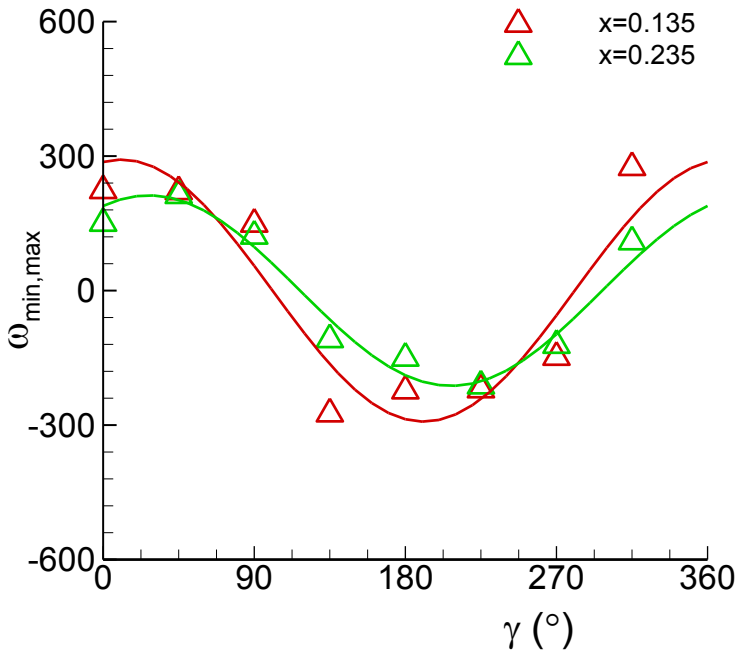

Figure 6-42 Time histories of maximum/minimum axial vorticity value of the sonar dorm vortex (SD) for pure sway.

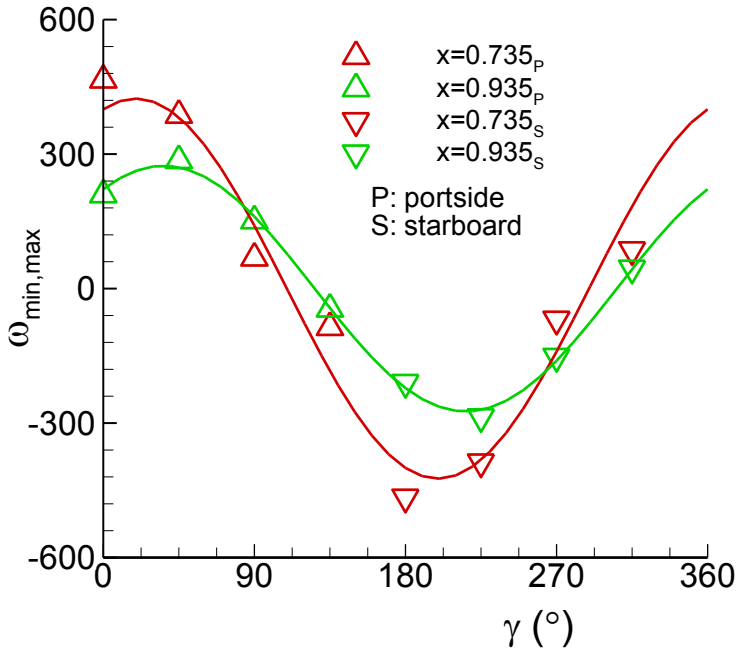

Figure 6-43 Time histories of maximum/minimum axial vorticity value of the bilge keel vortex (BK) for pure sway.

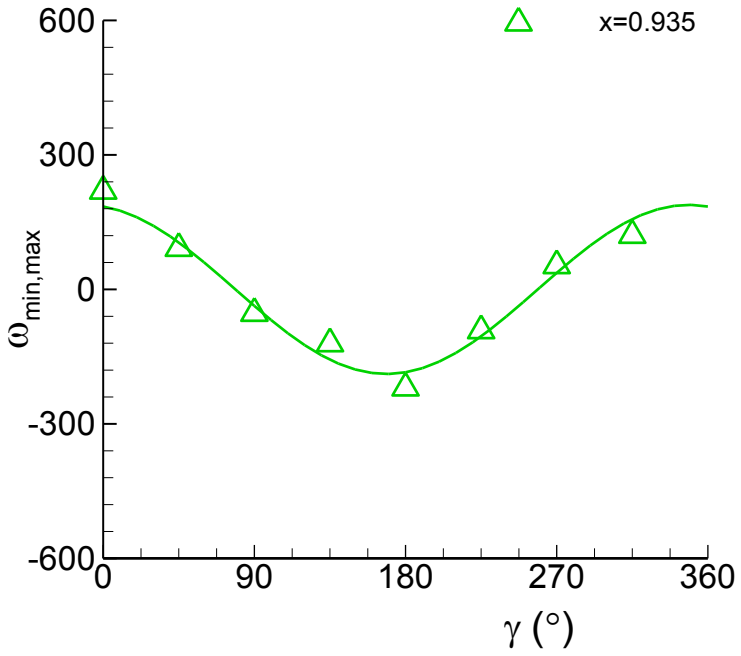

Figure 6-44 Time histories of maximum/minimum axial vorticity value of the aft-body keel vortex (AK) for pure sway test.

6.2.2 Pure yaw flow field

Presentations of the pure yaw flow field data herein are using the same format and methodology as for the discussions for pure sway at the previous section. The details of the presentation methodology and formats, thus, are not repeated in the discussions herein, such as: blanking out flow data and not showing in the contour plots for the data in a certain range, e.g. $U > 0.95$, $k < 0.001$, $-10 < \omega_x < 10$; defining $U_{\leq 0.9}$ as the mean U value over a flow region where $U \leq 0.9$ and $U_{\min}$ as the minimum U value (see Section 6.2.1.2); presenting the cross-flow field by showing the contours of the velocity (V, W) vector magnitude, $S = (V^2+W^2)^{1/2}$, with overlaid the cross-flow streamlines over the contours, to represent respectively the magnitude and direction of the flow (also see Section 6.2.1.1); defining $k_{\geq 0.005}$ (corresponding to $k_{\geq 0.01}$ for pure sway) and $k_{\geq 0.001}$ as the mean k values over the flow regions where $k \geq 0.005$ and $k \geq 0.001$, respectively, to represent the maximum and average k value, respectively, within the flow (see Section 6.2.1.3); and defining the maximum and minimum ω_x values as those values when $\omega_x > 0$ and $\omega_x < 0$, respectively, within a flow region of interest (see Section 6.2.1.4).

At the top of Fig. 6-45, the trajectory of model (shown as a dashed-line; the path-line of the model mid-ship point) in a pure yaw motion is shown. The model is in a rotary yaw (or its heading) $\psi = -\psi_0 \cdot \cos \omega t$ motion, turning about its mid-ship point, such that the model is always tangent to the path-line while towed at a constant speed U_C (depicted with a red colored arrow in the figure). Where, the maximum heading angle $\psi_0 = 10.2°$, the yaw motion angular frequency $\omega = 1.672\ U_C/L$ (or a cyclic frequency $f = \omega/2\pi = 0.134$ Hz), and the towing speed $U_C = 1.531$ m/s, and the model length $L = 3.048$ m, respectively. Angular velocity of the model rotation, yaw rate $r = \mathrm{d}\psi/\mathrm{d}t$, is positive when it turns to starboard (depicted with a blue colored circular arc arrow in the figure). At every $\gamma = \omega t = 45°$ phase angle positions of the path-line, the outline of the model is shown with numbered 1 to 9, respectively. Below the model trajectory, overviews of the flow around the model at each of those phase angles are shown, along with the model

path-line (the light-blue colored line) similarly as in Fig. 6-22 for pure sway. Flow data shown are the axial velocity U contours and the cross-flow (V,W) streamlines at five model-longitudinal locations, x = 0.135, 0.335, 0.535, 0.735, and 0.935, respectively. Under below the sonar dorm of the model drawing shown at each phase position, the turning direction, heading angle ψ and yaw rate r values of the model at the instant are presented. At (1) γ = 0°, model heading is the maximum to the negative direction, ψ = -10.2°, yet, the incoming flow is parallel to the model longitudinal as the model is tangent to its path-line. Whereas the model yaw rate r = 0 at the instant, thus the flow pattern exhibits a typical one for the case when the model is in a 'straight-ahead' condition; down- and outward at the bow and up- and inward at the stern as per Longo et al. (2007), Gui et al. (2001a), and Olivieri et al. (2001). However, the apparent size of the vortical flow from the figure is considerably bigger than those from the straight-ahead case (e.g. Fig. 6-23a), obviously formed at the previous cycle of the yaw motion and lasting. The model, then, begins turning to starboard with increasing yaw rate, at (2) γ = 45°, ψ = -7.2° with r = 0.21, until (3) γ = 90° where ψ = 0° and yaw rate is the maximum r = 0.3 (U_C/L), and continues turning but with decreasing yaw rate, at (4) γ = 135°, ψ = 7.2° with r = 0.21, and then finishes the turning at (5) γ = 180° where the heading ψ = 10.2° is the maximum to the positive direction with r = 0; which completes the first half cycle of the pure yaw motion. Through the yaw motion, due to the rotary motion of the model, the cross-flow at the bow typically becomes down- and inward at the wind side and transversal and outward at the leeward side; and at the stern, vice versa. The vortical flow, on the other hand, changes its size and the direction of its rotation. The model motion and the flow at the second half of the cycle are anti-symmetric mirrors of those at the first half cycle, such that γ = (5) 180°, (6) 225°, (7) 270°, and (8) 315° to γ = (1) 0°, (2) 45°, (3) 90°, and (4) 135°, respectively, and γ = 360° is identical with γ = 0°.

6.2.2.1 Vortical flow structure

The vortical flow around the DTMB 5512 geometry, the same geometry of the model, in two steady maneuvers, static drift and steady turn, are shown in Fig. 6-46 (a) and (b), respectively. In the figures, vortices in the flow were visualized from the CFD simulations by Sakamoto (2009), by using the Q = 30 iso-surfaces (Hunt et al., 1988) with colored by the normalized relative helicity density level. Simulation was with drift angle $\beta = 10°$ for the static drift maneuver (transversal incoming flow left to right from Fig. 6-46a) and with a constant yaw rate $r = 0.3$ for the steady turn maneuver (turning to the starboard side; transversal incoming flow right to left at the bow whereas in reverse at the stern from Fig. 6-46b), respectively. Note that Fig. 6-46 (a) for static drift is the same as Fig. 6-23 (b), repeated herein for comparisons with the steady turn flow. Compared to static drift, the same kind of vortices are observed from the steady turn maneuver, such as SD, BK, and AK vortices (major ones) from the sonar dome, bilge keels, and aft body keel, respectively and FK, FS, and T vortices (minor ones) from the fore body keel, free surface, and transom, respectively. Of the vortices, SD vortex exhibits opposite signs (red vs. blue in the figure; direction of rotation) between two maneuvers due to the different directions of transversal in coming flow, which is generated from the sonar dome at the fore body and then convected downstream, whereas the other vortices that formed at the aft body show the same signs for both maneuvers as the flow direction is same. The size of vortices for steady turn in general is relatively small compared to static drift (considerably small for BK) as the overall incoming flow direction is more aligned to the hull longitude (tangent to the circular path-line) for the former case. The shape of the vortices is rather straight for the static drift case, aligned with the incoming flow direction, whereas rather curvy for the steady turn case, following the circular path-line of the hull form.

Fig. 6-47 (a) and (b) shows the vortical structure of flow around the hull form in a pure yaw maneuvering, with visualized from the CFD simulations by Sakamoto (2009)

and from the SPIV measurements, respectively, at the four phases of pure yaw cycle, γ = 0°, 45°, 90°, and 135°, in a sequence. From the CFD simulation result shown at Fig. 6-47 (a), the overall vortical flow structure for pure yaw maneuver is similar as that of the steady turn shown previously in Fig. 6-46 (b) with the same kinds of vortices, whereas the sign (direction of vortex rotation), shape, size, and location of those vortices are changing dynamically in time along with the yaw motion. At γ = 0°, the SD vortex is the major one, with stretched along the ship length from the bow to the stern. FK and AK vortices are the second largest, whereas BK vortex is very small in size at both the port and starboard sides. At γ = 45°, the SD vortex generated from earlier phase (SD_S in the figure) is detached from the sonar dorm and a new one with opposite sign (SD_P in the figure) is formed. At γ = 90°, the newly generated SDP vortex is growing (i.e., convecting to the downstream), and the BK vortex at the portside (BKP in the figure) is as well growing, and then those vortices become the major ones at γ = 135°. Note that the steady turning maneuver shown in Fig. 6-46 (b) corresponds to the γ = 90° case where the yaw rate is the same as the steady turn case with $r = 0.3$ but with a non-zero yaw acceleration, $dr/dt = 0.5\ (U_C^2/L)$. On the other hand, from Fig. 6-47 (b), the SPIV measurement results shows a very similar vortical structure at each phase, with visualized with the axial vorticity ω_x contours. Each of the vortices are identified by comparing the sign and the positions of ω_x contours with those of the helicity iso-surfaces from the CFD simulations, and labeled in the figures.

6.2.2.2 Phase-averaged velocity field

In Fig. 6-48, shown are the phase-averaged axial velocity U field at four phase positions, γ = 0°, 45°, 90°, and 135°, and at six longitudinal locations, x = 0.135, 0.335, 0.535, 0.735, 0.935, and 1.035. The flow field is seen from behind the model, i.e. looking upstream, and the incoming flow is coming out of the paper from the figure, and the model is turning its head to the starboard side (from left to right in the figure) about the

mid-ship point. The overall trend of U field for pure yaw is similar as for pure sway; at the bow appears thin boundary layer that is growing with the model longitudinal length, and becomes very thick at the stern. Dead flow zone (e.g., where $U \leq 0.5$, the dark-blue colored contour level in the figures) appears at $x = 0.735$ and 0.935, locally inside the boundary layer, and at the wake region, $x = 1.035$, becomes considerably large near the free surface. The flow is also retarded at the regions where the vortices present, e.g. under below the model where the SD vortices are, near around aft body bilges where the BK vortices are, and at the aft body keel where the AK vortices are. The shape and size of the boundary layers are typically asymmetric about the model center plane, and change continuously with time, i.e. with γ, in accordance with the yaw motion, may possibly be interacting with the flows induced by the nearby vortices.

In Figs. 6-49 and 6-50, time histories (top) and FS harmonics (bottom) of $U_{\leq 0.9}$ and those of $U_{\min}$ are shown, respectively. $U_{\leq 0.9}$ is the average U value over the region where $U \leq 0.9$ and $U_{\min}$ is the minimum U value within the region, respectively, at a given γ and x. Time histories are shown for all the 32 phase positions available from the SPIV measurements, from 0° to 348.75° with a phase step $\Delta\gamma = 11.25°$, and FS harmonics are shown for the 0^{th}- and 2^{nd}-order with designated as H_0 and H_2, respectively, in the figures. From Fig. 49 (top), the $U_{\leq 0.9}$ values oscillate with γ for all x locations. The period mean values of $U_{\leq 0.9}$ time-history is almost flat along the model length, i.e. $H_0 \approx 0.8$ for $x = 0.135 \sim 0.935$ from Fig. 6-49 (bottom), except for $x = 1.035$ where $H_0 = 0.75$. The oscillation amplitude of $U_{\leq 0.9}$ time-history is as well nearly constant with $H_2 \approx 0.009$, about 1.2% of H_0, again except for $x = 1.035$ where $H_2 = 0.023$ that is about 3% of the H_0 at the same x location. Next for $U_{\min}$, from Fig. 50 (top), time-histories as well exhibit oscillations along with the γ position. Contrary to $U_{\leq 0.9}$, the period mean H_0 and the oscillation amplitude H_2 of $U_{\min}$ time histories are not flat, but change along the model length. From Fig. 6-50 (bottom), $H_0 = 0.67$ at $x = 0.135$ and decreases nearly linearly along x, $H_0 = 0.39$ at $x = 1.035$, whereas $H_2 = 0.015$ (2% of H_0) at $x = 0.135$ and increases

gradually with x, $H_2 = 0.038$ (9% of H_0) at $x = 0.935$, then sharply at $x = 1.035$ where $H_2 = 0.071$ (18% of H_0).

Cross-flow vector (V,W) field is shown in Fig. 6-51, and the contours of $S = (V^2+W^2)^{1/2}$ with overlaid the cross-flow streamlines, showing the magnitude and the direction of the cross-flow, respectively, are shown in Fig. 6-52. From Fig. 6-51, the cross-flow vectors are in general pointed to the portside at the bow and to the starboard at the stern, as the model is turning its head to the starboard and its tail to the portside, respectively. Whereas the vectors point outward at $x = 0.335$ and inward at $x = 0.535$, respectively, but the velocity magnitude is usually small compared with those at the bow or stern. On the other hand, cross-flow vectors visualize clearly the rotational motions of the fluid at the vortical flow regions, such as near around the sonar dome (from the figures as shown with the model projected into the paper), around the bilge keels at the port- and starboard-side, and below the aft body center keel, where the SD, BK, and AK vortices exist, respectively.

The directions of cross-flow are even more obvious with vortices exposed clearly from the cross-flow streamlines as shown in Fig. 6-52. At $x = 0.135$, cross-flow in general directs toward portside as the model is turning to the starboard side, with accelerated locally at the starboard side, i.e., the wind side, where the cross flow velocity magnitude $S = 0.2 \sim 0.3$. Compared to model tangential speed $V_t = r \cdot dx = 0.11$ at $\gamma = 90°$, where the model yaw rate $r = 0.3$ and the radial distance $dx = 0.365$ from the mid-ship, the cross-flow speed at the region is about $2 \sim 3$ times faster than the V_t in general. The cross-flow speed weakens at $x = 0.336$ and 0.535 typically with $S < 0.1$, where in general flow is diverging from and converging to the hull, respectively. At the aft body, $x = 0.735$, 0.935, and 1.035, cross-flow is usually toward the starboard side as the model in turning its tail to the portside. Typically cross-flow speed $S = 0.05 \sim 0.15$, usually slower than the model tangential velocity $V_t = 0.13$ at $x = 0.935$ at $\gamma = 90°$, except for the regions near the vortices. The SD vortex is clearly seen from the streamlines. Particularly at $\gamma = 0°$ where

the model yaw rate $r = 0$, the concentric or spiral flow discovers the size and position of the SD vortex along the entire model length. The approximate sizes of SD vortex $\phi \sim 0.01\ L$ at $x = 0.135$, and then grows along the model length, $\phi = 0.02 \sim 0.025\ L$ between $x = 0.335$ and 0.535, and $\phi = 0.03 \sim 0.04\ L$ between $x = 0.735 \sim 1.035$, where ϕ is an approximate outer diameter of the concentric streamlines at $\gamma = 0°$, respectively. The approximate center point of SD vortex at $\gamma = 0°$ is just below the model keel position, $(y,z) \approx (0,-0.05)$ at $x = 0.135$, and then shifted in both lateral and vertical directions. In lateral direction, the center point first remains near the center plane at the fore body and then gradually moves to portside at the aft body, and located at $y \approx -0.028$ at $x = 1.035$. In vertical direction, the center point first shifts down at the fore body, to $z \approx -0.065$ at $x = 0.535$, and then up at the aft body, to $z \approx -0.04$ at $x = 1.035$, following the model bottom profile. At the other γ positions, the size and location (including the direction of rotation) of the SD vortex is changing in time, i.e. with γ, and is often superposed with the parallel transverse flow at the aft body, the vortex streamlines open up or not clearly seen. The strength of the SD vortex including the difference kinds of the vortices will be discussed later together with the axial vorticity field.

6.2.2.3 Turbulent kinetic energy and Reynolds stresses

Turbulent kinetic energy k field (for $k \geq 0.001$) is shown in Fig. 6-53 for $\gamma = 0°$, 45°, 90°, and 135° cases. Reynolds number of the flow $\mathrm{Re} = U_C L/\nu = 4.6\times10^6$, same as for pure sway test. The overall structure of the field exhibit coherence with the phase-averaged axial velocity U field shown in Fig. 6-48; at the bow with thin layer that is growing along the model length and becomes very thick at the stern, i.e. within the boundary layers and inside the vortical flow regions. The core regions with high k values (e.g. $k \geq 0.01$) exist typically near at the model hull surfaces, at the center of the vortical flow regions, and near the free surface behind the model transom. The apparent shapes of the k field and the locations of the core region vary in time, i.e. along with the phase of pure

yaw motion. In Figs. 6-54 and 6-55, time histories (top) and FS harmonics (bottom) of k_{mean} and those of k_{max} are shown, respectively. Similarly for pure sway case, herein the k_{mean} and k_{max} are defined as the average k values respectively within the core regions where $k \geq 0.001$ and within the overall k field where $k \geq 0.01$, which respectively represents the approximate maximum and average k value within the turbulent flow. In the figures, time histories are from the all 32 phase positions of the SPIV measurement, and the FS harmonics are for the 0^{th}- and 2^{nd}-order harmonics (with designated respectively as H_0 and H_2) corresponding to the period mean value and to the dominant amplitude of the time-history oscillations. From Fig. 6-54 (top), $k_{mean} = 0.0025 \sim 0.0045$ oscillating with γ particularly at $x = 0.135$. From Fig. 6-54 (bottom), the period-mean value of the oscillating k_{mean} is nearly constant along the model length with $H_0 \approx 0.003$ whereas slightly larger H_0 values at $x = 0.135$ and 1.035. This indicates that in a mean sense the overall turbulence intensity $I = (2/3 \cdot k)^{1/2} \sim 0.045$ in the flow, or a turbulent velocity fluctuation ~ 4.5% of U_C. The k_{mean} oscillation amplitude is the maximum at $x = 0.135$ with $H_2 = 0.0007$ (19% of H_0), and then undulates with x with a mean $H_2 = 0.0002$ that is about 7% of H_0. On the other hand, at the core region, $k_{max} = 0.011 \sim 0.016$ from Fig. 6-55 (top) as well oscillating with γ. From Fig. 6-55 (bottom), the period mean k_{max} value decreases gradually along the model length from $H_0 = 0.014$ at $x = 0.135$ to $H_0 = 0.011$ at $x = 0.935$, and then just behind the model it increases sharply with $H_0 = 0.014$ at $x = 1.035$. Turbulence intensity $I = 0.086 \sim 0.097$ in the core region, or about 9 ~ 10% U_C of turbulent velocity fluctuations. The oscillation amplitude of k_{max} is the maximum at the bow with $H_2 = 0.0015$ (11% of H_0) at $x = 0.135$, and drops fast along the model length with $H_2 \approx 0.0005$ (3 ~ 4% of H_0) between $x = 0.335$ and 0.535 and with $H_2 \approx 0.00025$ (~ 2% of H_0) at the aft body.

Reynolds normal (uu, vv, ww) and shear (uv, uw, vw) stress fields are shown in Fig. 6-56 through Fig. 6-61, respectively. Despite the quite dissimilar flow structures between the phase-average axial U and cross-flow (V,W) velocity fields shown in Fig. 6-48

and Fig. 6-51 (or Fig. 6-52), respectively, the apparent structures of the Reynolds stress fields from the figures exhibit a coherence between the stress components, rather similar to the U field. In general, the order of magnitude of the normal stresses is larger than the shear stresses, and typically the uu and uv stresses respectively are the largest of the normal and shear stresses. In Figs. 6-62 and 6-63, the average normal (top) and shear (bottom) stress values over the regions for k_{mean} ($k \geq 0.001$) and k_{max} ($k \geq 0.01$) are shown, which are as well averaged values over the pure yaw motion period, i.e. corresponding to H_0's of the FS for those variables. Note that shear stresses shown in the figures are root-mean-squared (rms) values. From Fig. 6-62, both the normal and shear stresses are nearly constant along the model length with average values (uu, vv, ww) = (0.0029, 0.0019, 0.0009) and (uv, uw, vw) = (0.0012, 0.0005, 0.0003), respectively. The normal stress values, however, tend to increase at the bow (x = 0.135) and in the wake (x = 1.035). Of the normal stresses, uu is the largest, followed by vv, and ww is the smallest, whereas for the shear stresses, uv is the largest and uw and vw are both small. On the other hand, at the core region where $k \geq 0.01$, from Fig. 6-63 the normal (top) and shear (bottom) stresses are nearly constant with x, (uu, vv, ww) ≈ (0.0167, 0.0072, 0.0011) and (uv, uw, vw) ≈ (0.0077, 0.0013, 0.0008), up to x = 0.735, where the uu and uv are respectively the largest normal and shear stresses. After x = 0.735 at the stern part, nevertheless the sharp increase in k_{max} value as shown in Fig. 6-55 (bottom), those uu and uv stress values decrease fast whereas the other stresses values increase with x, respectively, thus the Reynolds stress field becomes more of isotropic than at the front part of the model. The Reynolds stress anisotropic tensor $b_{ij} = u_i u_j/2k - \delta_{ij}/3$ values shown in Fig. 6-64 for the normal (top) and the shear (bottom) stresses reveals this more clearly. The Reynolds stress anisotropic tensor b_{ij} is the deviatoric part of the Reynolds stress tensor, $a_{ij} = u_i u_j - (2/3)k\delta_{ij}$ with normalized with $2k$. The b_{ij} values show how far the elemental stress is deviated from the mean value, thus b_{ij} values close to zero indicate more isotropic stress tensor.

Consequently, the flow has a turbulent kinetic energy $k^{1/2} \approx 5.4\%$, the normal Reynolds stresses ($uu^{1/2}$, $vv^{1/2}$, $ww^{1/2}$) ≈ (5.4%, 4.4%, 3%), and the rms of the shear Reynolds stresses ($uv^{1/2}$, $uw^{1/2}$, $vw^{1/2}$) ≈ (3.5%, 2.2%, 1.7%) of U_C, respectively, in average over the turbulent flow field. Locally, the flow may have turbulent kinetic energy $k^{1/2} \geq$ 11.3%, and normal stresses ($uu^{1/2}$, $vv^{1/2}$, $ww^{1/2}$) ≥ (12.9%, 8.5%, 3.3%) of UC, and the rms values of the shear Reynolds stresses ($uv^{1/2}$, $uw^{1/2}$, $vw^{1/2}$) ≥ (8.8%, 3.6%, 2.8%) of U_C, respectively. The Reynolds stresses are anisotropic; however, locally those may become less anisotropic at the stern part and in the wake region. Those average k and Reynolds stress values are similar or smaller than the maximum values of ($k^{1/2}$, $uu^{1/2}$, $vv^{1/2}$, $ww^{1/2}$, $uv^{1/2}$, $uw^{1/2}$) = (5.4%, 5.3%, 4.1%, 3.7%, 2.4%, 2.8%) of U_C from the steady test by Longo et al. (2007). The steady test was using the same model with a straight-ahead condition and the flow was measured at the nominal wake region (i.e., $x = 0.935$).

6.2.2.4 Axial vorticity

Axial vorticity ω_x field (for $\omega_x \leq -10$ and $\omega_x \geq 10$) is shown in Fig. 6-65 for $\gamma = 0°$, 45°, 90°, and 135°. From the figures vortices such as the sonar dome (SD), bilge keel (BK), and aft body center keel (AK_C) vortices are more clearly seen than from the cross-flow vector or streamline field shown in Figs. 6-51 and 6-52, respectively, from which the vortices at certain phases are not obvious with superposed with the nearby parallel transverse flow and streamlines open up. SD vortex is the most dominant one, which can be seen most clearly from the Fig. 6-65 at $\gamma = 0°$ (the first column from the left), where the SD vortex is located at the portside of the model within a range of $y = -0.04 \sim 0.01$ and $z = -0.03 \sim -0.07$ in general. At $\gamma = 45°$, a new counter rotating SD vortex is formed at the fore body, $x = 0.135 \sim 0.535$, and the old one from $\gamma = 0°$ is detached from the sonar dome and weakens at the aft body, $x = 0.735 \sim 1.035$. At $\gamma = 90°$ and 135°, the new SD vortex strengthens and propagates to the aft body and moves to the starboard side. BK vortex is the second dominant one, which can be seen most clearly from the Fig. 6-65

at x = 0.735 (the third row from the bottom), where two BK vortices are respectively located near around the portside and starboard bilge keel positions (as appears in the figures with the model projected). The BK vortices are first generated at x = 0.535 near around the port- and starboard side bilge keels but very locally, and grows in size at x = 0.735, and then both BK vortices converge toward the model center plane at x = 0.935 and 1.035, but usually diffused and not clearly seen from the figures. AK_C vortex is the third dominant one, which can be seen most clearly from the Fig. 6-65 at x = 0.935 (the second row from the bottom), where the AD vortex is located near below the aft body center keel position at (y,z) = (0.0, -0.015). The AK_C vortex remains in the wake at x = 1.035, nearly at the similar (y,z) position, but typically defused and mixed with other vortices such as BK and not clearly seen from the figures. Other than those three vortices a couple of vortices as well can be seen from the figures. This includes the vortices near below the fore body keel (FK) at x = 0.335 and 0.535, near below the aft body keel (AK) at x = 0.735 and 0.935, and near the free surface (FS). Typically, however, these vortices are weak in strength compared to those dominant three vortices, and data were not sufficient for analysis due to limited longitudinal resolution of the measurement (six x locations along the model length), and data may contaminated for the FS vortex from the errors of SPIV measurement near the free surface, which precludes further discussions for those vortices.

In Fig. 6-66, shown are the SD vortex (top) time histories of the maximum/minimum ω_x values, $\omega_{x,\max/\min}$, for x = 0.135 ~ 1.035 and (bottom) the FS 1st-order amplitude H and phase angle ϕ values of the $\omega_{x,\max/\min}$ time histories such that $f(t) = H\cdot\sin(\omega t+\phi)$ at give x locations. The $\omega_{x,\max/\min}$ is defined herein such that the maximum ω_x value when $\omega_x > 0$ and the minimum ω_x value when $\omega_x < 0$ at a given phase position γ. From Fig. 6-66 (bottom), H = 292 is the largest at x = 0.135 and drops fast to H = 159 at x = 0.335 and increases gradually with x to H = 189 at x = 0.735 and then decreases to H =129 at x = 1.035. Whereas, phase angle ϕ decreases nearly linearly along the model length with a slop $d\phi/dx = -118.9°/L \approx -2\pi/3L$ where L is the model length and an inter-

cept $\phi_0 = 191.3° \approx \pi$. This suggests that the phase term ϕ in f(t) is a function of x such that $\phi(x) = -(m/L)x + \phi_0$ where $m = 2\pi/3$ and $\phi_0 = \pi$, and thus the $\omega_{x,max/min}$ propagates in space and time in a wave-like form such that $f(x,t) = H(x)\cdot\sin(kx - \omega t)$. The wave number $k = m/L$ (wave length $\lambda = 2\pi/k = 2\pi L/m$) and the circular frequency $\omega = 2\pi f$ where $f = T^{-1}$ and T is the period of pure yaw motion (note that the f is as well the shedding frequency for SD vortex). Then, the phase velocity $v_p = \omega/k = \lambda/T = 2\pi fL/m$, or in a non-dimensional form $v_p/U_C = (2\pi/m)\cdot St$, where m is the phase change over a ship length L and $St = fL/U_C$ is the Strouhal number of the SV vortex shedding. For $f = 0.134$ Hz, $L = 3.048$ m, and $U_C = 1.531$ m/s, which gives $St = 0.2668$, and with $m = 2\pi/3$, then the phase velocity $v_p = 0.8\ U_C$. This indicates that $\omega_{x,max/min}$ propagates along the model length with a speed about 80% of the model towing speed U_C. At a given x location, f(x,t) becomes pure sine waves with a amplitude H(x) and with a phase shift $\phi = \pi - kx$ as shown in Fig. 6-66 (top) for six x location. On the other hand, at a given time t (or at a phase angle γ), f(x,t) becomes a sine-like wave of which amplitude H(x) is not a constant value but changes with x and with a phase shift $\phi = -\omega t$ (or $\phi = -\gamma$). Examples of the wave form at four phase positions, $\gamma = 0°$, 45°, 90°, and 135° are shown in Fig. 6-67 with compared with the $\omega_{x,max/min}$ values measured from the SPIV. From the figure, the wave model (shown as lines) agrees well with the measured $\omega_{x,max/min}$ values (shown as symbols) except for $\gamma = 45°$ case, may possibly due to the effect of higher order of harmonics in the $\omega_{x,max/min}$ time histories shown in Fig. 6-66.

BK vortices are generated in pairs; one is the portside and another at the starboard side, which can be best seen from figures in Fig. 6-65 for $x = 0.735$ (the third row from the bottom), near around the bilge keels positions. These two vortices typically have the same direction of rotation whereas different strength according to direction and magnitude of the nearby incoming cross-flow velocity around the bilge keels. From the vector field figures in Fig. 6-51 (or Fig. 6-52 for streamlines) for $x = 0.535$ (the third row from the top), at first when $\gamma = 0°$ the cross-flow near the bilge keels is stronger at starboard

than at portside, next at $\gamma = 45°$ the flow weakens at both sides, and then at $\gamma = 90°$ and 135° the stronger cross-flow comes from the other side, i.e. from the portside. Accordingly the BK vortex and the axial vorticity is stronger first at the starboard side and then switches its position to the portside and continues to develop (with changed its sign), and vice versa for the weaker BK vortex at the other side. Herein the side where the incoming flow is stronger is referred as the 'wind' side and the other side as the 'leeward' side, respectively. In Fig. 6-68 the time histories of the $\omega_{x,max/min}$ values of the BK vortices at the wind and leeward sides for $x = 0.535$ (left) and $x = 0.735$ (right), respectively. In the figures two different symbols ('delta' and 'gradient') are use to indicate from which side came the vortices. At x = 0.535, although the BK vortices are very local and small in size, the ωx,max/min value is large with H = 115 at the wind side and H = 71 at the leeward side, respectively, from the FS, where the phase angle $\phi = -48.4°$ and -51.3°, respectively. At $x = 0.735$, the BK vortices grow in size but decayed in strength with H = 80 at the wind side and H = 25 at the leeward side, respectively, where the phase angle $\phi = -27.5°$ and -30.3°, respectively. Compared to H = 292 of the SD vortex at x = 0.135 (the strongest), the H's at $x = 0.535$ and 0.735 are about 39% and 27% for wind side, respectively, and about 24% and 9% for leeward side, respectively.

Time histories of the $\omega_{x,max/min}$ values of AK_C vortex is shown in Fig. 69 for $x = 0.935$ and 1.035. When FS reconstructed, at $x = 0.935$ and 1.035, H = 95 and 63, respectively, and ϕ -36.9° and -52.1°. The H's are about 33% and 22% of the SD vortex H value at $x = 0.135$.

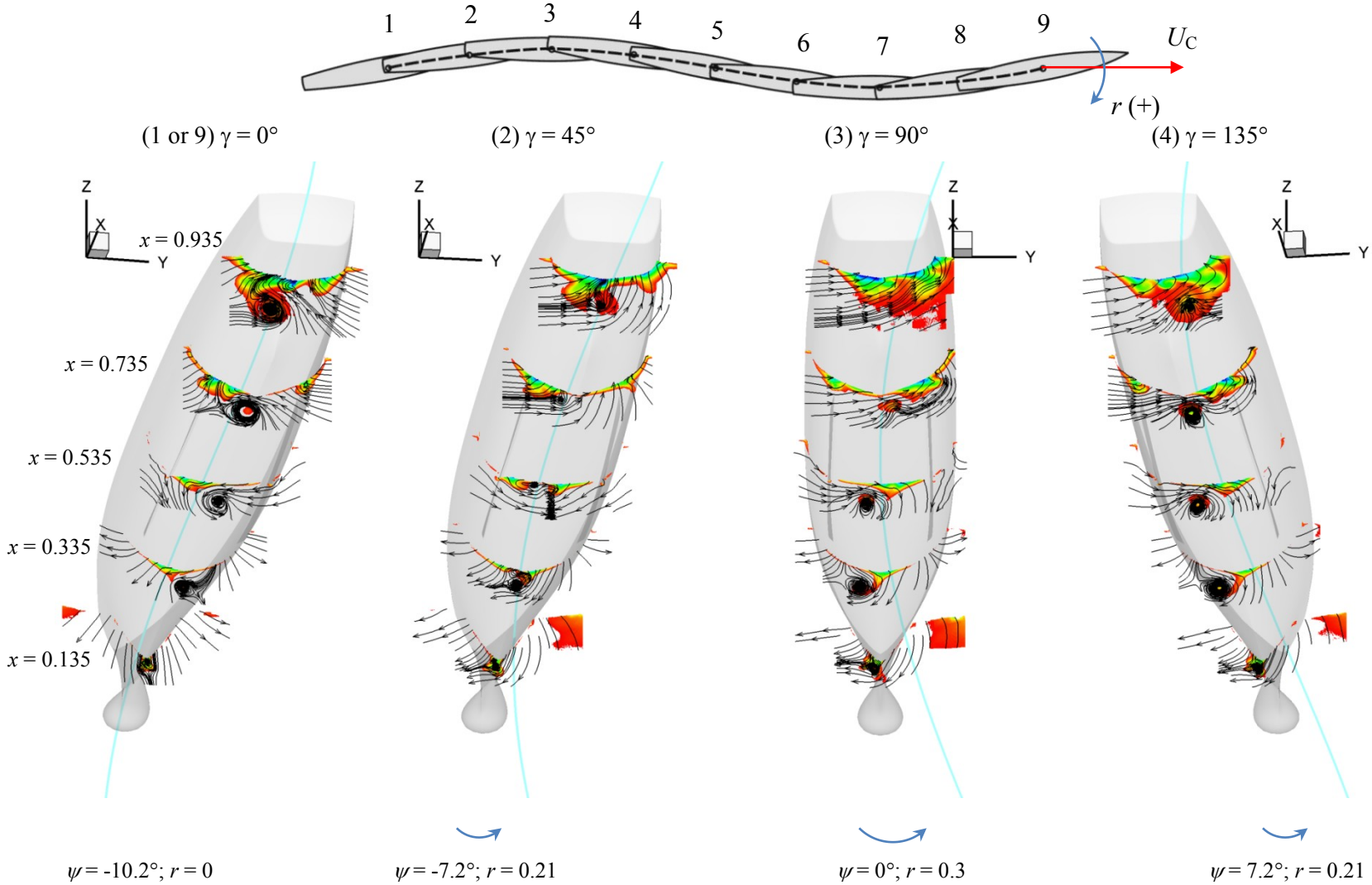

Figure 6-45 Trajectory of model (top) in pure yaw motion and overviews of the flow around the model (below).

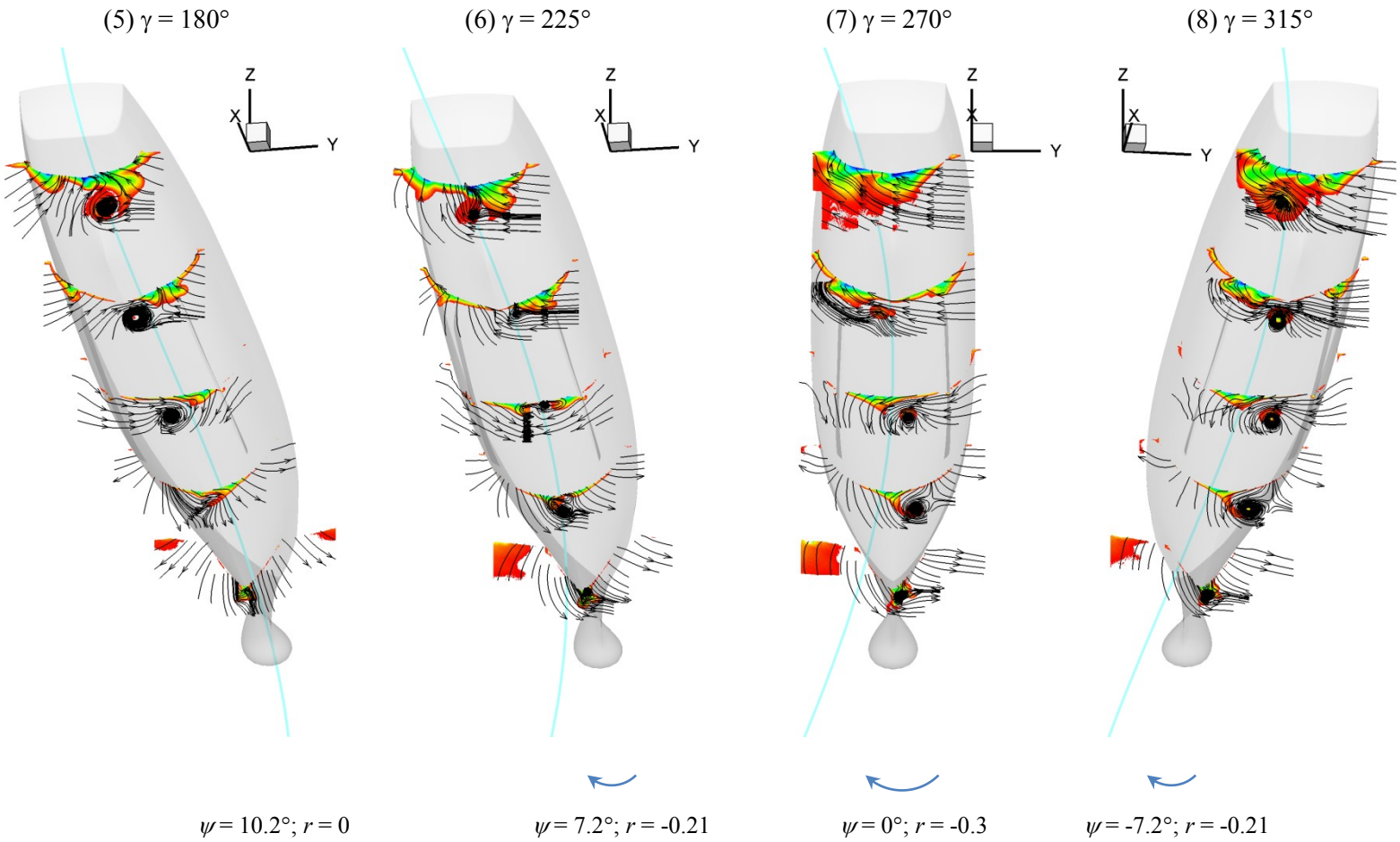

Figure 6-45–Continued

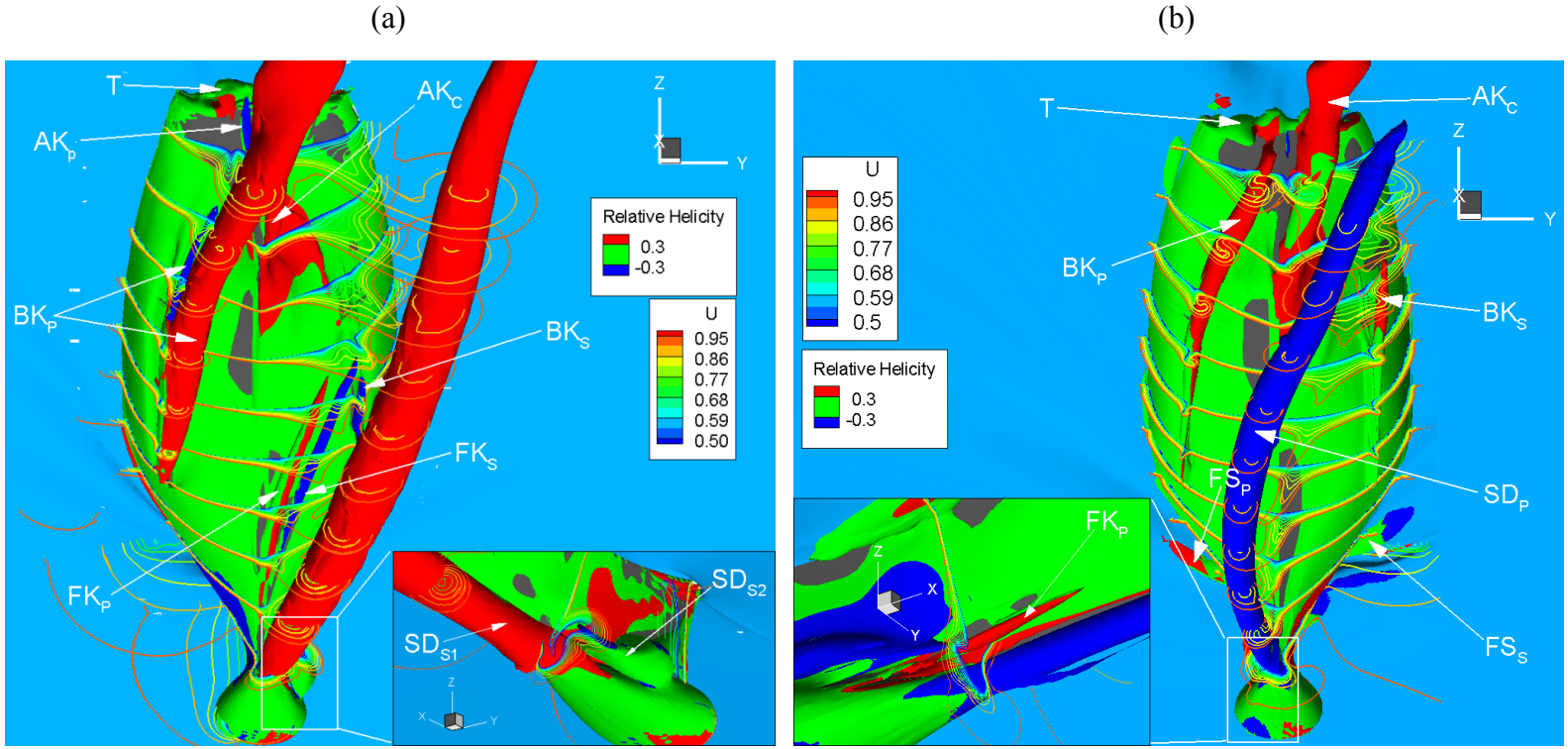

Figure 6-46 Vortical flow structures around the DTMB 5512 geometry in steady maneuver for: (a) static drift at $\beta = 10°$ and (b) steady turn at $r = 0.3$ cases. (CFD simulations by Sakamoto 2009).

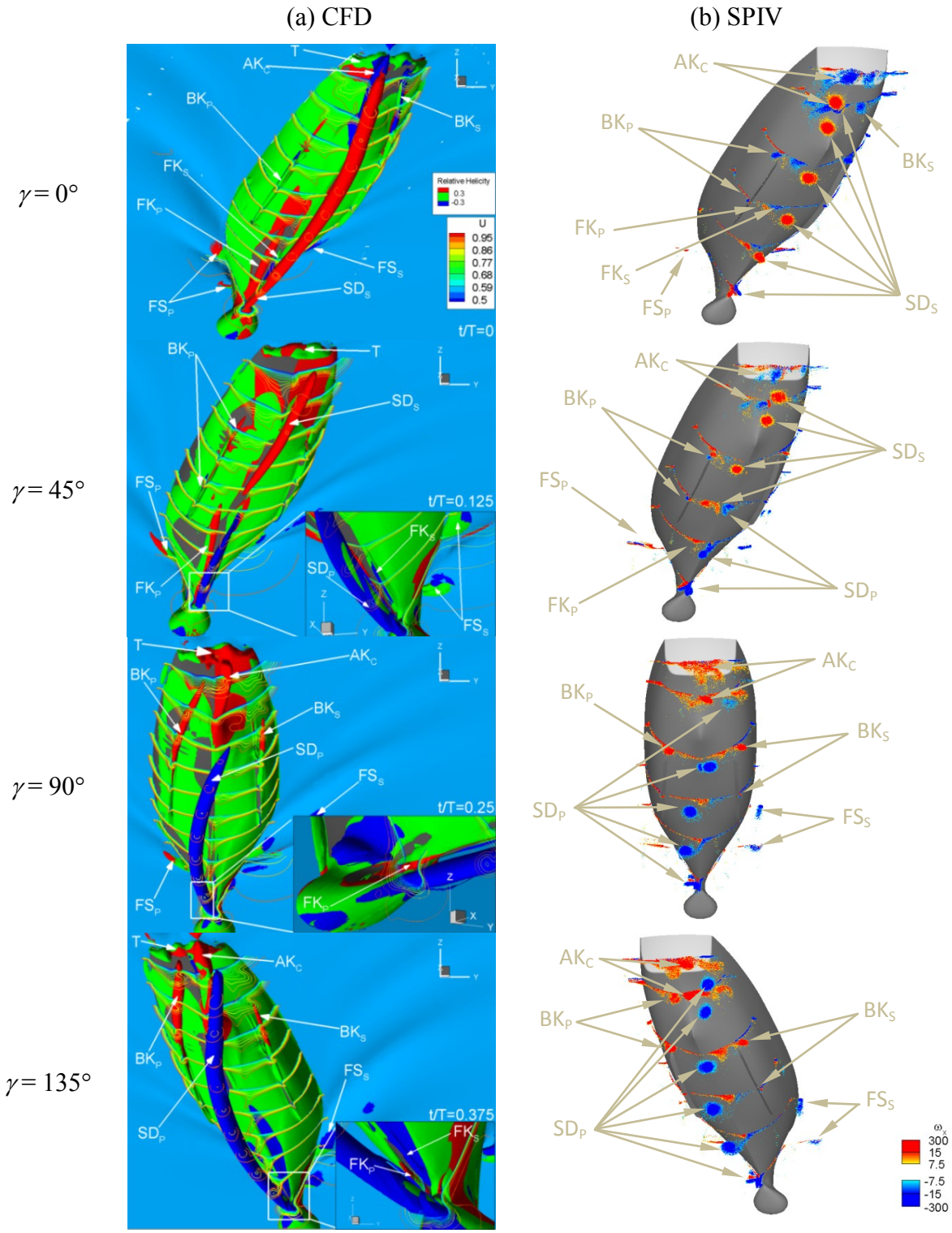

Figure 6-47 Vortical flow structures around the DTMB 5512 geometry in pure yaw maneuvering with r_{max} = 0.3: (a) Iso-surfaces of relative helicity (CFD simulations by Sakamoto 2009) and (b) contours of axial vorticity (SPIV).

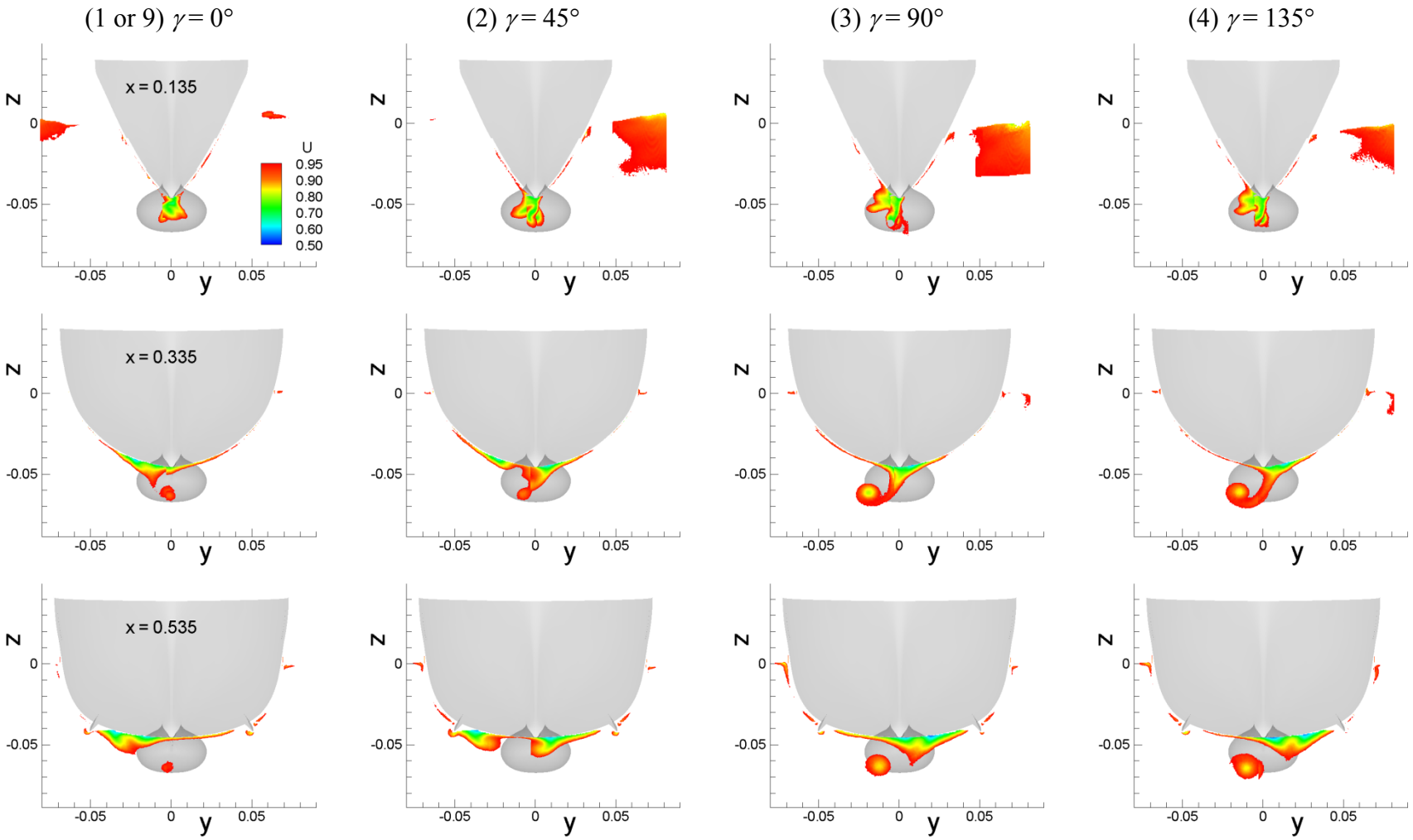

Figure 6-48 Phase-averaged axial velocity *U* field for pure yaw test.

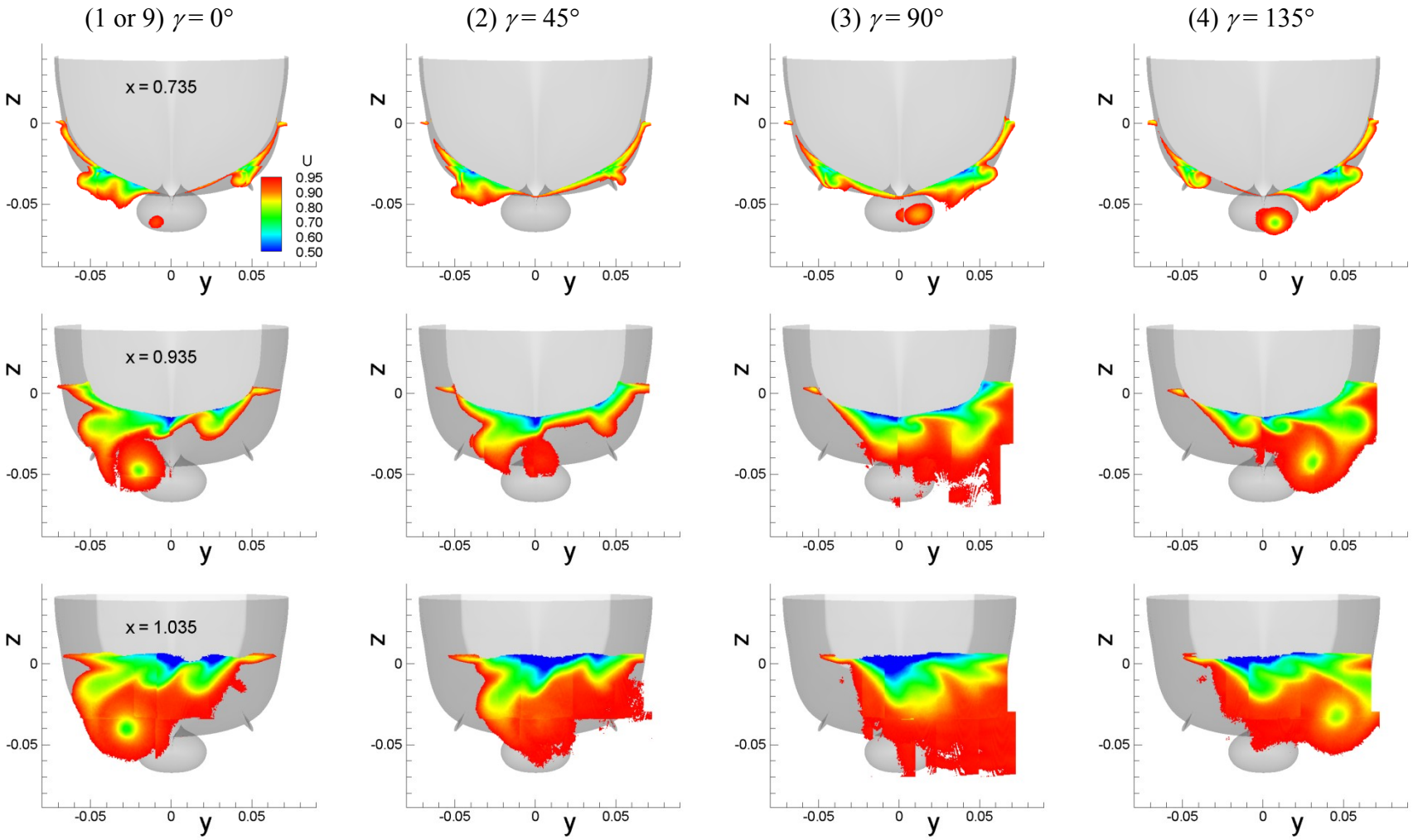

Figure 6-48–Continued

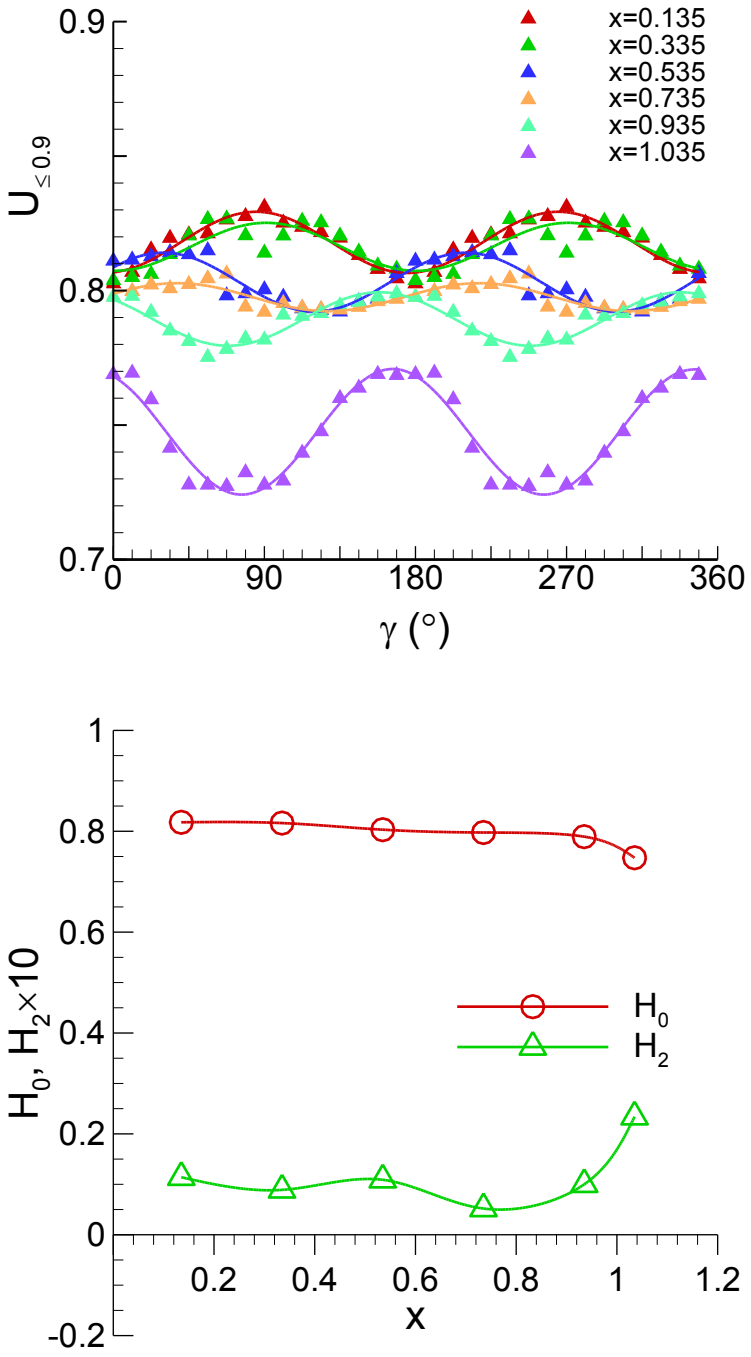

Figure 6-49 Average axial velocity for $U \leq 0.9$ (top) and FS harmonics (bottom).

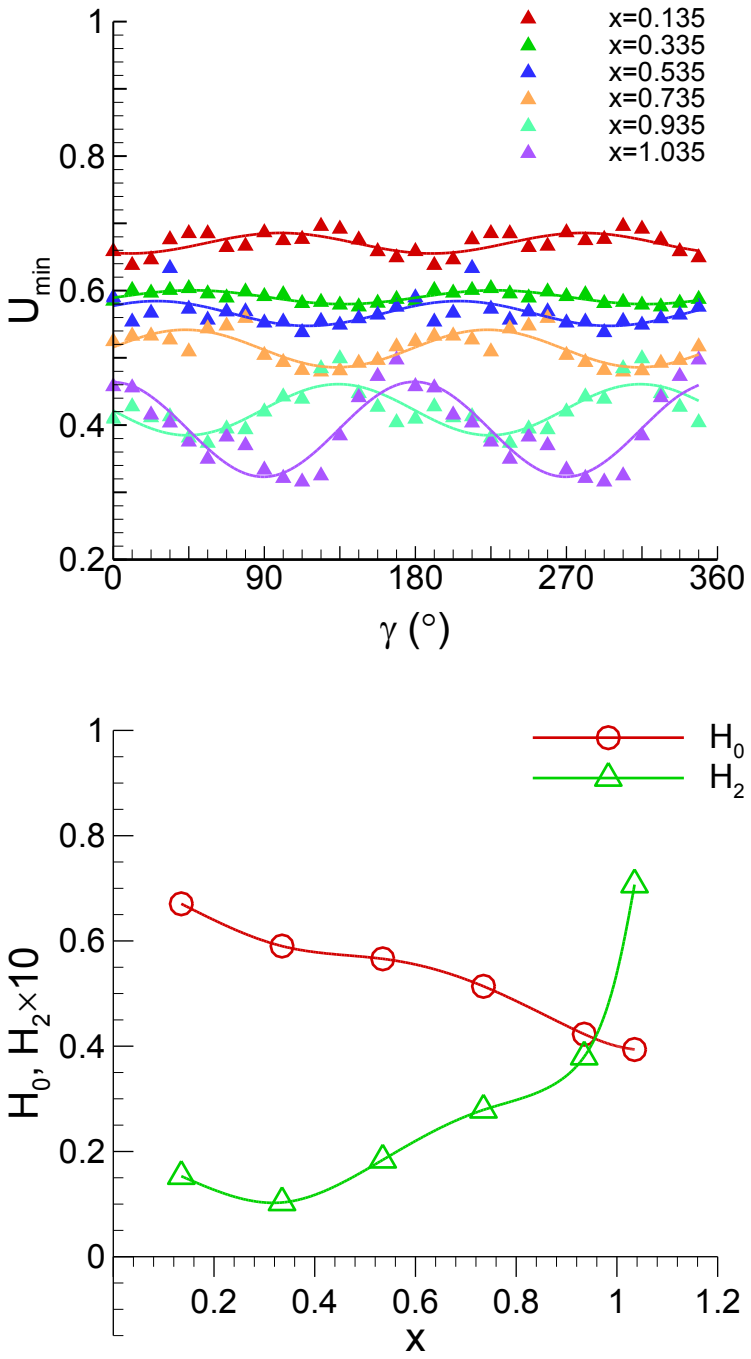

Figure 6-50 Minimum axial velocity (top) and FS harmonics (bottom).

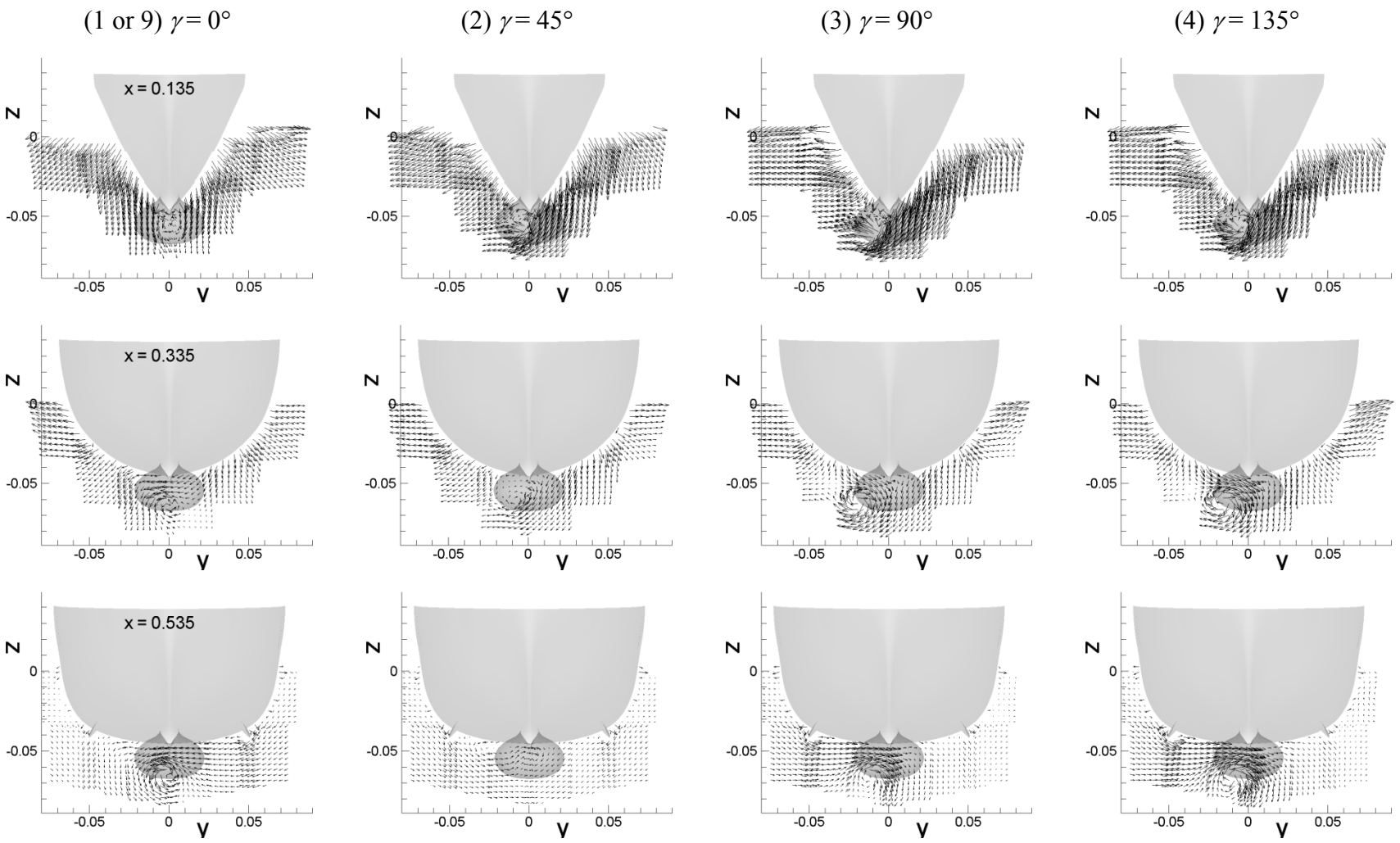

Figure 6-51 Phase-averaged cross-flow (V,W) vector field for pure yaw test.

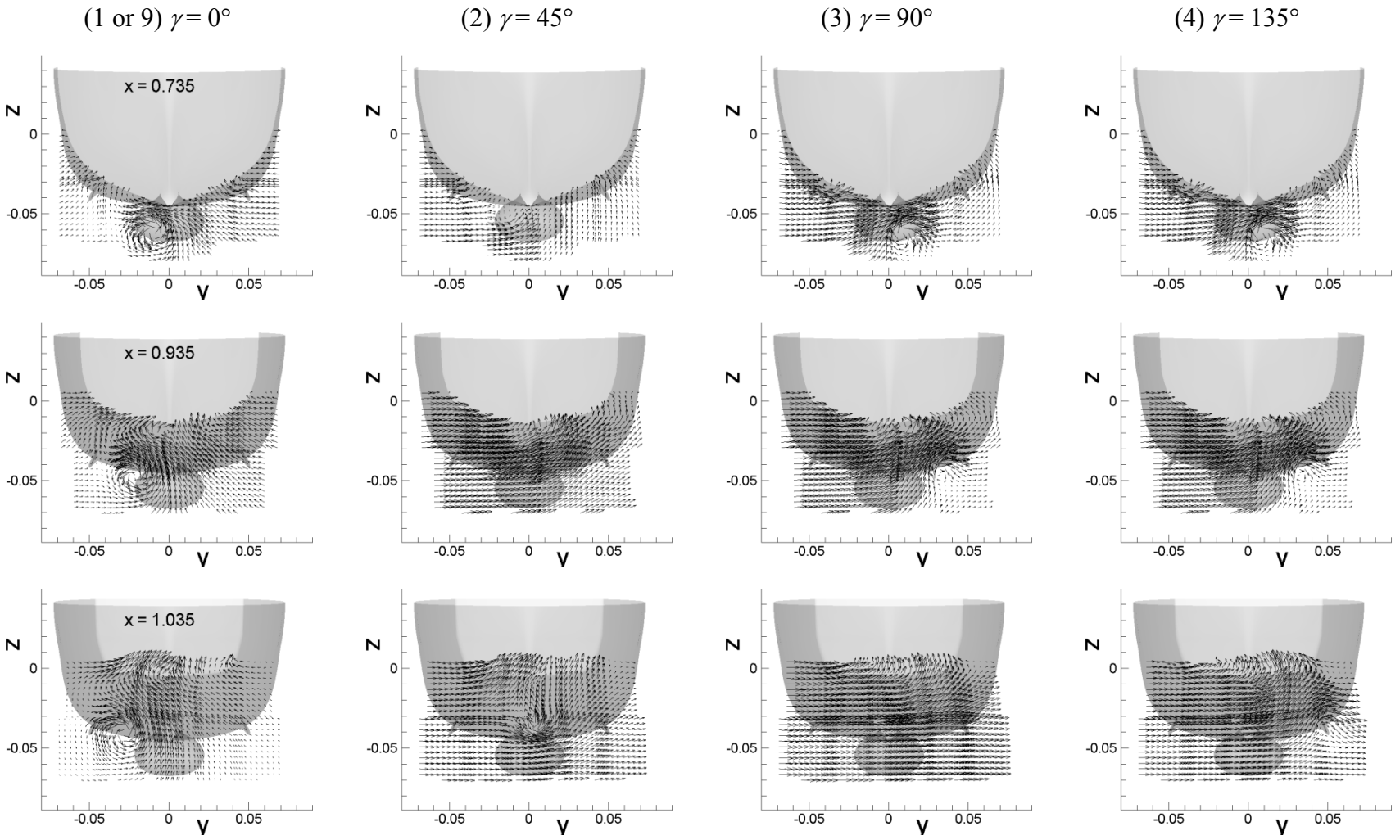

Figure 6-51–Continued

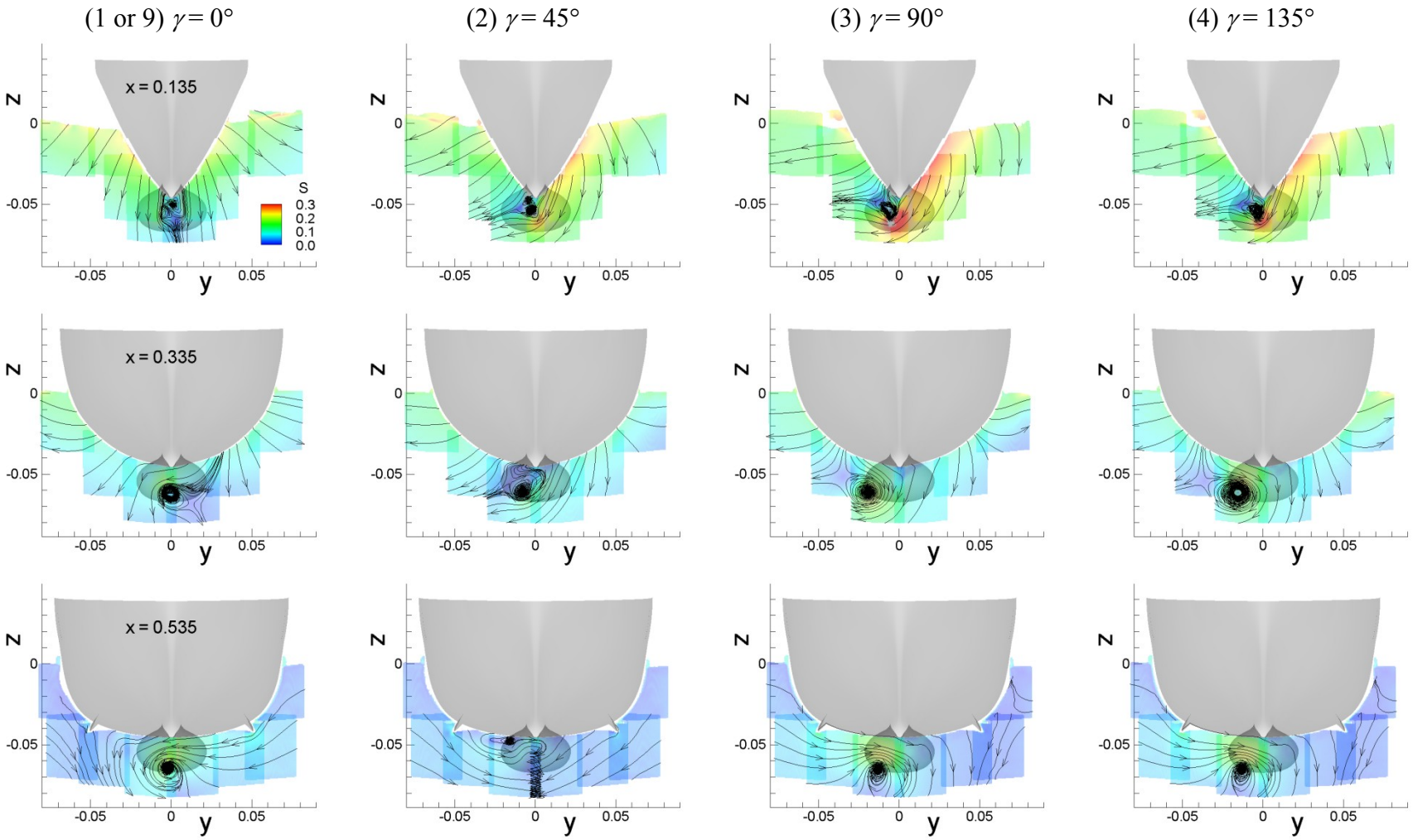

Figure 6-52 Cross flow velocity vector magnitude $S = (V^2 + W^2)^{1/2}$ and streamlines for pure yaw test.

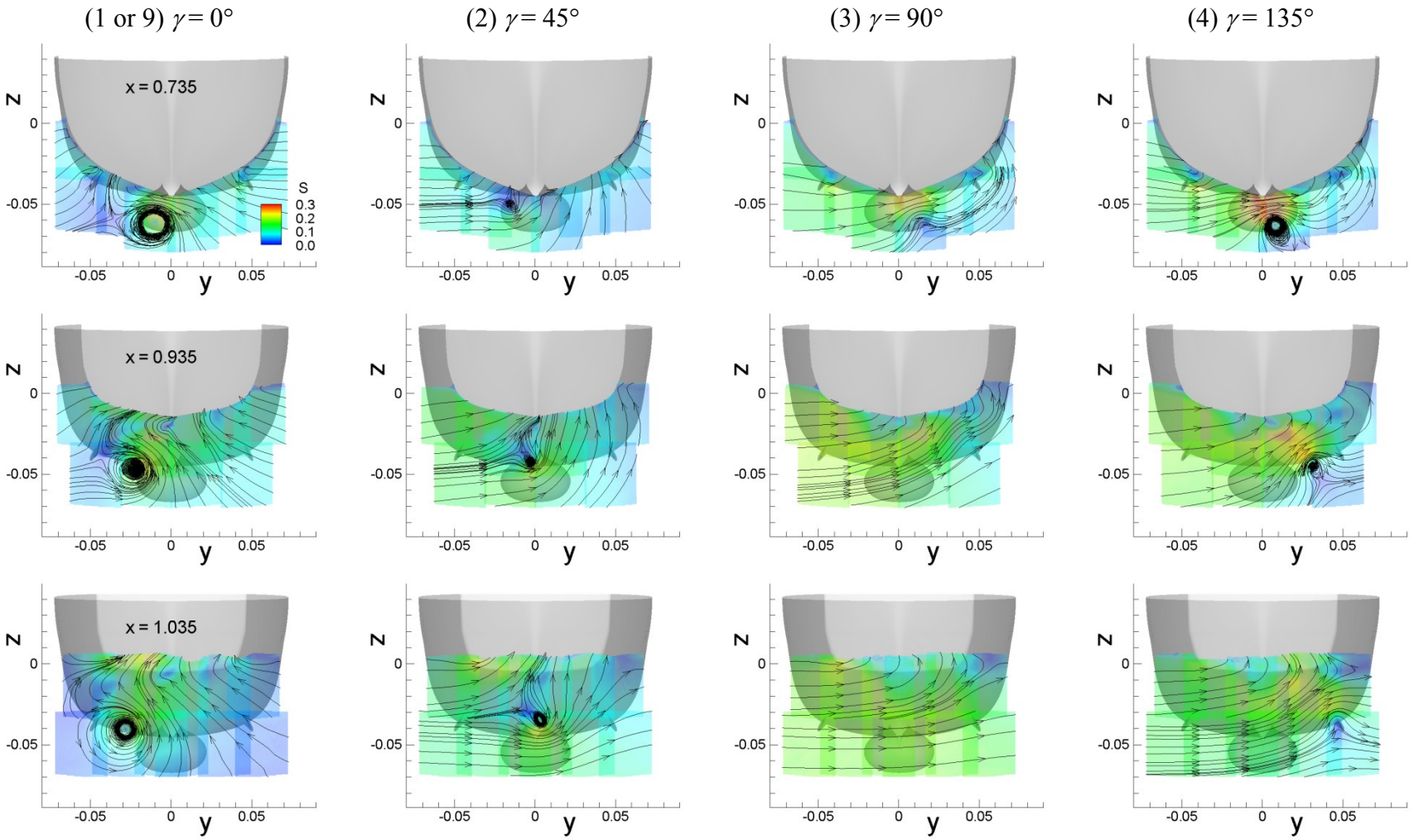

Figure 6-52–Continued

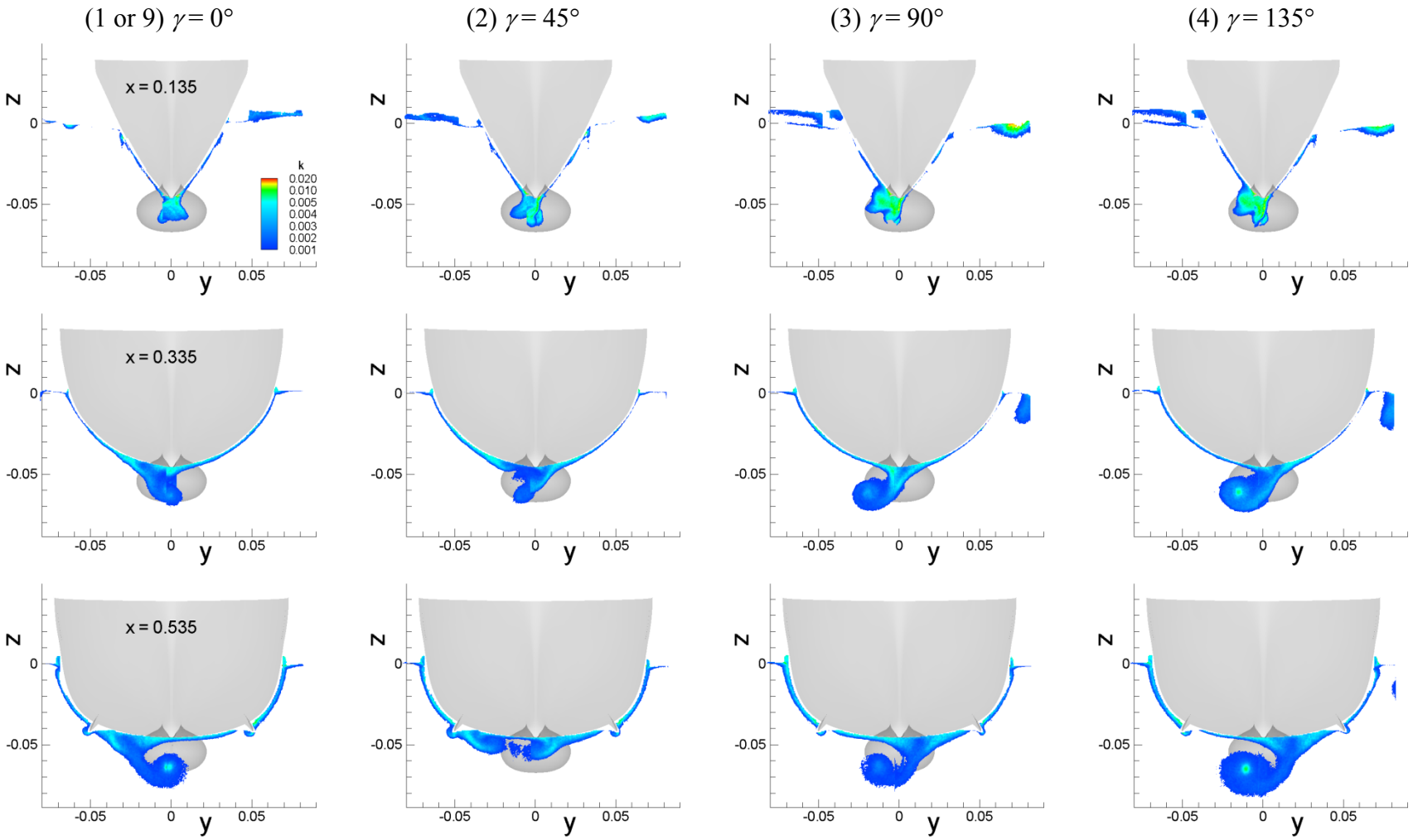

Figure 6-53 Phase-averaged turbulent kinetic energy *k* field for pure yaw test.

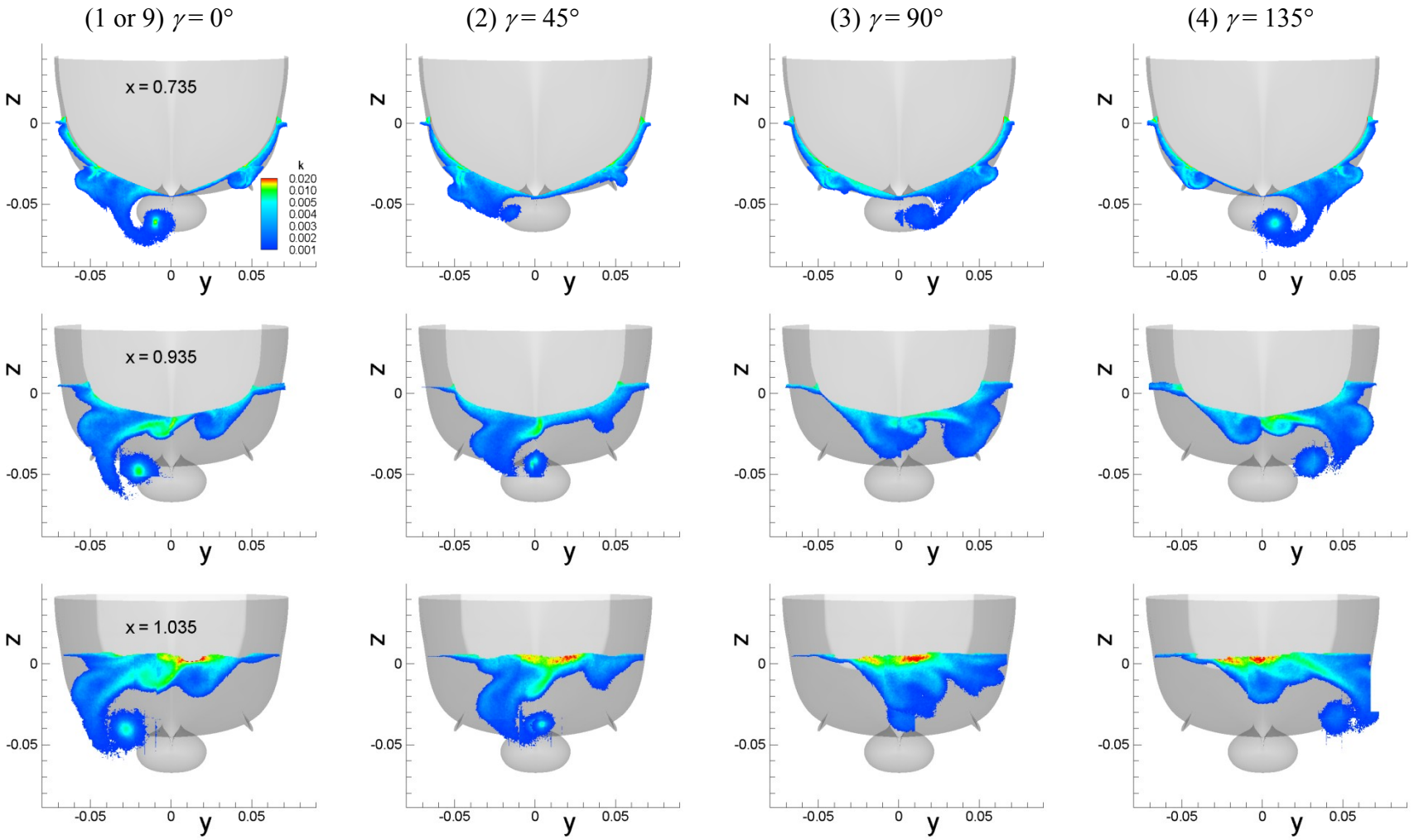

Figure 6-53–Continued

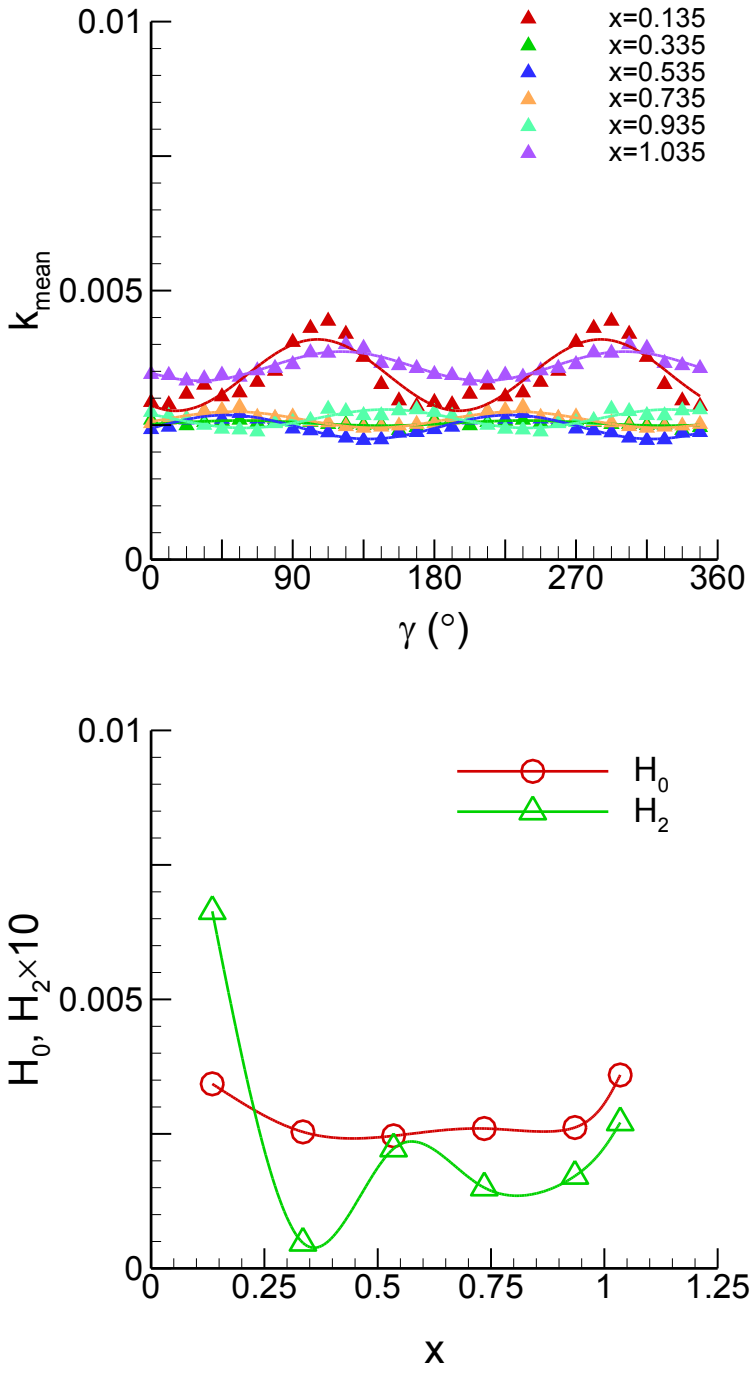

Figure 6-54 Average turbulent kinetic energy k_{mean} (top) and FS harmonics (bottom).

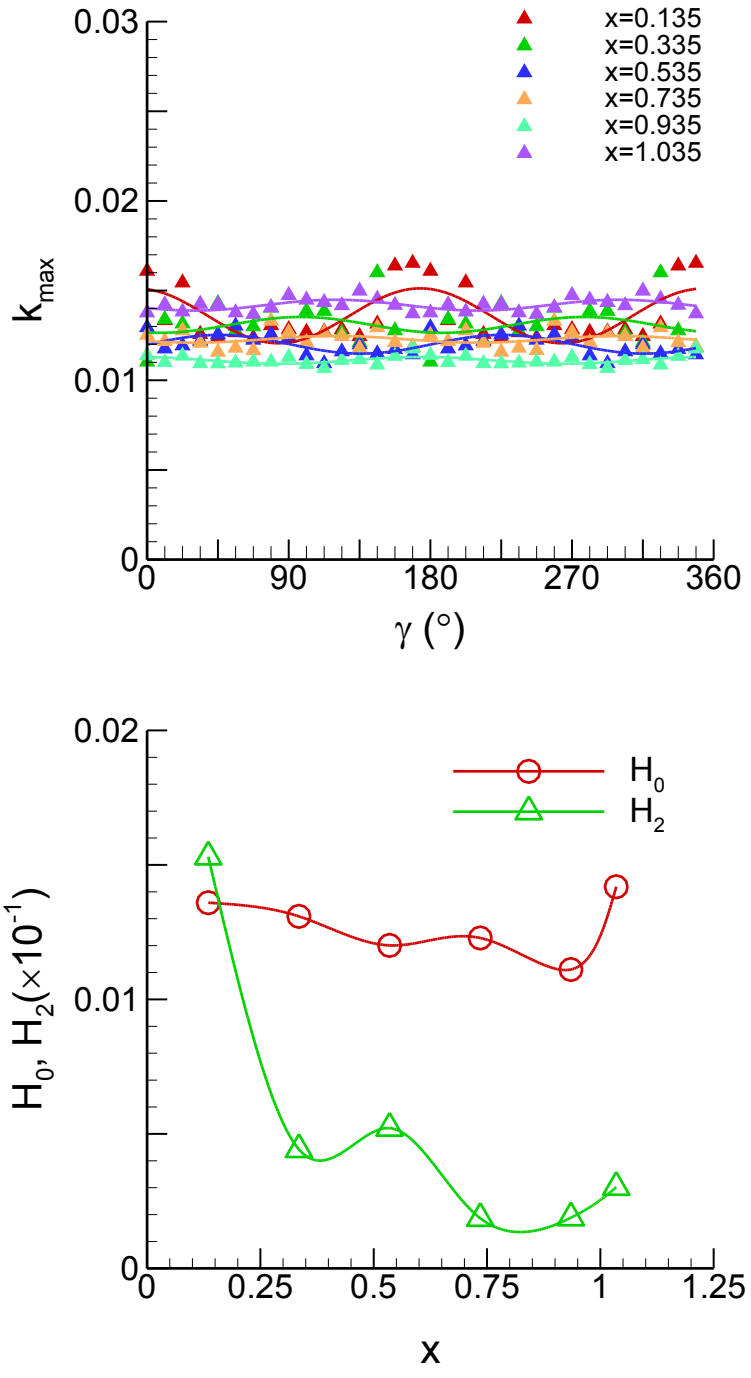

Figure 6-55 Maximum turbulent kinetic energy k_{max} (top) and FS harmonics (bottom).

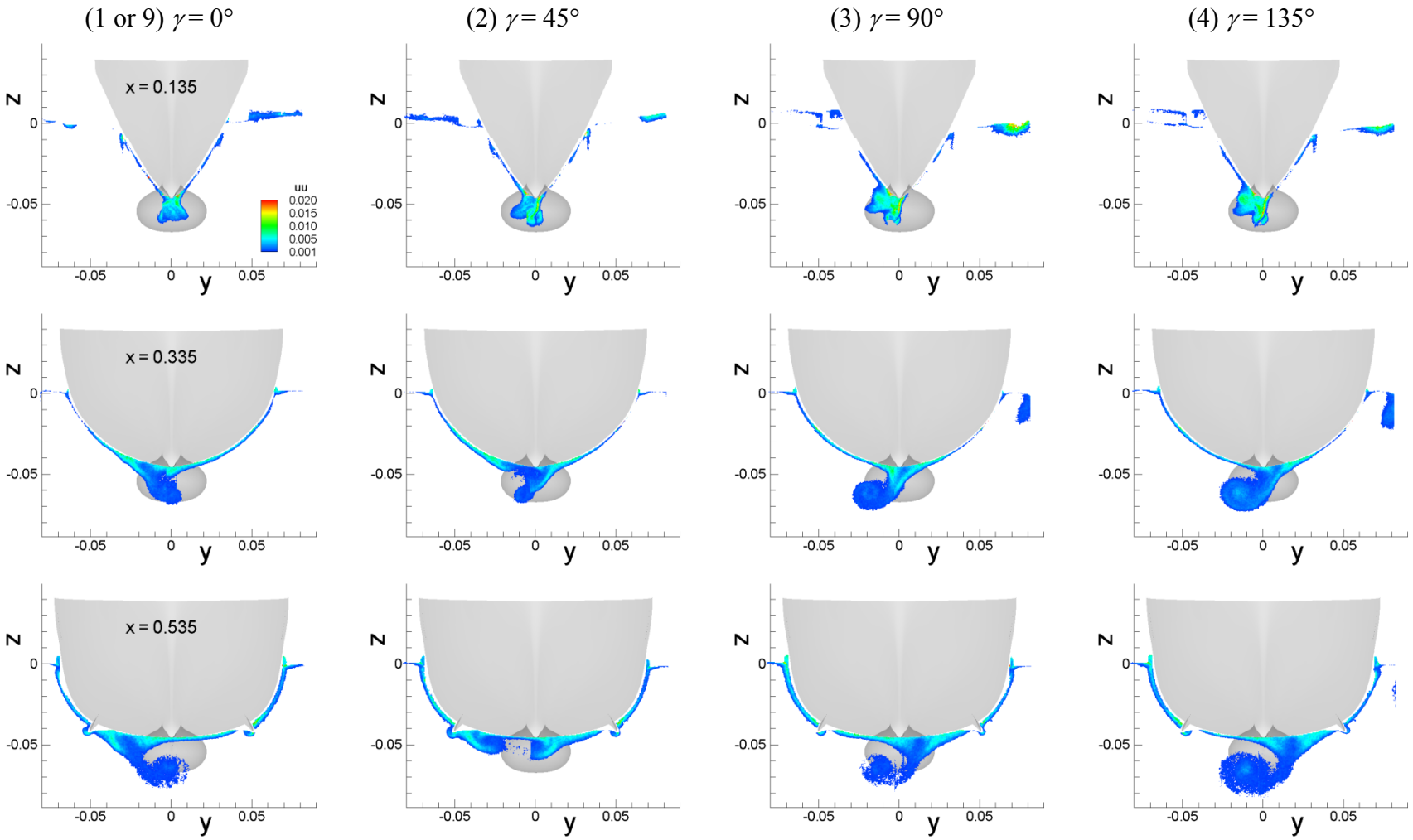

Figure 6-56 Phase-averaged Reynolds stress *uu* field for pure yaw test.

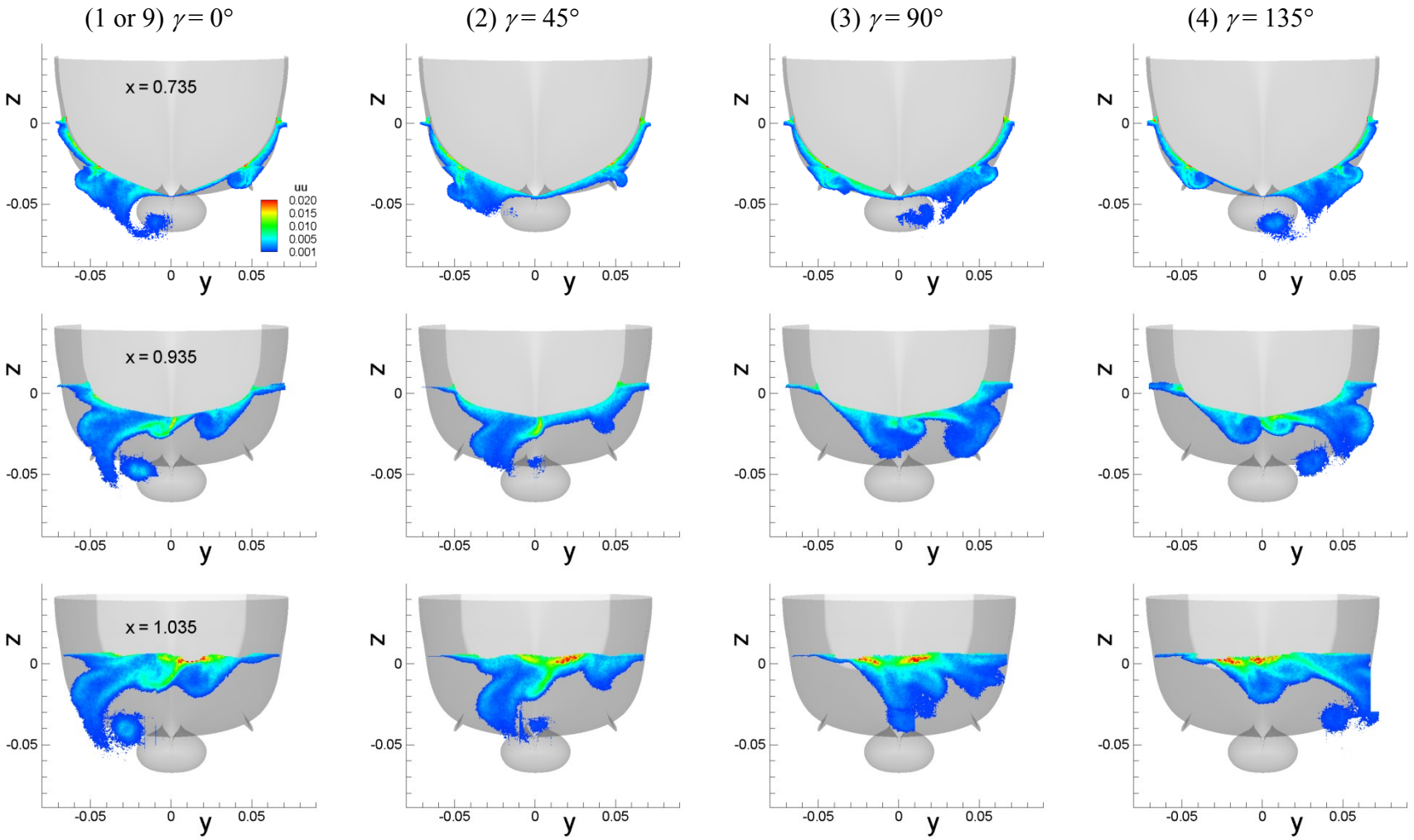

Figure 6-56–Continued

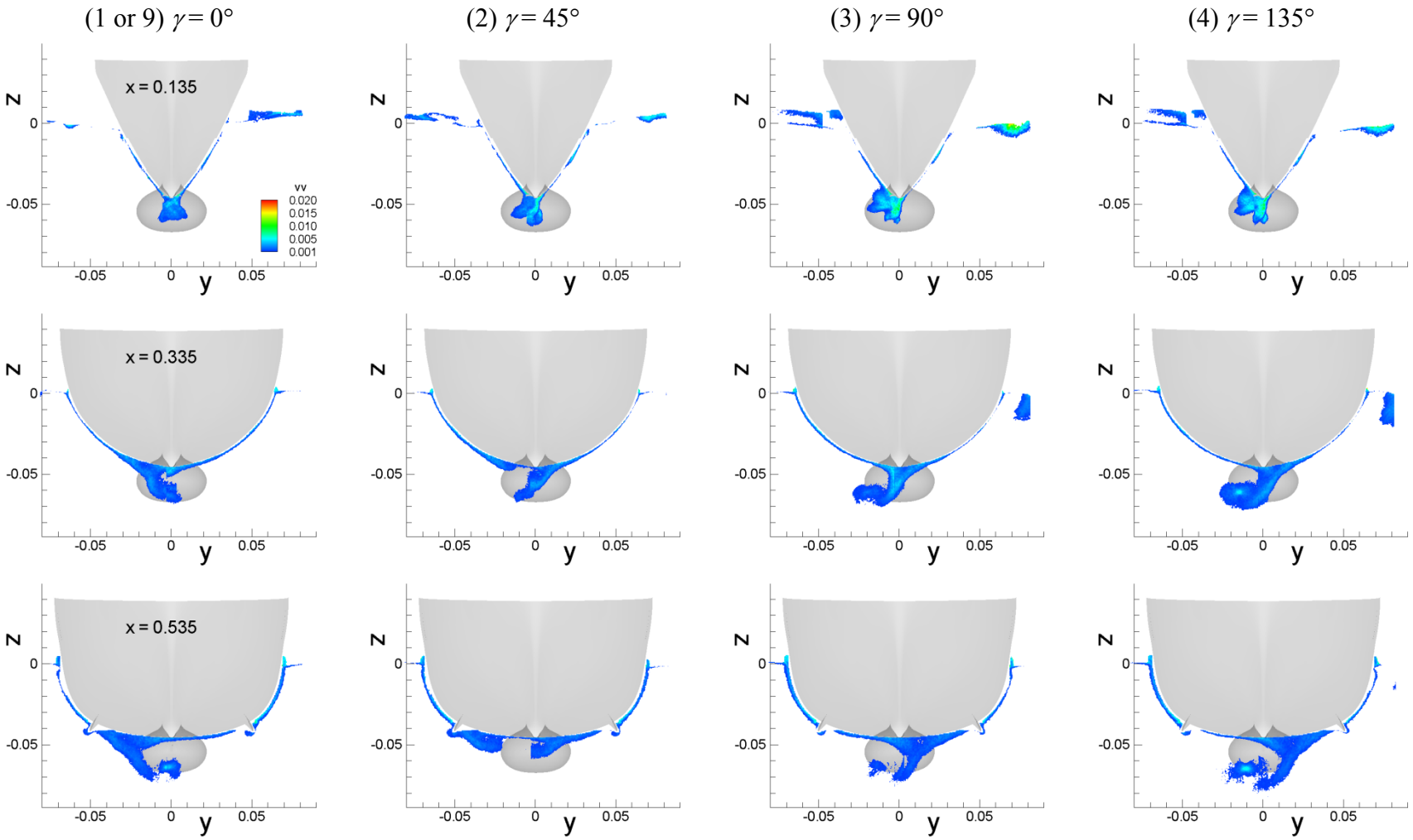

Figure 6-57 Phase-averaged Reynolds stress *vv* field for pure yaw test.

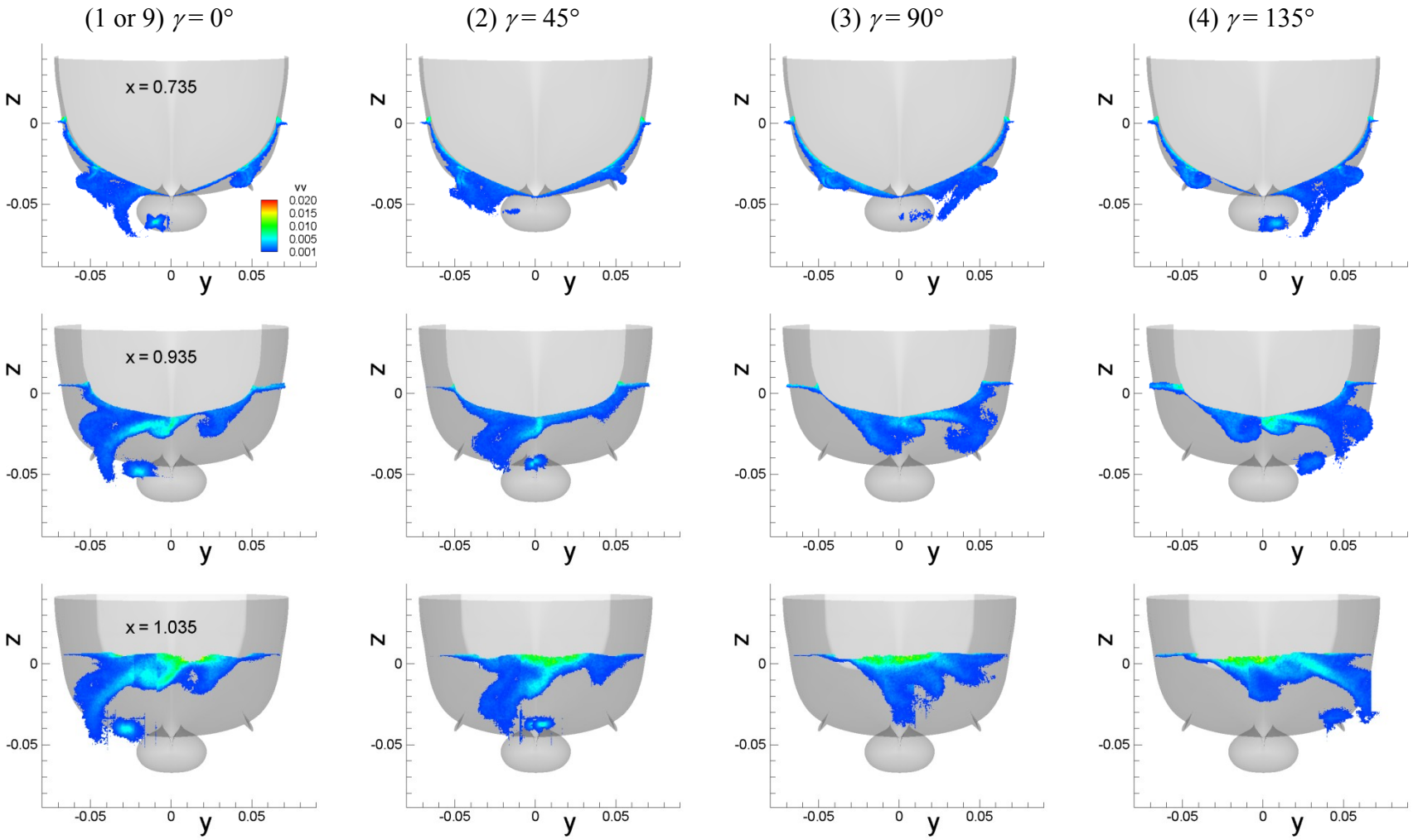

Figure 6-57–Continued

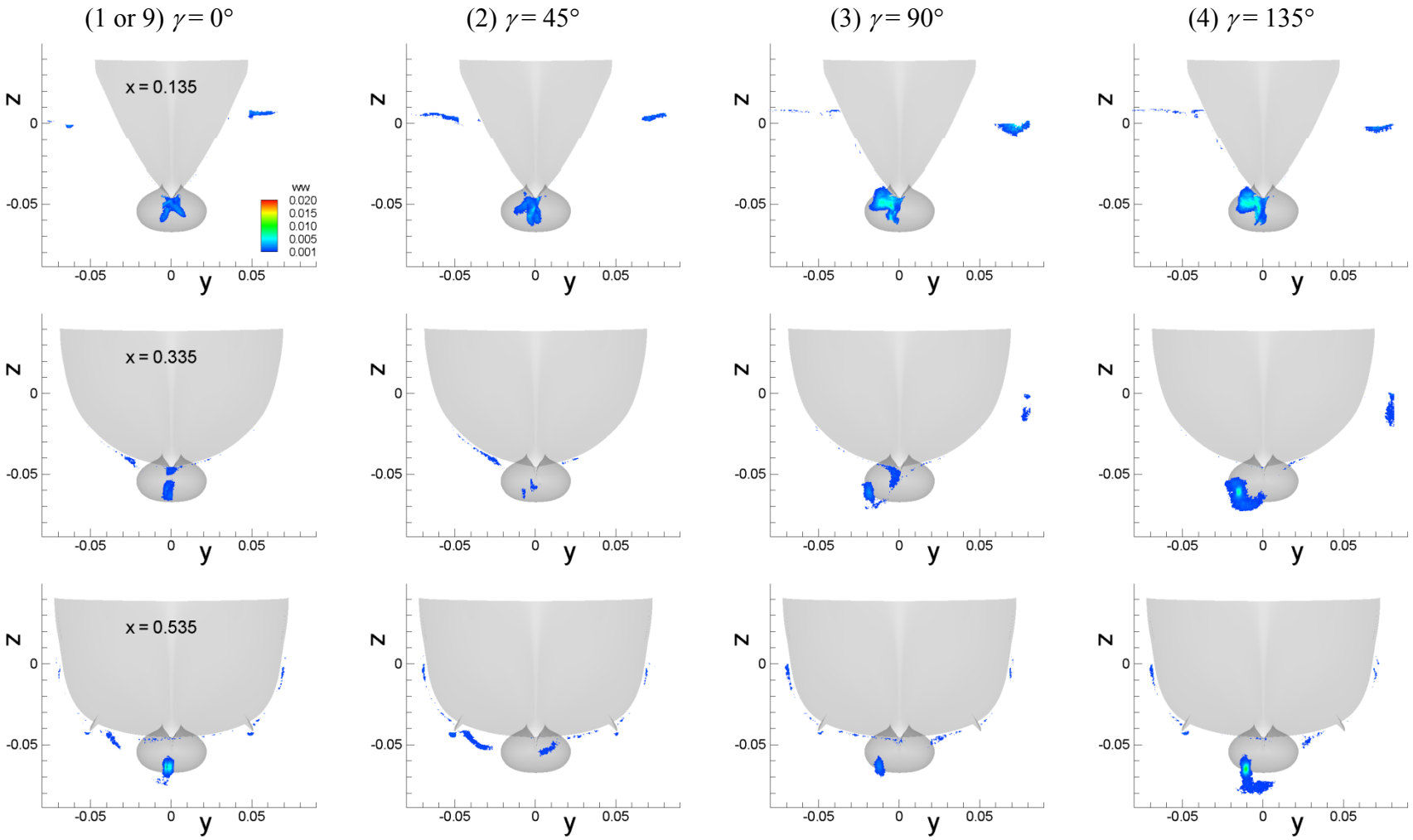

Figure 6-58 Phase-averaged Reynolds stress *ww* field for pure yaw test.

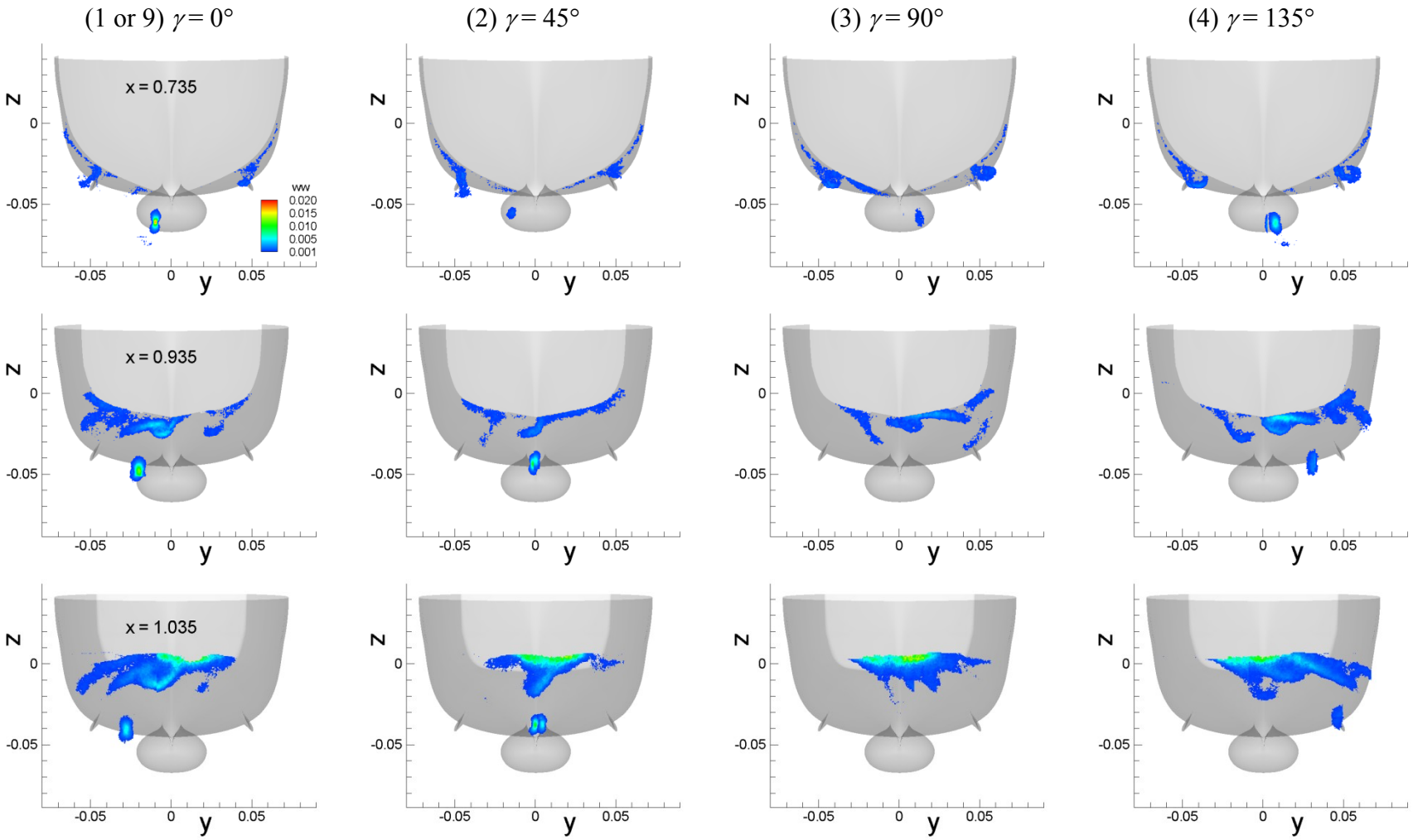

Figure 6-58–Continued

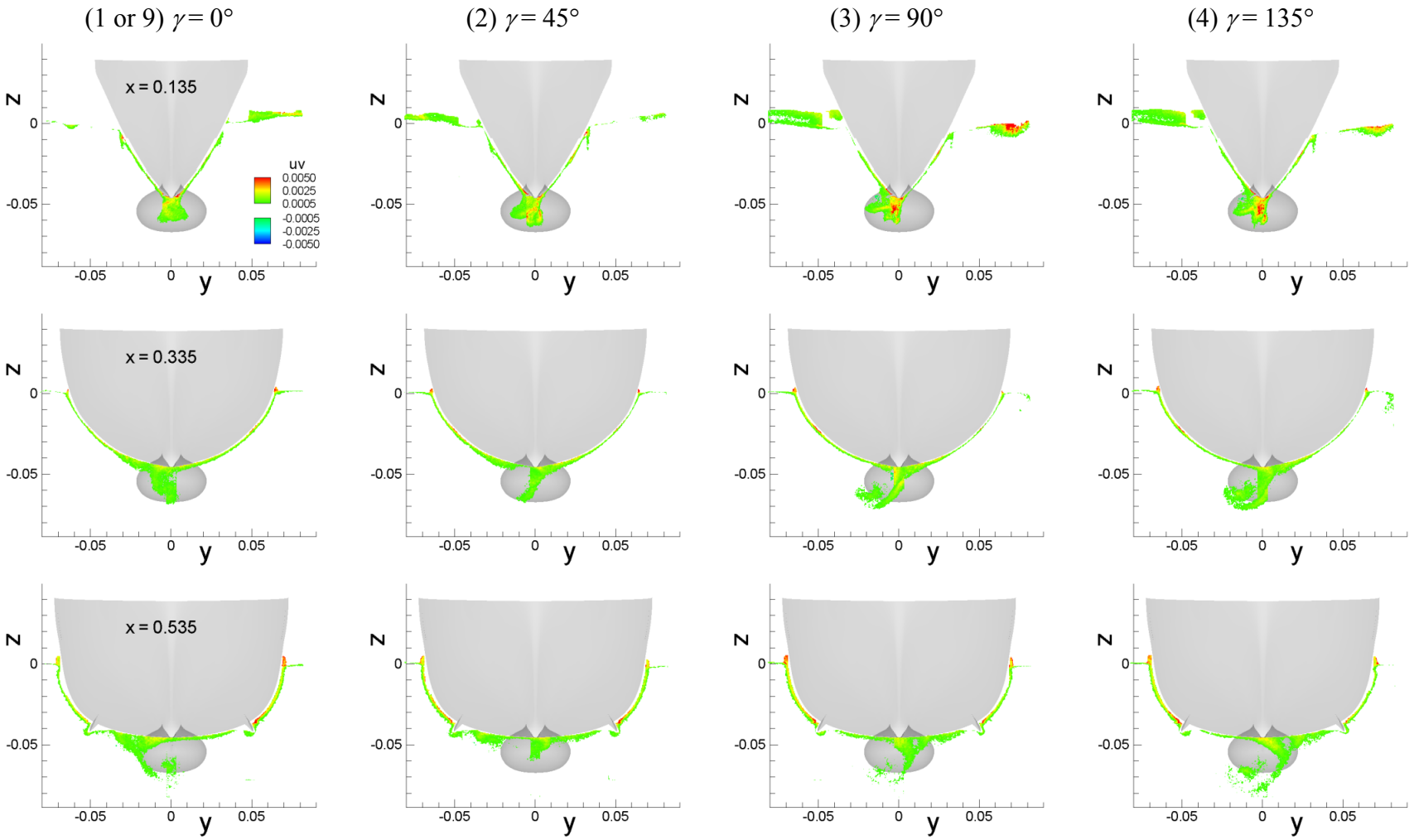

Figure 6-59 Phase-averaged Reynolds stress *uv* field for pure yaw test.

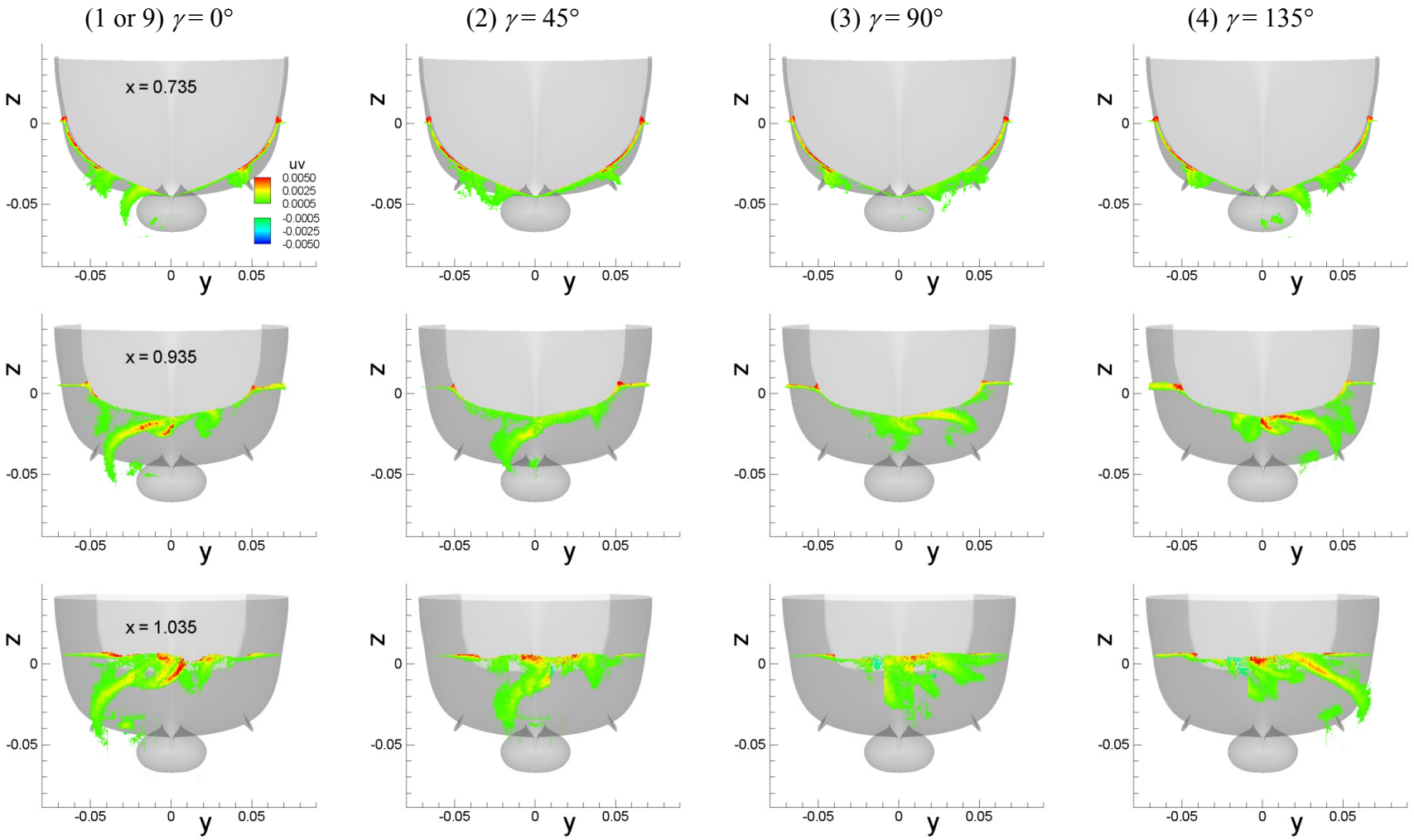

Figure 6-59–Continued

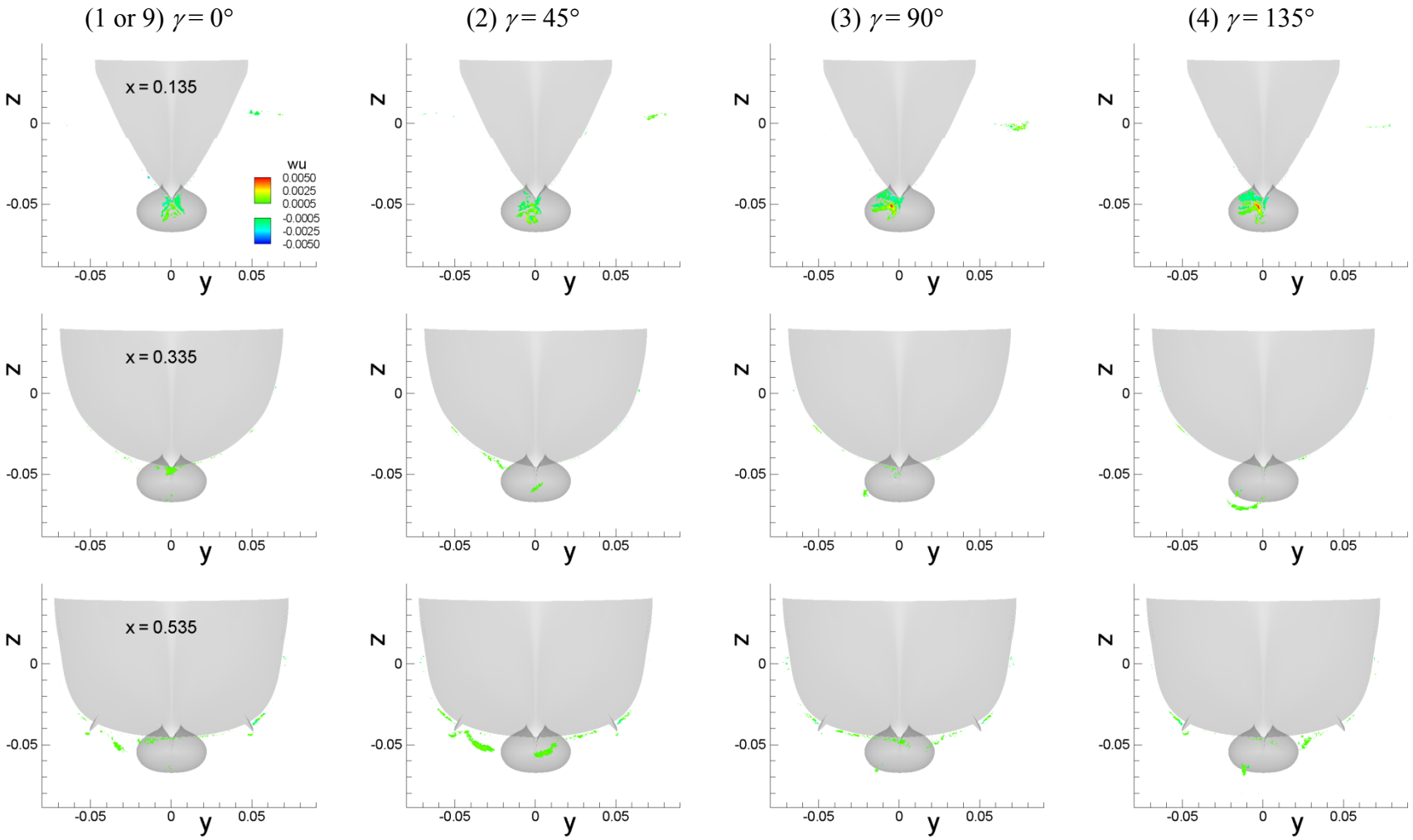

Figure 6-60 Phase-averaged Reynolds stress *uw* field for pure yaw test.

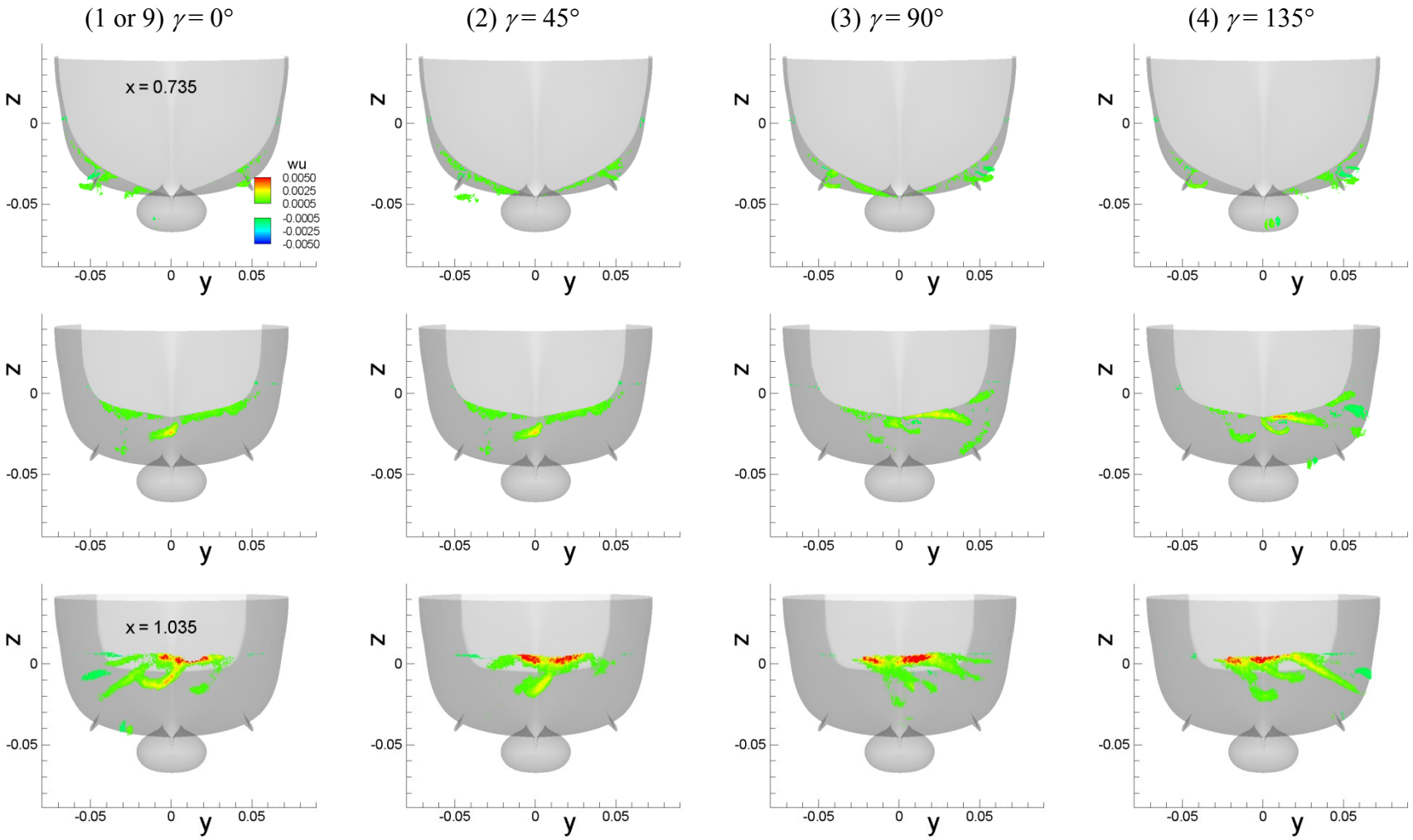

Figure 6-60–Continued

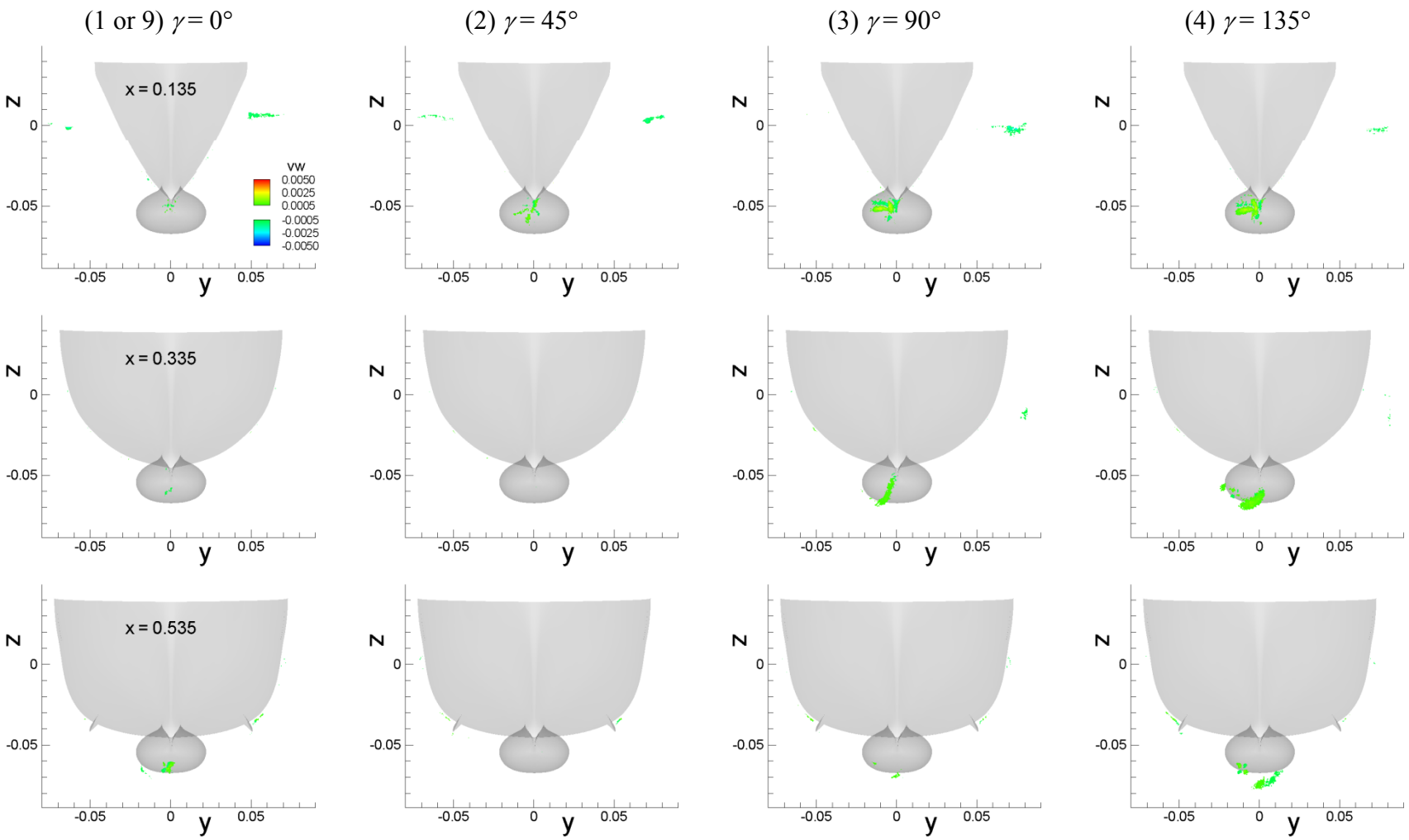

Figure 6-61 Phase-averaged Reynolds stress *vw* field for pure yaw test.

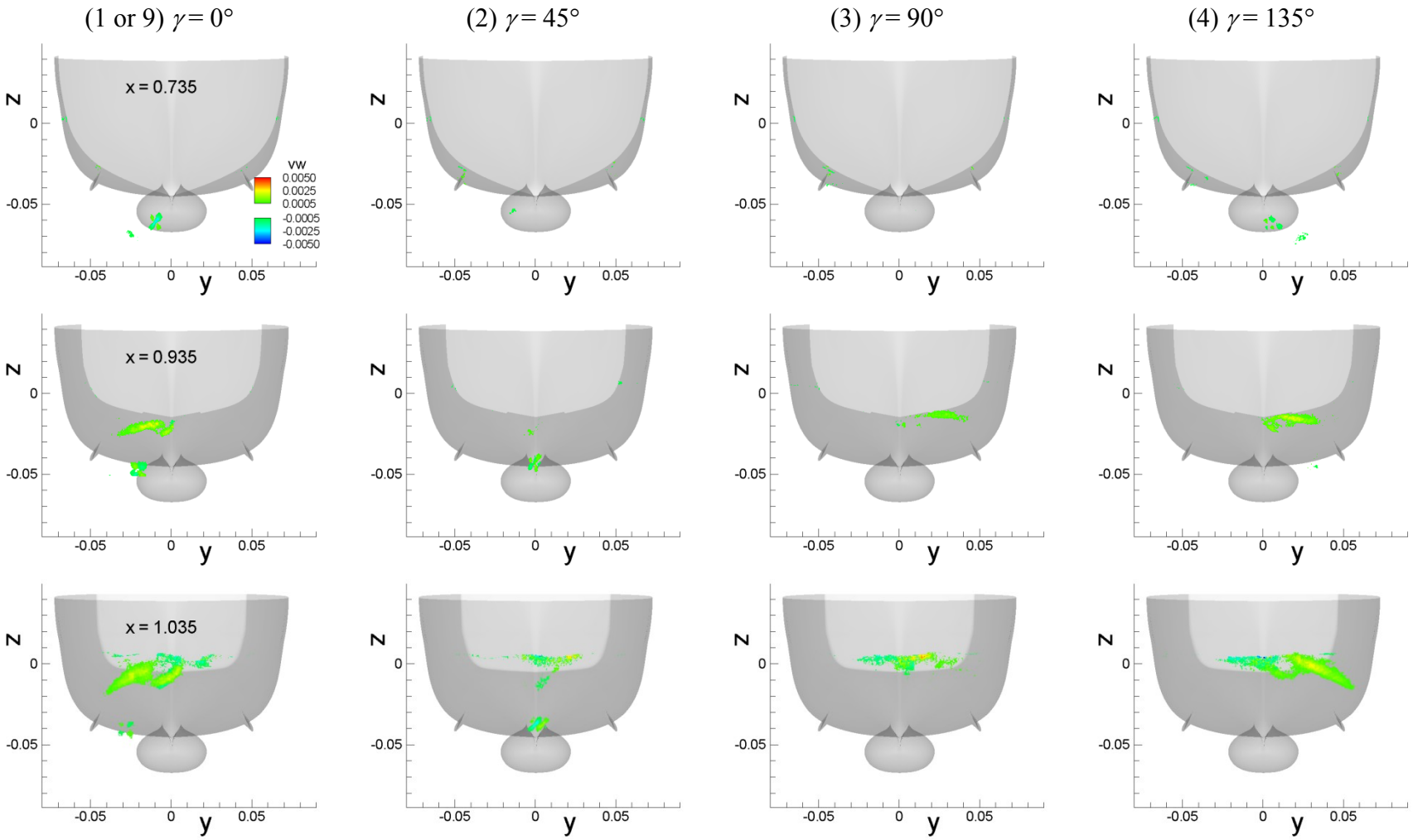

Figure 6-61–Continued

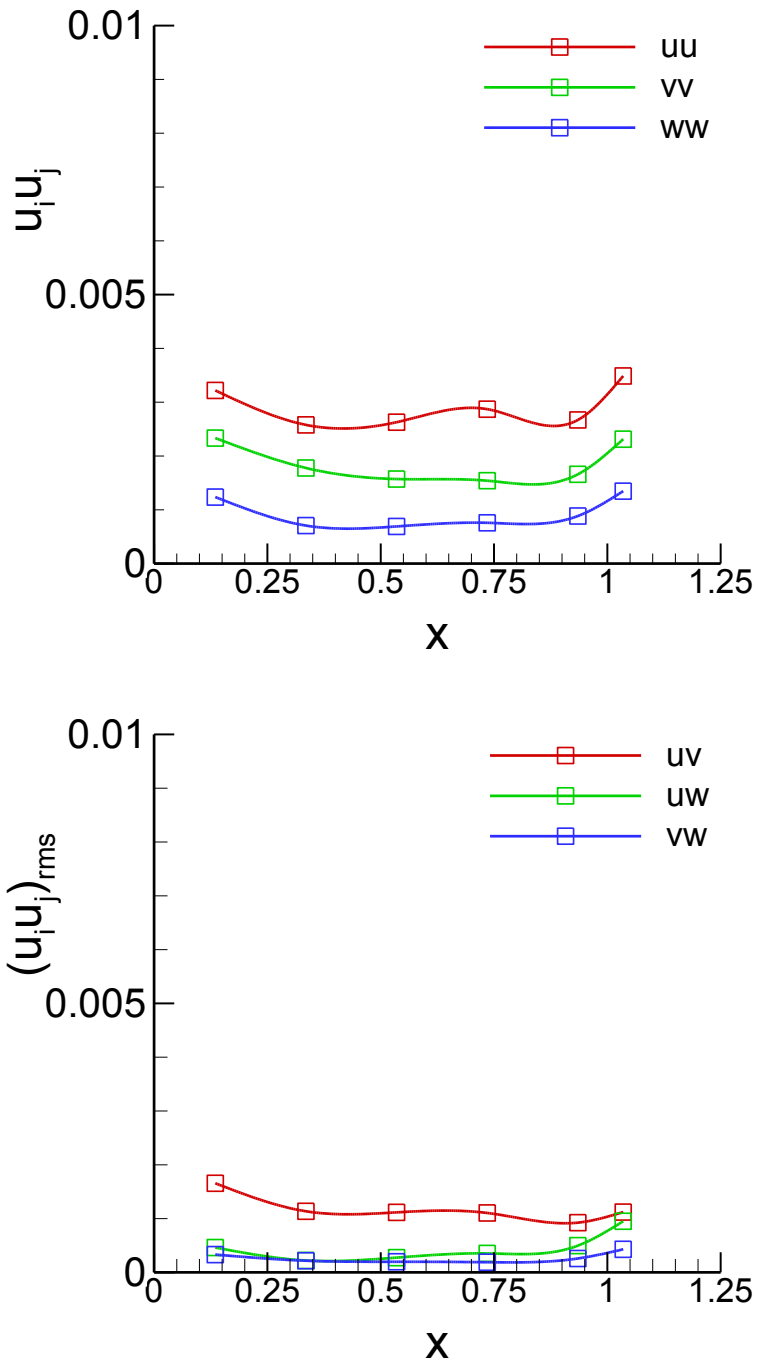

Figure 6-62 Average Reynolds normal (top) and shear (bottom) stresses for k_{mean}.

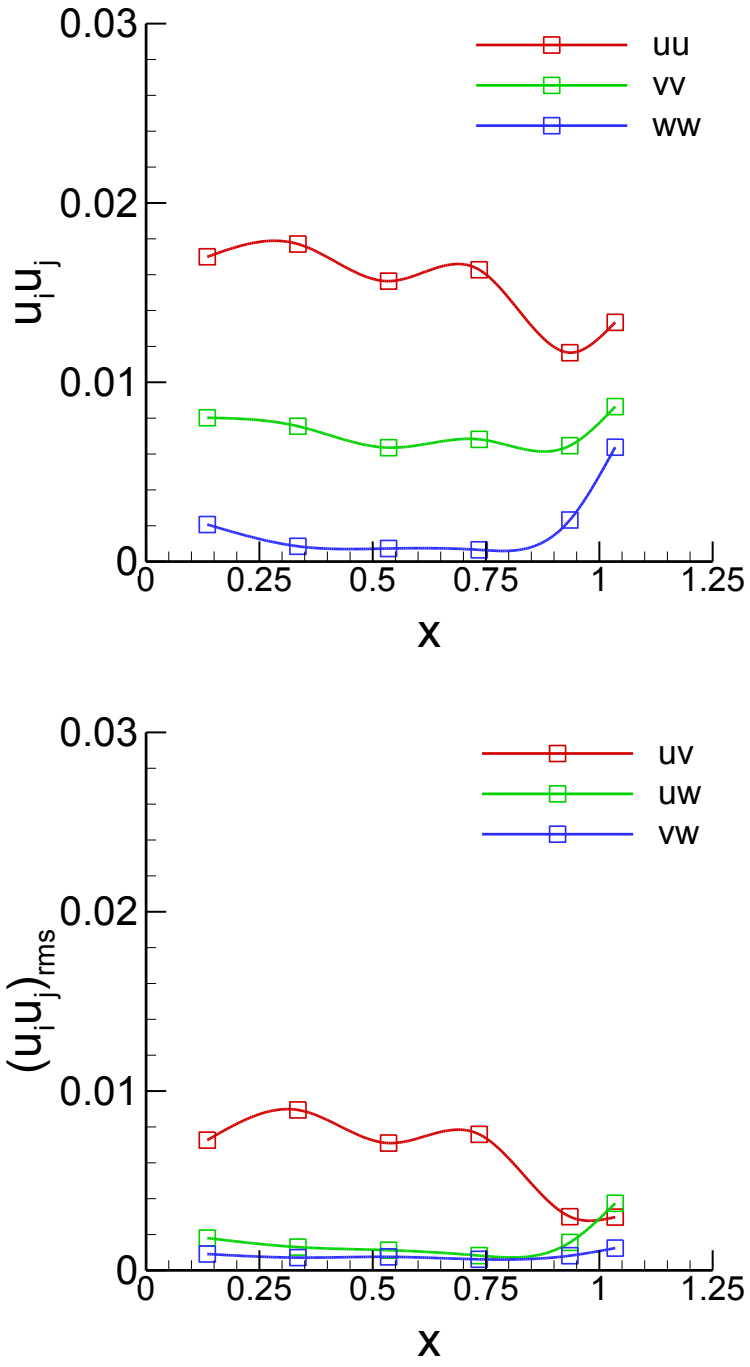

Figure 6-63 Average Reynolds normal (top) and shear (bottom) stresses for k_{max}.

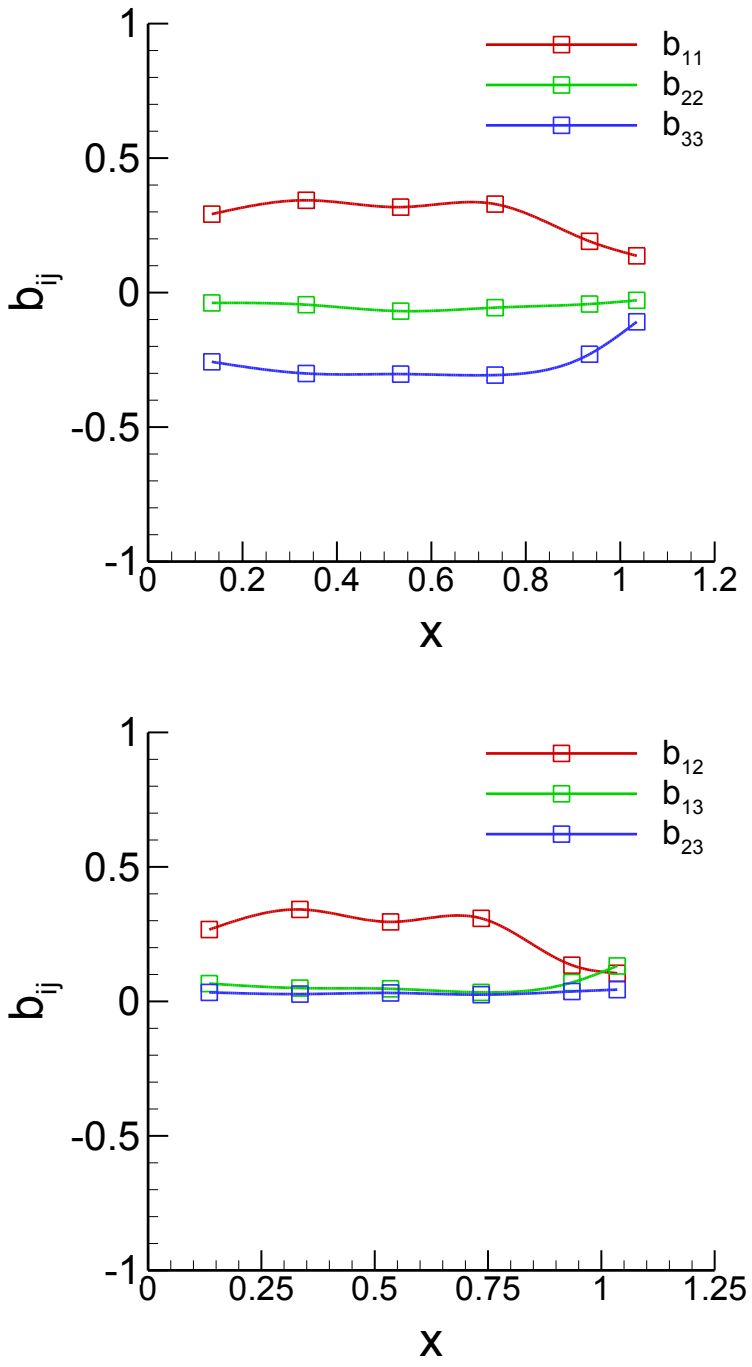

Figure 6-64 Average anisotropy b_{ij} of normal (top) and shear (bottom) Reynolds stresses for k_{max}.

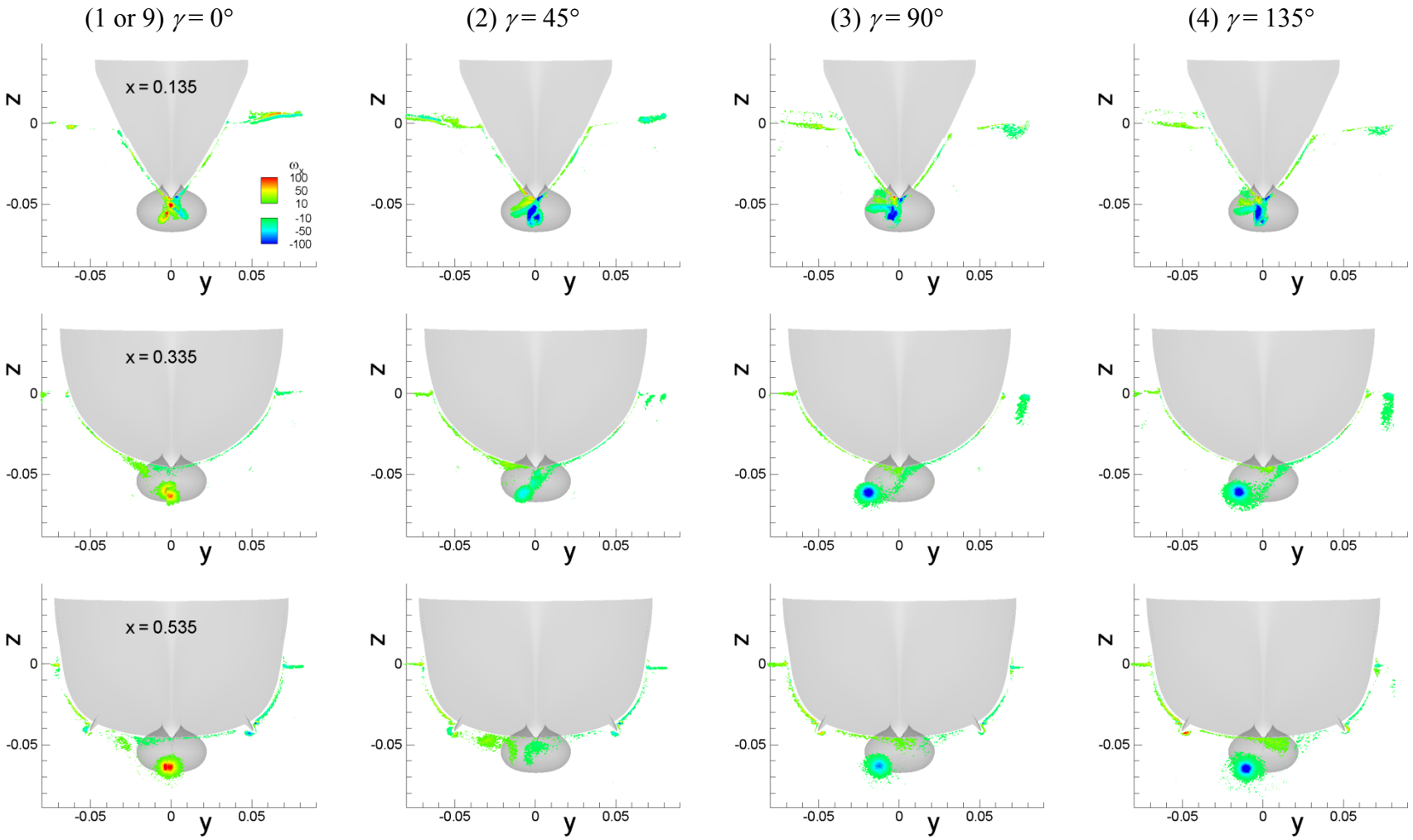

Figure 6-65 Axial vorticity ω_x field for pure yaw test.

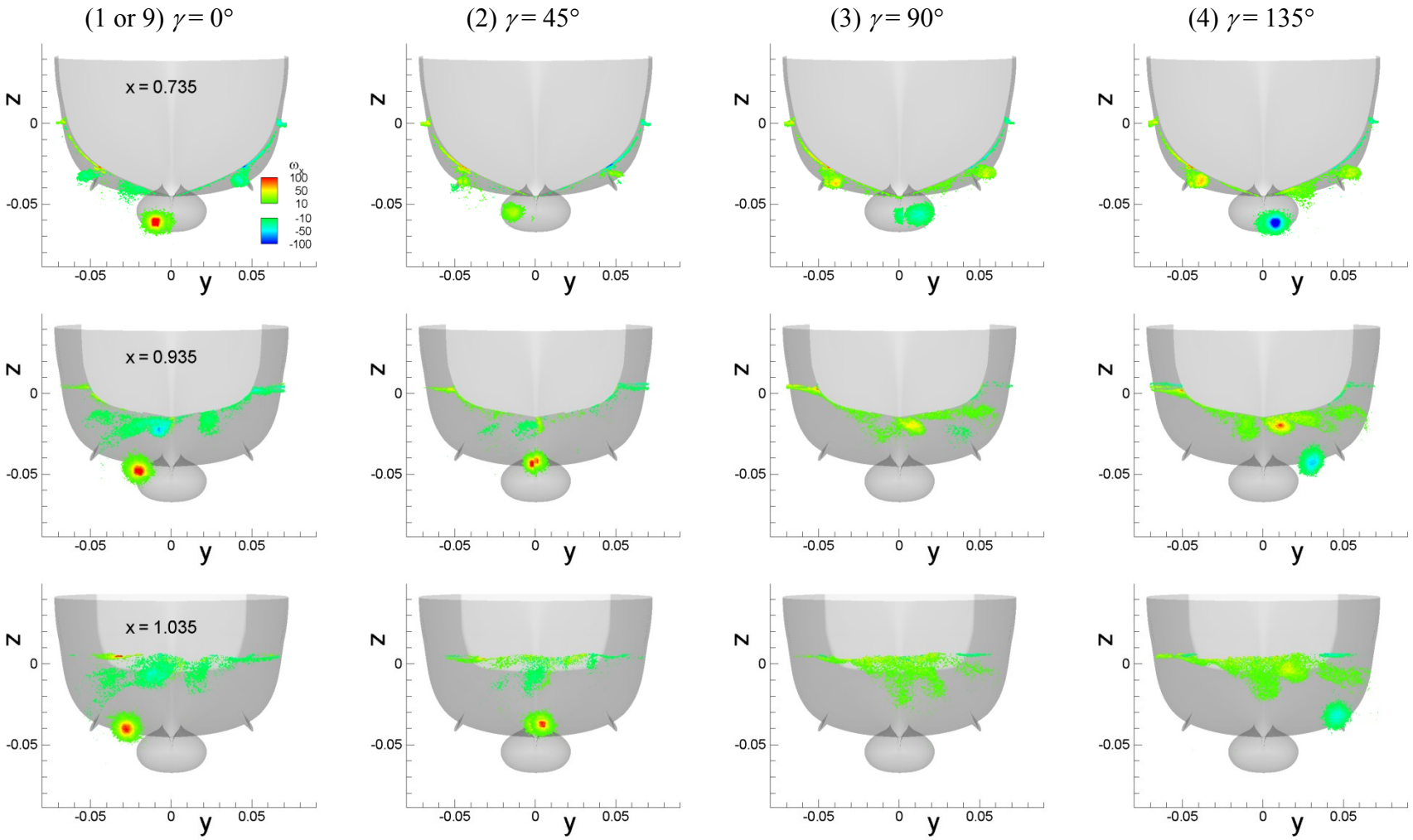

Figure 6-65–Continued

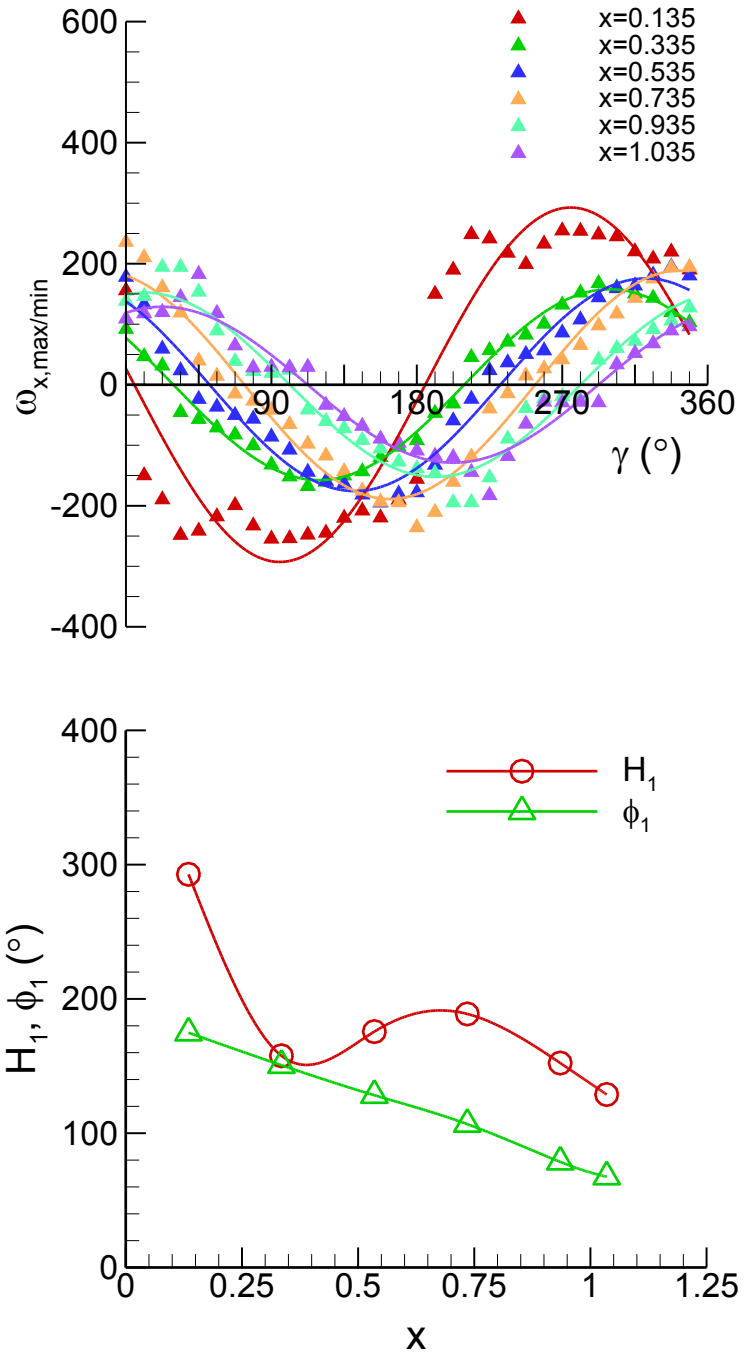

Figure 6-66 Time histories of the maximum/minimum axial vorticity ω_x values of sonar dome (SD) vortex (top) and FS harmonics (bottom) for pure yaw.

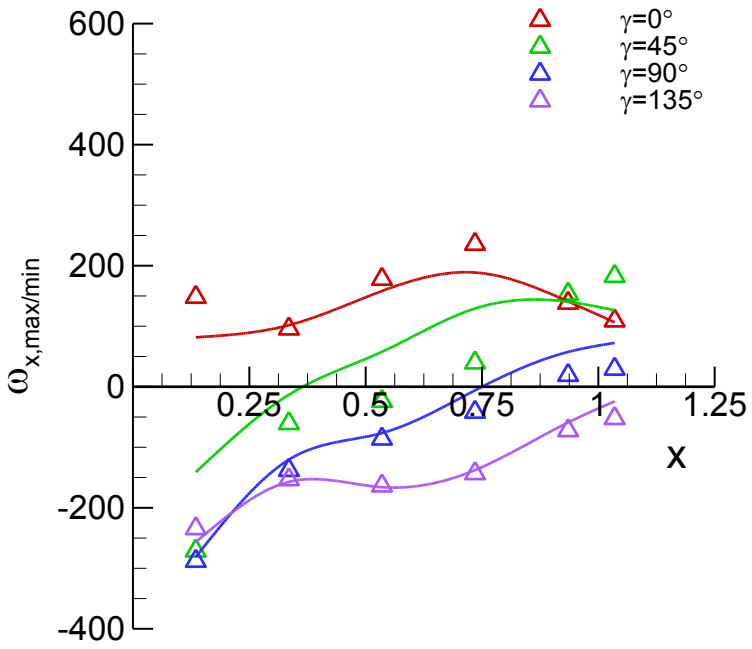

Figure 6-67 Measured (symbols) and reconstructed (lines) $\omega_{x,max/min}$ values of the sonar dome (SD) vortex for pure yaw.

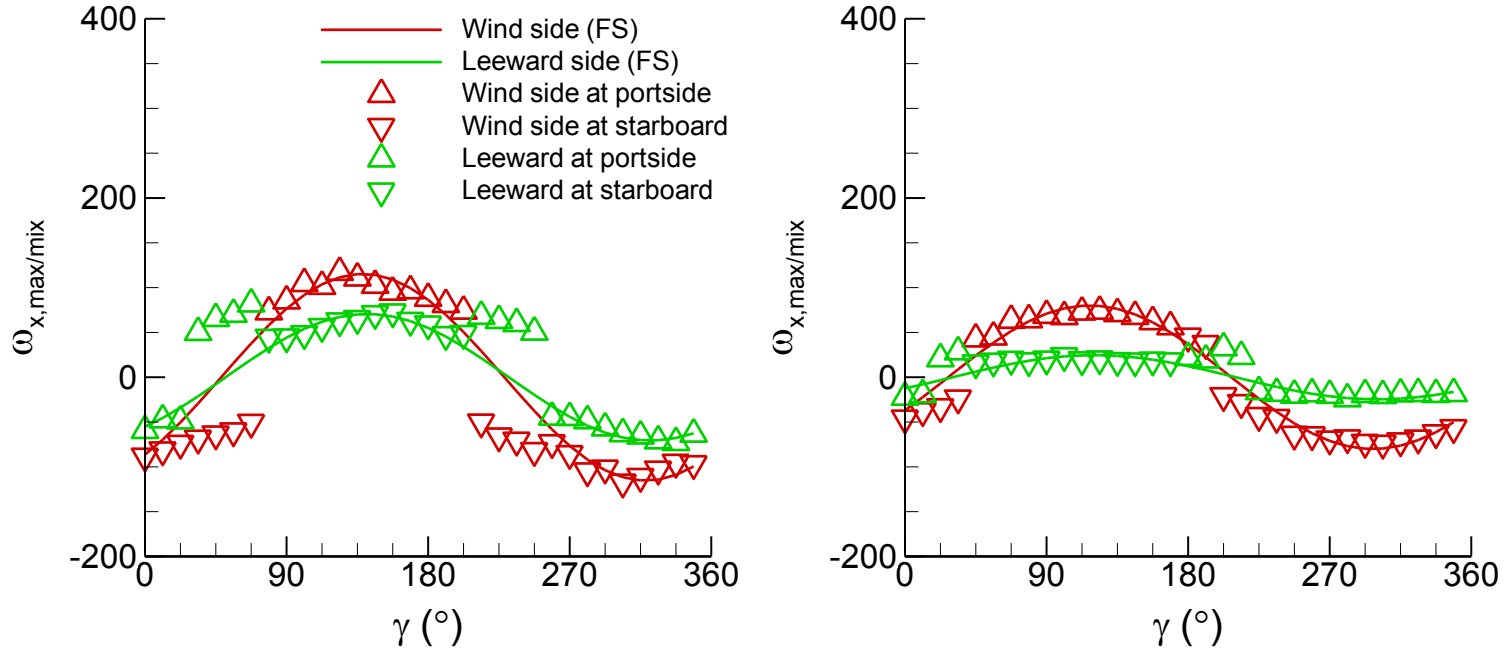

Figure 6-68 Time histories of the maximum/minimum axial vorticity ω_x values of the bilge keel (BK) vortices at x = 0.535 (left) and x = 0.735 (right), respectively, for pure yaw.

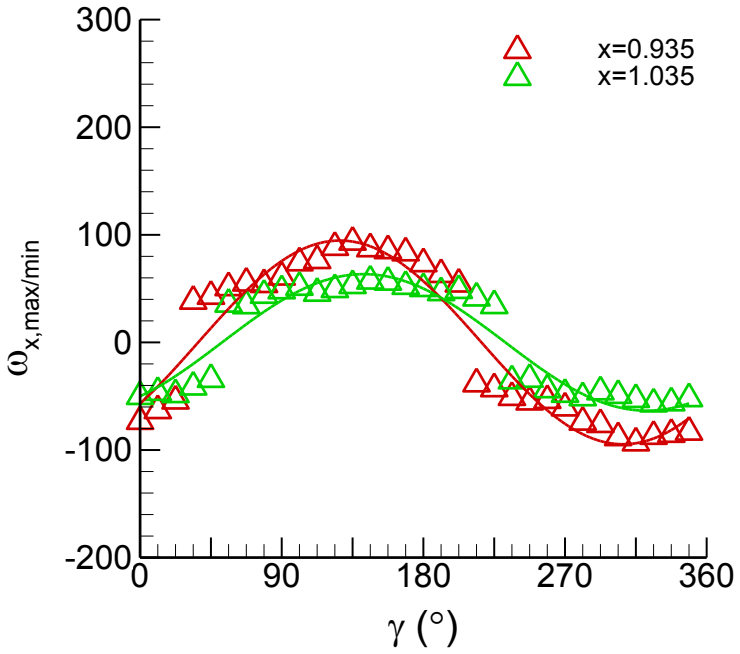

Figure 6-69 Time histories of the maximum/minimum axial vorticity ω_x values of the aft-body keel (AK) vortex for pure yaw test.